# TOPOLOGY OPTIMIZATION WITH MULTIPLE MATERIALS, MULTIPLE CONSTRAINTS, AND MULTIPLE LOAD CASES

A Dissertation
Presented to
The Academic Faculty

By

Xiaojia Shelly Zhang

In Partial Fulfillment
of the Requirements for the Degree
Doctor of Philosophy in the
School of Civil and Environmental Engineering

Georgia Institute of Technology

December 2018

**TOPOLOGY OPTIMIZATION WITH MULTIPLE MATERIALS, MULTIPLE CONSTRAINTS, AND MULTIPLE LOAD CASES**

Approved by:


Dr. Glaucio H. Paulino, Advisor
School of Civil and Environmental Engineering
*Georgia Institute of Technology*

Dr. Alexander Shapiro
School of Industrial and Systems Engineering
*Georgia Institute of Technology*

Dr. Yang Wang
School of Civil and Environmental Engineering
*Georgia Institute of Technology*

Dr. Eric de Sturler
Department of Mathematics
*Virginia Polytechnic Institute and State University*

Dr. Alok Sutradhar
Department of Mechanical and Aerospace Engineering
*Ohio State University*

Dr. Lucia Mirabella
Corporate Technology
*Siemens Corporation*



Date Approved: July 30, 2018

*To my family*

## ACKNOWLEDGMENTS

First and foremost, I would like to express my deep gratitude to my advisor, Professor Glaucio Paulino. He introduced me to the field of topology optimization, guided me through my graduate studies, and gave me the freedom to explore exciting research topics. I would like to thank him for offering me his tremendous support and encouragement from my early days as an undergraduate student, for his invaluable help and suggestions during my academic journey, and for providing me with numerous and exceptional opportunities to develop my academic and professional skills. I am also sincerely grateful to Berta, Professor Paulino's wife, who has offered me her kind support and warm hospitality during my graduate school years. I would not be where I am today without their selfless help and unwavering belief in me for the past six years for which I will always be grateful.

I am extremely fortunate to collaborate with many wonderful people throughout my graduate studies. These collaborations have led to not only numerous research topics but also long-lasting friendships. I would like to acknowledge Bill Baker, Adeildo Ramos Jr., and Eric de Sturler for their input to this thesis. I am grateful to Bill Baker for his support and guidance during my internship at Skidmore, Owings & Merrill (SOM), for his vision and insight about structural engineering practice, and for his initiation and valuable suggestions for the collaborative lectures about Michell's and Hemp's conditions for optimal structures, which led to the work in Chapter 2. I am thankful to Adeildo Ramos Jr., for many fruitful conversations and his contributions to Chapters 3, 4, and 5. His relentless passion for research always inspires me. I would like to extend my thanks to the entire Ramos family for being wonderful hosts and offering their continuous hospitality and generosity during my visits to Maceió. I am grateful to Eric de Sturler for his tremendous help and constant support during my graduate studies, for enriching my experience and expanding my knowledge with stimulating discussions, and for his contributions to Chapter 6. Sincere thanks are due to Alex Shapiro for his insights, guidance, and support during my

academic journey. He is an excellent mentor, and every discussion with him was pleasant and inspiring. I am grateful to Ivan Menezes for his continuous help, support, and encouragement throughout the years and for his incredible hospitality and generosity during my visits to Rio de Janeiro. I would like to thank Anderson Peirera who also made my visits to Brazil so pleasant. Sincere thanks are due to Professor Gholamreza Mesri, who helped me tremendously during my undergraduate and early graduate years. I very gratefully thank Drs. Eric de Sturler, Alex Shapiro, Yang Wang, Alok Sutradhar, and Lucia Mirabella for their support, suggestions, and taking part in my Ph.D. thesis committee.

I gratefully recognize the financial support of the US National Science Foundation through projects #1559594 (formerly #1335160) and #1321661. I am grateful for the endowment provided by the Raymond Allen Jones Chair at the Georgia Institute of Technology. In addition, I am very thankful to SOM for providing me with the internship experience.

I would also like to thank my friends and colleagues, including Aobai Wang, Heng Chi, Ke Liu, Evgueni Filipov, Cameron Talischi, Sofia Leon, Tomas Zegard, Tuo Zhao, Daniel Spring, Junho Chun, Arun Gain, Pradeep Phanisri, Kyoungsoo Park, Larissa Novelino, Fernando Senhora, Yang Jiang, Weichen Li, Emily Sanders, Erol Unal, Oliver Giraldo, Javier Vila Moran, Wei Peng, Xi Liu, Dan Li, Xinjun Dong, Xiaotang Du, Yang Zhang, Tao Zhu, Chen Zhang, Hugo Bastos, and Guilherme Barros. I am incredibly thankful for the camaraderie, support, kindness, and entertainment they have provided during my graduate life. I own my special gratitude to Heng Chi, for his invaluable help and support over the years and for countless fruitful conversations we had; Evgueni Filipov, for his selfless help and invaluable suggestions and for all the inspirations during each discussion; Cameron Talischi, for donating his time and providing insightful advice and guidance throughout the years; Aobai Wang, for her genuine support, encouragement, and lifelong friendship; and Ke Liu, for his constant support and all the stimulating conversations we had.

My deepest love and gratitude are for my family, my mother, Yanhua, my father, Jiguo,

and Lily and Cookie, for their unconditional love, constant support, encouragement, companionship, humor, and strength. My parents are ones of the strongest people I know, their wisdom, vision, and guidance have a profound influence on my life and have shaped my character. No words can describe my appreciation for everything they have done for me. I am proud to be their daughter, and it is with great pleasure that I dedicate this thesis to my family.

## TABLE OF CONTENTS

## LIST OF TABLES

## LIST OF FIGURES

## LIST OF SYMBOLS

$\alpha$ Exponent coefficient used in the OC method to define $\boldsymbol{y}_i$

$\alpha_{\text{select}}$ Threshold of the material selecting algorithm

$\alpha_{\text{Top}}$ Resolution of the structural topology

$\alpha_f$ Filter value

$\alpha_k$ Step length at iteration $k$ in the line search scheme

$\boldsymbol{\rho}^*$ Optimal solution obtained by the standard algorithm in the density-based method

$\boldsymbol{\xi}$ Random vector with its entries drawn from the Rademacher distribution

$\delta\Omega$ External virtual work of the structure

$\delta\boldsymbol{u}^j$ The virtual displacment vector at location $\mathbf{r}^j$

$\delta U$ Internal virtual work of the structure

$\eta$ Damping factor in the update scheme

$\gamma$ Scale factor in the damping scheme

$\Gamma, \Gamma_0$ Tikhonov regularization parameters

$\gamma_i, \beta_i, \hat{M}$ Ogden material parameters

$\hat{\boldsymbol{\rho}}^S$ Optimal solution obtained by the randomized algorithm in the density-based method

$\hat{\boldsymbol{x}}^S$ Optimal solution obtained by the randomized algorithm in the GSM

$\hat{C}$ Estimated objective function by the randomized algorithm

$\kappa$ Scale parameter of the step length in the line search scheme

$\lambda$ Linearized stretch

$\Lambda, \mu$ Lamé constants

$\lambda_i$ Principal stretches

$\mathscr{E}_C$ The set of members in compression

$\mathscr{E}_T$ The set of members in tension

$\mathscr{G}^j$ the set of material indices associated with the $j$th volume constraint in the ZPR update scheme

$\Omega$ Potential energy of external loads

$\overline{\boldsymbol{\rho}}$ Filtered density vector

$\overline{\varepsilon}$ Limit on the virtual strain field in Michell's conditions

$\overline{\sigma}$ Average stress limit of tension and compression members in the modified Michell's conditions.

$\overline{\sigma}_C$ Compressive stress limit

$\overline{\sigma}_T$ tensile stress limit

$\overline{\boldsymbol{x}}_i$ Vector of filtered design variables (cross-sectional areas) for material $i$

$\overline{x}_i^{(e)}$ Filtered cross-sectional area of member $e$ for material $i$

$\phi_V^j$ Lagrange multiplier introduced for the $j$th volume constraint in the ZPR update scheme

$\phi_V^{j*}$ The optimal Lagrange multiplier introduced for the $j$th volume constraint in the dual problem of the ZPR update scheme

$\Pi$ Total potential energy

$\Pi_{\text{min}}$ Total potential energy in equilibrium configuration

$\Psi$ Strain energy function

$\Psi_i^{(e)}$ Specific energy of member $e$ for material $i$

$\Psi_{Bi}$ Bilinear strain energy function

$\Psi_{OG}$ Ogden strain energy function

$\rho$ Global equilibrium tolerance in nonlinear FEM

$\rho^{(e)}$ Density of element $e$ ($e$th design variable in the density-based method)

$\rho_{\text{min}}$ Lower bound for density in the density-based method

$\sigma^{(e)}$ Stress in truss member $e$

$\sigma_c$ Reference Cauchy stress in compression

$\sigma_{ij}$ Components of the Cauchy stress tensor

$\sigma_t$ Reference Cauchy stress in tension

$\tau$ Guard constant in the line search scheme

$\tau_{\text{opt}}$ Tolerance for the optimization process

$\tau_{\text{step}}$ Tolerance for the damping scheme

$\boldsymbol{B}^{(e)}$ Unit directional vector in global coordinates of member $e$

$\boldsymbol{b}_i(\boldsymbol{x}_1^k,...,\boldsymbol{x}_m^k)$ Sensitivity vector of the objective function $J$ with respect to $\mathbf{y}_i$ evaluated at the $k$th step

$\boldsymbol{F}$ Weighted external force matrix

$\boldsymbol{f}$ External force vector

$\boldsymbol{f}^j$ The external force applied on at location $\mathbf{r}^j$

$\boldsymbol{f}_{\text{Top}}$ External force vector in the structural topology defined by the filter

$\boldsymbol{f}_i$ External force vector for the $i$th load case

$\boldsymbol{H}$ Filter matrix for density

$\boldsymbol{K}$ Global stiffness matrix

$\boldsymbol{K}_t$ Global tangent stiffness matrix

$\boldsymbol{K}_t^{(e)}$ Tangent stiffness matrix for member $e$ in global coordinates

$\boldsymbol{k}_t^{(e)}$ Tangent stiffness matrix for member $e$ in local coordinates

$\boldsymbol{K}_t^{\text{Top}}$ Global tangent stiffness matrix for structural topology defined by filter

$\boldsymbol{L}$ Truss member length vector

$\boldsymbol{L}_i$ Vector of member length for material $i$

$\boldsymbol{N}$ Unit directional vector of a truss member

$\boldsymbol{R}$ Residual force vector

$\boldsymbol{T}$ Internal force vector

$\boldsymbol{t}^{(e)}$ Internal force vector in local coordinates for member $e$

$\boldsymbol{U}$ Weighted displacement matrix

$\boldsymbol{u}$ Displacement vector

$\boldsymbol{u}^{(e)}$ Displacement vector for member $e$

$\boldsymbol{u}_{\text{Top}}$ Displacement vector in structural topology defined by filter

$\boldsymbol{u}_i$ Displacement vector for the $i$th load case

$\boldsymbol{u}_p, \boldsymbol{u}_q$ Displacements of nodes $p$ and $q$

$\boldsymbol{x}^*$ Optimal solution obtained by the standard algorithm in the GSM

$\boldsymbol{x}_f$ Filtered subset of the design variables

$\boldsymbol{x}_i$ Vector of design variables (cross-sectional areas) for material $i$

$\boldsymbol{y}_i$ Vector of intervening variables for material $i$ in the ZPR update scheme

$\mathbf{r}^j$ The position vector where $\boldsymbol{f}^j$ is applied

$C$ Weighted compliance (objective function)

$d$ Number of dimensions (e.g., $d = 2, 3$)

$E_0$ Initial tangent modulus (Young's modulus)

$E_t$ Tangent modulus

$f_{\text{axial}}^{(e)}$ Axial force in truss member $e$

$g$ Global volume constraint

$g^j$ The $j$th volume constraint in the ZPR update scheme

$J$ Objective function

$J^k$ Approximated objective function in the subproblem at optimization step $k$

$L^{(e)}$ Length of truss member $e$

$L_i^{(e)}$ Length of truss member $e$ for material $i$

$M$ Number of elements in the mesh/initial ground structure

$m$ Total number of materials

$M_i$ Number of truss members in material $i$

$m_\ell$ Number of load cases

$move$ Move limit in the OC method

$N$ Number of nodes in the mesh/initial ground structure

$n$ Sample size

$N^{(e)}$ Unit directional vector for member $e$

$N_{\text{select}}$ Step number to initiate the material selecting algorithm

$N_f$ Specified frequency of applying the discrete filter

$n_f$ Number of monitored steps for the discrete filter in the randomized algorithm

$n_s$ Frequency to select a new sample

$N_{\text{solve}}$ Total number of linear system solves in the optimization process

$n_{\text{step}}$ Sample window size in the damping scheme

$nc$ Total number of volume constraints in the ZPR update scheme

$P$ Magnitude of an applied load

$p$ Penalization parameter in the density-based method

$R$ Effective step ratio in the damping scheme

$T_{\text{torsion}}$ Magnitude of torsion applied at both ends of the Michell's torsional ball and torsional disc.

$U$ Internal energy

$U_c$ Complementary energy at the equilibrium configuration

$V_{\max}^j$ Prescribed maximum volume in the $j$th volume constraint of the ZPR update scheme

$V^{(e)}$ Volume of member $e$

$V_{\max}$ Prescribed maximum global volume

$V_M$ The volume of Michell's structure

$w_i$ Weighting factor for the $i$th load case

$x^{(e)}$ Cross-sectional area of member $e$ ($e$th design variable in the GSM)

$x_f^{(e)}$ Filtered cross-sectional area of member $e$

$x_i^{(e)}$ Cross-sectional area of member $e$ for material $i$

$x_{\min}, x_{\max}$ Lower and upper bounds for the cross-sectional area of the member in the GSM

$x_{i,L}^{(e),k}$ The lowerbound of the $e$th design variable for material $i$ in the subproblem at optimization step $k$.

$x_{i,U}^{(e),k}$ The upperbound of the $e$th design variable for material $i$ in the subproblem at optimization step $k$.

$Y$ Maxwell number

$Z$ Michell number

## SUMMARY

Topology optimization is a practical tool that allows for improved structural designs. This thesis focuses on developing both theoretical foundations and computational algorithms for topology optimization to effectively and efficiently handle many materials, many constraints, and many load cases. Most work in topology optimization is restricted to linear material with limited constraint settings for multiple materials. To address these issues, we propose a general multi-material topology optimization formulation with material nonlinearity. This formulation handles an arbitrary number of materials with flexible properties, features freely specified material layers, and includes a generalized volume constraint setting. To efficiently handle such arbitrary constraints, we derive an update scheme, named ZPR, that performs robust updates of design variables associated with each constraint independently. The derivation is based on the separable feature of the dual problem of the convex approximated primal subproblem with respect to the Lagrange multipliers, and thus the update of design variables in each constraint only depends on the corresponding Lagrange multiplier. This thesis also presents an efficient filtering scheme, with reduced-order modeling, and demonstrates its application to 2D and 3D topology optimization of truss networks. The proposed filtering scheme extracts valid structures, yields the displacement field without artificial stiffness, and improve convergence, leading to drastically improved computational performance. To obtain designs under many load cases, we present a randomized approach that efficiently optimizes structures under hundreds of load cases. This approach only uses 5 or 6 stochastic sample load cases, instead of hundreds, to obtain similar optimized designs (for both continuum and truss approaches). Through examples using Ogden-based, bilinear, and linear materials, we demonstrate that proposed topology optimization frameworks with the new multi-material formulation, update scheme, and discrete filtering lead to a design tool that not only finds the optimal topology but also selects the proper type and amount of material with drastically reduced computational cost.

# CHAPTER 1
# INTRODUCTION

Topology optimization is a powerful computational tool that enables the designs of engineering systems and materials with greater efficiency, higher performance, and better functionality. Given loads and boundary conditions, this powerful tool can be used to obtain the optimal layout of a design domain. Because of its unique capability, topology optimization offers vast potential for various applications and has been applied to many engineering fields across a wide range of length scales, from structural engineering and aerospace engineering to material science and biomedical engineering. For example, as shown in Figure 1.1a, topology optimization is applied to the design of the upper bridge-like structure spanning across several towers. The optimized structure leads to a design that is not only innovative and organic but also structurally efficient. By using topology optimization, the total weight of the Airbus 380 aircraft design was decreased by approximately 1000kg (per airplane), as shown in Figure 1.1b. Other application examples of topology optimization include designing nano-robotics (Figure 1.1c), manufacturable and deformable porous structures using a single material (Figure 1.1d), facial bone replacement (Figure 1.1e), and microstructure of materials to achieve engineered properties(Figure 1.1f).

This thesis focuses both the theoretical foundations as well as the algorithmic developments for topology optimization to enable various innovative applications. More specifically, we develop theories and computational frameworks for the topology optimization to effectively and efficiently handle many materials, many constraints, and many load cases. This thesis explores and contributes to several topics and areas, including Michell's optimality conditions, multi-material topology optimization, nonlinear material properties, constructible structures, randomized algorithms with stochastic sampling, as well as update algorithms to efficiently handle multi-objective and multi-constraint optimization.

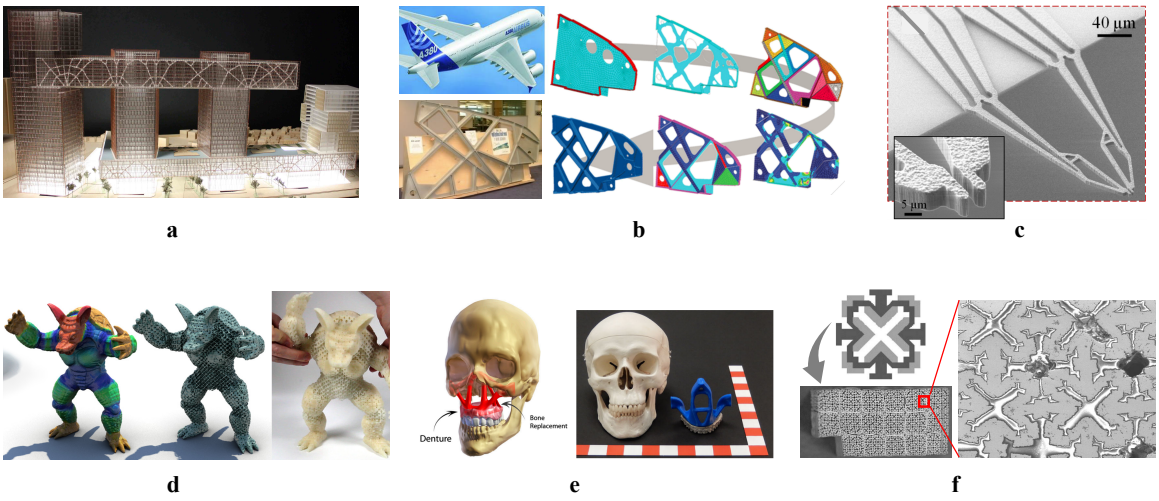


Figure 1.1: Examples of engineering applications of topology optimization. **a** Conceptual design for the Zendai bridge (courtesy of SOM) [1]; **b** optimized airplane wing design and manufactured model for Airbus 380 aircraft (www.altair.com) [2]; **c** optimized design and fabricated model of a micro-gripper [3]; **d** design and 3D-printed model using a single material to resemble a deformable structure that approximates the desired elastic behavior [4]; **e** optimized bone replacement design and 3D-printed model for facial reconstruction [5], [6]; **f** design and fabricated material microstructure with negative thermal expansion coefficient [7], [8].

## 1.1 Truss Layout and Continuum Topology Optimization

Topology optimization is a mathematical design tool that determines the location to place material in a design domain with given load and boundary conditions for a specific objective (volume, compliance, displacement, frequency, energy dissipation, etc.). In this technique, either a gradient-based or a non-gradient-based algorithm is used to update the designs iteratively. The design domain is usually discretized into small elements, and the finite element method (FEM) is used to perform structural analysis. Depending on the type of elements considered, topology optimization can be classified into discrete-element optimization using truss or beam elements, continuum-element optimization, and a combination of both. The discrete type is known as the truss layout optimization, which is more suitable for structural engineering applications and is typically solved by the ground structure method (GSM). The GSM aims to find the optimal layout of a truss system by sizing cross-sectional

areas of all the members in the truss. This method can be used to study the flow of forces within a domain, numerically obtain optimal structures and design truss/lattice networks. The continuum topology optimization aims to determine the optimal material distribution within a given design domain discretized by continuum finite elements. Among various methods for continuum topology optimization, the density-based method is one of the most commonly used approaches in continuum topology optimization. In addition, some studies have integrated both truss layout and continuum optimizations for the purpose of designing high-rise buildings [9] and for the purpose of designing reinforced concrete structures and studying strut and tie models by considering concrete as a continuum solid and steel rebars as truss members (see, e.g., [10]–[14]). An alternative approach that extracts discrete structures from the solution of homogenization-based continuum topology optimization can be found in [15].

### 1.1.1 Truss layout optimization

In the literature, several researchers provide closed-form analytical solutions for truss layout optimization. In 1904, Michell [16] has derived the optimality conditions for trusses to have least-weight trusses with given allowable stresses. Since then, a large amount of work has followed the pioneering work, for example, the work in [17]–[26]. These analytical solutions are widely used as benchmark problems for verifying computational frameworks. However, there are a few problems with analytical solutions. For problems with no known analytical solutions, numerical approaches can offer close-to-optimal solutions. Among those approaches, a commonly used technique for optimizing the truss lattice networks is the GSM (see, e.g., [27]–[31]). In this technique, the design domain is discretized by a set of nodes, which are interconnected by truss members to form an initial ground structure (GS). By means of an update scheme and sensitivity information, the final design is then obtained by gradually removing unnecessary members from the initial GS (subtractive method). Other GS methods include the adaptively generative/growing method [32]–[34].

Various objective functions have been examined in the literature, including compliance, volume, displacement, frequency, and so on. Because the goal of this thesis is to explore fundamental theories and establish computational algorithms for topology optimization, we mainly consider compliance (and potential energy) as the objective function. The standard GSM formulation for minimum compliance problems considering linear elastic materials is as follows

$$\begin{aligned} \min_{\boldsymbol{x}} \quad & C(\boldsymbol{x}) = \min_{\boldsymbol{x}} \boldsymbol{f}^T \boldsymbol{u}(\boldsymbol{x}), \\ \text{s.t.} \quad & g(\boldsymbol{x}) = \sum_{e=1}^{M} L^{(e)} x^{(e)} - V_{\max} \leq 0, \\ & 0 < x_{\min} \leq x^{(e)} \leq x_{\max}, e = 1, ..., M, \\ & \text{with } \boldsymbol{u}(\boldsymbol{x}) = \boldsymbol{K}(\boldsymbol{x})^{-1} \boldsymbol{f}, \end{aligned} \tag{1.1}$$

For an initial GS with $M$ truss members, the vector $\boldsymbol{x} \in \mathbb{R}^M$ is a vector of design variables, with component $x^{(e)}$ being the cross-sectional area of truss member $e$. It is subjected to lower bound $x_{\min}$ and upper bound $x_{\max}$. Furthermore, $L^{(e)}$ is the length of truss member $e$, and $V_{\max}$ is the prescribed upper bound on the total volume. Other types of constraint functions include stress, "slenderness constraints" [35], [36], and failure probability constraints. Note that the above optimization formulation (1.1) has been proven to be convex in [37] for a positive definite stiffness matrix and in [38] for a positive semi-definite stiffness matrix.

In addition to the elastic formulation in (1.1), another common formulation used in the GSM is the plastic formulation [33], [39], [40], which minimizes the total volume of the structure under stress constraints. For a linear material with equal tension and compression stress limits, plastic formulation leads to the same optimized structure (up to a rescaling) as the elastic one (1.1) [17], [41]. In the case of materials with different tension and compression strengths, the two formulations may lead to the same solution if the material properties are defined properly [41]. The theoretical developments in this thesis are based on the elastic formulation.

### 1.1.2 Continuum topology optimization

In the continuum topology optimization, the goal is to determine the optimal material distribution within a given design domain discretized by continuum finite elements. The continuum approach has varied applications to mechanical, aerospace, and material design fields. Among various methods in continuum topology optimization (e.g., density-based, level set, phase field, evolutionary structural optimization, and so on.), this thesis focuses on the density-based method.

Similar to the truss layout optimization, this thesis mainly considers compliance as the objective function. For a given load $\boldsymbol{f}$, the standard formulation for the minimum compliance design using the density-based method can be written as [30],

$$\begin{aligned} \min_{\boldsymbol{\rho}} C(\boldsymbol{\rho}) &= \min_{\boldsymbol{\rho}} \boldsymbol{f}^T \boldsymbol{u}(\boldsymbol{\rho}), \\ \text{s.t.} \quad & g(\bar{\boldsymbol{\rho}}) = \sum_{e=1}^{M} v^{(e)} \bar{\rho}^{(e)} - V_{\max} \leq 0, \\ & 0 < \rho_{\min} \leq \rho^{(e)} \leq 1, e = 1, ..., M, \\ & \text{with } \boldsymbol{u}(\bar{\boldsymbol{\rho}}) = \boldsymbol{K}(\boldsymbol{E}(\bar{\boldsymbol{\rho}}))^{-1} \boldsymbol{f}, . \end{aligned} \tag{1.2}$$

In this minimization problem, the objective function $C$ is the compliance of the corresponding structure, $\boldsymbol{\rho} \in \mathbb{R}^M$ is the vector of design variables (the density field), and $M$ is the number of elements in the finite element mesh. We define $\bar{\boldsymbol{\rho}}$ and $\boldsymbol{H}$ as the filtered physical density and the filter matrix such that $\bar{\boldsymbol{\rho}} = \boldsymbol{H}\boldsymbol{\rho}$ [42]. In order to ensure a positive definite stiffness matrix $\boldsymbol{K} \in \mathbb{R}^{dN \times dN}$, a lower bound $\rho_{\min}$ is prescribed on $\rho^{(e)}$, where $N$ is the number of nodes and $d$ is the dimension of the problem, so $dN$ is the number of degrees of freedom. The volume (area) of element $e$ is given by $v^{(e)}$, and $V_{\max}$ is the prescribed upper bound on the total volume. The Young's modulus $\boldsymbol{E}$ is defined by, for example, the Solid Isotropic Material with Penalization (SIMP) [43], [44] approach. Other models, e.g., RAMP (Rational Approximation of Material Properties) [30], [45], can be used and would

not alter the conceptual presentation of the topic. For the SIMP approach with the density filter, we have $E^{(e)} = [\bar{\rho}^{(e)}]^p(E_0)$, where $E_0$ is the elastic modulus for solid material, and $p$ is a penalization factor.

If the SIMP approach is used, the formulation (1.2) is known to be convex when $p = 1$ [46]. Using $p > 1$ to obtain a solid-void solution, one makes the problem non-convex and, as expected, the solution obtained from the optimization algorithm may not be the global minimum.

## 1.2 Connection Between Topology Optimization and Additive Manufacturing

An important aspect of topology optimization is the realization and fabrication of the designs. In fact, all the engineering applications shown in Figure 1.1 include physical models manufactured by various techniques. As a fast emerging technique, additive manufacturing (AM) has been widely used in the engineering science to construct structures that are difficult or even impossible to fabricate with the traditional approaches. Additive manufacturing has a natural connection with topology optimization. Topology optimization typically produces the final topologies that are too complex to be manufactured by traditional methods, and AM offers a practical approach for the realization of the optimized complex structures.

Several attempts have been made in the literature to bridge the connection between topology optimization and AM. Some work has proposed to use 3D printing to manufacture material microstructures designed by topology optimization, which typically contain unconventional materials, for instance, materials with negative Poisson's ratio [47]–[49]. Other studies apply AM in the biomedical field to manufacture medical devices or biological tissues, such as bone implant scaffolds [50]–[53] and facial implants [5], [54]. Several practical issues of manufacturing topology optimization results have also been discussed. While the density-based approach typically contains gray regions (intermediate densities), the interpretation of these regions in AM becomes an issue. With the inspiration from the SIMP method, the authors in [55] propose to use the lattice cells with different volume

fractions to replace intermediate densities at each element, leading to a manufacturable structure which is a combination of the solids and lattice cells. A similar approach is also pursued in [56], but with different cells layout. Additionally, designs for additive manufacture need to include requirements associated with minimum feature size, manufacturable inclination angle, allowable bridging distance, and the robust accommodation of heat transfer, which needs to be accounted in or after the optimization process. Typically, these design requirements are either accommodated by intuitive modification of the intended geometry [57], or by the use of support material to enable acute inclination angles and to transfer heat as required, which adds additional material cost and manufacturing times. In [58], a method is proposed which modifies the optimal structure to ensure manufacturability without the need of support materials. Another issue is the interface between topology optimization and AM. Typical topology optimization results need to be converted to CAD before being manufactured. The recent study by [6] creates a piece of software, TopSlicer, that converts the topology optimization output to AM input (.stl files). A comprehensive review of the current and future trends in connecting topology optimization with AM can be found in [59].

To study the connection between topology optimization and AM, we have explored AM techniques. Various designs obtained using the proposed topology optimization frameworks, developed in this thesis, are further printed by AM techniques. Figure 1.2 shows some examples of the printed prototypes, which are manufactured with 3D printing using a fused filament fabrication (FFF) process. Typical topology optimization results need to be converted to CAD before being manufactured, in this work, we use the techniques proposed in [6] to export geometry data to .stl format. We highlight that manufacturing of optimal trusses generated by the GSM is a challenging task because the GSM formulation by its nature (a size optimization method) introduces thin members. Those thin members impose great difficulty in the manufacturing process because their sizes may fall below the resolution of the printer. Chapter 3 of this thesis addresses the issue mentioned above. With the

discrete filtering technique described in Chapter 3, we can improve the constructability of the optimal trusses by using a prescribed threshold to control the resolution of the structure throughout the entire optimization process.

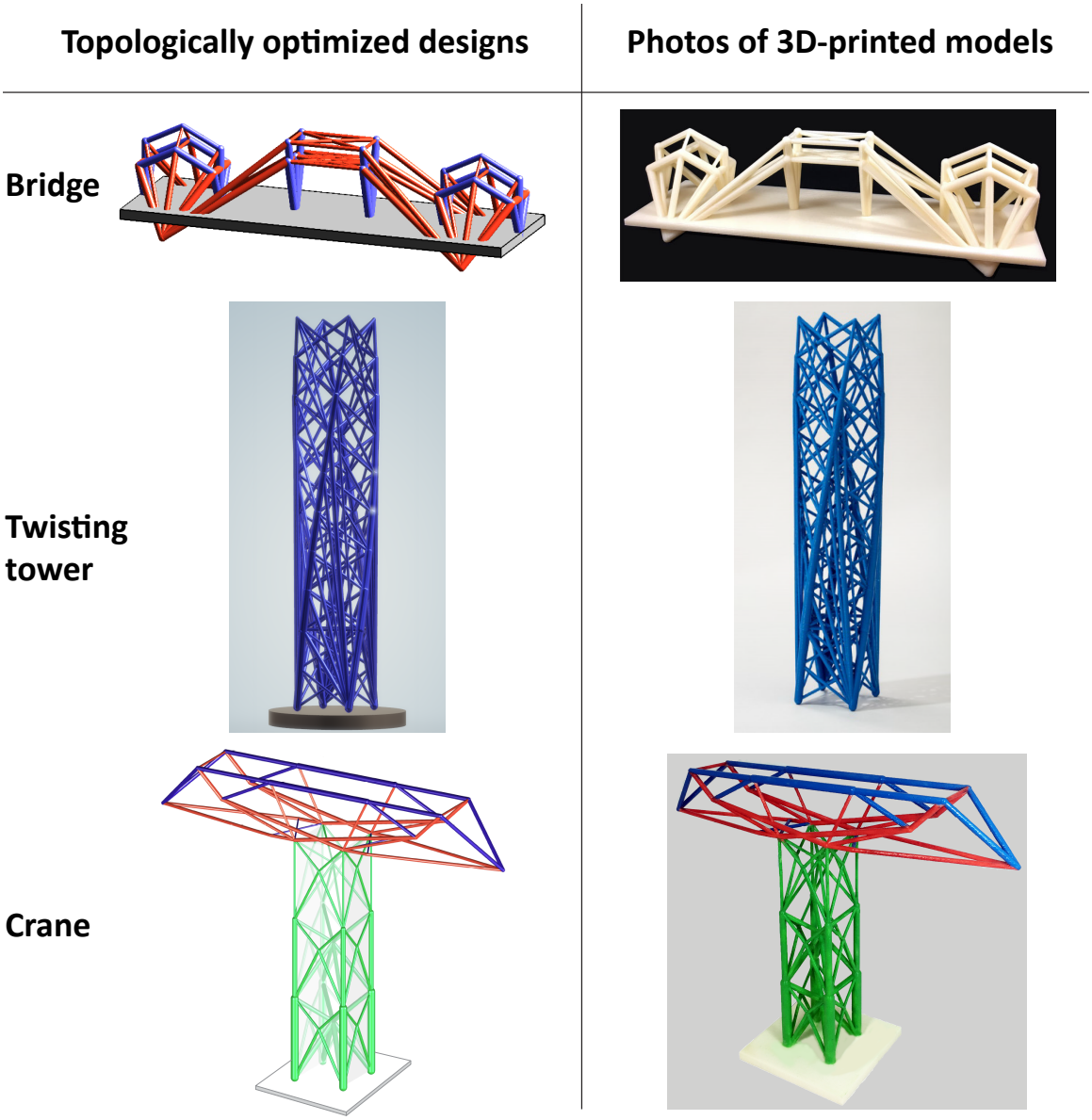


Figure 1.2: Examples of optimized designs (obtained by proposed methods in this thesis) and the corresponding 3D-printed models using a fused filament fabrication (FFF) process. Top: bridge design with material nonlinearity in Chapter 3; middle: twisting tower design using stochastic sampling in Chapter 6; bottom: multi-material crane design in Chapter 4.

## 1.3 Research Motivation

The limited resources and increasing demand for extreme structures contribute to the importance of studying optimal structures. Analytical solutions and their geometric implications not only bring insights into functional and creative structural designs, but also provide analytical benchmarks for numerical methods to verify with. Thus, Chapter 2 provides a primer of Michell's optimality conditions [16], which are the first sufficient conditions that offer analytical closed-form solutions for optimal structures. We explain the main idea of the original and modified optimality conditions, and discuss the geometric characteristics of Michell structures, and derive the analytical solution of the Michell torsional sphere.

Topology optimization considering linear material behavior (the prevailing approach in the literature) has a limited scope, because real materials generally display nonlinear constitutive relationship. For example, specific heat treatment methods change the constitutive relationships of a material dramatically. Although the influence of material properties on optimization design is well known, the exact changes that take place may not be predictable in the optimized design. Thus, it is essential to take into account material nonlinearity. This thesis proposes frameworks that account for material nonlinearity. Chapter 3 incorporates material nonlinearity into single material topology optimization with combinations of Ogden-based and bilinear materials. It also presents an elegant approach to solve nonlinear state equations with singular stiffness matrix. Material nonlinearity is also adopted in Chapter 4 and 5 for topology optimization considering multiple materials.

From the perspective of computational efficiency, a major challenge associated with topology optimization that accounts for material nonlinearity is the high computational cost of the iterative procedure for solving nonlinear structural systems. Moreover, the incorporation of the multiple load cases into the nonlinear problems leads to higher computational cost, because each load case requires an independent iterative nonlinear FE analysis. To handle material nonlinearity efficiently, a fully reduced-order model in both nonlinear

state equation and optimization update is proposed in Chapter 3 together with the discrete filtering scheme. As a result of the smaller sizes of the tangent stiffness matrix and the sensitivity vector, the fully reduced-order model significantly improves the computational performance of the optimization algorithm.

One limitation of the GSM is its inability to define a valid final structure that is constructable, because a cut-off value is needed to define the final design for the standard GSM (a sizing problem). If the cut-off threshold is too small, the topology may consist of a large number of undesirable thin bars, which makes it almost impossible to be fabricated by neither conventional nor additive manufacturing techniques. On the other hand, if the threshold is too high, we may obtain a design that violates the global equilibrium as a result of the removal of some structurally important bars. Thus, in an effort to provide a practical design tool that manufacturable designs, Chapter 3 of the thesis proposes a discrete filter that can be used to control the final resolution of the optimized structure and ensure global equilibrium of the design throughout the entire optimization process.

Multi-material topology optimization is an emerging trend because practical engineering designs, such as buildings, aircraft, and composite materials typically consist of multiple material types. The literature on multi-material topology optimization is vast and growing but mostly deals with the continuum approaches (e.g., the density-based approach [45], [60]–[63], phase-field approach [64], [65], and level set approach [66]–[69]) as well as linear material behaviors. Few multi-material topology optimization studies focus on truss networks as well as nonlinear material behaviors. In addition, most studies in this field use limited settings of volume constraints. Thus, in Chapter 4 of this thesis, we propose a general formulation that applies to both truss-layout and density-based optimization considering material nonlinearity. The proposed formulation handles an arbitrary number of candidate materials with flexible material properties, features freely specified material layers, and includes a generalized volume constraint setting.

One challenging of multi-material topology optimization is how to efficiently and effec-

tively handle the multiple volume constraints. The commonly used design update schemes, such as the Optimality Criteria (OC) method [31], [70] and the Method of Moving Asymptotes (MMA) [71], suffer several drawbacks when applied to multi-material topology optimization. To efficiently handle many constraints in multi-material topology optimization, Chapter 4 of this thesis derives a novel design update scheme that performs efficient and robust updates of the design variables associated with each volume constraint independently. In addition, an alternative derivation of the design update scheme based on the KarushKuhnTucker (KKT) conditions of the convex approximated primal subproblem is provided in Chapter 5.

Multi-material topology optimization may lead to members containing more than one material in the design, which is another major challenge in this field. The existing techniques in the literature either penalize mixing of material through material interpolations (e.g., Discrete Material Optimization technique [72]) or introduce material selection constraints through discrete design variables (e.g., [62]), both of which is not suitable for multi-material topology optimization formulation for nonlinear truss-networks. To overcome this issue, Chapter 5 of this thesis proposes a material selection algorithm for multi-material truss layout optimization that ensures the selection of a single material for each member. This algorithm, based on the evaluation of both the strain energy and the cross-sectional area of each member, performs iteratively and actively throughout the optimization process.

For structural topology optimization to be applied to real-world structural designs, developing frameworks that account for many load cases is essential. Because practical engineering designs generally involve numerous load cases [73]. However, the incorporation of many load cases in standard topology optimization is computationally expensive, because we need to solve the structure response for each load case at every optimization iteration. For instance, to consider hundreds of load cases in topology optimization, the associated computational cost can be enormous. To that efficiently and effectively optimize designs under many load cases, Chapter 6 of this thesis proposes a randomized approach that drasti-

cally reduces the computational cost of optimizing structures under hundreds of load cases. This approach only uses a few stochastic sample load cases, instead of hundreds, to obtain similar optimized designs for both continuum and truss topology optimization.

## 1.4 Thesis Scope and Organization

This thesis is devoted to developing novel and effective frameworks for topology optimization to enable efficient and practical designs and to target the real-life demands of material, structural design, and manufacturing aspects. We aim to develop both the theoretical foundations and computational frameworks for truss layout and continuum topology optimizations to effectively and efficiently handle many materials, many constraints, and many load cases.

The remainder of this thesis is organized as follows: Chapter 2 reviews Michell's optimality conditions and derive some Michell's analytical solutions. In Chapter 3, we present the reduced-order filter scheme that applies to material nonlinear truss topology optimization considering multiple load cases. In Chapter 4, we introduce the multi-material formulation and derive the update scheme to handle many linear constraints. Chapter 5 addresses the material selection scheme for multi-material topology optimization of truss layouts. In Chapter 6, we introduce the randomized optimization approach and the corresponding damping scheme for both continuum and discrete topology optimization under many load cases. Finally, concluding remarks and discussions on the future research directions can be found in Chapter 7.

# CHAPTER 2
# MICHELL STRUCTURES

The limited resources and increasing demand for extreme structures contribute to the importance of studying optimal structures. Understanding optimality conditions and the geometric implications of the optimal structures provide guidance/insights for functional and creative designs. In 1904, Michell [16] has derived the well-known conditions for trusses to be optimal, i.e., least-weight trusses with given allowable stresses (also known as minimal total load path). These conditions are known as Michell's optimality conditions, which are the first ones that provide analytical ways to find optimal structures. In his seminal paper [16], Michell also provides closed-form solutions for several structural problems (Michell structures), which are widely used as benchmark problems for verifying numerical methods. Later, Hemp [17] derives modified optimal conditions that correct the previous ones for the cases with unequal permissible stresses. In [17], Hemp also develops a unified theory in curvilinear coordinates for deriving the geometry of Michell structures based on Hencky nets [74], [75]. Since then, a large amount of work has followed the pioneering work of Michell [16] and Hemp [17], and has provided extensions, corrections, and additional closed-form solutions, for example, the work in [18]–[26].

The significance of Michell's optimality conditions is that they not only establish the first sufficient conditions for optimal structures, but also inform the designers of some characteristics of the optimal structure. For example, the truss members of an optimal structure must lie in the principal directions of the virtual strain field, and the tension and compression members in the optimal structure must be orthogonal when they intersect. Moreover, the derived Michell structures provide analytical benchmarks for numerical optimization methods to verify against [76]. The goal of this chapter is to elucidate the main idea of Michell's optimality conditions. In addition, we introduce the concepts of Hencky nets and

derive the analytical solutions of several two-dimensional (2D) and three-dimensional (3D) Michell structures.

The remainder of this chapter is organized as follows. Section 1 states the scope and reviews several preliminary concepts. Section 2 introduces the original and modified optimality conditions, followed by a proof of the conditions. Section 3 analyzes the types of the structures that satisfy the conditions, and Section 4 introduces ways to construct optimal structures. Section 5 derives the closed-form solutions for 2D and 3D Michell structures, and finally, Section 6 provides a summary of the chapter.

## 2.1 Introduction and Preliminaries

The first fundamental properties of optimal truss-like continua were established starting with Michell's revolutionary paper "The Limits of Economy of Material in Frame-structures" [16]. This paper was later studied and expanded upon by [18]–[26], which has become the well-known truss layout optimization theory. The definition of the optimal structure is the frame that has the least weight in a given domain for given load and boundary conditions with allowable stresses. Mathematically, for a set of given external load, the optimization statement is as follows:

$$\begin{aligned} &\min_{\boldsymbol{x}} \sum_{e} x^{(e)} L^{(e)} \\ &\text{s.t.} \quad -\overline{\sigma}_C \leq \frac{f^{(e)}_{\text{axial}}}{x^{(e)}} \leq \overline{\sigma}_T \quad \text{for all } e \\ &\qquad \text{and equilibrium,} \end{aligned} \tag{2.1}$$

where $x^{(e)}$, $L^{(e)}$, and $f^{(e)}_{\text{axial}}$ denote the cross-sectional area, length, and internal axial force of the $e$th truss member in the structure, respectively; $\overline{\sigma}_T$ and $\overline{\sigma}_C$ are the tensile and compressive stress limits, respectively. The stress of member $e$ is defined as $\sigma^{(e)} = f^{(e)}_{\text{axial}}/x^{(e)}$.

Note that we have the following assumptions: the structure is in statics (i.e., in equilibrium) and is subjected to a single load case, and the structural elements considered are

frames and trusses. To solve this original optimization problem analytically is difficult because the feasible space is infinite. Instead, Michell establishes the optimal conditions that provide analytical solutions to problem (2.1) and derives closed-form solutions for several structural problems, which are widely used as benchmark problems for verifying numerical methods.

We first introduce two quantities that Michell's conditions are based upon. The first quantity is the Maxwell number, which is introduced by Maxwell [77]:

$$\sum_e f_{\text{axial}}^{(e)} L^{(e)} = \sum_{e \in \mathscr{E}_T} |f_{\text{axial}}^{(e)}| L^{(e)} - \sum_{e \in \mathscr{E}_C} |f_{\text{axial}}^{(e)}| L^{(e)} = Y, \tag{2.2}$$

where $\mathscr{E}_T$ and $\mathscr{E}_C$ denote the sets of tension and compression members. The Maxwell's theorem states that for the same boundary and loading conditions, $Y$, which is commonly known as the Maxwell number, is independent of the form of structure layouts. Next, we introduce the Michell number, $Z$, defined as follows,

$$\sum_e |f_{\text{axial}}^{(e)}| L^{(e)} = \sum_{e \in \mathscr{E}_T} |f_{\text{axial}}^{(e)}| L^{(e)} + \sum_{e \in \mathscr{E}_C} |f_{\text{axial}}^{(e)}| L^{(e)} = Z. \tag{2.3}$$

The Michell number $Z$ is also known as the load path. Different from the Maxwell number (2.2), both tension and compression members add to the Michell number (2.3). For any statically determinate truss that is fully stressed (to the stress limits $\overline{\sigma}_T$ and $\overline{\sigma}_C$), the volume can be calculated as follows,

$$V = \frac{\sum_{e \in \mathscr{E}_T} |f_{\text{axial}}^{(e)}| L^{(e)}}{\overline{\sigma}_T} + \frac{\sum_{e \in \mathscr{E}_C} |f_{\text{axial}}^{(e)}| L^{(e)}}{\overline{\sigma}_C} = \frac{(\overline{\sigma}_T + \overline{\sigma}_C) Z - (\overline{\sigma}_T - \overline{\sigma}_C) Y}{2 \overline{\sigma}_T \overline{\sigma}_C}. \tag{2.4}$$

Thus, if the structure is fully stressed, minimizing the quantity $Z$ for a given problem is equivalent to minimizing the volume $V$.

As a demonstration of these two quantities, Figure 2.1 shows two trusses, A and B, under the same load and boundary conditions. Because both trusses are statically determi-

nate, we can calculate the axial forces in all the members, as shown in Figure 2.1. Using the axial forces and the geometry and assuming all members are fully stressed to $\overline{\sigma}$, we can obtain that the Maxwell number, Michell number, and volume for the two structures according to (2.2), (2.3), and (2.4), as shown in Table 2.1. Note that structures A and B have the same Maxwell numbers and varied Michell numbers. The Michell numbers (load paths) of these two structures have indications about their volumes. The structure B, with a smaller Michell number, has a smaller volume than A.

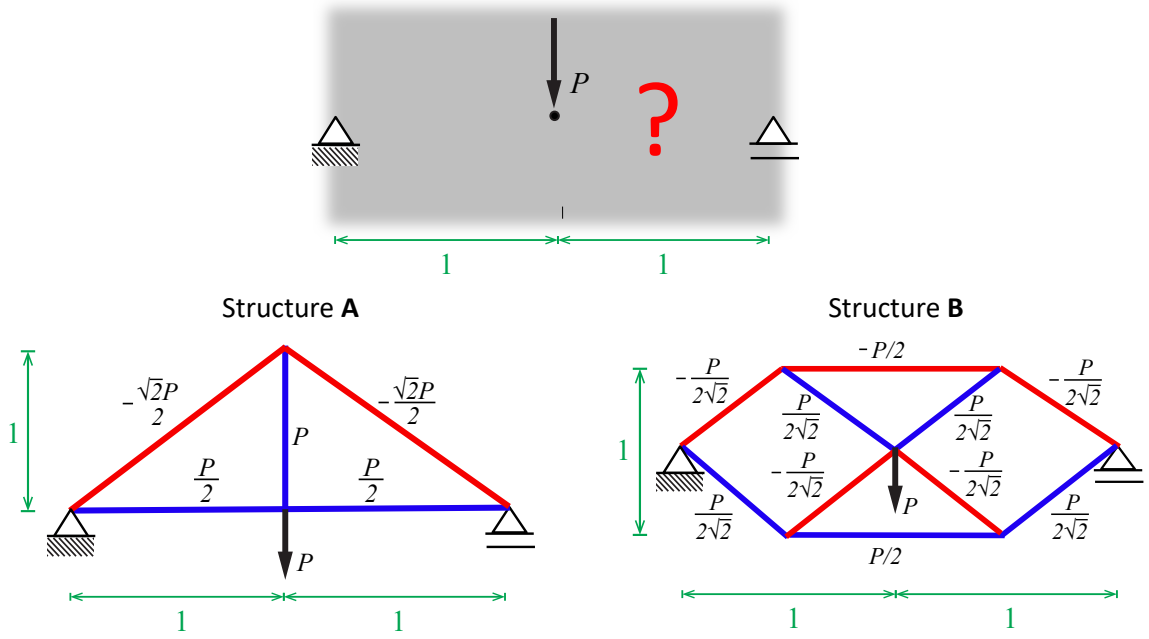


Figure 2.1: A design domain with load and boundary conditions, and two trusses (A and B) subjected to the same load and boundary conditions. Blue members are in tension and red members are in compression.

A concept we used in the proof of Michell's conditions is the principle of virtual work, which states that, for any structures that satisfy equilibrium, if we let the structure experience an arbitrary virtual displacement field, $\delta \boldsymbol{u}$, which satisfies the displacement boundary conditions, the following relation holds:

$$\delta U - \delta \Omega = \sum_e f_{\text{axial}}^{(e)} (\varepsilon^{(e)} L^{(e)}) - \sum_j \boldsymbol{f}^j \delta \boldsymbol{u}(\mathbf{r}^j) = 0, \tag{2.5}$$

Table 2.1: Maxwell number and Michell number

| Structure | A | B |
|---|---|---|
| Maxwell Number | $2\sqrt{2}(-\frac{\sqrt{2}}{2}P)+2(\frac{P}{2})+P=0$ | $\frac{P}{2}+(-\frac{P}{2})+4(-\frac{P}{2\sqrt{2}})\frac{\sqrt{2}}{2}+4(\frac{P}{2\sqrt{2}})\frac{\sqrt{2}}{2}=0$ |
| Michell Number | $2\sqrt{2}(\frac{\sqrt{2}}{2}P)+2(\frac{P}{2})+P=4P$ | $\frac{P}{2}+(\frac{P}{2})+4(\frac{P}{2\sqrt{2}})\frac{\sqrt{2}}{2}+4(\frac{P}{2\sqrt{2}})\frac{\sqrt{2}}{2}=3P$ |
| Volume (fully stressed) | $2\sqrt{2}(\frac{\sqrt{2}P}{2\overline{\sigma}})+2(\frac{P}{2\overline{\sigma}})+\frac{P}{\overline{\sigma}}=\frac{4P}{\overline{\sigma}}$ | $\frac{P}{2\overline{\sigma}}+(\frac{P}{2\overline{\sigma}})+4(\frac{P}{2\sqrt{2}\overline{\sigma}})\frac{\sqrt{2}}{2}+4(\frac{P}{2\sqrt{2}\overline{\sigma}})\frac{\sqrt{2}}{2\overline{\sigma}}=\frac{3P}{\overline{\sigma}}$ |

where $\varepsilon^{(e)}$ is the virtual strain generated by $\delta\boldsymbol{u}$ in truss member $e$; $\boldsymbol{f}^j$ and $\delta\boldsymbol{u}(\mathbf{r}^j)$ are the applied force and the corresponding virtual displacement at location $\mathbf{r}^j$, respectively.

## 2.2 Michell's Optimality Conditions

In this section, we review the original and modified Michell's optimality conditions, followed by the proof of the conditions. Michell's optimality conditions for a frame to have the least volume are as follows:

> *"A frame attains the limit of economy of material possible in any frame-structure under the same applied force, if the space occupied by it can be subjected to an appropriate small deformation, such that the strains in all the bars of the frame are increased by equal fractions of their lengths, not less than the fractional change of length of any element of the space."* — A. G. M. Michell [16]

Essentially, for the given load and boundary conditions, any frame that satisfies the following conditions has the least weight:

**Michell Conditions**:

**1**: all the members are fully stressed, namely,

$$\sigma^{(e)}=\frac{f^{(e)}_{\text{axial}}}{x^{(e)}}=\begin{cases}+\overline{\sigma}_T & \forall e\in\mathscr{E}_T\\ -\overline{\sigma}_C & \forall e\in\mathscr{E}_C\end{cases} \tag{2.6}$$

**2**: there exists a kinematically admissible virtual displacement field $\boldsymbol{\delta u}$, which generates virtual strains $\boldsymbol{\varepsilon}^{(e)}$ in each member as follows,

$$\boldsymbol{\varepsilon}^{(e)} = \begin{cases} +\overline{\varepsilon} & \forall \boldsymbol{e} \in \mathscr{E}_T \\ -\overline{\varepsilon} & \forall \boldsymbol{e} \in \mathscr{E}_C \end{cases} \tag{2.7}$$

In the condition (2.7), $\overline{\varepsilon}$ is the limit on virtual strains for both tension and compression members. However, the original conditions derived by Michell have been proven to be valid *only* for trusses with equal stress limits in tension and compression [17], [20], i.e., $\overline{\sigma}_T = \overline{\sigma}_C$. For unequal stress limits, the original conditions are valid only for a narrow class of structures [20]. To generalize the optimal conditions for the majority class of problems (including cases with unequal stress limits, $\overline{\sigma}_T \neq \overline{\sigma}_C$), Hemp [17] derives modified optimal conditions for frames to have the least volume of material, stated as follows,

> *"A pin-jointed framework has the least volume of material, if it can carry its given forces, with stresses in its tension members equal to $\overline{\sigma}_T$ and stresses in its compression members equal to $-\overline{\sigma}_C$ and if a virtual deformation of a region of space, in which the competing framework must lie, satisfies the kinematic conditions imposed on the framework and gives strains of $\overline{\sigma}\ \overline{\varepsilon}/\overline{\sigma}_T$ in its tension members, strain of $-\overline{\sigma}\ \overline{\varepsilon}/\overline{\sigma}_C$ in its compression members and has no direct strain lying outside these limits."* — W. S. Hemp [17]

We denote that $\overline{\sigma} = (\overline{\sigma}_T + \overline{\sigma}_C)/2$. In the modified conditions, Hemp introduces individual (virtual) strain limits for tension and compression members. We summarize the modified conditions as follows,

**Modified Michell Conditions (Hemp Conditions):**

**1**: all the members are fully stressed, namely,

$$\sigma^{(e)} = \frac{f^{(e)}_{\text{axial}}}{x^{(e)}} = \begin{cases} +\overline{\sigma}_T & \forall e \in \mathscr{E}_T \\ -\overline{\sigma}_C & \forall e \in \mathscr{E}_C \end{cases} \tag{2.8}$$

**2**: there exists a kinematically admissible virtual displacement field $\boldsymbol{\delta u}$, which generates virtual strains $\varepsilon^{(e)}$ in each member as follows,

$$\varepsilon^{(e)} = \begin{cases} +\frac{\overline{\sigma}}{\overline{\sigma}_T}\overline{\varepsilon} & \forall e \in \mathscr{E}_T \\ \\ -\frac{\overline{\sigma}}{\overline{\sigma}_C}\overline{\varepsilon} & \forall e \in \mathscr{E}_C \end{cases} \tag{2.9}$$

The modified optimality conditions (2.8) and (2.9) are sufficient conditions for frames to be the lightest. Note that an additional implication of the conditions is that the signs of $\sigma^{(e)}$ (caused by the set of external force) and $\varepsilon^{(e)}$ (caused by the virtual displacement field) of each member have to be the same. Hereafter, we denote *Michell structures* as the ones satisfy conditions (2.8) and (2.9). In addition, the conditions suggest that all the members of a Michell structure must lie in the principal directions of the chosen virtual strain field. Notice that both virtual strain and corresponding virtual displacement fields are continuous, thus, a Michell structure resembles truss-like continua, which consists of infinitely many bars and joints.

Next, we provide a proof of the modified Michell's optimality conditions (2.8) and (2.9) by comparing the volumes of a Michell structure and an arbitrary structure that satisfy the same set of loads. For a given set of external force $\boldsymbol{f}^j$ applied at location $\mathbf{r}^j$, if we find a Michell structure with volume $V_M$ and a proper virtual displacement field $\boldsymbol{\delta u}$ that satisfies condition (2.9), then both $\sigma^{(e)}$ and $\varepsilon^{(e)}$ of each member in the Michell structure will achieve the corresponding stress and virtual strain limits. Thus, by employing the principle of

virtual work (2.5), the following relation holds for a Michell structure:

$$\begin{aligned}\sum_j \boldsymbol{f}^j \delta\boldsymbol{u}(\mathbf{r}^j) &= \sum_e (\sigma^{(e)} x^{(e)})(\varepsilon^{(e)} L^{(e)}) \\ &= \sum_{e\in\mathscr{E}_T} (\overline{\sigma}_T x^{(e)}) \left[\frac{\overline{\sigma}}{\overline{\sigma}_T}\overline{\varepsilon} L^{(e)}\right] + \sum_{e\in\mathscr{E}_C} (-\overline{\sigma}_C x^{(e)}) \left[-\frac{\overline{\sigma}}{\overline{\sigma}_C}\overline{\varepsilon} L^{(e)}\right] \\ &= \overline{\sigma}\,\overline{\varepsilon}\,(\sum_{e\in\mathscr{E}_T} x^{(e)} L^{(e)} + \sum_{e\in\mathscr{E}_C} x^{(e)} L^{(e)}) \\ &= \overline{\sigma}\,\overline{\varepsilon}\,V_M.\end{aligned} \tag{2.10}$$

For an arbitrary structure with volume $V_A$ that supports the same set of external force, $\boldsymbol{f}^j$ applied at location $\mathbf{r}^j$, the stress of each member within the stress limits,

$$-\overline{\sigma}_C \le \sigma^{(e)} < \overline{\sigma}_T, \tag{2.11}$$

if we impose this arbitrary structure with the same virtual displacement field $\delta\boldsymbol{u}$, the virtual strain generated in each member then satisfies the following relation,

$$-\frac{\overline{\sigma}}{\overline{\sigma}_C}\overline{\varepsilon} \le \varepsilon^{(e)} \le \frac{\overline{\sigma}}{\overline{\sigma}_T}\overline{\varepsilon}. \tag{2.12}$$

Plugging relations (2.11) and (2.12) into the principle of virtual work in (2.5), we have

$$\begin{aligned}\sum_j \boldsymbol{f}^j \delta\boldsymbol{u}(\mathbf{r}^j) &= \sum_e (\sigma^{(e)} x^{(e)})(\varepsilon^{(e)} L^{(e)}) \\ &\le \sum_{e\in\mathscr{E}_T} (\overline{\sigma}_T x^{(e)}) \left[\frac{\overline{\sigma}}{\overline{\sigma}_T}\overline{\varepsilon} L^{(e)}\right] + \sum_{e\in\mathscr{E}_C} (-\overline{\sigma}_C x^{(e)}) \left[-\frac{\overline{\sigma}}{\overline{\sigma}_C}\overline{\varepsilon} L^{(e)}\right] \\ &= \overline{\sigma}\,\overline{\varepsilon}\,(\sum_{e\in\mathscr{E}_T} x^{(e)} L^{(e)} + \sum_{e\in\mathscr{E}_C} x^{(e)} L^{(e)}) \\ &= \overline{\sigma}\,\overline{\varepsilon}\,V_A.\end{aligned} \tag{2.13}$$

Because the external virtual work $\sum_j \boldsymbol{f}^j \delta\boldsymbol{u}(\mathbf{r}^j)$ is independent of the structure layout, by comparing (2.10) and (2.13), we conclude that $V_M \le V_A$.

Finally, based on (2.10), we obtain the following expression for $V_M$,

$$V_M = \frac{\sum_j \boldsymbol{f}^j \delta \boldsymbol{u}(\mathbf{r}^j)}{\overline{\sigma}\,\overline{\varepsilon}}. \tag{2.14}$$

The expression (2.14) suggests that, for a given set of external force and feasible design space, if we can find a proper virtual displacement field $\delta \boldsymbol{u}$ that satisfies condition (2.9), we can directly compute the volume of the Michell structure, even without knowing the structural layout.

## 2.3 Types of Structures that Satisfy Michell's Optimality Conditions

This section introduces two general types of structures that satisfy Michell's conditions. **Type I**: the first type of Michell structures are the trusses with members that are either all in tension or all in compression. In this case, the proper virtual displacement field that satisfies (2.9) is either a uniform dilation or contraction (according to either the truss is in tension or compression). Here, we use the case that all the members are in tension, then a proper virtual displacement field $\delta \boldsymbol{u} = [\delta u_x, \delta u_y]^T$ is uniform dilation, that is,

$$\frac{\partial \delta u_x}{\partial x} = \frac{\overline{\sigma}\,\overline{\varepsilon}}{\overline{\sigma}_T}, \quad \frac{\partial \delta u_y}{\partial y} = \frac{\overline{\sigma}\,\overline{\varepsilon}}{\overline{\sigma}_T}, \quad \frac{\partial \delta u_x}{\partial y} + \frac{\partial \delta u_y}{\partial x} = 0. \tag{2.15}$$

Solving the above set of partial differential equations (PDEs) (2.15), we get

$$\delta u_x = A_1 + By + \frac{\overline{\sigma}\,\overline{\varepsilon}}{\overline{\sigma}_T} x, \quad \text{and} \quad \delta u_y = A_2 - Bx + \frac{\overline{\sigma}\,\overline{\varepsilon}}{\overline{\sigma}_T} y, \tag{2.16}$$

where $A_1, A_2$ and $B$ are constants represent the rigid body motion components of the virtual displacement field. Having obtained the form of the virtual displacement field $\delta \boldsymbol{u}$ that satisfies condition (2.9), using relation (2.14), we obtain the following expression for the

volume of the first type of Michell structures for the tension case:

$$V_M = \frac{\sum_j \boldsymbol{f}^j \boldsymbol{\delta u}(\mathbf{r}^j)}{\overline{\sigma}\,\overline{\varepsilon}} = \sum_j \frac{1}{\overline{\sigma}_T}\left(f_x^j x^j + f_y^j y^j\right), \tag{2.17}$$

where $f_x^j$ and $f_y^j$ are the $x$ and $y$ components of the applied load $\boldsymbol{f}^j$ at location $\mathbf{r}^j = [x^j, y^j]^T$.

**Type II**: the second type of Michell structures contains both tension and compression members. According to the second condition (2.9), there should exist a virtual displacement $\boldsymbol{\delta u}$ that has a principal virtual strain of $\overline{\sigma}\,\overline{\varepsilon}/\overline{\sigma}_T$ in all members in tension and a principal virtual strain of $-\overline{\sigma}\,\overline{\varepsilon}/\overline{\sigma}_C$ in all members in compression. The virtual strain field with principal strains $\overline{\sigma}\,\overline{\varepsilon}/\overline{\sigma}_T$ and $-\overline{\sigma}\,\overline{\varepsilon}/\overline{\sigma}_C$ form an orthogonal system of lines. This implies the orthogonality condition of the second type of Michell structures, that is, the tension and compression members are always perpendicular to each other when they intersect. Mathematically, we can parametrize the curves of tensile principal virtual strain $\overline{\sigma}\,\overline{\varepsilon}/\overline{\sigma}_T$ and compressive principal virtual strain $\overline{\sigma}\,\overline{\varepsilon}/\overline{\sigma}_C$ along the two axes $\alpha$ and $\beta$ as a general curvilinear orthogonal coordinate system, as shown in Figure 2.2.

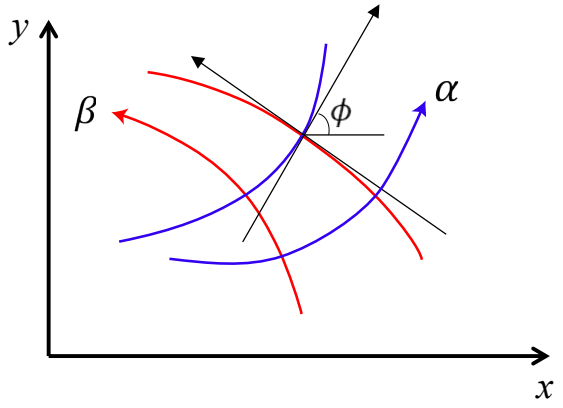


Figure 2.2: Curvilinear orthogonal coordinate system $(\alpha, \beta)$.

In order to ensure that the virtual displacement $\boldsymbol{\delta u}$ exists from the virtual strain field, such curvilinear coordinate system has to satisfy the compatibility condition, which requires that the angle $\phi$ between the tangent of $\alpha$ lines and $x$-axis has to satisfy this differ-

ential form,

$$\frac{\partial^2 \phi}{\partial \alpha \partial \beta} = 0, \tag{2.18}$$

or alternatively, the two equations

$$\phi(\alpha_k, \beta) - \phi(\alpha_{k-1}, \beta) = \Delta\phi_\alpha = C_1 \text{ and } \phi(\alpha, \beta_k) - \phi(\alpha, \beta_{k-1}) = \Delta\phi_\beta = C_2, \tag{2.19}$$

where $C_1$ and $C_2$ are constants. The compatibility of the virtual displacement field requires that the change of angle $\Delta\phi_\alpha$ (obtained by turning through two tangent lines to an $\alpha$ line as it moves through two fixed $\beta$ lines) along all $\beta$ lines are the same, and the change of angle $\phi_\beta$ (obtained by turning through two tangent lines to an $\beta$ line as it moves through two fixed $\alpha$ lines) along all $\alpha$ lines are the same. This geometric property is demonstrated in Figure 2.3. The approaches that employ this geometric property to construct Michell structures can be found in [78], [79]. The sets of orthogonal curves that satisfies (2.18) are commonly known as the Hencky nets [74], [75], which are introduced in Section 2.4.

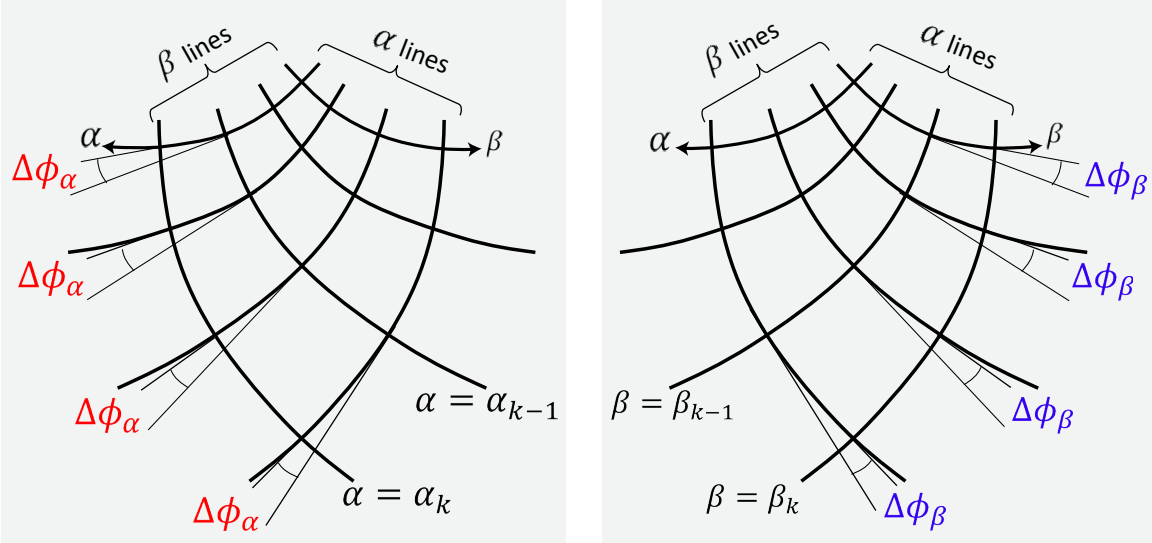


Figure 2.3: Geometric implication of the compatibility condition.

## 2.4 Construction of Michell Structures

This section introduces several classes of Hencky nets, which are useful tools to construct Michell structures. Hencky nets (known as Hencky-Prandtl nets [74], [75] for slip lines in two-dimensional perfectly plastic flow) are essentially orthogonal curvilinear coordinates that satisfy the compatibility condition (2.18). Techniques for constructing and calculating Hencky nets can be found in [80], [81]. The use of Hencky nets to derive the geometry and volume of Michell structures are introduced by Hemp [17].

To find Michell structures using Hencky nets, we first choose the proper Hencky net (and the associated virtual strain field) that satisfy the displacement boundary conditions and equilibrium for a given problem. Then, we integrate the virtual strain field (associated with that Hencky net) to obtain the virtual displacement field. Finally, the closed-form optimal volume can be calculated through (2.14), and the geometric layout of the Michell structure can be found on the virtual strain fields of the Henchy nets. In general, the explicit expression of the Henchy nets in the orthogonal curvilinear coordinate systems with $\alpha, \beta$ are cumbersome to obtain [17]. However, some simple Hencky nets can be constructed in traditional coordinate systems. Thus, the virtual strain fields governed for those Hencky nets are readily available. Next, we introduce four Hencky nets and provide the corresponding virtual strain fields.

**Hencky net 1**: the first Hencky net consists of sets of orthogonal and parallel straight lines, as shown in Figure 2.4a. This Hencky net can be parametrized in Cartesian coordinates as follows,

$$\frac{\partial \delta u_x}{\partial x} = \frac{\overline{\sigma}\,\overline{\varepsilon}}{\overline{\sigma}_T}, \quad \frac{\partial \delta u_y}{\partial y} = -\frac{\overline{\sigma}\,\overline{\varepsilon}}{\overline{\sigma}_C}, \quad \frac{\partial \delta u_x}{\partial y} + \frac{\partial \delta u_y}{\partial x} = 0. \tag{2.20}$$

Solving the set of PDEs in (2.20), we obtain the corresponding virtual displacement field,

$$\delta u_x = A_1 + By + \frac{\overline{\sigma}\,\overline{\varepsilon}}{\overline{\sigma}_T} x, \quad \text{and} \quad \delta u_y = A_2 - Bx - \frac{\overline{\sigma}\,\overline{\varepsilon}}{\overline{\sigma}_C} y, \tag{2.21}$$

where $A_1$, $A_2$ and $B$ are constants represent the rigid body motion components of the virtual displacement field.

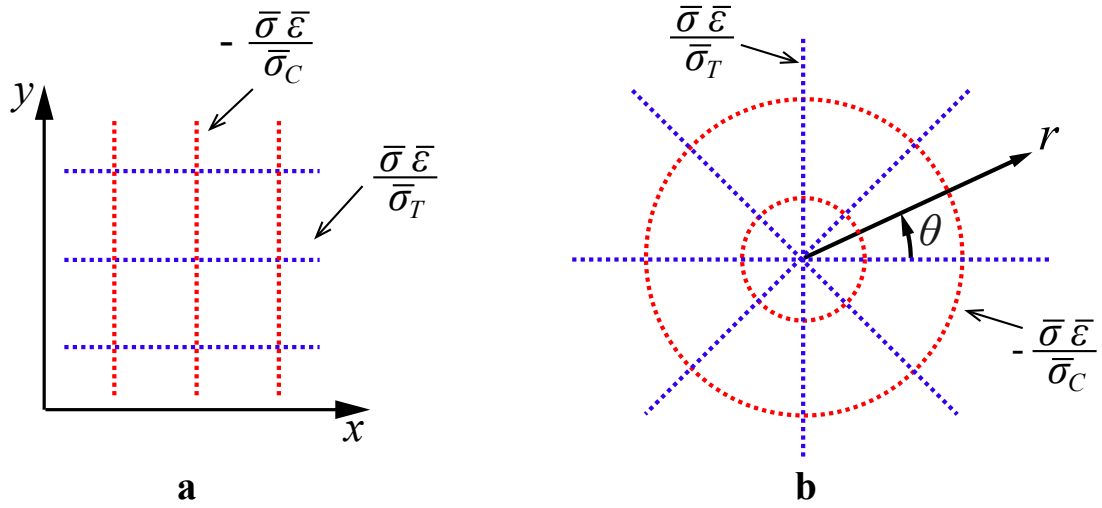


Figure 2.4: Hencky nets in **a** Cartesian coordinates and **b** polar coordinates.

**Hencky net 2**: the second Hencky net is constructed by straight lines and circles, as shown in Figure 2.4b. This Hencky net can be parametrized in polar coordinates and the corresponding virtual strain field is as follows,

$$\frac{\partial \delta u_r}{\partial r} = \frac{\overline{\sigma}\,\overline{\varepsilon}}{\overline{\sigma}_T}, \quad \frac{1}{r}\frac{\partial \delta u_\theta}{\partial \theta} + \frac{\delta u_r}{r} = -\frac{\overline{\sigma}\,\overline{\varepsilon}}{\overline{\sigma}_C}, \quad \frac{1}{r}\frac{\partial \delta u_r}{\partial \theta} + \frac{\partial \delta u_\theta}{\partial r} - \frac{\delta u_\theta}{r} = 0. \tag{2.22}$$

Solving the set of PDEs in (2.22), the following virtual displacement field is obtained,

$$\delta u_r = \frac{\overline{\sigma}\,\overline{\varepsilon}}{\overline{\sigma}_T} r + A_1 \cos\theta + A_2 \sin\theta, \tag{2.23}$$

and

$$\delta u_\theta = -\left[\frac{\overline{\sigma}\,\overline{\varepsilon}}{\overline{\sigma}_T} + \frac{\overline{\sigma}\,\overline{\varepsilon}}{\overline{\sigma}_C}\right] r\theta - A_1 \sin\theta + A_2 \cos\theta + Br, \tag{2.24}$$

where $A_1$, $A_2$ and $B$ are constants represent the rigid body motion components of the virtual displacement field. Assuming the virtual displacement field is fixed at $r = 1$ with no rigid

body rotation (i.e., $B = 0$), (2.23) and (2.24) simplify to following expressions,

$$\delta u_r = \frac{\overline{\sigma}\,\overline{\varepsilon}}{\overline{\sigma}_T} r, \quad \text{and} \quad \delta u_\theta = -\left[\frac{\overline{\sigma}\,\overline{\varepsilon}}{\overline{\sigma}_T} + \frac{\overline{\sigma}\,\overline{\varepsilon}}{\overline{\sigma}_C}\right] r\theta. \tag{2.25}$$

**Hencky net 3**: we can construct a Hencky net that is a hybrid of other nets. For this type of hybrid systems, we need to enforce continuity of the virtual displacement field at the interfaces of the constituents. The third Hencky net is constructed by a combination of Cartesian and polar coordinates, as shown in Figure 2.5.

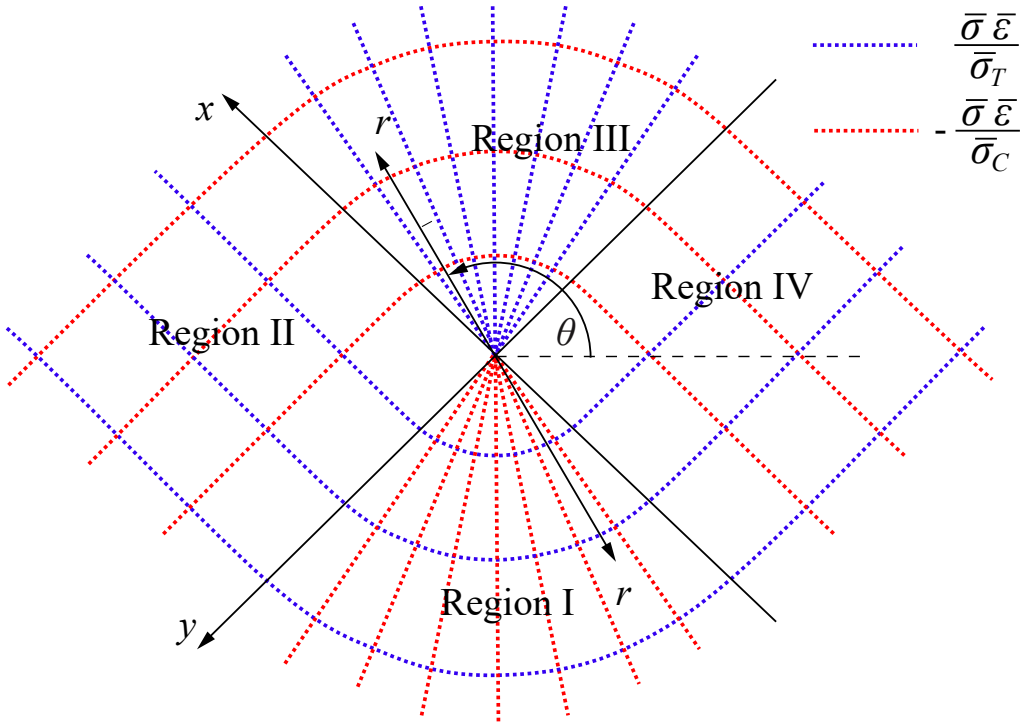


Figure 2.5: Hencky net constructed by Cartesian and polar coordinates.

Regions I and III consist of straight lines and circles. According to (2.23) and (2.24), the virtual displacement fields in these two regions, denoted by $\delta \boldsymbol{u}^{\mathrm{I}}$ and $\delta \boldsymbol{u}^{\mathrm{III}}$, are described

in polar coordinates as

$$
\begin{aligned}
\delta u_r^{\mathrm{I}} &= -\frac{\overline{\sigma}\,\overline{\varepsilon}}{\overline{\sigma}_C} r + A_1^{\mathrm{I}} \cos\theta + A_2^{\mathrm{I}} \sin\theta \,, \\
\delta u_\theta^{\mathrm{I}} &= \left[ \frac{\overline{\sigma}\,\overline{\varepsilon}}{\overline{\sigma}_T} + \frac{\overline{\sigma}\,\overline{\varepsilon}}{\overline{\sigma}_C} \right] r\theta - A_1^{\mathrm{I}} \sin\theta + A_2^{\mathrm{I}} \cos\theta + B^{\mathrm{I}} r \,, \\
\delta u_r^{\mathrm{III}} &= \frac{\overline{\sigma}\,\overline{\varepsilon}}{\overline{\sigma}_T} r + A_1^{\mathrm{III}} \cos\theta + A_2^{\mathrm{III}} \sin\theta \,, \\
\delta u_\theta^{\mathrm{III}} &= -\left[ \frac{\overline{\sigma}\,\overline{\varepsilon}}{\overline{\sigma}_T} + \frac{\overline{\sigma}\,\overline{\varepsilon}}{\overline{\sigma}_C} \right] r\theta - A_1^{\mathrm{III}} \sin\theta + A_2^{\mathrm{III}} \cos\theta + B^{\mathrm{III}} r \,.
\end{aligned}
\tag{2.26}
$$

Unlike regions I and III, regions II and IV consist two sets of orthogonal straight lines and thus the virtual displacement in these regions can be more conveniently described in Cartesian coordinates as

$$
\begin{aligned}
\delta u_x^{\mathrm{II}} &= A_1^{\mathrm{II}} + B^{\mathrm{II}} y + \frac{\overline{\sigma}\,\overline{\varepsilon}}{\overline{\sigma}_T} x \,, \\
\delta u_y^{\mathrm{II}} &= A_2^{\mathrm{II}} - B^{\mathrm{II}} x - \frac{\overline{\sigma}\,\overline{\varepsilon}}{\overline{\sigma}_C} y \,, \\
\delta u_x^{\mathrm{IV}} &= A_1^{\mathrm{IV}} - B^{\mathrm{IV}} y - \frac{\overline{\sigma}\,\overline{\varepsilon}}{\overline{\sigma}_C} x \,, \\
\delta u_y^{\mathrm{IV}} &= A_2^{\mathrm{IV}} + B^{\mathrm{IV}} x + \frac{\overline{\sigma}\,\overline{\varepsilon}}{\overline{\sigma}_T} y \,.
\end{aligned}
\tag{2.27}
$$

To obtain the undetermined constants, we assume that virtual displacement field is $\mathbf{0}$ at the origin and then enforce the continuity at the interfaces between all regions, namely,

$$
\begin{aligned}
&\delta u_\theta^{\mathrm{I}}(r, -\frac{3\pi}{4}) = -\delta u_x^{\mathrm{II}}(0,y) \quad \text{and} \quad \delta u_r^{\mathrm{I}}(r, -\frac{3\pi}{4}) = \delta u_y^{\mathrm{II}}(0,y) \,, \\
&\delta u_y^{\mathrm{II}}(x,0) = \delta u_\theta^{\mathrm{III}}(r, \frac{3\pi}{4}) \quad \text{and} \quad \delta u_x^{\mathrm{II}}(x,0) = \delta u_r^{\mathrm{III}}(r, \frac{3\pi}{4}) \,, \\
&\delta u_\theta^{\mathrm{III}}(r, \frac{\pi}{4}) = \delta u_x^{\mathrm{IV}}(0,y) \quad \text{and} \quad \delta u_r^{\mathrm{III}}(r, \frac{\pi}{4}) = -\delta u_y^{\mathrm{IV}}(0,y) \,, \\
&\delta u_y^{\mathrm{IV}}(x,0) = -\delta u_\theta^{\mathrm{I}}(r, -\frac{\pi}{4}) \quad \text{and} \quad \delta u_x^{\mathrm{IV}}(x,0) = -\delta u_r^{\mathrm{I}}(r, -\frac{\pi}{4}) \,.
\end{aligned}
\tag{2.28}
$$

Finally, we obtain the following virtual displacement field for Hencky net 3,

$$
\begin{aligned}
\delta u_r^{\mathrm{I}} &= -\frac{\overline{\sigma}\,\overline{\varepsilon}}{\overline{\sigma}_C} r\,, \\
\delta u_\theta^{\mathrm{I}} &= \left[\frac{\overline{\sigma}\,\overline{\varepsilon}}{\overline{\sigma}_T} + \frac{\overline{\sigma}\,\overline{\varepsilon}}{\overline{\sigma}_C}\right] r\theta\,, \\
\delta u_x^{\mathrm{II}} &= \left[\frac{\overline{\sigma}\,\overline{\varepsilon}}{\overline{\sigma}_T} + \frac{\overline{\sigma}\,\overline{\varepsilon}}{\overline{\sigma}_C}\right] \frac{3\pi}{4} y + \frac{\overline{\sigma}\,\overline{\varepsilon}}{\overline{\sigma}_T} x\,, \\
\delta u_y^{\mathrm{II}} &= -\left[\frac{\overline{\sigma}\,\overline{\varepsilon}}{\overline{\sigma}_T} + \frac{\overline{\sigma}\,\overline{\varepsilon}}{\overline{\sigma}_C}\right] \frac{3\pi}{4} x - \frac{\overline{\sigma}\,\overline{\varepsilon}}{\overline{\sigma}_C} y\,, \\
\delta u_r^{\mathrm{III}} &= \frac{\overline{\sigma}\,\overline{\varepsilon}}{\overline{\sigma}_T} r\,, \\
\delta u_\theta^{\mathrm{III}} &= -\left[\frac{\overline{\sigma}\,\overline{\varepsilon}}{\overline{\sigma}_T} + \frac{\overline{\sigma}\,\overline{\varepsilon}}{\overline{\sigma}_C}\right] r\theta\,, \\
\delta u_x^{\mathrm{IV}} &= \left[\frac{\overline{\sigma}\,\overline{\varepsilon}}{\overline{\sigma}_T} + \frac{\overline{\sigma}\,\overline{\varepsilon}}{\overline{\sigma}_C}\right] \frac{\pi}{4} y - \frac{\overline{\sigma}\,\overline{\varepsilon}}{\overline{\sigma}_C} x\,, \\
\delta u_y^{\mathrm{IV}} &= -\left[\frac{\overline{\sigma}\,\overline{\varepsilon}}{\overline{\sigma}_T} + \frac{\overline{\sigma}\,\overline{\varepsilon}}{\overline{\sigma}_C}\right] \frac{\pi}{4} x + \frac{\overline{\sigma}\,\overline{\varepsilon}}{\overline{\sigma}_T} y\,.
\end{aligned}
\tag{2.29}
$$

**Hencky net 4**: The forth Hencky net consists of equiangular spirals, as shown in Figure 2.6. This Hencky net can be parametrized in a polar coordinate. Here we consider a special case $\overline{\sigma}_T = \overline{\sigma}_C = \overline{\sigma}$. The virtual strain field is as follows,

$$
\frac{\partial \delta u_r}{\partial r} = 0, \quad \frac{1}{r}\frac{\partial \delta u_\theta}{\partial \theta} + \frac{\delta u_r}{r} = 0, \quad \frac{1}{r}\frac{\partial \delta u_r}{\partial \theta} + \frac{\partial \delta u_\theta}{\partial r} - \frac{\delta u_\theta}{r} = -2\overline{\varepsilon}. \tag{2.30}
$$

Solving the PDEs in (2.30), we obtain the following virtual displacement field for this type of Hencky net,

$$
\delta u_r = A_1 \cos\theta + A_2 \sin\theta\,, \tag{2.31}
$$

and

$$
\delta u_\theta = -2\overline{\varepsilon} r \ln(\frac{r}{B}) - A_1 \sin\theta + A_2 \cos\theta\,, \tag{2.32}
$$

where $A_1, A_2$ and $B$ are constants represent the rigid body motion components of the virtual displacement field. If the circle $r = R_0$ is a fixed support and has zero rotation, then the

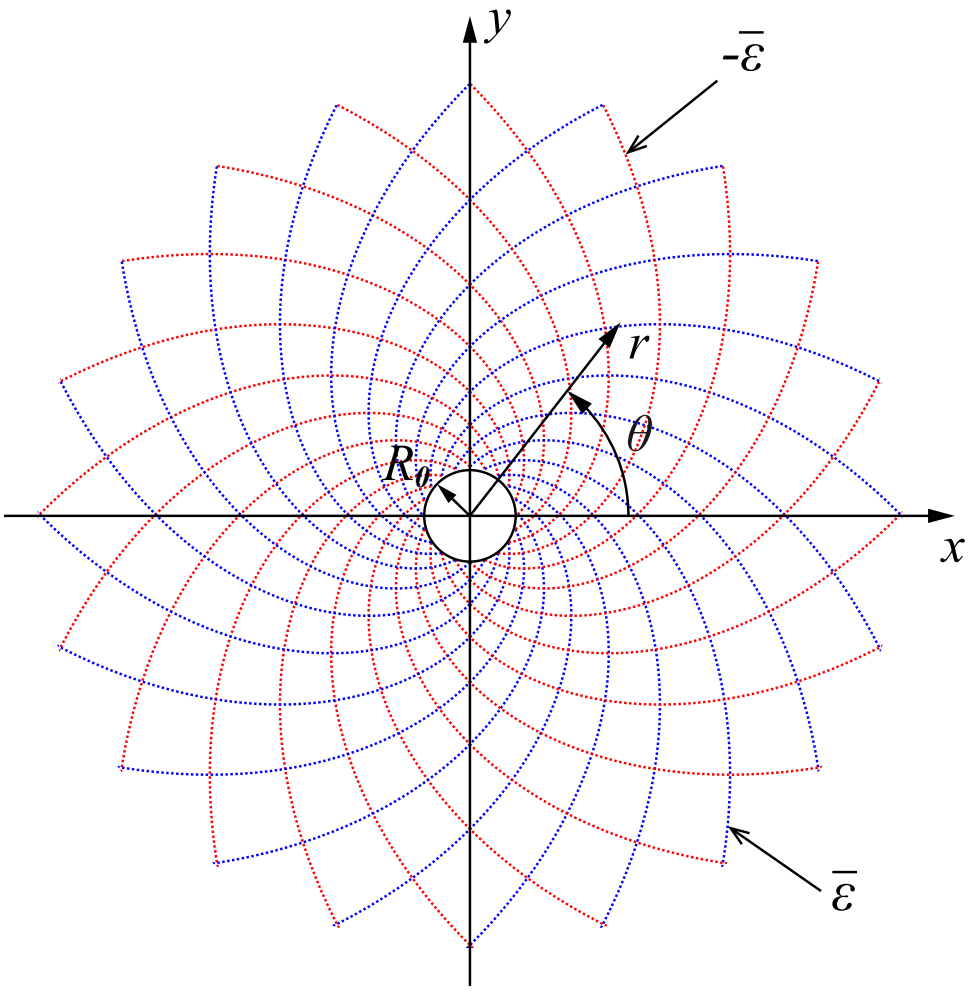


Figure 2.6: Hencky net constructed by equiangular spirals.

virtual displacement field becomes

$$\delta u_r = 0 \quad \text{and} \quad \delta u_\theta = -2\overline{\varepsilon} r \ln(\frac{r}{R_0}) \, . \tag{2.33}$$

## 2.5 Michell Solutions

In this section, we use Michell's optimality conditions and Hencky nets to derive the analytical solutions of several 2D and 3D Michell structures.

### 2.5.1 Derivation of the 2D Michell solutions

In this subsection, we derive the close-form optimal volume and the geometric layout for four 2D examples. The first 2D example considers a centrally loaded beam, as shown in Figure 2.7a, the design domain is limited to the semi-infinite plane above the line AB. We first assume that all the members of the Michell structure are fully stressed to the stress limits $\overline{\sigma}_T$ and $\overline{\sigma}_C$. To find the Michell structure by using Hencky nets, we choose the proper Hencky net that satisfies the displacement boundary conditions and equilibrium for the problem in Figure 2.7a. Among the four Hencky nets introduced in Section 2.4, the second Hencky net with polar coordinates is the proper one (with point $O$ as the origin), as shown in Figure 2.7b. Other Hencky nets violate the displacement boundary conditions and equilibrium. Thus, we use the corresponding virtual displacement field (2.25) in the polar coordinates. The three loaded points $O, A$, and $B$ have coordinates $[r^O, \theta^O]^T = [0,0]^T$, $[r^A, \theta^A]^T = [L, \pi]^T$, and $[r^B, \theta^B]^T = [L, 0]^T$, respectively. By plugging these coordinates into (2.25), we obtain the expressions for $\delta \boldsymbol{u}$. We also observe that $\delta u_{r,O} = \delta u_{\theta,O} = \delta u_{\theta,B} = 0$. In addition, points $A$ and $B$ contribute to the external virtual work only from the tangential component (zero force in the radial direction), i.e., $f_r^A = 0$, $f_\theta^A = -P$, $f_r^B = 0$, $f_\theta^B = P$. Thus, the external virtual work and the closed-form optimal volume can be calculated through

(2.14) as follows:

$$\delta\Omega = f_\theta^A(\delta u_{\theta,A}) + f_\theta^B(\delta u_{\theta,B}) = PL\pi\left[\left(\frac{\overline{\sigma}\,\overline{\varepsilon}}{\overline{\sigma}_T} + \frac{\overline{\sigma}\,\overline{\varepsilon}}{\overline{\sigma}_C}\right)\right], \tag{2.34}$$

and

$$V_M = PL\pi\left[\left(\frac{1}{\overline{\sigma}_T} + \frac{1}{\overline{\sigma}_C}\right)\right]. \tag{2.35}$$

Following the virtual strain field in the Hencky net 2, we obtain the geometric layout of this Michell structure, as shown in Figure 2.7c, which consists of infinitely many bars and joints.

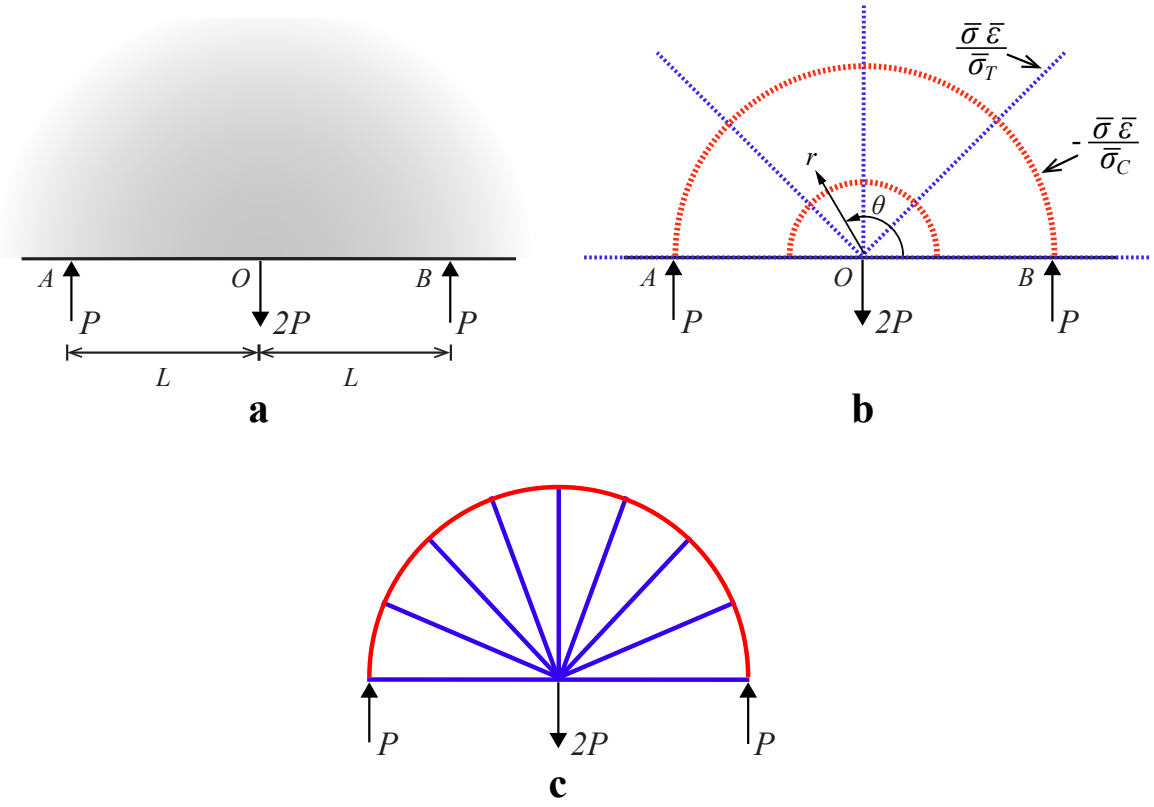


Figure 2.7: Centrally loaded beam with semi-infinite plane domain. **a** Load and boundary conditions, the design domain is subjected to the semi-infinite 2D plane above line $AB$; **b** applying Hencky net 2 to the problem; **c** corresponding analytical solution.

The second example considers the same load and boundary conditions as the first example, however, we subject the domain to the infinite 2D plane (instead of semi-infinite),

as shown in Figure 2.8a. We first assume that all the members of the Michell structure are fully stressed to the stress limits $\overline{\sigma}_T$ and $\overline{\sigma}_C$. In this example, Hencky net 3 provides virtual displacement field (2.29) that satisfies the displacement boundary conditions and equilibrium, as shown in Figure 2.8b. In Hencky net 3 with the combination of Cartesian and polar coordinates, the three loaded points $O$, $A$, and $B$ have coordinates $[r^O, \theta^O]^T = [0,0]^T$, $[x^A, y^A]^T = [L/\sqrt{2}, L/\sqrt{2}]^T$, and $[x^B, y^B]^T = [-L/\sqrt{2}, -L/\sqrt{2}]^T$, respectively. Because the force at point $O$ does not contribute to the external virtual work and points $A$ and $B$ are in regions II and IV of Hencky net 3, we obtain the virtual displacement at $A$ and $B$, denoted by $\delta u^{\text{II}}_{x,A}$, $\delta u^{\text{II}}_{y,A}$, $\delta u^{\text{IV}}_{x,B}$, and $\delta u^{\text{IV}}_{y,B}$, by plugging in the corresponding coordinates of $A$ and $B$ to (2.29). In addition, $[f^A_x, f^A_y]^T = [P/\sqrt{2}, -P/\sqrt{2}]^T$, and $[f^B_x, f^B_y]^T = [P/\sqrt{2}, -P/\sqrt{2}]^T$. Thus, the external virtual work and the closed-form optimal volume can be calculated through (2.14) as follows:

$$\begin{aligned} \delta\Omega &= f^A_x(\delta u^{\text{II}}_{x,A}) + f^A_y(\delta u^{\text{II}}_{y,A}) + f^B_x(\delta u^{\text{IV}}_{x,B}) + f^B_y(\delta u^{\text{IV}}_{y,B}) \\ &= PL\left(1+\frac{\pi}{2}\right)\left[\left(\frac{\overline{\sigma}\,\overline{\varepsilon}}{\overline{\sigma}_T} + \frac{\overline{\sigma}\,\overline{\varepsilon}}{\overline{\sigma}_C}\right)\right], \end{aligned} \tag{2.36}$$

and

$$V_M = PL\left(1+\frac{\pi}{2}\right)\left[\left(\frac{1}{\overline{\sigma}_T} + \frac{1}{\overline{\sigma}_C}\right)\right]. \tag{2.37}$$

Using the virtual strain fields in the Hencky net 3, we obtain the geometric layout of this Michell structure consists of infinitely many bars and joints, as shown in Figure 2.8c.

A smaller (restrained) design space may lead to the optimal structure with a larger volume [16]. Comparing the analytical optimal volume expressions of these two Michell structures in (2.35) and (2.37), we observe that structure with a larger design space (i.e., infinite 2D plane) has smaller optimal volume than the one with a smaller design space (i.e., semi-infinite 2D plane). Specifically, the ratio of (2.35) to (2.37) is $\pi/(1+\pi/2)$.

The third example is the Michell torsional disc. The load and displacement boundary conditions are shown in Figure 2.9a, where a pair of uniformly distributed torques is ap-

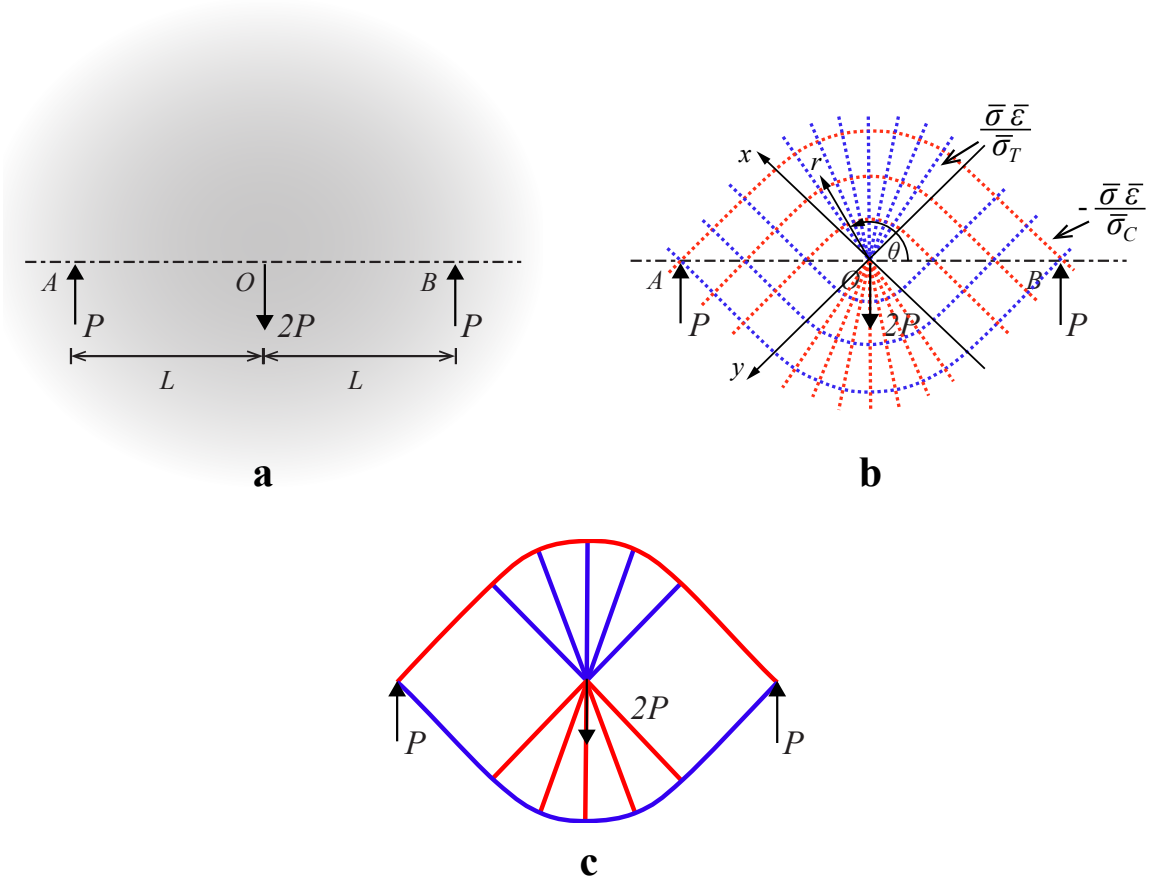


Figure 2.8: Centrally loaded beam with infinite plane domain. **a** Load and boundary conditions, the design domain is subjected to the infinite 2D plane; **b** applying Hencky net 3 to the problem; **c** corresponding analytical solution.

plied at the inner circular ($r = R_0$) and outer circular ($r = R$) boundaries. For this problem, assuming that all the members in the Michell structure are fully stressed to the same stress limit $\overline{\sigma}_T = \overline{\sigma}_C = \overline{\sigma}$, Hencky net 4 in Figure 2.6 provides the proper virtual displacement field, where the displacement is fixed at the inner circle with radius $R_0$. Using the expression of the virtual displacement $\delta u_\theta$ (and $\delta u_r = 0$) in (2.33), we can compute the external virtual work as follows:

$$\delta\Omega = \left( \int_0^{2\pi} -\tau_0 R \mathrm{d}\theta \right) \delta u_\theta = 4\pi\overline{\varepsilon} R^2 \tau_0 \ln(\frac{R}{R_0}) \,. \tag{2.38}$$

By defining $T_{\text{torsion}} = 2\pi(R)^2\tau_0$ as the total torque applied and using relation (2.14), we obtain the volume of the Michell torsional disc as follows,

$$V_M = \frac{2T_{\text{torsion}}}{\overline{\sigma}} \ln(\frac{R}{R_0}) \,. \tag{2.39}$$

Next, we use the virtual strain field in the Hencky net 4 to obtain the geometric layout of the Michell torsional disc, which is constructed by equiangular spirals, as shown in Figure 2.9b.

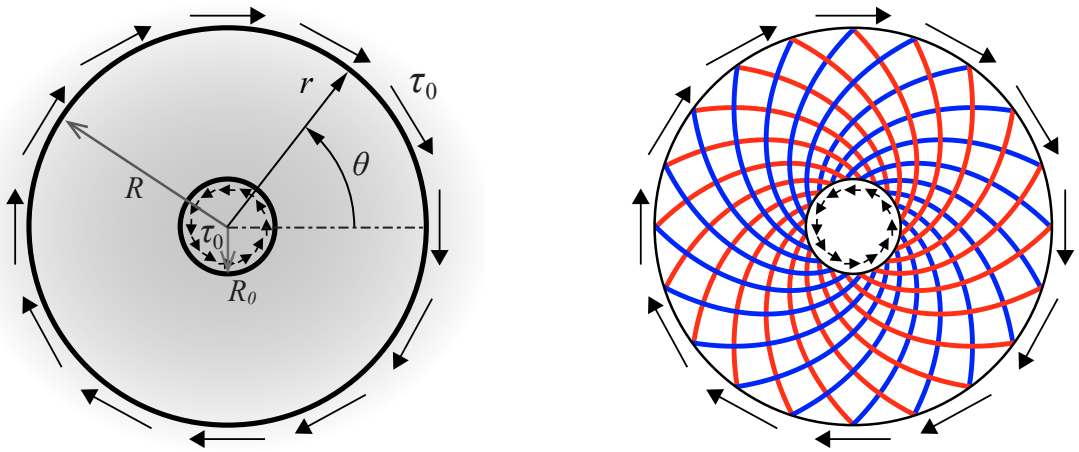


Figure 2.9: Michell torsional disc. **a** Load and boundary conditions, the design domain is subjected to infinite 3D space; **b** corresponding analytical solution.

The last 2D example considers a cantilever beam. The load and displacement boundary conditions are shown in Figure 2.10a, where the left circle with radius $R_0$ is a fixed support. Similar to the Michell torsional disc, we have the stress limit $\overline{\sigma}_T = \overline{\sigma}_C = \overline{\sigma}$. In addition, Hencky net 4 provides the proper virtual displacement field for this example. Thus, we use the polar coordinates $(r, \theta)$ with point $O$ as the origin and $r = R_0$ on the edge of the left circle. The location of the point $A$ is denoted by $[r^A, \theta^A]^T = [L, 0]^T$, hence, point $A$ has the virtual displacement $\delta u_{r,A} = 0$ and $\delta u_{\theta,A} = -2\overline{\varepsilon} L \ln(L/R_0)$. Given that $f_r^A = 0, f_\theta^A = -P$, we can compute the external virtual work and closed-form optimal volume as follows:

$$\delta\Omega = f_\theta^A \delta u_{\theta,A} = 2PL\overline{\varepsilon} \ln(\frac{L}{R_0}) \,, \tag{2.40}$$

and

$$V_M = \frac{2PL}{\overline{\sigma}} \ln(\frac{L}{R_0}) \,. \tag{2.41}$$

By using the virtual strain field in the Hencky net 4, we obtain the geometric layout of the Michell cantilever, which is constructed by equiangular spirals, as shown in Figure 2.10b.

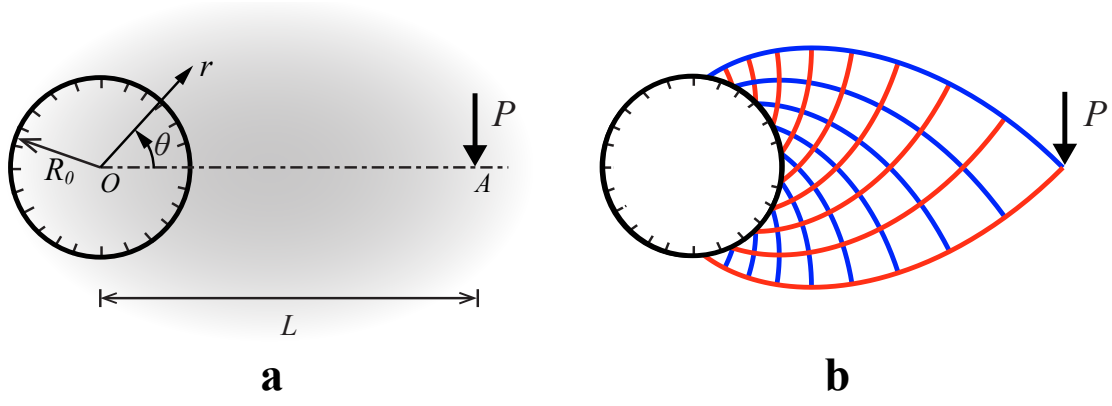


Figure 2.10: Michell cantilever. **a** Load and boundary conditions, the design domain is subjected to infinite 3D space; **b** corresponding analytical solution.

### 2.5.2 Derivation of the 3D Michell torsional sphere and torsional cylinder

Michell torsional sphere is one of the few available closed-form solutions for 3D problems, which suggests that the lightest structure to transfer a pair of distributed torques over small circumferences is a spherical shape. The load and boundary conditions are provided in Figure 2.11a, and the design domain is subjected to the infinite three-dimensional space. The corresponding optimal solution, torsional sphere, is shown in Figure 2.11b. Details of the derivations are not included in Michell's paper [16], and the solution is re-derived in [17], [23]. The derivation by Hemp [17] assumes that (1) $\overline{\sigma}_T = \overline{\sigma}_C = \overline{\sigma}$ and (2) the meridian of the optimal shape is a segment of a circle. With the same assumptions, in this subsection, we derive the analytical solution of the Michell torsional sphere by using Michell's conditions.

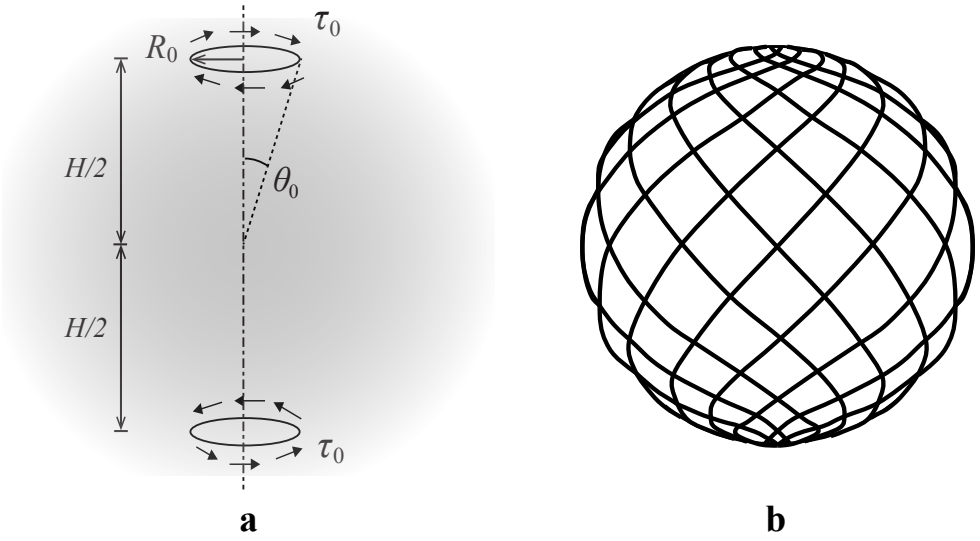


Figure 2.11: Michell torsional sphere. **a** Load and boundary conditions, the design domain is subjected to the infinite 3D space; **b** corresponding analytical solution.

To begin with, we start by examining the stress state to determine the proper virtual strain field to use. Because we assume that the optimal structure is on a sphere of radius $R = R_0/\sin\theta_0$, making use of the spherical coordinate in Figure 2.12a, the stress at any

given point on the sphere surface is given by

$$\boldsymbol{\sigma}(r,\theta,\phi) = \begin{bmatrix} 0 & 0 & 0 \\ 0 & 0 & \tau(\theta) \\ 0 & \tau(\theta) & 0 \end{bmatrix}. \tag{2.42}$$

By using analysis shown in Figure 2.12c, we obtain $\tau(\theta) = \tau_0(\sin\theta_0)^2/(\sin\theta)^2$. The stress tensor suggests that any location on this spherical surface is under pure shear state, as shown in Figure 2.12b. Inspired by this stress state, we look for a virtual displacement $\delta\boldsymbol{u}$, which generates virtual strains of the form

$$\boldsymbol{\varepsilon}(r,\theta,\phi) = \begin{bmatrix} 0 & 0 & 0 \\ 0 & 0 & \overline{\varepsilon} \\ 0 & \overline{\varepsilon} & 0 \end{bmatrix}. \tag{2.43}$$

Plugging in the virtual strain (2.43) into the strain-displacement relationship in spherical coordinates, we arrive at the following set of PDEs:

$$\begin{aligned}
&\frac{\partial \delta u_r}{\partial r} = 0\,, \\
&\frac{1}{r}\left(\frac{\partial \delta u_\theta}{\partial \theta} + \delta u_r\right) = 0\,, \\
&\frac{1}{r\sin\theta}\left(\frac{\delta u_\phi}{\partial \phi} + \delta u_r \sin\theta + \delta u_\theta \cos\theta\right) = 0\,, \\
&\frac{1}{2}\left(\frac{1}{r}\frac{\partial \delta u_r}{\partial \theta} + \frac{\partial \delta u_\theta}{\partial r} - \frac{\delta u_\theta}{r}\right) = 0\,, \\
&\frac{1}{2r}\left(\frac{1}{\sin\theta}\frac{\partial \delta u_\theta}{\partial \phi} + \frac{\partial \delta u_\phi}{\partial \theta} - \delta u_\phi \cot\theta\right) = \overline{\varepsilon}\,, \\
&\frac{1}{2}\left(\frac{1}{r\sin\theta}\frac{\partial \delta u_r}{\partial \phi} + \frac{\partial \delta u_\phi}{\partial r} - \frac{u_\phi}{r}\right) = 0\,.
\end{aligned} \tag{2.44}$$

Solving the set of PDEs (2.44) gives the following virtual displacement field $\delta\boldsymbol{u}$

$$\delta u_r = 0, \quad \delta u_\theta = 0, \quad \text{and} \quad \delta u_\phi(r,\theta) = 2\overline{\varepsilon} r \sin\theta \ln(\tan\frac{\theta}{2}). \tag{2.45}$$

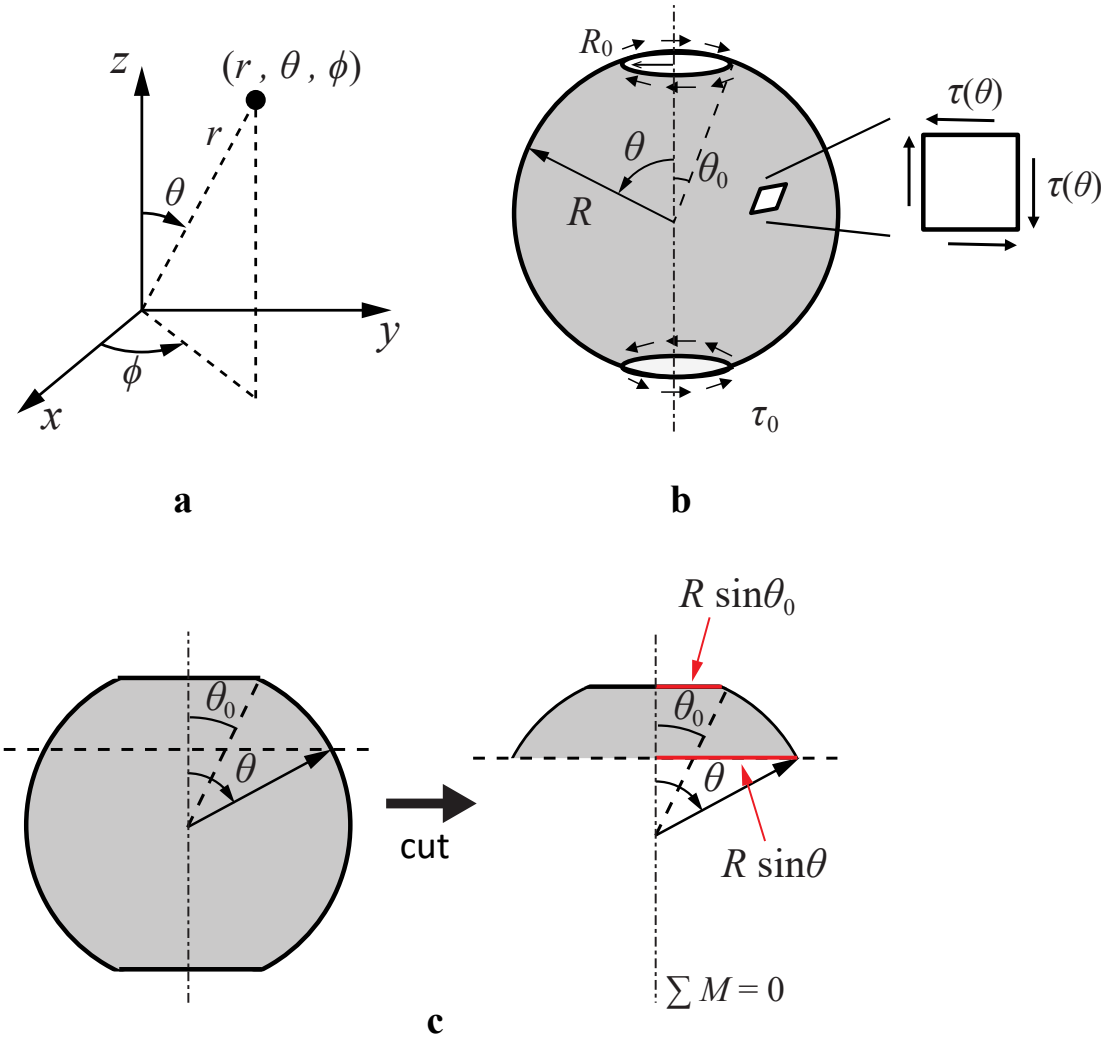


Figure 2.12: **a** Spherical coordinate system; **b** stress state on the spherical surface; **c** equilibrium analysis of the sphere.

Using the expression of the virtual displacement $\boldsymbol{\delta u}$ in (2.45), we can compute the external virtual work as follows:

$$\begin{aligned}\delta\Omega &= \int_0^{2\pi}\left[-\tau_0(R\sin\theta_0)\delta u_\phi(R,\theta_0)\mathrm{d}\phi\right] + \int_0^{2\pi}\left[\tau_0(R\sin\theta_0)\delta u_\phi(R,\pi-\theta_0)\mathrm{d}\phi\right] \\ &= 8\pi\overline{\varepsilon}R^2\sin^2\theta_0\tau_0\ln(\cot\frac{\theta_0}{2})\,.\end{aligned} \tag{2.46}$$

By defining $T_{\text{torsion}} = 2\pi(R\sin\theta_0)^2\tau_0 = 2\pi(R_0)^2\tau_0$ as the total torque applied and using relation (2.14), we can obtain the volume of the Michell torsional ball as a function of $T_{\text{torsion}}$ as

$$V_{M,\text{sphere}} = \frac{4T_{\text{torsion}}}{\overline{\sigma}}\ln(\cot\frac{\theta_0}{2})\,. \tag{2.47}$$

According to the optimality conditions, all the members in Michell structures must lie in the principal strain directions, thus, the members for this Michell sphere lie in the principal directions of the virtual strain in (2.43), constructing a series of rhumb lines inclined at angles $\pm\Pi/4$, which is a grid-like continua consists of infinitely many bars and joints, as shown in Figure 2.11b. The optimal solution for the case $\overline{\sigma}_T \neq \overline{\sigma}_C$ could be generalized [20], in this case, the tension and compression members are no longer with same lengths inclined at same angles. For example, the tension members would be longer and compression members shorter for $\overline{\sigma}_T > \overline{\sigma}_C$.

The second 3D example, torsional cylinder, solves the same load and boundary conditions as the Michell torsional sphere. However, instead of an infinite 3D space, we restrain the design domain to the cylindrical surface with radius $R_0$ in the 3D space, as shown in Figure 2.13a. Similar to the torsional sphere, the stress and the virtual strain any given point on the cylindrical surface in cylindrical coordinates (Figure 2.13b) are given by

$$\boldsymbol{\sigma}(r,\theta,z) = \begin{bmatrix} 0 & 0 & 0 \\ 0 & 0 & \tau(\theta) \\ 0 & \tau(\theta) & 0 \end{bmatrix}, \quad \text{and} \quad \boldsymbol{\varepsilon}(r,\theta,z) = \begin{bmatrix} 0 & 0 & 0 \\ 0 & 0 & \overline{\varepsilon} \\ 0 & \overline{\varepsilon} & 0 \end{bmatrix}. \tag{2.48}$$

Using the strain-displacement relationship and solving the corresponding PDEs in cylindrical coordinates, we obtain

$$\delta u_r = 0, \quad \delta u_\theta(z) = -2\overline{\varepsilon} z, \quad \text{and} \quad \delta u_z = 0. \tag{2.49}$$

Using (2.49), we compute the external virtual work as follows:

$$\begin{aligned} \delta\Omega &= -2\pi R_0 \tau_0 \delta u_\theta + 2\pi R_0 \tau_0 \delta u_\theta \\ &= 4\pi R_0 H \overline{\varepsilon} \tau_0 \, . \end{aligned} \tag{2.50}$$

By defining $T_{\text{torsion}} = 2\pi (R_0)^2 \tau_0$ as the total torque applied, we can obtain the volume of the Michell torsional cylinder as a function of $T_{\text{torsion}}$ as

$$V_{M,\text{cylinder}} = \frac{2HT_{\text{torsion}}}{R_0 \overline{\sigma}} = \frac{4T_{\text{torsion}}}{\overline{\sigma}} \cot\theta_0 \, . \tag{2.51}$$

Using the principal directions of virtual strain field in (2.48), we obtain the layout of this Michell cylinder as a grid-like continua on the cylindrical surface (Figure 2.13c).

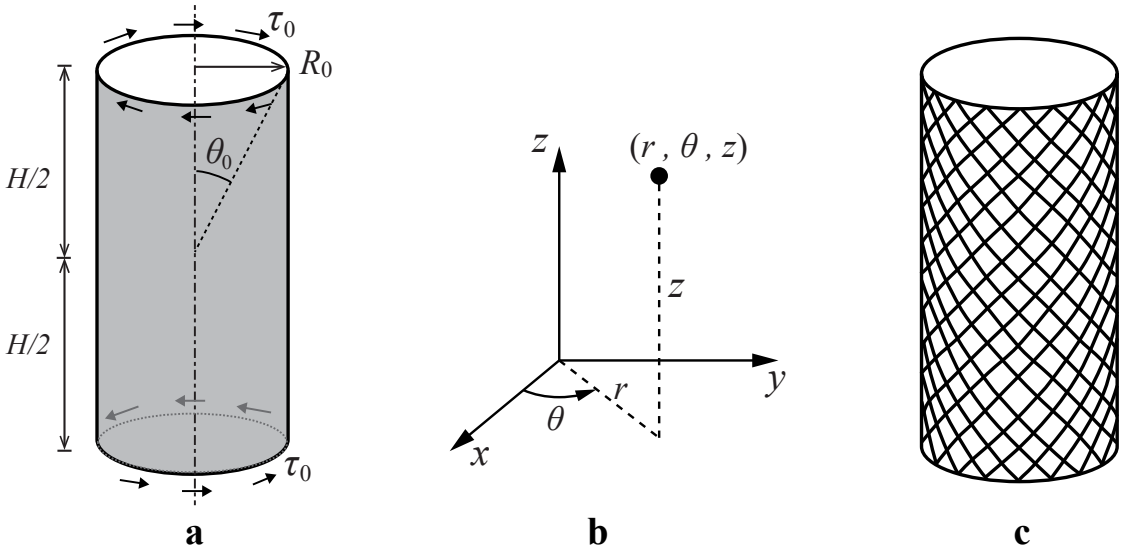


Figure 2.13: Torsional cylinder. **a** Design domain with load and boundary conditions, the design domain is subjected to the cylindrical surface; **b** cylindrical coordinate system; **c** corresponding analytical solution.

Next, we compare the close-form optimal volumes of the two 3D structures, the ratio of (2.51) to (2.47) is

$$\frac{V_{M,\text{cylinder}}}{V_{M,\text{sphere}}} = \frac{\cot\theta_0}{\ln(\cot\frac{\theta_0}{2})}\,. \tag{2.52}$$

By defining $\overline{V}_M = V_M\overline{\sigma}/4T_{\text{torsion}}$ as the normalized volume for the two 3D examples, we plot $\overline{V}_M$ for torsional cylinder and torsional sphere with varied $\theta_0$ in Figure 2.14. The optimal volumes for both torsional sphere and torsional cylinder approach to zero as $\theta_0$ increases to $\pi/2$. We observe that, for $0 < \theta_0 < \pi/2$, the torsional sphere (obtained from a larger design space) always has smaller optimal volume than the torsional cylinder (obtained from a smaller design space). This observation confirms that a smaller (restrained) design space may lead to the optimal structure with a larger volume [16]. Relevant discussions can also be found in [23].

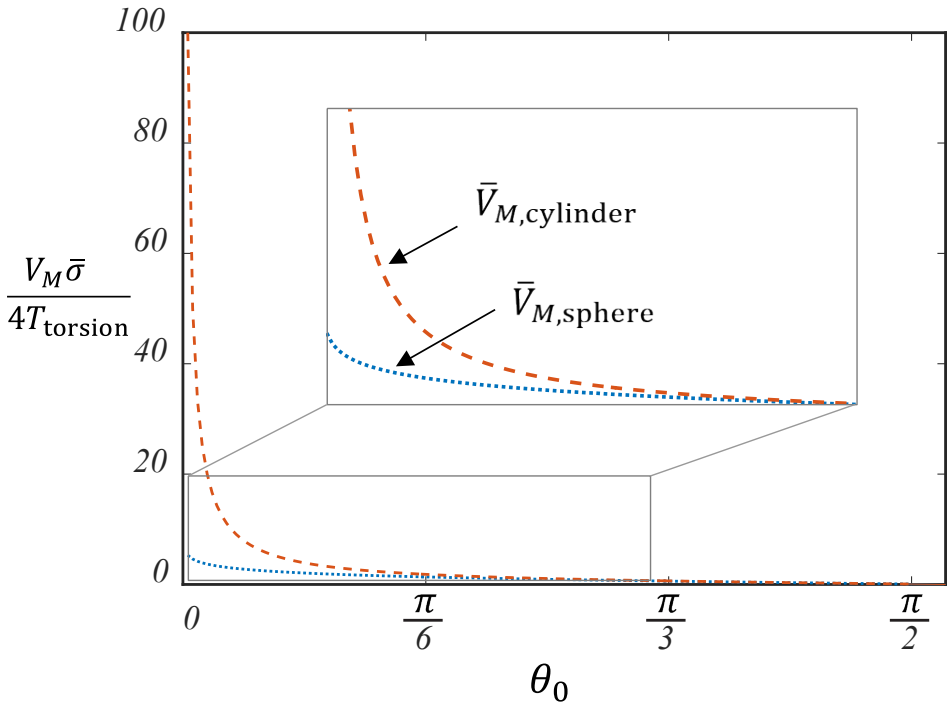


Figure 2.14: Comparison of the optimal volumes of Michell torsional sphere and torsional cylinder.

## 2.6 Summary and Discussion

In this chapter, we review Michell's original optimality conditions [16] and Hemp's modified optimality conditions [17] for trusses to have the least weight with given allowable stresses. The first condition requires the members to be fully stressed to the tensile and compressive stress limits ($\overline{\sigma}_T, \overline{\sigma}_C$). The second condition requires the existence of a kinematically admissible virtual displacement field that gives tensile and compressive principal virtual strains in all tension and compression members, respectively. Based on the conditions, all the members of a Michell structure must lie in the principal directions of the chosen virtual strain field, thus, a Michell structure resembles truss-like continua, which consists of infinitely many bars and joints. Using the principle of virtual work, we provide a proof of the optimality conditions. In addition, we present two types of Michell structures and illustrate their geometric properties, i.e., orthogonality and compatibility conditions. We introduce four types of Hencky nets, which are useful tools to derive the geometry and volume of Michell structures. Finally, we derive the closed-form solutions for four 2D structures and two 3D structures by using Michell's conditions and Hencky nets. We observe that a smaller (restrained) design space may lead to the optimal structure with a larger volume. For example, with the same load and boundary conditions, if we restrain the design space to a cylindrical surface rather than the infinite 3D space, the optimal structure obtained (a torsional cylinder) has larger a volume than the torsional sphere.

We remark that studying Michell's optimality conditions, the geometric implications, and derived closed-form solutions not only brings insights for functional and creative structural designs, but also provides analytical benchmarks for numerical optimization methods to verify with. However, there are a few problems with analytical solutions. For more complex problems with no known analytical solutions, computational approaches (e.g., ground structure and density-based methods) can offer close-to-optimal solutions. Another approach using the graphic statics to obtain optimal structures is developed in [82]. Thus,

Chapters 3-6 of this thesis focus on developing new computational approaches for topology optimization.

# CHAPTER 3

# A NEW DISCRETE FILTERING SCHEME FOR MATERIAL NONLINEAR TOPOLOGY OPTIMIZATION USING THE GROUND STRUCTURE METHOD

Topology optimization of truss lattices, using the ground structure method, is a practical tool that allows for improved structural designs. However, in general, the final topology consists of a large number of undesirable thin bars that may add artificial stiffness and degenerate the condition of the system of equations, sometimes even leading to an invalid structural system. Moreover, most work in this field has been restricted to linear material behavior, yet real materials generally display nonlinear behavior. To address these issues, in this chapter, we present an efficient filtering scheme, with reduced-order modeling, and demonstrate its application to two- and three-dimensional topology optimization of truss networks considering multiple load cases and nonlinear constitutive behavior. The proposed scheme accounts for proper load levels during the optimization process, yielding the displacement field without artificial stiffness by simply using the truss members that actually exist in the structure (no spurious members), and improving convergence performance. The nonlinear solution scheme is based on a Newton-Raphson approach with line search, which is essential for convergence. In addition, the use of reduced-order information significantly reduces the size of the structural and optimization problems within a few iterations, leading to drastically improved computational performance. For instance, the application of our method to a problem with approximately 1 million design variables shows that the proposed filter algorithm, while offering almost the same optimized structure, is more than 40 times faster than the standard ground structure method.

## 3.1 Introduction

In an effort to attain structural efficiency, a technique used for optimizing the truss lattice networks is the ground structure method (GSM) (see, e.g., [27]–[31]). In the field of structural topology optimization of trusses using the GSM, it is important to take into account material nonlinearity, because real materials generally display nonlinear constitutive relationship. For example, certain heat treatment methods change the constitutive relationships of a material dramatically. Although the influence of material properties on optimization design is well known, the exact changes that take place may not be predictable in the optimized design. Topology optimization considering linear material behavior (the prevailing approach in the literature [30]) has a limited scope, which can be extended by accounting for nonlinear material as it can significantly alter the optimized structure layout. In fact, the studies of material nonlinearity using the GSM (e.g., [39], [41], [83], [84]) show the importance of accounting for nonlinear material properties and load levels in structural optimization. Figure 3.1 further illustrates and motivates the influence of material nonlinearity in optimization. Two hyperelastic material models with convex specific strain energy, representing tension-dominated and compression-dominated Ogden-based materials, lead to completely different final topologies. In addition, the self-equilibrated filtered structure in Figure 3.1d (from the compression-dominated material) is a motivation for solving systems with a singular stiffness matrix.

**Structural Engineering Perspective:**

From the perspective of structural engineering, one limitation of the standard GSM is its inability to define a valid final structure and the unlikelihood of manufacturing an optimized structure. Since a cut-off value is needed to define the final topology for the standard GSM (a sizing problem), the topology may either consist of a large number of undesirable thin bars (if the cut-off value is too small) or violate the global equilibrium (if the cut-off value

[1]The tension-dominated material has $(\beta_1, \beta_2) = (4264.0, -0.9)$ and the compression-dominated material has $(\beta_1, \beta_2) = (1.1, -4253.4)$, where $\beta_1$ and $\beta_2$ are material parameters for Ogden-based material models – see Section 3.1 for the constitutive model definition.

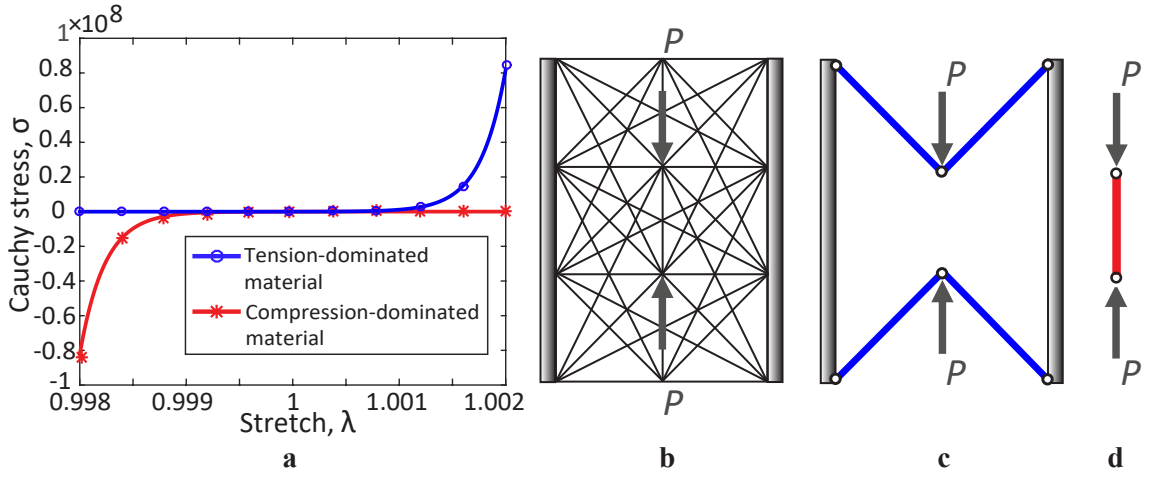


Figure 3.1: Influence of material properties in topology optimization: **a** Hyperelastic Ogden-based material models with convex[1] specific strain energy; **b** initial ground structure and boundary conditions; **c** final filtered topology from the tension-dominated Ogden-based material model; **d** either linear elastic material or the compression-dominated Ogden-based material model yields a self-equilibrated filtered topology. Blue bars are in tension and the red bar is in compression.

is too large) because of the removal of some structurally important bars. This is illustrated by means of Figure 3.2, which shows a bridge (Figure 3.2a) with a bilinear material model (Figure 3.2b). For comparison purposes, Figure 3.2c shows the case when a proper cut-off is chosen and Figure 3.2d shows the case when global equilibrium is violated because of an improper choice of the final cut-off value, both of them using the same lower bound on the design variable, $x_{\min} = 1.36 \times 10^{-8}$. Figures 3.2e and 3.2f illustrate the final topologies without a cut-off value. Figure 3.2e is obtained using the standard GSM with an arbitrarily small lower bound of the design variable, $x_{\min} = 1.36 \times 10^{-14}$. As a result, the entire ground structure is included in the final topology. Figure 3.2f shows the final topology with $x_{\min} = 0$ as the lower bound, in which the final topology consists of numerous thin bars. Note that the zero lower bound on design variables leads to singular tangent stiffness matrices. In this case, state equations were solved by minimization of potential energy with Tikhonov regularization [85]. For other methods of solving the state equations, readers are referred to [86]–[88]. Attempts have been made to treat undesirable thin members and obtain valid and constructible structures. By introducing discrete variables (either as

design variables or as the existence variable) into the optimization, the undesirable thin bars may be avoided. For example, [89] impose a realistic design constraint with a binary variable (to represent presence or absence) on the braces with geometric nonlinearity, which only selects braces within specific bound limits. However, these formulations with discrete variables to treat thin members become mixed integer linear/nonlinear problems. For a detailed review of the truss optimization with discrete design variables, readers are referred to [90]. Another approach consists of including "slenderness constraints" using a plastic formulation [35], [36]. Here we adopt an elastic formulation as motivated by a recent study by [85], who propose a discrete filter that can be used to control the final resolution of the optimized structure, resulting in a valid structure in which global equilibrium is guaranteed. This discrete filter has only been applied to linear optimization problems; therefore, in an effort to provide a practical design tool that targets the real-life demands of material, structural design, and manufacturing aspects, we propose a filtering scheme with reduced-order modeling that accounts for material nonlinearity in this chapter.

**Analysis Perspective:**

From an analysis perspective, the standard GSM considering material nonlinearity, contains numerous small area truss members, which can be problematic in two aspects: first, since small area members are included to solve the structural problem, they add artificial stiffness to the structure, leading to a degree of unreliability of the optimization results. Moreover, in the nonlinear finite element method (FEM) of the standard GSM, certain nodes that only connect to thin members produce small eigenvalues in the stiffness matrix, which could degenerate the condition of the state equations and result in difficulties in convergence. Nevertheless, the removal of these thin members can result in a violation of global equilibrium, as shown in Figure 3.2d. The proposed filter algorithm, however, filters out the small area members and the associated nodes of the structure thus solving such structural problems (state equations) solely by using other relevant members in the structure. As a result, the displacement field is obtained, preventing local instability in the low stiffness re-

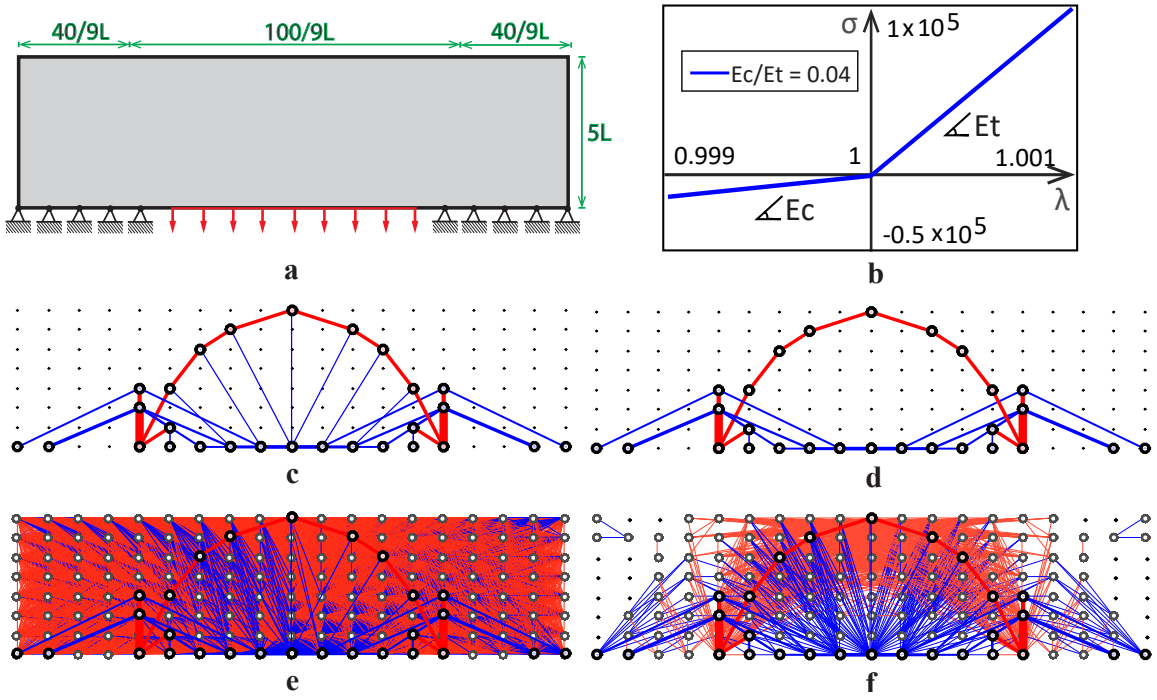


Figure 3.2: Some pitfalls of the standard GSM through a case study of a bridge design with a full-level standard GS containing 7,083 non-overlapping members: **a** Bridge domain and boundary conditions; **b** bilinear material model with $E_c/E_t = 0.04$ (hyperelastic formulation); **c** final topology (41 members) considering a lower bound on area $x_{\min} = 1.36 \times 10^{-8}$ with a proper cut-off value which shows that global equilibrium holds; **d** final topology (34 members) considering a lower bound on area $x_{\min} = 1.36 \times 10^{-8}$ with an improper cut-off value which shows that global equilibrium does not hold; **e** final topology (7,083 members) without the cut-off value considering a relatively small lower bound on area $x_{\min} = 1.36 \times 10^{-14}$; **f** final topology (975 members) without the cut-off value considering zero lower bound on area $x_{\min} = 0$. Blue bars are in tension and red bars are in compression.

gions (regions associated with the small area members), which improves the convergence performance in the nonlinear FEM and allows global equilibrium and stability verification in the actual topology.

**Efficiency Perspective:**

From the perspective of efficiency, another major problem with the GSM that accounts for material nonlinearity is the high computational cost of the iterative procedure for solving nonlinear structural systems. Furthermore, the incorporation of the multiple load cases into the nonlinear problems leads to higher computational cost, because each load case requires an independent iterative nonlinear FE analysis. To minimize the cost, a fully reduced-order model is used in the filtering scheme, which solves both the state and optimization problems of the filtered structures. As a result of the smaller sizes of the tangent stiffness matrix and the sensitivity vector, the use of the proposed filtering scheme with the fully reduced-order model significantly improves the computational performance of the optimization algorithm.

**Chapter Context and Content:**

This work is based on an elastic formulation with the total potential energy used in both the objective function and the structural problem[2] (see, e.g., [84], [91]–[97]). Other types of objective functions in nonlinear problems have been studied by other authors (see, e.g., [98]–[100]).

The remainder of the chapter is organized as follows. Section 2 presents the standard, modified standard, and filter formulations adopted for the nonlinear optimization problem under multiple load cases, followed by sensitivity analysis, convexity proof, and KKT conditions. Section 3 describes the truss models with material nonlinearity, corresponding potential energy, linearization of the governing equations, and the methods of solving the state equations. Section 4 introduces the reduced-order model in the state and the optimization problems. Section 5 presents numerical examples in two- and three-dimensions highlighting the properties of the proposed method, and Section 6 provides concluding

[2]In general, it can be seen as a surrogate for understanding the field of nonlinear topology optimization.

remarks with suggestions for extending the work.

## 3.2 Nested Optimization Formulations for Nonlinear Problems Considering Multiple Load Cases

In this section, we examine the standard and the modified standard nested formulations as well as the filter formulation of the nonlinear optimization problem considering multiple load cases. In addition, the sensitivity analysis, convexity proof, a conceptual example with unbounded solution, and the KKT conditions are presented.

### 3.2.1 Standard and modified standard formulations (without filter)

First, we present the *standard nested formulation* and the solution algorithm of topology optimization for trusses with nonlinear constitutive models and small deformation. The topology design consists of determining the cross-sectional areas of the truss elements using the ground structure (GS) approach. By definition, the standard total potential energy of the structure is $\Pi(\boldsymbol{u}) = U(\boldsymbol{u}) + \Omega(\boldsymbol{u})$, where $\boldsymbol{u}$ is the displacement vector, $U(\boldsymbol{u})$ is the strain energy, and $\Omega(\boldsymbol{u})$ is the total potential of the loads, given by

$$U(\boldsymbol{u}) = \sum_{e=1}^{M} \int_{V^{(e)}} \Psi^{(e)}(\boldsymbol{u})\, \mathrm{d}V = \sum_{e=1}^{M} V^{(e)} \Psi^{(e)}(\boldsymbol{u}) = \sum_{e=1}^{M} x^{(e)} L^{(e)} \Psi^{(e)}(\boldsymbol{u}), \tag{3.1}$$

and

$$\Omega(\boldsymbol{u}) = -\boldsymbol{f}^{\mathrm{T}}\boldsymbol{u}, \tag{3.2}$$

where $\Psi^{(e)}(\boldsymbol{u})$, $x^{(e)}$, $L^{(e)}$, and $V^{(e)}$ are the specified strain energy function, the cross-sectional area, the length, and the volume of truss member $e$, respectively. The specified strain energy function, $\Psi^{(e)}(\boldsymbol{u})$, is assumed to be convex and differentiable for any given $\boldsymbol{u}$. The parameter $n$ denotes the total number of truss members and $\boldsymbol{f}$ is the external load vector. We use the following nested formulation for the optimization problem under $m_\ell$

load cases:

$$\begin{aligned} \min_{\boldsymbol{x}} \; & J(\boldsymbol{x}) = \min_{\boldsymbol{x}} \sum_{j=1}^{m_\ell} -w_j \Pi_j \left(\boldsymbol{x}, \boldsymbol{u}_j(\boldsymbol{x})\right) \\ \text{s.t. } & g(\boldsymbol{x}) = \boldsymbol{L}^{\mathrm{T}} \boldsymbol{x} - V_{\max} \leq 0 \\ & 0 < x_{\min}^{(e)} \leq x^{(e)} \leq x_{\max}^{(e)}, \, e = 1, ..., M \\ \text{with } & \boldsymbol{u}_j(\boldsymbol{x}) = \arg\min_{\boldsymbol{u}} \Pi_j(\boldsymbol{x}, \boldsymbol{u}), \, j = 1, ..., m_\ell, \end{aligned} \tag{3.3}$$

where the objective function[3] $J(\boldsymbol{x}) = \sum_{j=1}^{m_\ell} -w_j \Pi_j \left(\boldsymbol{x}, \boldsymbol{u}_j(\boldsymbol{x})\right)$ is the additive inverse of a weighted sum of the total potential energy of the system in equilibrium state from each load case [84], where $\Pi_j$ is the total potential energy of the equilibrated system under the $j$th load $\boldsymbol{f}_j$, $w_j$ is the corresponding weight (strictly positive), $\boldsymbol{u}_j$ is the equilibrating displacement field (state variable) under load case $\boldsymbol{f}_j$, $\boldsymbol{x}$ and $\boldsymbol{L}$ are the vectors of cross-sectional area (design variable) and length, respectively, $V_{\max}$ is the maximum material volume, and $x_{\min}^{(e)}$ and $x_{\max}^{(e)}$ denote the positive lower and upper bounds of the design variable of member $e$, respectively.

The objective function is based on the min-max formulation described in [96] and [97]. Following common practice [31], in this standard approach, we introduce the strictly positive lower bound $x_{\min}^{(e)}$ to prevent the singular tangent stiffness matrix from forming [31]. As a result, this standard nested formulation in Eq. (3.3) is a sizing problem. At the end of the optimization scheme, we use a "cut-off" approach for design variables to define the final topology. In this chapter, we assume that the specific strain energy is a convex function and the structural model can carry each load case $\boldsymbol{f}_j, j = 1, ..., m_\ell$, (i.e., the equilibrium condition is satisfied, $\boldsymbol{T}\left(\boldsymbol{x}, \boldsymbol{u}_j\right) = \boldsymbol{f}_j, j = 1, ..., m_\ell$ ). For the standard formulation (Eq. (3.3)), these assumptions, with the strictly positive lower bound on design variables, lead to the convexity of the potential energy with respect to the displacement field $\boldsymbol{u}$ (strict convexity of the potential energy requires the strictly convex specific strain energy and $x_{\min}^{(e)} > 0$),

[3] In order to provide a physical explanation for the objective function, notice that when the prescribed displacements is zero on the boundary $S_u$, $J = U_c$ where $S_u$ is the portion of the boundary where displacement boundary condition is applied and $U_c$ is the complementary energy at the equilibrium configuration (see [84]).

which ensures the attainability of a finite solution, $\boldsymbol{u}_j$, for each load case $\boldsymbol{f}_j$ in the structural model for any fixed feasible $\boldsymbol{x}$.

For the *modified standard optimization formulation* for trusses with material nonlinearity, we relax the lower bound of the design variables and require $x^{(e)} \geq 0$ for $e = 1,...,M$. The formulation then becomes,

$$\begin{aligned} &\min_{\boldsymbol{x}} \; J(\boldsymbol{x}) = \min_{\boldsymbol{x}} \; \sum_{j=1}^{m_\ell} -w_j \Pi_j \left(\boldsymbol{x}, \boldsymbol{u}_j(\boldsymbol{x})\right) \\ &\text{s.t. } g(\boldsymbol{x}) = \boldsymbol{L}^{\mathrm{T}}\boldsymbol{x} - V_{\max} \leq 0 \\ &\qquad 0 \leq x^{(e)} \leq x^{(e)}_{\max},\, e = 1,...,M \\ &\text{with } \boldsymbol{u}_j(\boldsymbol{x}) = \arg\min_{\boldsymbol{u}} \left[\Pi_j(\boldsymbol{x}, \boldsymbol{u}) + \frac{\Gamma_j}{2}\boldsymbol{u}^{\mathrm{T}}\boldsymbol{u}\right], j = 1,...,m_\ell. \end{aligned} \tag{3.4}$$

In the modified standard formulation, the lower bound of the design variables becomes the value of zero, showing that truss members can be removed by the update scheme from the problem [85]. This modification on the lower bound of design variables transforms the sizing problem in Eq. (3.3) into a topology optimization problem. In addition, to prevent the possibility of a singular tangent stiffness matrix from forming in the Newton-Raphson method for the structural nonlinear equations, we introduce a Tikhonov regularization term [85], [101]–[103], $\frac{\Gamma_j}{2}\boldsymbol{u}^{\mathrm{T}}\boldsymbol{u}$, for $j$th load case, where $\Gamma_j$ is the regularization parameter. The details of the Tikhonov regularization on the potential energy are shown in Section 3.4. For the modified standard formulation in Eq. (3.4), because we assume that specific strain energy is a convex function and the structural model can carry each load case $\boldsymbol{f}_j, j = 1,...,m_\ell$, (i.e., the equilibrium condition is satisfied, $\boldsymbol{T}\left(\boldsymbol{x}, \boldsymbol{u}_j\right) = \boldsymbol{f}_j, j = 1,...,m_\ell$ ), the potential energy is a convex function with respect to the displacement field $\boldsymbol{u}$ and the obtained $\boldsymbol{u}_j$ is a global minimum. By further including the Tikhonov regularization in the potential energy in the structural problem, the potential energy becomes strictly convex with respect to $\boldsymbol{u}$, in this case, the global minimum $\boldsymbol{u}_j$ for load case $j$ is unique.

### 3.2.2 Filter formulation

Here, denoting $\alpha_f$ as the filter parameter for controlling the resolution of the topology, we introduce the filter operation as follows:

$$Filter\left(\boldsymbol{x},\alpha_f,e\right)=\begin{cases}0, & \text{if } \frac{x^{(e)}}{\max(\boldsymbol{x})}<\alpha_f<1,\\ \\ x^{(e)}, & \text{otherwise.}\end{cases} \tag{3.5}$$

We perform the filter operation every $N_f$ steps during the optimization process to remove the information associated with the set of truss members with normalized areas below the filter parameter $\alpha_f$, where $N_f$ is prescribed by the user to determine how frequently to perform the filter operation. We denote $x_f^{(e)}$ as the filtered cross-sectional area associated with truss member $e$. In order to compare the final resolution of the results, we define the resolution of the filtered structure, $\alpha_{\text{Top}}$, as follows,

$$\alpha_{\text{Top}}=\frac{\min\left(\boldsymbol{x}_f\right)}{\max\left(\boldsymbol{x}_f\right)}. \tag{3.6}$$

Figure 3.3 illustrates the filtering scheme. With the filter operation above, we introduce the filter formulation for optimization of trusses with material nonlinearity as follows:

$$\begin{aligned}
&\min_{\boldsymbol{x}}\ J(\boldsymbol{x})=\min_{\boldsymbol{x}}\ \sum_{j=1}^{m_\ell}-w_j\Pi_j\left(\boldsymbol{x}_f(\boldsymbol{x}),\boldsymbol{u}_j(\boldsymbol{x})\right)\\
&\text{s.t. } g(\boldsymbol{x})=\boldsymbol{L}^{\mathrm{T}}\boldsymbol{x}_f(\boldsymbol{x})-V_{\max}\le 0\\
&\qquad 0\le x^{(e)}\le x_{\max}^{(e)},\ e=1,...,M\\
&\text{with } \boldsymbol{u}_j(\boldsymbol{x})=\arg\min_{\boldsymbol{u}}\left[\Pi_j\left(\boldsymbol{x}_f(\boldsymbol{x}),\boldsymbol{u}\right)+\frac{\Gamma_j}{2}\boldsymbol{u}^{\mathrm{T}}\boldsymbol{u}\right],\ j=1,...,m_\ell\\
&\text{and } x_f^{(e)}=Filter\left(\boldsymbol{x},\alpha_f,e\right),\ e=1,...,M.
\end{aligned} \tag{3.7}$$

where the subscript $f$ denotes a filtered value. The Algorithm 1 shows the implementation of our proposed algorithm. We note that this is a simplified procedure aiming at relatively low values of the filter $\alpha_f$. For a more detailed discussion of the filter, see [85]. In the numerical examples, we use a relatively small filter, $\alpha_f = 10^{-4}$, because the main purpose of the discrete filter in this work is to improve computational efficiency for nonlinear topology optimization, yield the displacement field without artificial stiffness, and improve convergence performance for the nonlinear structural analysis.

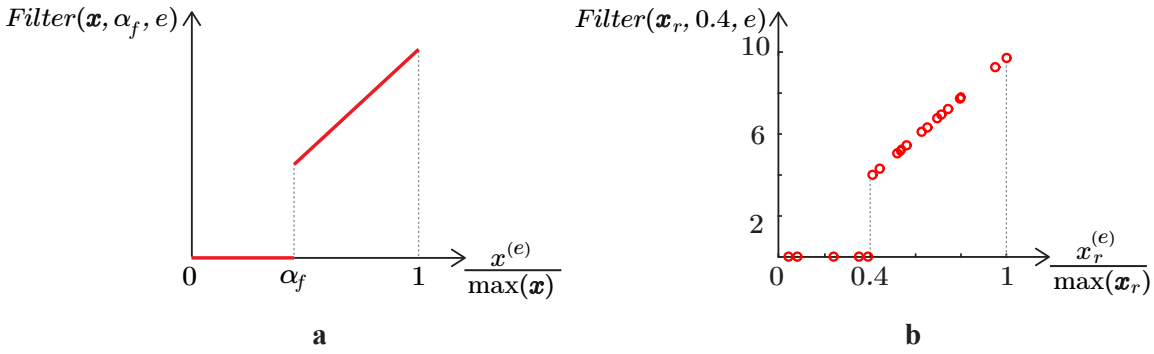


Figure 3.3: Illustration of the filter operator: **a** theoretical and **b** numerical, displaying the output of a function with $\alpha_f = 0.4$ and a given random vector $\boldsymbol{x}_r$ for $e = 1, ..., 20$.[4] The function, implemented in Matlab, is provided in Appendix A.

### 3.2.3 Sensitivity analysis

In this chapter, we perform sensitivity analysis in the filtered structure, i.e. by means of a reduced-order model in the optimization problem, which indicates that the dimension of the sensitivity vector is the same as that of the filtered design variables. Under the assumption of global equilibrium, and since $\boldsymbol{u}_j$ is the equilibrating displacement field under load case

[4]The given random vector $\boldsymbol{x}_r = [7.78, 7.23, 0.76, 4.30, 0.38, 9.25, 3.80, 5.05, 6.94, 3.99, 6.77, 5.24, 7.74, 3.41, 6.10, 9.73, 5.44, 6.33, 2.32, 5.19]^T$. In the full-order model, the filtered vector $\boldsymbol{x}_{rf} = [7.78, 7.23, 0, 4.30, 0, 9.25, 0, 5.05, 6.94, 3.99, 6.77, 5.24, 7.74, 0, 6.10, 9.73, 5.44, 6.33, 0, 5.19]^T$. In the reduced-order model, the filtered vector $\boldsymbol{x}_{rf} = [7.78, 7.23, 4.30, 9.25, 5.05, 6.94, 3.99, 6.77, 5.24, 7.74, 6.10, 9.73, 5.44, 6.33, 5.19]^T$. For related content, see Section 4 (and Figure 3.6).

**Algorithm 1** Optimization with the discrete filter

**Initialize:** $\boldsymbol{x}^0$, $\alpha_f$, $\text{iter}_{\max}$, $\tau_{\text{opt}}$, $\text{tol}_{\text{obj}}$, $\text{tol}_{\text{eqm}}$
**for** $k = 0, 1, ..., \text{iter}_{\max}$ **do**
  Filter: $x_f^{(e),k} = Filter\left(\boldsymbol{x}^k, \alpha_f, e\right),\ e = 1, ..., M.$
  **for** $j = 1, 2, ..., m$ **do**
    Solve: $\boldsymbol{u}_j\left(\boldsymbol{x}^k\right) = \arg\min_{\boldsymbol{u}} \left[\Pi_j\left(\boldsymbol{x}_f^k\left(\boldsymbol{x}^k\right), \boldsymbol{u}\right) + \frac{\Gamma_j}{2}\boldsymbol{u}^{\mathrm{T}}\boldsymbol{u}\right]$
  **end for**
  Compute: $J\left(\boldsymbol{x}^k\right)$, $g\left(\boldsymbol{x}^k\right)$, $\partial J\left(\boldsymbol{x}^k\right)/\partial x^{(e)}$, and $\partial g\left(\boldsymbol{x}^k\right)/\partial x^{(e)}$ using (3.7), (3.9), and (3.10)
  **if** $J\left(\boldsymbol{x}^k\right) - J\left(\boldsymbol{x}^{k-1}\right) > \text{tol}_{\text{obj}}$ or $||\boldsymbol{R}_{\text{Top}}^k||/||\boldsymbol{f}_{\text{Top}}|| > \text{tol}_{\text{eqm}}$ **then**
    quit
  **end if**
  Update: $\boldsymbol{x}^{k+1}$ using Optimality Criteria
  **if** $||\boldsymbol{x}^{k+1} - \boldsymbol{x}^k||_\infty < \tau_{\text{opt}}$ **then**
    quit **for**
  **end if**
**end for**
$\boldsymbol{x}^{\text{final}} = \boldsymbol{x}^{k+1}$
End-filter: $x_f^{(e),\text{final}} = Filter\left(\boldsymbol{x}^{\text{final}}, \alpha_f, e\right),\ e = 1, ..., M.$
Solve: $\boldsymbol{u}_j\left(\boldsymbol{x}^{\text{final}}\right), j = 1, ..., m_\ell.$
**if** $||\boldsymbol{R}_{\text{Top}}^{\text{final}}||/||\boldsymbol{f}_{\text{Top}}|| > \text{tol}_{\text{eqm}}$ **then**
  quit
**end if**
Compute: $J\left(\boldsymbol{x}^{\text{final}}\right)$
Remove aligned nodes
Plot final topology

$\boldsymbol{f}_j$, then the sensitivity of the objective function is given by,

$$\frac{\partial J(\boldsymbol{x})}{\partial x^{(e)}} = -\sum_{j=1}^{m_\ell} w_j \frac{\partial \Pi_j}{\partial x^{(e)}} \left(\boldsymbol{x}, \boldsymbol{u}_j(\boldsymbol{x})\right). \tag{3.8}$$

The external work in Eq. (3.2) for each load case is (explicitly) independent of the design variables. By using Eq. (3.1), we obtain the sensitivity as,

$$\begin{aligned} \frac{\partial J(\boldsymbol{x})}{\partial x^{(e)}} = -\sum_{j=1}^{m_\ell} w_j \frac{\partial \Pi_j}{\partial x^{(e)}} \left(\boldsymbol{x}, \boldsymbol{u}_j(\boldsymbol{x})\right) &= -\sum_{j=1}^{m_\ell} w_j \frac{\partial \left[\sum_{k=1}^{n} x^{(k)} L^{(k)} \Psi^{(k)} \left(\boldsymbol{u}_j\right)\right]}{\partial x^{(e)}} \\ &= -\sum_{j=1}^{m_\ell} w_j L^{(e)} \Psi^{(e)} \left(\boldsymbol{u}_j(\boldsymbol{x})\right). \end{aligned} \tag{3.9}$$

Note that the sensitivity given by Eq. (3.9) is always non-positive because $L^{(e)}\Psi^{(e)}\left(\boldsymbol{u}_j(x)\right) \geq 0, j = 1, ..., m_\ell$. The sensitivity of the volume constraint for member $e$ is calculated as

$$\frac{\partial g(\boldsymbol{x})}{\partial x^{(e)}} = L^{(e)}. \tag{3.10}$$

### 3.2.4 Convexity proof

In this subsection, we investigate the convexity condition of the modified standard topology optimization formulation in Eq. (3.4), i.e. the optimization formulation considering multiple load cases with hyperelastic nonlinear materials with convex specific strain energy and design variables $\boldsymbol{x} \geq \boldsymbol{0}$ under small deformations. Note that the standard nested formulation with linear structural model and end-compliance objective function has been proved to be convex by [37] for positive definite stiffness matrix, and by [38] for positive semi-definite stiffness matrix. The standard formulation in Eq. (3.3) with hyperelastic truss model and the objective function of total potential energy under single load case has been proved to be convex by [84] for positive definite tangent stiffness matrix and small deformations. Since the constraint function, $\boldsymbol{L}^{\mathrm{T}}\boldsymbol{x} - V_{\max} \leq 0$ is convex, we need to study the convexity of the

objective function,

$$
\begin{aligned}
J(\boldsymbol{x}) &= -\sum_{j=1}^{m_\ell} w_j \min_{\boldsymbol{u}} \Pi_j(\boldsymbol{x},\boldsymbol{u}) = \sum_{j=1}^{m_\ell} w_j \max_{\boldsymbol{u}} \left[-\Pi_j(\boldsymbol{x},\boldsymbol{u})\right] \\
&= \sum_{j=1}^{m_\ell} w_j \max_{\boldsymbol{u}} \left\{\boldsymbol{f}_j^{\mathrm{T}}\boldsymbol{u} - U(\boldsymbol{x},\boldsymbol{u})\right\} = \sum_{j=1}^{m_\ell} w_j J_j(\boldsymbol{x}),
\end{aligned}
\tag{3.11}
$$

to prove the convexity of the optimization formulation. Assuming that the strain energy is a convex function[5] and the structural model can carry each load case $\boldsymbol{f}_j, j = 1,...,m_\ell$, (the equilibrium condition is satisfied, i.e., $\boldsymbol{T}(\boldsymbol{x},\boldsymbol{u}_j) = \boldsymbol{f}_j, j = 1,...,m_\ell$ ), we then have a finite solution, i.e. $\boldsymbol{u}_j(\boldsymbol{x})$, for each load case $\boldsymbol{f}_j$ in the structural model for a fixed $\boldsymbol{x}$. Under these conditions, since the strain energy $U(\boldsymbol{x},\boldsymbol{u}) = \sum_{e=1}^{M} x^{(e)} L^{(e)} \Psi^{(e)}(\boldsymbol{u})$ is a linear function in $\boldsymbol{x}$ for a fixed $\boldsymbol{u}$, then $J_j(\boldsymbol{x})$ is a pointwise supremum function of a set of linear functions in $\boldsymbol{x}$,

$$
J_j(\boldsymbol{x}) = \sup_{\boldsymbol{u}} \left\{ J_{j,\boldsymbol{u}}(\boldsymbol{x}) \,|\boldsymbol{u} \in \mathbb{R}^N \right\}, \tag{3.12}
$$

where $J_{j,\boldsymbol{u}}(\boldsymbol{x}) = \boldsymbol{f}_j^{\mathrm{T}}\boldsymbol{u} - \sum_{e=1}^{M} x^{(e)} L^{(e)} \Psi^{(e)}(\boldsymbol{u})$ is convex, and $N$ denotes the number of degrees of freedom (DOFs). We know that a function defined as the pointwise supremum of a set of convex functions is convex [104] and the weighted sum (with strictly positive weights) of convex functions is still convex. Therefore, $J(\boldsymbol{x})$ is convex under the assumptions that specific strain energy of the structural model is convex and the equilibrium condition is satisfied (see [38], [45] for proofs in the linear case under single load case). This proof is valid even when the tangent stiffness matrix is positive semidefinite, i.e., $\boldsymbol{x} \geq \boldsymbol{0}$ for the design variables and $\mathrm{d}\sigma(\lambda)/\mathrm{d}\lambda \geq 0$ for the nonlinear structural model (no requirement on the strict convexity), generalizing the convexity proof of [84] for positive definite tangent stiffness matrix and small deformations.

[5] Both Odgen-based and bilinear materials with the condition $\mathrm{d}\sigma(\lambda)/\mathrm{d}\lambda \geq 0$ have convex specific strain energy – see Section 3.1 for constraints on the model parameters.

### 3.2.5 Conceptual example: Unbounded solution

Figure 3.4 illustrates the case with unbounded solution because the structural model cannot carry the load, i.e., the equilibrium condition cannot be satisfied: $\boldsymbol{T}(\boldsymbol{x},\boldsymbol{u}(\boldsymbol{x})) \neq \boldsymbol{f}$, with the bilinear model 1 (compression is not allowed in this material). Although the specific strain energy of this material model is convex, this case results in $J(\boldsymbol{x}) \rightarrow +\infty$ and leads to unbounded solution [38], as shown in Figure 3.4c [6]. The compression-dominated bilinear model 2 leads to a self-equilibrated structure in Figure 3.4d. Note that the specific strain energy of these material models (Figure 3.4a) is convex (not strictly convex). For the modified formulation (Eq. (3.4)), the potential energy with these material models and Tikhonov regularization becomes strictly convex. For the standard formulation (Eq. (3.3)), the potential energy with these material models is convex (not strictly convex).

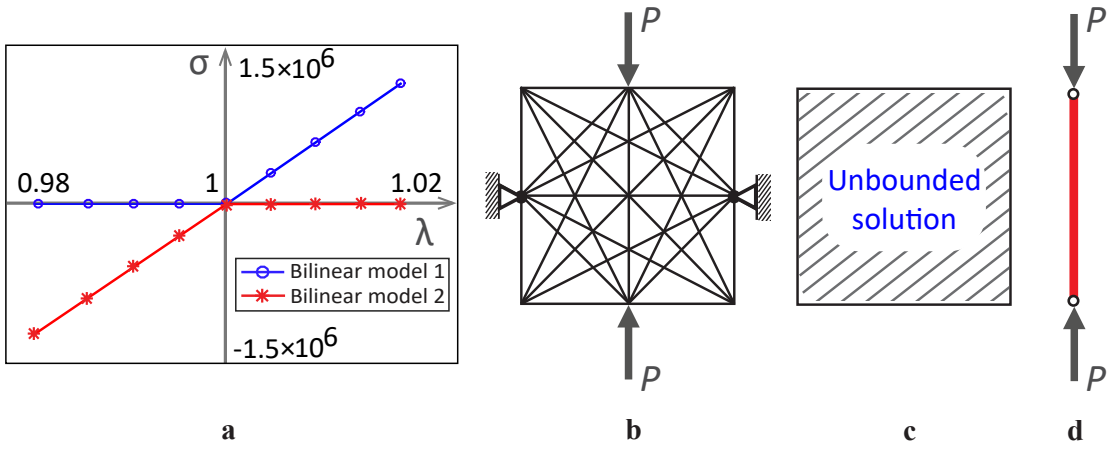


Figure 3.4: Topology optimization: Unbounded versus bounded solutions. **a** Bilinear material models; **b** initial ground structure and boundary conditions; **c** the tension-dominated bilinear model 1 leads to unbounded solution because the structural model cannot carry the loads (the equilibrium condition is not satisfied, i.e., $\boldsymbol{T}(\boldsymbol{x},\boldsymbol{u}(\boldsymbol{x})) \neq \boldsymbol{f}$) with this material model; **d** the compression-dominated bilinear model 2 leads to a bounded solution and self-equilibrated structure.

[6] Notice that the theoretical unbounded solution is represented by a numerical solution displaying infeasible displacements (i.e., relatively large values).

### 3.2.6 KKT conditions

Since we have shown that the modified standard optimization formulation in Eq. (3.4) is convex, its KKT conditions are both necessary and sufficient optimality conditions. To derive the KKT conditions, the Lagrangian of Eq. (3.4) takes the following form by introducing a Lagrange multiplier $\phi$ corresponding to the volume constraint:

$$\mathscr{L}(\boldsymbol{x},\phi) = J(\boldsymbol{x}) + \phi\left(\sum_{e=1}^{M} x^{(e)} L^{(e)} - V_{\max}\right). \tag{3.13}$$

If we denote $\boldsymbol{x}^*$ as the optimal solution of design variables, and $\phi^*$ as the optimal solution for the Lagrange multiplier, we have [31],

$$\begin{aligned}
\frac{\partial \mathscr{L}}{\partial x^{(e)}}(\boldsymbol{x}^*,\phi^*) &\leq 0, \quad \text{if} \quad x^{(e)^*} = x_{\max}^{(e)}, && (3.14)\\
\frac{\partial \mathscr{L}}{\partial x^{(e)}}(\boldsymbol{x}^*,\phi^*) &= 0, \quad \text{if} \quad 0 < x^{(e)^*} < x_{\max}^{(e)}, && (3.15)\\
\frac{\partial \mathscr{L}}{\partial x^{(e)}}(\boldsymbol{x}^*,\phi^*) &\geq 0, \quad \text{if} \quad x^{(e)^*} = 0, && (3.16)
\end{aligned}$$

where the derivative of the Lagrangian is given by

$$\frac{\partial \mathscr{L}}{\partial x^{(e)}}(\boldsymbol{x},\phi) = -\sum_{j=1}^{m_\ell} w_j L^{(e)} \Psi^{(e)}\left(\boldsymbol{u}_j(\boldsymbol{x})\right) + \phi L^{(e)}. \tag{3.17}$$

Combining Eq. (3.17) with Eqs. (3.14) – (3.16), we obtain the KKT conditions for the optimal solution $(\boldsymbol{x}^*,\phi^*)$ of the optimization formulation in Eq. (3.4):

$$\begin{aligned}
\sum_{j=1}^{m_\ell} w_j \Psi^{(e)}\left(\boldsymbol{u}_j(\boldsymbol{x}^*)\right) &\geq \phi^*, \quad \text{if} \quad x^{(e)^*} = x_{\max}^{(e)}, && (3.18)\\
\sum_{j=1}^{m_\ell} w_j \Psi^{(e)}\left(\boldsymbol{u}_j(\boldsymbol{x}^*)\right) &= \phi^*, \quad \text{if} \quad 0 < x^{(e)^*} < x_{\max}^{(e)}, && (3.19)\\
\sum_{j=1}^{m_\ell} w_j \Psi^{(e)}\left(\boldsymbol{u}_j(\boldsymbol{x}^*)\right) &\leq \phi^*, \quad \text{if} \quad x^{(e)^*} = 0. && (3.20)
\end{aligned}$$

From Eq. (3.19), we observe that for those members whose optimal design variables fall between the upper and lower bounds (with inactive area constraints), the weighted sums of the corresponding specific strain energy over $m_\ell$ load cases in the optimal topology are identical, which equal to $\phi^*$. Moreover, we note that under the single load case, i.e., $m_\ell = 1$, Eq. (3.19) implies that the specific strain energy for all the members with inactive area constraints in the optimal topology is identical [84], [95], which corresponds to the full stress design in the linear case [31].

## 3.3 Truss Model with Material Nonlinearity

We present the theory in which the structural analysis part of the chapter is based upon. This includes the kinematics, hyperelastic constitutive models, the potential energy, the linearization of the nonlinear equations, the Tikhonov regularization, and the line search. In fact, the use of line search to solve topology optimization problems governed by nonlinear state equations is an important aspect of this work.

### 3.3.1 Kinematics and constitutive models

To construct the kinematics and constitutive models, we assume small deformation kinematics and nonlinear constitutive relationships. For a given truss element, its linearized stretch $\lambda$ is computed as [105]

$$\lambda = 1 + \frac{\boldsymbol{N}^{\mathrm{T}} \left( \boldsymbol{u}_q - \boldsymbol{u}_p \right)}{L}, \tag{3.21}$$

where $\boldsymbol{u}_p$ and $\boldsymbol{u}_q$ are the nodal displacement vectors of nodes $p$ and $q$ of the truss element, $\boldsymbol{N}$ is the member's unit directional vector, and $L$ is the length of the element. To account for the nonlinear constitutive relation, we use the energy density function based on [106], which provides flexibility to specify the material behavior and thus has the capability to reproduce a variety of hyperelastic models. For the hyperelastic Ogden material, the strain

energy per unit of the undeformed volume is given as

$$\Psi_{OG}(\lambda_1,\lambda_2,\lambda_3) = \sum_{j=1}^{\hat{M}} \frac{\gamma_j}{\beta_j}\left(\lambda_1^{\beta_j} + \lambda_2^{\beta_j} + \lambda_3^{\beta_j} - 3\right), \tag{3.22}$$

where $\lambda_i$, $i = 1,2,3$, denote the principal stretches in three directions, and $\hat{M}$, $\gamma_j$, and $\beta_j$ are material parameters (constants). We assume that the axial stretch of the truss member is the principal stretch $\lambda_1$, namely, $\lambda_1 = \lambda$, and the stretches in the other two directions are taken to be $\lambda_2 = \lambda_3 = 1$, such that Eq. (3.22) becomes

$$\hat{\Psi}_{OG}(\lambda) = \sum_{j=1}^{\hat{M}} \frac{\gamma_j}{\beta_j}\left(\lambda^{\beta_j} - 1\right). \tag{3.23}$$

Accordingly, the principal (Cauchy) stress for the Ogden-based model is obtained as

$$\sigma_{OG,1} = \frac{\partial \Psi_{OG}}{\partial \lambda_1} \text{ and } \sigma_{OG,2} = \sigma_{OG,3} = 0. \tag{3.24}$$

Throughout this work, the energy density function is used with $\hat{M} = 2$; thus, we obtain

$$\sigma_{OG}(\lambda) = \frac{\mathrm{d}\hat{\Psi}_{OG}}{\mathrm{d}\lambda}(\lambda) = \gamma_1\left(\lambda^{\beta_1 - 1} - \lambda^{\beta_2 - 1}\right), \tag{3.25}$$

with $\gamma_2 = -\gamma_1$. By taking the derivative of the stress, the tangent modulus is obtained as follows:

$$E_T(\lambda) = \frac{\mathrm{d}\sigma_{OG}}{\mathrm{d}\lambda}(\lambda) = \gamma_1\left[(\beta_1 - 1)\lambda^{\beta_1 - 2} - (\beta_2 - 1)\lambda^{\beta_2 - 2}\right]. \tag{3.26}$$

Notice that, at undeformed state, the tangent modulus reduces to the Young's modulus in linear elasticity, namely,

$$E_T(1) = \gamma_1(\beta_1 - \beta_2) = E_0 = \Lambda + 2\mu, \tag{3.27}$$

where $\Lambda$ and $\mu$ are the usual Lamé constants.

In terms of the convexity of this Ogden-based material model, if the parameters satisfy the following conditions: $\beta_1 \geq 1$, $\beta_2 \leq 1$, $\beta_1 \neq \beta_2$, and $\gamma_1 > 0$, which results in $E_T > 0$ ($\mathrm{d}\sigma_{OG}(\lambda)/\mathrm{d}\lambda > 0$), then the material model is convex, i.e., $\hat{\Psi}_{OG}(\lambda)$ is convex for $\lambda > 0$. The material parameters $(\beta_1, \beta_2, \gamma_1)$ are solved using Eq. (3.27) and the relation

$$\frac{\sigma_t}{\sigma_c} = \frac{\overline{\sigma}_t}{\overline{\sigma}_c}, \tag{3.28}$$

where

$$\overline{\sigma}_t = \frac{\sigma_t}{\gamma_1^0} = \left(\lambda_t^{\beta_1 - 1} - \lambda_t^{\beta_2 - 1}\right) \text{ and } \overline{\sigma}_c = \frac{\sigma_c}{\gamma_1^0} = \left(\lambda_c^{\beta_1 - 1} - \lambda_c^{\beta_2 - 1}\right). \tag{3.29}$$

Note that $\sigma_t$, $\sigma_c$, $E_0$, $\lambda_t$, $\lambda_c$ and $\gamma_1^0$ are specified by the user. Therefore, the stress-stretch relationship of the Ogden model is obtained as,

$$\sigma_{OG}(\lambda) = \frac{E_0}{\beta_1 - \beta_2}\left(\lambda^{\beta_1 - 1} - \lambda^{\beta_2 - 1}\right). \tag{3.30}$$

By varying the set of parameters $(\beta_1, \beta_2)$, this Ogden-based model generates a variety of material behavior, as shown in Figure 3.5a.

In this work, we also adopt a bilinear material to account for constitutive relationships. The bilinear constitutive model has a kink at the origin (see Figure 3.5b). To treat this class of nonsmooth problems, we refer the reader to [107]. Within the same context of the Ogden-based model, the energy density function can be written as,

$$\Psi_{Bi}(\lambda) = \begin{cases} \frac{1}{2}E_t(\lambda - 1)^2, & \text{if } \lambda > 1, \\ \\ \frac{1}{2}E_c(\lambda - 1)^2, & \text{otherwise,} \end{cases} \tag{3.31}$$

where $E_t$ and $E_c$ are the Young's moduli for tension and compression, respectively. Ac-

cordingly, the Cauchy stress for the bilinear material is then obtained as,

$$\sigma_{Bi}(\lambda) = \begin{cases} E_t(\lambda - 1), & \text{if } \lambda > 1, \\ \\ E_c(\lambda - 1), & \text{otherwise.} \end{cases} \tag{3.32}$$

Note that this bilinear material model is always convex as $\mathrm{d}\sigma_{\mathrm{Bi}}(\lambda)/\mathrm{d}\lambda \geq 0$. The term $\mathrm{d}\sigma_{\mathrm{Bi}}(\lambda)/\mathrm{d}\lambda$ may become zero, which occurs, for example, when the material that is unable to carry compression (e.g., cables, $E_c = 0$), that is $\mathrm{d}\sigma_{\mathrm{Bi}}(\lambda)/\mathrm{d}\lambda = 0$ in the compression range.

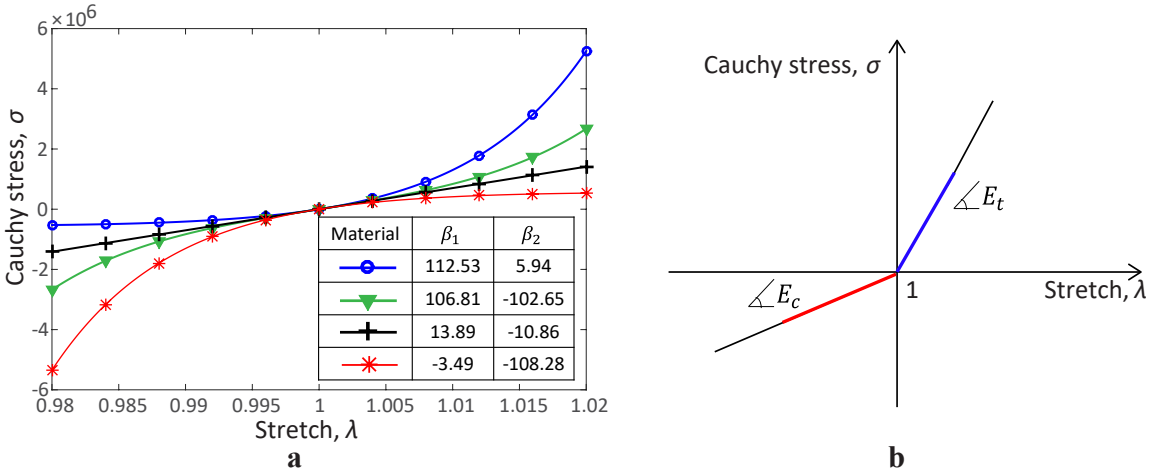


Figure 3.5: Material models: **a** Hyperelastic Ogden-based models with different parameters $(\beta_1, \beta_2)$; **b** bilinear material model with elastic behavior (different Young's moduli for tension and for compression).

### 3.3.2 Potential energy

A brief derivation of the equilibrium equations is given here for the sake of completeness– details of the derivation were reviewed in [84]. By definition, the standard total potential energy of the structure is $\Pi(\boldsymbol{u}) = U(\boldsymbol{u}) + \Omega(\boldsymbol{u})$. The equilibrium of the structure is en-

forced by requiring $\Pi$ to be stationary; that is,

$$\boldsymbol{R}(\boldsymbol{u}) = \frac{\partial U}{\partial \boldsymbol{u}} + \frac{\partial \Omega}{\partial \boldsymbol{u}} = \boldsymbol{T}(\boldsymbol{u}) - \boldsymbol{f} = 0, \tag{3.33}$$

where $\boldsymbol{T}(\boldsymbol{u})$ is the internal force vector in terms of the state variable $\boldsymbol{u}$, and $\boldsymbol{f}$ is the external force vector. The internal force vector $\boldsymbol{T}(\boldsymbol{u})$ is given as,

$$\boldsymbol{T}(\boldsymbol{u}) = \sum_{e=1}^{M} x^{(e)} L^{(e)} \frac{\partial \Psi^{(e)}}{\partial \boldsymbol{u}}. \tag{3.34}$$

In the above relation, $\partial \Psi^{(e)} / \partial \boldsymbol{u}$ is obtained as

$$\frac{\partial \Psi^{(e)}}{\partial \boldsymbol{u}} = \frac{\mathrm{d}\Psi^{(e)}}{\mathrm{d}\lambda^{(e)}} \frac{\partial \lambda^{(e)}}{\partial \boldsymbol{u}}. \tag{3.35}$$

Using Eq. (3.21), we obtain

$$\frac{\partial \lambda^{(e)}}{\partial \boldsymbol{u}} = \frac{1}{L^{(e)}} \begin{Bmatrix} \vdots \\ -\boldsymbol{N}^{(e)} \\ \vdots \\ \boldsymbol{N}^{(e)} \\ \vdots \end{Bmatrix} = \frac{1}{L^{(e)}} \boldsymbol{B}^{(e)}, \text{ where } \boldsymbol{B}^{(e)} = \begin{Bmatrix} \vdots \\ -\boldsymbol{N}^{(e)} \\ \vdots \\ \boldsymbol{N}^{(e)} \\ \vdots \end{Bmatrix}. \tag{3.36}$$

Therefore, the local internal force vector is obtained by substituting Eqs. (3.35) and (3.36) into Eq. (3.34), which gives

$$\boldsymbol{T}(\boldsymbol{u}) = \sum_{e=1}^{M} x^{(e)} \boldsymbol{\sigma}^{(e)} \boldsymbol{B}^{(e)}. \tag{3.37}$$

### 3.3.3 Linearization of the nonlinear algebraic equations (Newton-Raphson method)

In solving the nonlinear system of equations, the residual force $\boldsymbol{R}(\boldsymbol{u})$ of Eq. (3.33) can be linearized and rewritten for iteration $k$ as follows:

$$\boldsymbol{R}\left(\boldsymbol{u}^{k+1}\right) = \boldsymbol{R}\left(\boldsymbol{u}^{k}\right) + \boldsymbol{K}_t\left(\boldsymbol{u}^{k}\right)\Delta\boldsymbol{u}^{k}, \tag{3.38}$$

where $\boldsymbol{K}_t$ is the global tangent stiffness matrix,

$$\boldsymbol{K}_t\left(\boldsymbol{u}^{k}\right) = \frac{\partial \boldsymbol{R}}{\partial \boldsymbol{u}}\left(\boldsymbol{u}^{k}\right) = \frac{\partial \boldsymbol{T}}{\partial \boldsymbol{u}}\left(\boldsymbol{u}^{k}\right). \tag{3.39}$$

The nonlinear structural problem is solved using the Newton-Raphson method [108]:

$$\boldsymbol{R}\left(\boldsymbol{u}^{k+1}\right) = \boldsymbol{R}\left(\boldsymbol{u}^{k}\right) + \boldsymbol{K}_t\left(\boldsymbol{u}^{k}\right)\Delta\boldsymbol{u}^{k} = 0, \tag{3.40}$$

therefore,

$$\boldsymbol{K}_t\left(\boldsymbol{u}^{k}\right)\Delta\boldsymbol{u}^{k} = -\boldsymbol{R}\left(\boldsymbol{u}^{k}\right) = \boldsymbol{f} - \boldsymbol{T}\left(\boldsymbol{u}^{k}\right), \tag{3.41}$$

and

$$\boldsymbol{u}^{k+1} = \boldsymbol{u}^{k} + \Delta\boldsymbol{u}^{k}, \tag{3.42}$$

where $\boldsymbol{K}_t = \sum_{e=1}^{M} \boldsymbol{K}_t^{(e)}$, and $\boldsymbol{K}_t^{(e)}$ is the element tangent stiffness matrix in global coordinates. For a given truss element $e$ with nodes $p$ and $q$, the associated internal force vector $\boldsymbol{t}^{(e)}$ and local tangent stiffness matrix $\boldsymbol{k}_t^{(e)}$ are expressed as follows:

$$\boldsymbol{t}^{(e)}\left(\boldsymbol{u}^{(e)}\right) = x^{(e)}\boldsymbol{\sigma}^{(e)}\left(\boldsymbol{u}^{(e)}\right)\begin{Bmatrix} -\boldsymbol{N}^{(e)} \\ \boldsymbol{N}^{(e)} \end{Bmatrix}, \tag{3.43}$$

and

$$\boldsymbol{k}_t^{(e)} = \frac{\partial \boldsymbol{t}^{(e)}}{\partial \boldsymbol{u}^{(e)}} = \begin{bmatrix} \boldsymbol{k}_{pp} & \boldsymbol{k}_{pq} \\ \boldsymbol{k}_{qp} & \boldsymbol{k}_{qq} \end{bmatrix}, \tag{3.44}$$

where

$$\boldsymbol{k}_{pp} = \boldsymbol{k}_{qq} = -\boldsymbol{k}_{pg} = -\boldsymbol{k}_{qp} = \frac{x^{(e)}}{L^{(e)}} \frac{\mathrm{d}\sigma^{(e)}}{\mathrm{d}\lambda^{(e)}} \boldsymbol{N}^{(e)} \left(\boldsymbol{N}^{(e)}\right)^{\mathrm{T}}. \tag{3.45}$$

### 3.3.4 Solving the state equations: Tikhonov regularization

To prevent the possibility of a singular tangent stiffness matrix from forming in the Newton-Raphson method of the structural nonlinear equations in the proposed scheme, we introduce a regularization term ([85], [101]–[103]). The total potential energy accounting for the Tikhonov regularization term is written as

$$\Pi^{\Gamma}(\boldsymbol{u}) = U(\boldsymbol{u}) + \Omega(\boldsymbol{u}) + \frac{\Gamma}{2}\boldsymbol{u}^{\mathrm{T}}\boldsymbol{u}, \tag{3.46}$$

where $\Gamma$ is a positive Tikhonov regularization parameter. By taking the derivative of the above equation,

$$\boldsymbol{R}^{\Gamma}(\boldsymbol{u}) = \frac{\partial \Pi^{\Gamma}}{\partial \boldsymbol{u}} = \frac{\partial U}{\partial \boldsymbol{u}} + \frac{\partial \Omega}{\partial \boldsymbol{u}} + \Gamma \boldsymbol{u} = \boldsymbol{T}(\boldsymbol{u}) - \boldsymbol{f} + \Gamma \boldsymbol{u} = 0. \tag{3.47}$$

In the Newton-Raphson method, the residual force $\boldsymbol{R}^{\Gamma}(\boldsymbol{u})$ of Eq. (3.47) can be rewritten for the iteration $k+1$ as follows:

$$\boldsymbol{R}^{\Gamma}\left(\boldsymbol{u}^{k+1}\right) = \boldsymbol{R}^{\Gamma}\left(\boldsymbol{u}^{k} + \Delta\boldsymbol{u}^{k}\right) = \boldsymbol{R}^{\Gamma}\left(\boldsymbol{u}^{k}\right) + \frac{\partial \boldsymbol{R}^{\Gamma}\left(\boldsymbol{u}^{k}\right)}{\partial \boldsymbol{u}^{k}} \Delta\boldsymbol{u}^{k}, \tag{3.48}$$

where

$$\frac{\partial \boldsymbol{R}^{\Gamma}\left(\boldsymbol{u}^{k}\right)}{\partial \boldsymbol{u}^{k}} = \boldsymbol{K}_{t}\left(\boldsymbol{u}^{k}\right) + \Gamma \boldsymbol{I}. \tag{3.49}$$

Hence, the linearized equilibrium equation of the nonlinear system becomes

$$\left[\boldsymbol{K}_{t}\left(\boldsymbol{u}^{k}\right) + \Gamma \boldsymbol{I}\right] \Delta\boldsymbol{u}^{k} = \boldsymbol{f} - \boldsymbol{T}\left(\boldsymbol{u}^{k}\right) - \Gamma \boldsymbol{u}^{k}. \tag{3.50}$$

In above equations, the term $\Gamma \boldsymbol{I}$ is the regularization term for the tangent stiffness matrix. We select the value of $\Gamma$ as

$$\Gamma = \frac{\Gamma_0}{N} \mathrm{tr}\left(\boldsymbol{K}_{t,\mathrm{Top}}\right), \tag{3.51}$$

where typically $\Gamma_0 = 10^{-8}$, and $\boldsymbol{K}_{t,\mathrm{Top}}$ is the stiffness matrix of the filtered structure that will be discussed in the subsequent section. Note that the term $\Gamma \boldsymbol{u}^k$ on the right-hand side of Eq. (3.50) can be neglected since $\Gamma$ has relatively small value and we seek to satisfy equilibrium condition, $\boldsymbol{T}\left(\boldsymbol{u}^k\right) = \boldsymbol{f}$.

### 3.3.5 Inexact line search

In an effort to improve the convergence of the first several iterations of the nonlinear FEM (the structural configuration tends to be more flexible than the solution being sought), we adopt an inexact (Armijo-type) line search strategy ([109]; [110]; [111]) within the Newton-Raphson procedure, which modifies Eq. (3.42) to

$$\boldsymbol{u}^{k+1} = \boldsymbol{u}^k + \xi^k \Delta \boldsymbol{u}^k. \tag{3.52}$$

A scalar step length $\xi^k$ is calculated in each iteration, which guarantees a decrease in the potential energy, $\Pi\left(\boldsymbol{u}^{k+1}\right)$. The rationale is to search along $\boldsymbol{u}^k + \xi \Delta \boldsymbol{u}^k$ to find $\xi = \xi^k$ such that

$$\Pi\left(\boldsymbol{u}^{k+1}\right) = \Pi\left(\boldsymbol{u}^k + \xi^k \Delta \boldsymbol{u}^k\right) \leq \Pi\left(\boldsymbol{u}^k\right) + \tau \xi^k \nabla \Pi\left(\boldsymbol{u}^k\right)^{\mathrm{T}} \Delta \boldsymbol{u}^k, \tag{3.53}$$

where $\tau$ is the guard constant, e.g., $\tau = 10^{-4}$. Note that $\nabla \Pi\left(\boldsymbol{u}^k\right) = \boldsymbol{R}\left(\boldsymbol{u}^k\right)$. If the current step length $\overline{\xi}^k$ is unsatisfactory, the following procedure is used to decrease the step length. We first calculate a quadratic polynomial and minimize the interpolant based on Eq. (3.53), obtaining a scale $\kappa$ of the step length for the next potential step length:

$$\kappa = -\frac{\overline{\xi}^k \nabla \Pi\left(\boldsymbol{u}^k\right)^{\mathrm{T}} \Delta \boldsymbol{u}^k}{2\left(\Pi\left(\boldsymbol{u}^k + \overline{\xi}^k \Delta \boldsymbol{u}^k\right) - \Pi\left(\boldsymbol{u}^k\right) - \overline{\xi}^k \nabla \Pi\left(\boldsymbol{u}^k\right)^{\mathrm{T}} \Delta \boldsymbol{u}^k\right)}, \tag{3.54}$$

and updating $\xi^k$ as $\xi^k = \kappa\bar{\xi}^k$. If a relatively small scalar value, e.g., $\kappa < 0.1$, is obtained, we simply use $\kappa = 0.5$. Under the assumptions in Section 2.1, the Newton-Raphson method with this line search method ensures the convergence to a displacement field that is a stationary point [110] in the potential energy. Furthermore, if the potential energy is strictly convex with respect to $\boldsymbol{u}$, which is the case in this chapter with the Tikhonov regularization, then the stationary point ($\boldsymbol{u}$) is the unique global minimum.

## 3.4 Reduced-Order Model

This section introduces the fully reduced-order model (ROM) in nonlinear topology optimization with GSM using the discrete filter. The ROM is applied to both the nonlinear structural system analysis (the state problem) and the optimization analysis.

### 3.4.1 Reduced-order model in nonlinear structural system analysis

Utilizing the reduced-order model, after each filtering process, we form a reduced-sized structure and a new set of degrees of freedom (DOFs). The subscript (Top) represents the new set of variables associated with the filtered structure. Solving the nonlinear structural problem requires filtering out the topology from the ground structure based on the following mapping of variables:

$$\boldsymbol{u} = \boldsymbol{Q}\boldsymbol{u}_{\text{Top}}, \tag{3.55}$$

where the matrix $\boldsymbol{Q}$ maps the DOFs between the ground structure and the actual topology after applying the filter. This matrix is defined based on the nodes connected with those elements with finite cross-sectional area value (larger than zero) and the associated new set of DOFs. Based on this mapping, we establish the associated structural problem as follows ([85]):

$$\boldsymbol{T}_{\text{Top}}\left(\boldsymbol{u}_{\text{Top}}\right) = \boldsymbol{f}_{\text{Top}}, \tag{3.56}$$

$$\left(\boldsymbol{K}_{t,\mathrm{Top}}+\Gamma\mathbf{I}\right)\Delta\boldsymbol{u}_{\mathrm{Top}}^{k}=\boldsymbol{f}_{\mathrm{Top}}-\boldsymbol{T}_{\mathrm{Top}}^{k}=\boldsymbol{R}_{\mathrm{Top}}^{k}, \tag{3.57}$$

and

$$\boldsymbol{u}_{\mathrm{Top}}^{k+1}=\boldsymbol{u}_{\mathrm{Top}}^{k}+\Delta\boldsymbol{u}_{\mathrm{Top}}^{k}, \tag{3.58}$$

where $\boldsymbol{K}_{t,\mathrm{Top}}$, $\boldsymbol{f}_{\mathrm{Top}}$, and $\boldsymbol{T}_{\mathrm{Top}}^{k}$ are the tangent stiffness, the external and internal load vectors, respectively, associated with the actual topology, defined by

$$\boldsymbol{K}_{t,\mathrm{Top}}=\boldsymbol{Q}^{\mathrm{T}}\boldsymbol{K}_{t}\boldsymbol{Q},\quad \boldsymbol{f}_{\mathrm{Top}}=\boldsymbol{Q}^{\mathrm{T}}\boldsymbol{f},\quad \text{and}\ \ \boldsymbol{T}_{\mathrm{Top}}^{k}=\boldsymbol{Q}^{\mathrm{T}}\boldsymbol{T}^{k}. \tag{3.59}$$

For simplicity, we use notations $\boldsymbol{T}^{k}$, $\boldsymbol{T}_{\mathrm{Top}}^{k}$, and $\boldsymbol{R}_{\mathrm{Top}}^{k}$ to denote $\boldsymbol{T}\left(\boldsymbol{u}^{k}\right)$, $\boldsymbol{T}_{\mathrm{Top}}\left(\boldsymbol{u}_{\mathrm{Top}}^{k}\right)$, and $\boldsymbol{R}_{\mathrm{Top}}\left(\boldsymbol{u}_{\mathrm{Top}}^{k}\right)$. A mapping example for the ROM in the nonlinear structural system analysis is presented in Appendix B. As mentioned in Section 2.1, the tangent stiffness matrix from the formulation in Eq. (3.7) can be singular when truss members are removed. Therefore, we minimize the potential energy with the Tikhonov regularization. After solving for $\boldsymbol{u}_{\mathrm{Top}}$, we use this displacement field to calculate the sensitivity of the filtered structure. Thus, for the proposed filtering scheme, during and after the optimization process we check the global equilibrium residual by

$$||\boldsymbol{R}_{\mathrm{Top}}^{k}||\leq\rho||\boldsymbol{f}_{\mathrm{Top}}||, \tag{3.60}$$

where $\rho$ represents the tolerance. We choose the value of $\rho$ as $10^{-4}$ throughout this chapter. For the standard GSM, we check the global equilibrium residual on the structure after applying the final cut-off, i.e. a posteriori. For the linear cases with the filter that are used in the examples, we check the global equilibrium residual using

$$||\boldsymbol{K}_{\mathrm{Top}}\boldsymbol{u}_{\mathrm{Top}}-\boldsymbol{f}_{\mathrm{Top}}||\leq\rho||\boldsymbol{f}_{\mathrm{Top}}||. \tag{3.61}$$

We remove information about the deleted members, including the areas, stiffness matrix, from the problem. We do not simply set areas of the removed members to zero or store nodes, but instead, remove the information from the entire problem, as shown in Figure 3.6. This reduced number of truss members significantly influences the size of the global stiffness matrix. Typically, the formation and inversion of the stiffness matrix is one of the most time-consuming parts of nonlinear FEM. To quantify the influence of using the ROM, we conduct studies in Sections 5.1 and 5.3. As we will see, the size of the problem significantly decreases as the iteration proceeds.

The application of the filtering scheme with the ROM in truss optimization that accounts for material nonlinearity has the advantage of solving structural problems in the filtered topology. As a result of the smaller sizes of the tangent stiffness matrices, the use of the ROM incorporated into the proposed scheme significantly improves the performance of the computations in the iterative Newton-Raphson algorithm.

### 3.4.2 Reduced-order model in optimization analysis

To reduce the order of information needed in the sensitivity analysis and update scheme to achieve fully reduced-order in the entire optimization process, we further use the reduced-order model in the optimization analysis, because we assume that the null area members do not return to the topology. This situation is automatically considered by the construction of the optimality criteria (OC) [70], which is the update scheme that we choose. The size of the information input for the update (i.e., vectors of sensitivity and design variables) is the same as that used for solving the nonlinear structural system. Note that the proposed scheme uses reduced-order information in sensitivity and design variable vectors with the removal of information associated with null-area members; this excludes the sensitivity information of members with zero areas but non-zero nodal displacement (because according to Eq. (3.9), the sensitivities of those null-area members are not zero). As a result, regardless of which update scheme is adopted (the optimality criteria or the method of moving

asymptotes (MMA) by [71]), the removed members will not return to the topology once they have been removed. Therefore, although the OC by its construction does not allow the return of the members, it is sufficient for the reduced-order model and is adopted in this chapter.

However, we note that the return of the bars may be helpful when a large filter value is used. Application of a large filter may lead to the removal of many bars, and thus the resulting structure may not be in equilibrium, or the objective may increase dramatically (large displacement). For instance, if some structurally important members are removed, large displacements may occur. In such cases, the excluded sensitivity information is potentially useful for accomplishing the optimization and maintaining equilibrium, in which case the MMA could be used, which enables the return of the bars.

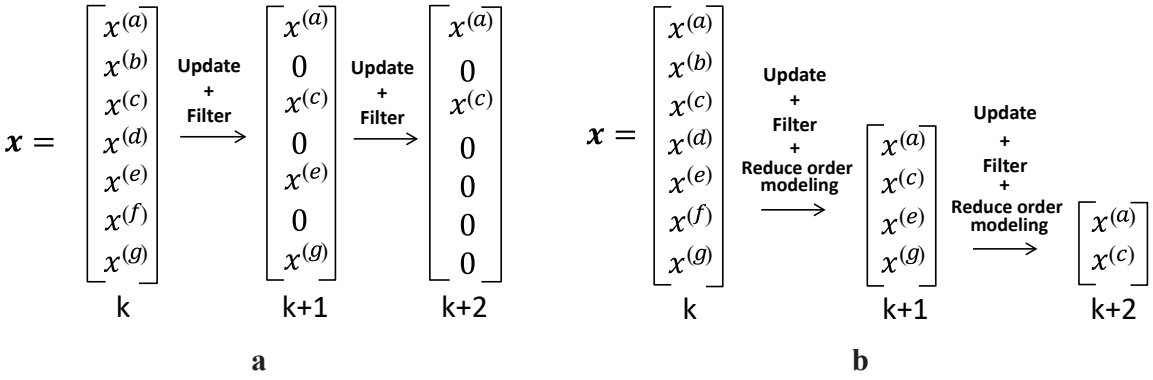


Figure 3.6: Design variables during the optimization process: **a** full-order model; **b** reduced-order model.

## 3.5 Numerical Examples

This section illustrates the proposed formulation using four representative examples. The first example verifies the methodology in two dimensions; the second example demonstrates how altering the material constitutive relation changes the final topology. Then we compare the optimized structures from the proposed scheme under single and multiple load cases with those from the linear plastic formulation under single load case. The last two examples, which are in three dimensions, establish the capability of the proposed method,

including a practical structural design with various materials. All of the examples, except Example 2, use hyperelastic Ogden-based materials under small displacements. Example 2 uses bilinear material models. The examples are illustrated by Table 3.1.

Table 3.1: Numerical examples.

| Example | Dimension | Description | Feature |
|---|---|---|---|
| 1 | 2D | Central load in a simply supported square domain | Verification |
| 2 | 2D | Long-span bridge design using bilinear materials | Comparison of elastic and plastic formulations of the ground structure |
| 3 | 3D | Central load on top surface of a laterally constrained parallelepiped | Influence of load level in the nonlinear response |
| 4 | 3D | Arch bridge | Potentially translational design: from academia to structural engineering practice |

For all of the examples, we generate the initial ground structure and remove overlapped bars [30]. For the generation of three-dimensional (3D) initial ground structures and the plotting of the 3D final structures, we employ the software GRAND3 and the collision zone technique by [112], [113]. The CPU run-time in this chapter reflects the time spent on the optimization process, not including the time spent on problem formulation. Both the standard GSM in Eq. (3.3) with a final cut-off and the proposed filter formulation in Eq. (3.7) may lead to structures with unstable nodes, i.e., hinges connecting two collinear members that cause mechanism. In this work, for the standard formulation after the final cut-off, we remove unstable nodes (and floating members) by replacing the two collinear members with one long member that takes the larger area from the two, and the resulting objective value decreases. For the proposed filter, we remove unstable nodes by replacing the two collinear members with one long member that takes the same area, and the resulting objective value stays unchanged. All the data presented in this chapter are obtained after removing unstable nodes. For both methods, we check the final topologies to ensure that

they are at equilibrium. However, we do not verify the instability of the members because the issue of stability is beyond the scope of this work. All examples have the initial tangent modulus, $E_0 = 7 \times 10^7 (= E_t$ for Example 2); the stopping criteria: $\tau_{\text{opt}} = 10^{-9}$; move value: $move = x^0 \times 10^4$, where $x^0$ is the initial guess of the design variables; and damping factor for the OC update scheme:$\eta = 0.5$. For the standard GSM, we apply a cut-off value that defines the final structure at the end of the optimization process; the cut-off value for Examples 1 and 3 is $10^{-2}$ for the cases that use the standard GSM. For the cases with the proposed filtering scheme, we use a relatively small filter, $\alpha_f = 10^{-4}$, in all the examples during the optimization process, and the filter operation is performed at every optimization step, i.e., $N_f = 1$. The lower and upper bounds for the standard GSM are defined by $x_{\text{min}} = 10^{-2} x^0$ and $x_{\text{max}} = 10^4 x^0$, respectively. For the proposed filter algorithm, $x_{\text{min}} = 0$ and $x_{\text{max}} = 10^4 x^0$ (unbounded in practical terms).

### 3.5.1 Central load in a simply supported square domain

The purpose of Example 1 is to verify the present methodology with the results obtained from standard GSM using two hyperelastic Ogden-based material models without the filtering scheme [84]. We also study the influence of material models on the resulting structural topology by comparing the two Ogden-based models with a linear model. The geometry, load, and support conditions (two fixed supports) are shown in Figure 3.7a. The initial ground structure contains 6,920 non-overlapped members and 169 nodes using full-level generation. We use two Ogden-based material models, illustrated in Figure 3.7b. The figure shows that the tension of Material 1 ($\beta_1 = 188, \beta_2 = -68$) is stronger than its compression, and the compression of Material 2 ($\beta_1 = 71, \beta_2 = -182$) is stronger than its tension. We use a small filter $\alpha_f = 10^{-4}$ throughout the optimization process.

The filtering scheme yields topologies almost identical to those obtained using the standard GSM with a final cut-off for both linear and nonlinear materials, as shown in Figure 3.8, and in the chapter by [84]. This comparison verifies the proposed filtering scheme.

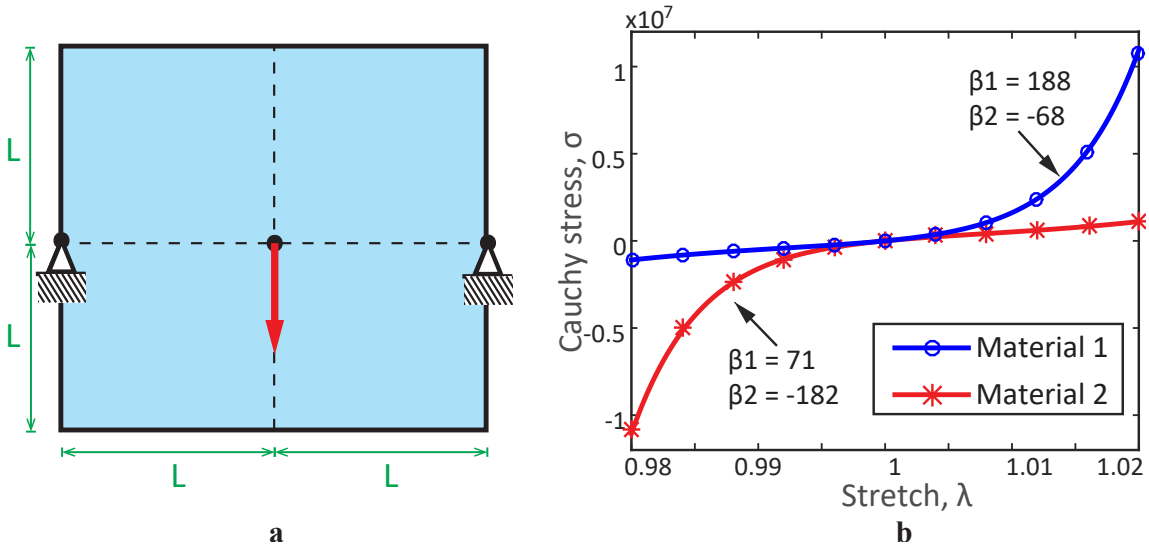


Figure 3.7: Example 1 with a full-level ground structure ($12 \times 12$ grid) and $6,920$ non-overlapped bars: **a** Geometry ($L = 6m$), load ($P = 100kN$) and support conditions; **b** Ogden-based material models. Material 1 is tension dominated, while Material 2 is compression dominated.

The choice of material models significantly influences the final topology. Note that each material model results in a unique topology, and each differs from the linear case. If a material used in practical design exhibits nonlinear behavior, an analysis based on a linear material may be misleading. Various topologies resulting from the use of several materials show the importance of accounting for material nonlinearity. In addition, since single load case is used here, we observe that in every model considering material nonlinearity, the members in the optimized structure all have the same value of strain energy density, which corresponds to the full stress design in the linear case, as discussed in Section 2.6. The final topologies, corresponding convergence plots for the objective function, and stress-stretch plots are shown in Figures 3.8a, 3.8c, and 3.8e. The normalized cross-sectional areas for the truss members in the final designs are shown in Figures 3.8b, 3.8d, and 3.8f for linear material, Ogden-based materials 1 and 2, respectively.

Table 3.2 presents a summary of the data associated with Example 1, all the data are obtained after removing unstable nodes. From the CPU run-time comparison, the computational efficiency using the filtering scheme is greater than those without the proposed

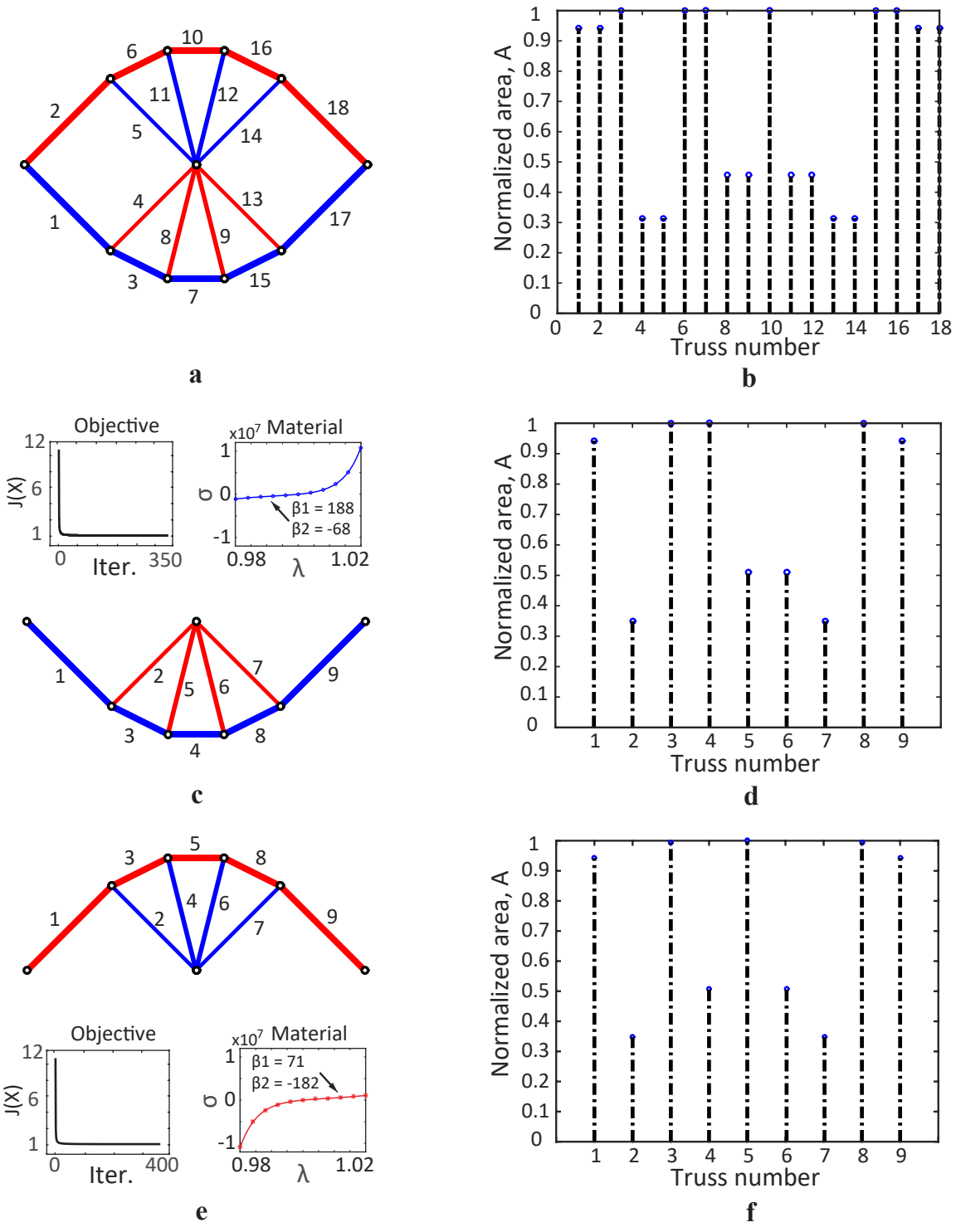


Figure 3.8: Results of the optimization for Example 1: **a** Final topology of the linear model; **b** corresponding final normalized cross-sectional areas for the truss members of the linear model; **c** final topology and convergence plot of Ogden-based Material 1; **d** corresponding final normalized cross-sectional areas for truss members of Ogden-based Material 1; **e** final topology and convergence plot of Ogden-based Material 2; **f** corresponding final normalized cross-sectional areas for truss members of Ogden-based Material 2. The blue bars are in tension and the red bars are under compression.

filter, which shows the advantages of using the filtering technique, particularly for a nonlinear problem. Figure 3.9 further shows the size reduction history for optimization using Ogden-based Material 2 with the proposed filtering scheme, the numbers of nodes and truss members at optimization steps 50, 150, 250, and 355 (final step) are shown together with the corresponding topologies during the optimization process. The numbers of truss members and nodes in the problem are reduced dramatically by the use of the proposed filtering scheme (with ROM) during the optimization process. For the nonlinear cases, note that the objective values from the proposed filtering scheme are smaller than those without the filtering scheme even though both cases generate identical topologies (for the same material), and from the Max $|\boldsymbol{u}|$ column (maximum value of the absolute displacement), the structures from the proposed filter have less maximum displacement than those with the standard GSM (the maximum displacement for all cases occurs at the loading point). When the proposed filter is applied, it takes into account only the members that appear in the filtered topology at every optimization step. However, for cases of the standard GSM, all the small area members in the nonlinear FEM process are taken into consideration throughout the optimization process; the members with small area, not plotted in the final topology, still support the load and contribute to the stiffness and objective function (total potential energy at the equilibrium configuration) of the structure, and after applying the cut-off, the resulting objective values increase. This observation shows that the proposed filtering scheme addresses the artificial stiffness problem associated with the standard GSM.

### 3.5.2 Long-span bridge design using bilinear materials

This example shows the influence of different levels of tension and compression of the yield stresses in structural optimization and improvement in the final resolution after using the filter technique. The optimized structures obtained by the proposed algorithm with the single load case and multiple load cases (i.e., the elastic nonlinear formulation with a filter) are then compared with those obtained by the plastic linear formulation with the single load

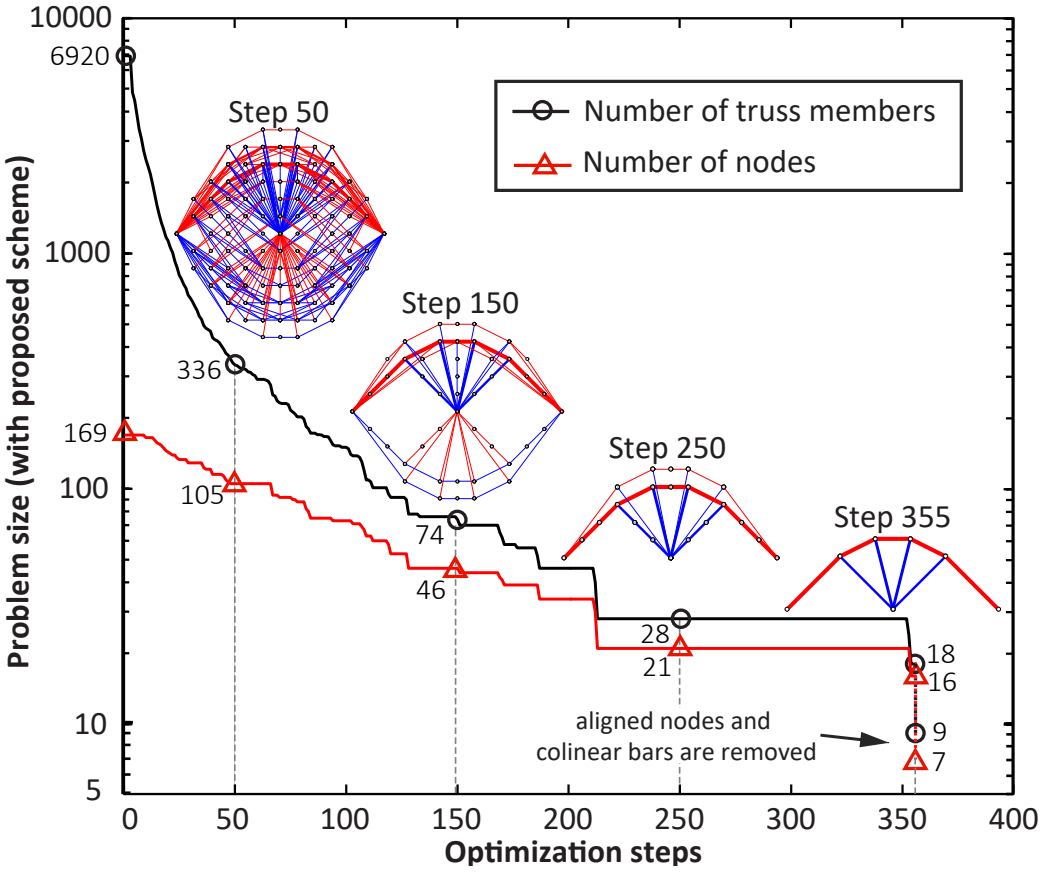


Figure 3.9: Size reduction history for optimization using Ogden-based Material 2 with the proposed filtering scheme. Numbers of truss members and nodes are reduced dramatically by the proposed filtering scheme during the optimization process, which shows the evolution of the ROM.

Table 3.2: Numerical information for Example 1 (Figure 3.7, 3.8, and 3.9). For the standard GSM, we use an end filter with $\alpha_f = 10^{-2}$ at the end of the optimization.

| Model | $J(\boldsymbol{x}^*)$ $(\text{kN}\cdot m)$ | $\Psi(\boldsymbol{u}(\boldsymbol{x}^*))$ $(\text{kN}/m^2)$ | Max$\lvert\boldsymbol{u}\rvert$ $(cm)$ | Max $\lambda$ | Min $\lambda$ | # Opt. Steps | CPU (sec) | $\alpha_f$ | $\alpha_{\text{Top}}$ |
|---|---|---|---|---|---|---|---|---|---|
| Linear (Filter) | 1.096 | 68.48 | 2.19 | 1.0014 | 0.9986 | 465 | 20 | $10^{-4}$ | 0.3143 |
| Mat.1 (Filter) | 1.073 | 65.62 | 2.12 | 1.0013 | 0.9986 | 353 | 24 | $10^{-4}$ | 0.3494 |
| Mat.2 (Filter) | 1.073 | 65.67 | 2.12 | 1.0014 | 0.9987 | 355 | 24 | $10^{-4}$ | 0.3485 |
| Mat.1 (Standard) | 1.085* | 67.12 | 2.15 | 1.0013 | 0.9986 | 428 | 300 | N/A | 0.3497 |
| Mat.2 (Standard) | 1.085* | 67.18 | 2.15 | 1.0014 | 0.9987 | 432 | 302 | N/A | 0.3487 |

* The objective value in standard GSM for both Materials 1 and 2 before applying final cutoff is 1.081.

case given in [41]. A schematic plot for plastic behavior is shown in Figure 3.10. A bridge is modeled using a two-dimensional (2D) domain, shown in Figure 3.11a for the single load case and Figure 3.11b for the multiple load cases. The domain is discretized by an $18 \times 7$ grid, followed by the generation of a full-level initial ground structure that contains 7,083 non-overlapping members and 152 nodes. For the multiple load cases, the weighting factor for each load case is the same, i.e., $w_1 = w_2 = 0.5$. To study how an alteration of the tension and compression yield stresses can change the final topology, we use various bilinear materials, each has a unique ratio between the compression and tension Young's moduli, denoted by $E_c/E_t$. For a linear material with equal tension and compression stress limits, elastic and plastic formulations lead to the same optimized structure up to a rescaling [17], [41]. In the case of materials with different tension and compression strengths, the two formulations may not lead to the same solution unless the material properties are defined properly. To compare the results of the elastic nonlinear and plastic linear formulations, the relationship between yield stresses in the plastic formulation and Young's moduli in the

elastic formulation is as follows [41],

$$\frac{\sigma_c}{\sigma_t} = \sqrt{\frac{E_c}{E_t}}. \tag{3.62}$$

The compression-tension ratios $E_c/E_t$ that we use here are 1, 0.09, 0.04, and 0.0225, shown in Figure 3.12, where $E_t = 7 \times 10^7$. In the plastic formulation, the absolute yield stress for tension is fixed, and the absolute yield stress for compression varies from 1 to 0.15. We use a small filter $\alpha_f = 10^{-4}$ throughout the optimization process.

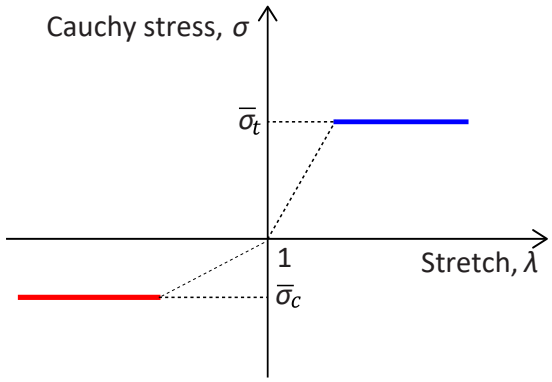


Figure 3.10: Stress-stretch diagram for plastic behavior with different stress limits for tension and for compression.

Figure 3.13 shows the final topologies of the long-span bridge for the four material models considered. While the top and bottom figures in each sub-figure show the optimized structures from the proposed scheme (i.e., the elastic nonlinear formulation with the filtering scheme for single load case and multiple load cases), those in the middle in each sub-figure show the optimized structures from the plastic linear formulation for single load case by [41]. An observation of the final topologies using different ratios of compression-tension strength ratio reveals that the optimized structure transforms from an arch bridge to a suspension bridge. A weaker compression modulus results in fewer bars under compression and more bars under tension. As we decrease the ratio, the arch gradually disappears.

Tables 3.3 and 3.4 provide summaries of the numerical information for single load case and multiple load cases in Example 2, respectively. All the data are obtained after removing

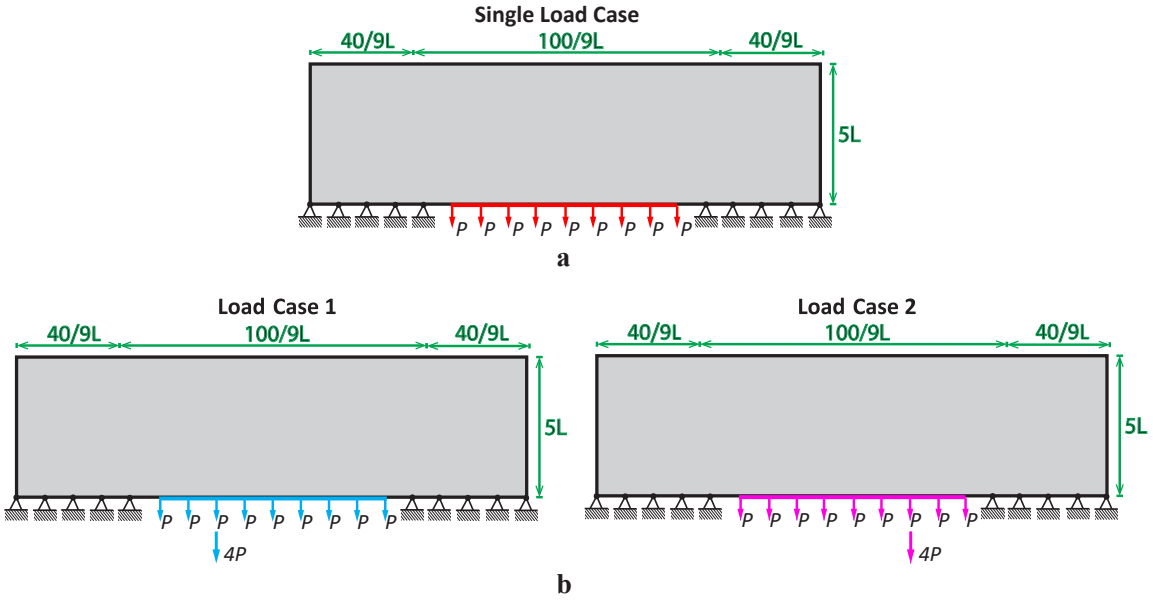


Figure 3.11: Two-dimensional bridge domain with a full-level ground structure ($18 \times 7$ grid) and $7,083$ non-overlapped bars: geometry ($L = 1m$), load ($P = 40kN$), and support conditions of **a** single load case; **b** multiple load cases.

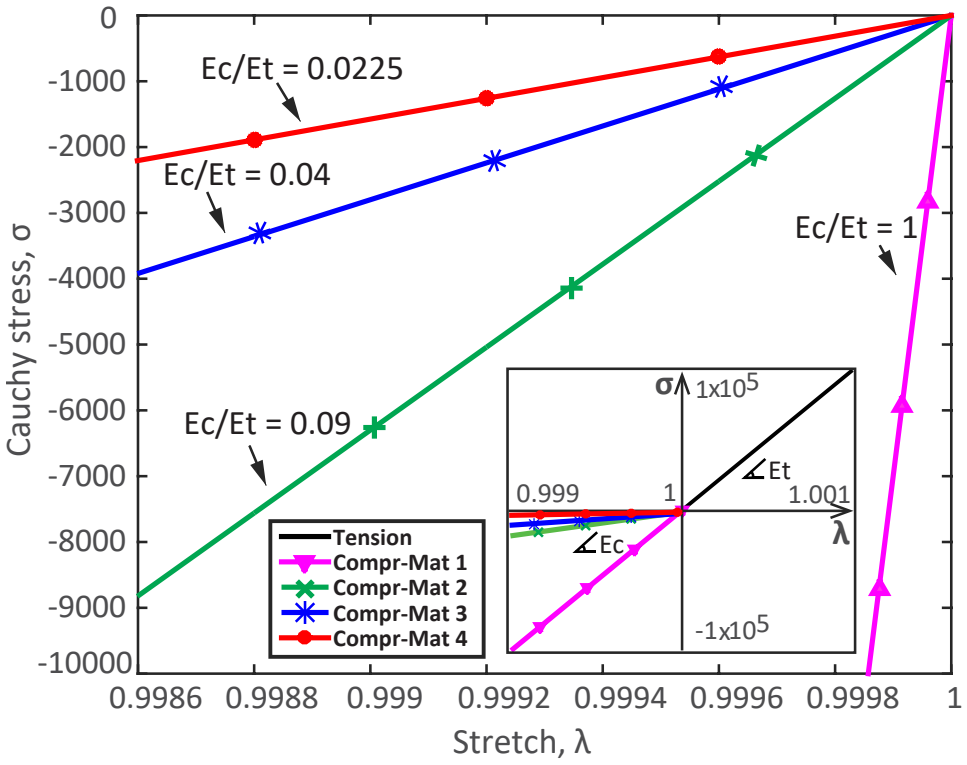


Figure 3.12: Bilinear material models. Tension modulus is fixed, the compression-tension ratios $E_c/E_t$ are 1, 0.09, 0.04, and 0.0225.

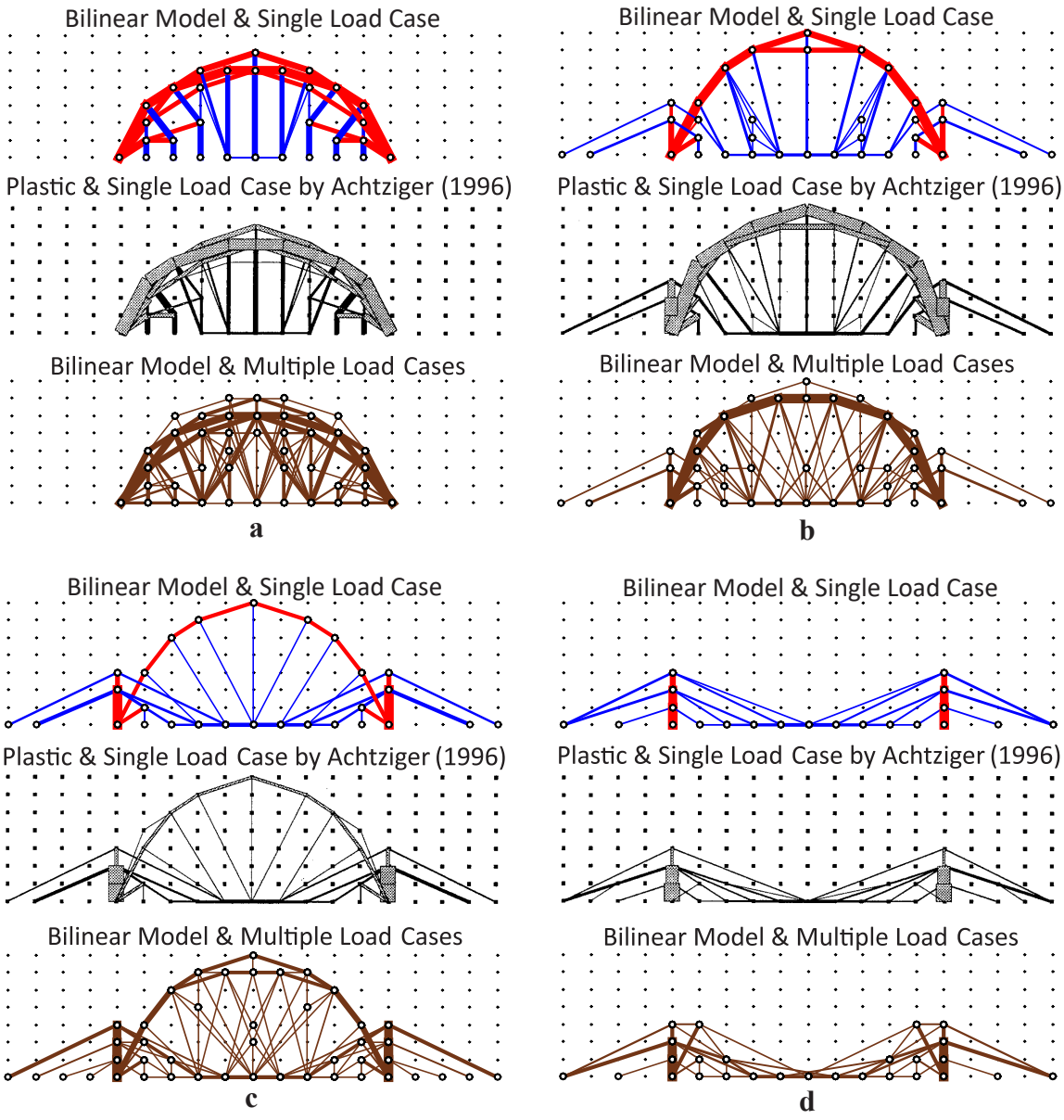


Figure 3.13: Optimized structures for **a** Material 1 with $E_c/E_t = 1$ and $\sigma_c/\sigma_t = 1$; **b** Material 2 with $E_c/E_t = 0.09$ and $\sigma_c/\sigma_t = 0.3$; **c** Material 3 with $E_c/E_t = 0.04$ and $\sigma_c/\sigma_t = 0.2$; **d** Material 4 with $E_c/E_t = 0.0225$ and $\sigma_c/\sigma_t = 0.15$. The blue bars are in tension and the red bars are under compression. The brown bars represent results from multiple load cases (online version in color).

unstable nodes. Since the tension is fixed and the compression properties vary, a comparison of the final objective values of the different material models indicates the stiffness of each structure differs. When the tension and compression moduli are balanced (Material 1), the final topologies (Figure 3.13a) for both the single and multiple load cases have the smallest objective values among all materials, which suggest that those structures have the greatest stiffnesses for this design problem. We confirm this observation by comparing the maximum displacement and strain energy density of all the materials, the topology of Material 1 exhibits the smallest deflection and strain energy density. In contrast, the topology using Material 4 (i.e., Figure 3.13d), which has the weakest compressive strength, exhibits the most flexible optimal structures for both single and multiple load cases. Since tension is preferable, the distributed loads must be supported by truss members under tension, forming a suspension bridge in which compression does not appear in the topology except in the supporting two columns. Nevertheless, optimization using Material 4 requires the least amount of computational time. Therefore, the different tension and compression strengths of truss members significantly influence the optimization of a structure.

We further compare the optimized structures from the proposed algorithm (i.e., the elastic nonlinear formulation with a filter) under single load case with those from the plastic linear formulation under single load case used by [41]. The comparison shows that the two formulations lead to similar optimal structures for each material and that the proposed filtering scheme improves the resolution of the final topologies and eliminates some of the small area members from the final topology, shown in Figures 3.13a, 3.13c and 3.13d. Comparison between the single and multiple load cases shows that the designs accounting for multiple load cases provide alternative structures, showing the capability of the elastic formulation in accounting for multiple load cases as oppose to the plastic formulation.

Table 3.3: Numerical information for the long-span bridge (Example 2) considering the elastic formulation with the proposed filter under single load case.
We use $\alpha_f = 10^{-4}$ during the optimization process.

| $E_t/E_c$ | $J(\boldsymbol{x}^*)$ (kN$m$) | $\Psi(\boldsymbol{u}(\boldsymbol{x}^*))$ $\left(\text{kN}/m^2\right)$ | Max$\lvert\boldsymbol{u}\rvert$ $(cm)$ | Max $\lambda$ | Min $\lambda$ | # Opt. Steps | CPU (Sec) | $\alpha_{Top}$ | #Top Elem. |
|---|---|---|---|---|---|---|---|---|---|
| 1 | 1.92 | 38.4 | 1.43 | 1.0010 | 0.9990 | 2,284 | 49 | 0.0165 | 50 |
| 0.09 | 12.25 | 245.0 | 8.98 | 1.0026 | 0.9912 | 950 | 23 | 0.000382 | 58 |
| 0.04 | 21.96 | 439.3 | 18.05 | 1.0035 | 0.9823 | 585 | 17 | 0.00657 | 41 |
| 0.0225 | 29.57 | 591.4 | 25.85 | 1.0041 | 0.9726 | 272 | 12 | 0.0265 | 30 |

Table 3.4: Numerical information for the long-span bridge (Example 2) considering the elastic formulation with the proposed filter under multiple load cases.
We use $\alpha_f = 10^{-4}$ during the optimization process.

| $E_t/E_c$ | $J(\boldsymbol{x}^*)$ (kN$\cdot m$) | $\sum_{j=1}^{2} w_j \Psi\left(\boldsymbol{u}_j(\boldsymbol{x}^*)\right)$ $\left(\text{kN}/m^2\right)$ | #Opt. Steps | CPU (Sec) | $\alpha_{Top}$ | #Top Elem. |
|---|---|---|---|---|---|---|
| 1 | 5.40 | 108.1 | 6399 | 216 | 0.00111 | 117 |
| 0.09 | 31.28 | 625.6 | 2891 | 116 | 0.000198 | 94 |
| 0.04 | 56.60 | 1132.0 | 1193 | 66 | 0.000207 | 96 |
| 0.0225 | 75.77 | 1515.4 | 224 | 32 | 0.00532 | 52 |

### 3.5.3 Top central Load on a laterally constrained parallelepiped domain

In this example, we first show the influence of the load level on the resulting topology when both linear and nonlinear material behavior are taken into account, followed by the demonstration of the computational capability of the proposed method on models with varying number of design variables. We use a small filter $\alpha_f = 10^{-4}$ throughout the optimization process, followed by a larger filter $\alpha_f = 10^{-2}$ in the final step of the optimization to control the resolution of the final topology. After the last filter, we ensure equilibrium of the final structure by checking the global equilibrium. The comparison of different load levels utilizes a coarse discretization with an Ogden-based material and has three imposed load levels (5kN, 20kN, and 100kN). This comparison also includes a linear material with one imposed load level (5kN) since the linear case is independent of the load level. We use a $14 \times 14 \times 5$ grid for the coarse discretization and generate a level 5 initial ground structure containing 279,653 non-overlapped members. The geometry, the load, and support condi-

tions are shown in Figure 3.14a, and the Ogden-based material model with greater strength in tension is shown in Figure 3.14b.

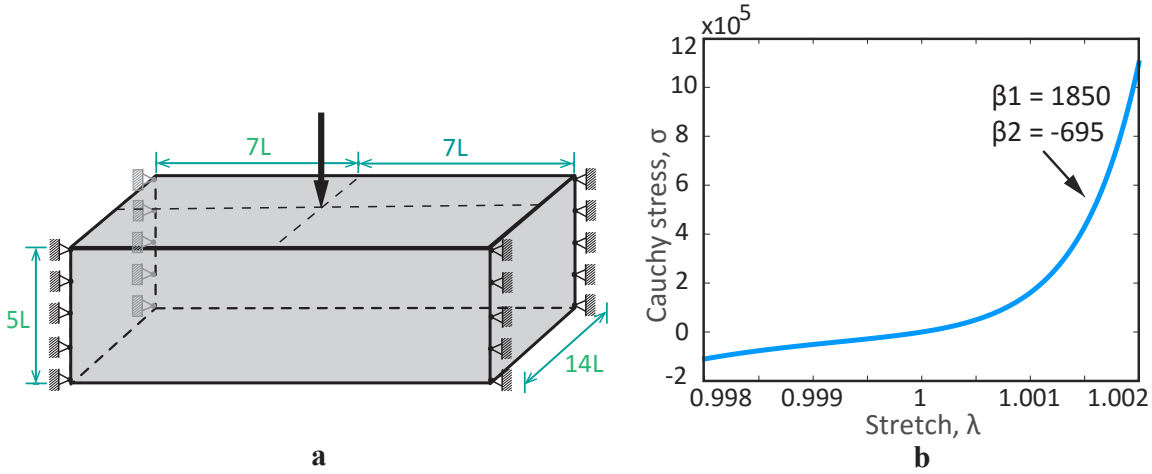


Figure 3.14: A laterally constrained rectangular domain with single load case. **a** Problem domain ($L = 1m$), load, and boundary conditions; **b** Ogden material model. This material shows stronger behavior in tension than in compression.

Figure 3.15 shows the optimized topologies for the nonlinear material under three load levels: $P = 5$kN, $P = 20$kN, and $P = 100$kN. Note that Figure 3.15a also represents the topology of the linear material case. At the 5kN load, the nonlinear material case yields the same topology as the linear material case. The small differences in their objective and displacement values are due to the minor nonlinearity that exists at this load level in the nonlinear material case. As the load level increases, the topology of the linear model does not change; the corresponding topologies of the nonlinear cases, however, change dramatically. As a consequence of the relatively stiffer tension strength of the chosen material model, a higher load leads to a relatively larger stretch, which results in more truss members under tension than at the lower load levels. This observation shows the importance of accounting for material nonlinearity. In addition, to demonstrate the influence of the line search method, which is described in Section 3.4, we solve the nonlinear model of $P = 100$kN by the Newton-Raphson method with and without the line search method. The nonlinear FEM iterations for first, second, and final optimization steps are shown in Table 3.5. In the initial optimization step, while the case without the line search method fails to

converge, the case with the line search converges within 11 FEM iterations. As a result, the Newton-Raphson method with line search reaches the optimal solution. Table 3.6 presents a summary of the numerical information for the comparison of different load levels with Max $|\boldsymbol{u}|$ confirming the small displacement assumption used in this work, all the data are obtained after removing unstable nodes.

Table 3.5: Influence of the line search method for the case $P = 100$kN with Newton-Raphson (Example 3).

| NR **with** line search | | | | NR **without** line search | | |
|---|---|---|---|---|---|---|
| Opt. step | FEM iter. | Step length, $\xi$ | $\frac{\|\|\boldsymbol{R}_{\text{Top}}\|\|}{\|\|\boldsymbol{f}_{\text{Top}}\|\|}$ | Opt. step | FEM iter. | $\frac{\|\|\boldsymbol{R}_{\text{Top}}\|\|}{\|\|\boldsymbol{f}_{\text{Top}}\|\|}$ |
| 1 | 1 | 0.0313 | $7.408 \times 10^{-1}$ | | | |
| | 2 | 0.250 | 1.277 | | | |
| | 3 | 1.000 | 9.015 | | | |
| | 4 | 1.000 | 3.323 | | | |
| | 5 | 1.000 | 1.206 | | | |
| | ⋮ | ⋮ | ⋮ | | Fails to converge. | |
| | 12 | 1.000 | $1.095 \times 10^{-9}$ | | | |
| 2 | 1 | 1.000 | $2.778 \times 10^{1}$ | | | |
| | 2 | 1.000 | $1.000 \times 10^{1}$ | | | |
| | ⋮ | ⋮ | ⋮ | | | |
| | 9 | 1.000 | $1.378 \times 10^{-9}$ | | | |
| 522 (Final) | 1 | 1.000 | $2.800 \times 10^{-5}$ | | | |
| | 2 | 1.000 | $5.023 \times 10^{-9}$ | | | |

Furthermore, we demonstrate the potential of the filtering scheme in dealing with problems with a relatively large number of design variables by comparing the computational efficiency of the proposed filtering scheme with that of the standard GSM without the proposed filter. For a fair comparison, both approaches (filter and standard GSM) use the same Ogden-based material (Figure 3.14b), initial grid ($18 \times 18 \times 6$), connectivity level (level 7), and load level ($P = 1,000$KN), leading to the same initial ground structures with 1,062,090 non-overlapped members and 2,527 nodes. The final topologies for both cases are shown in Figure 3.16, and their associated numerical data are recorded in Tables 3.7 and 3.8. Using the standard GSM, since numerous small area bars are not plotted on the final topology while still supporting the structure, after the final cut-off, we observe a larger maximum

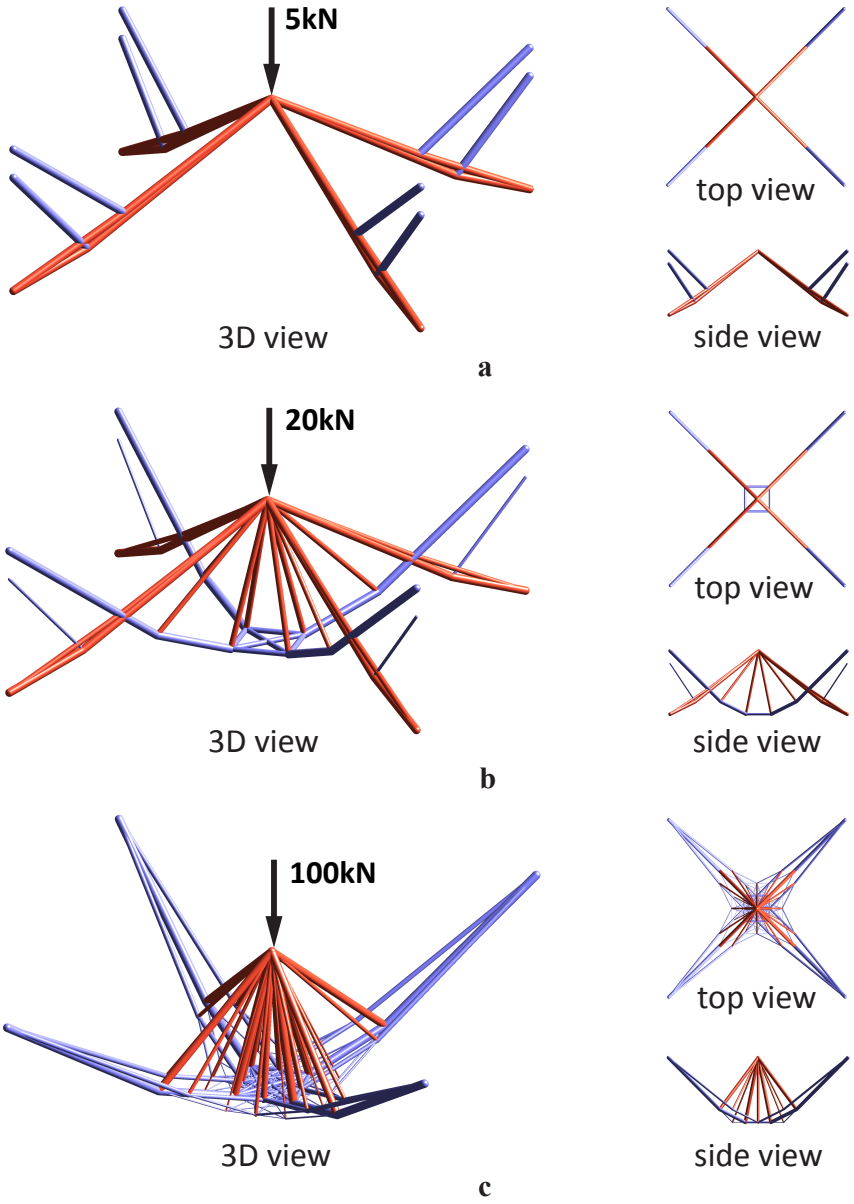


Figure 3.15: Final topologies for imposing different load levels from the proposed filtering scheme with a level 5 ground structure ($14 \times 14 \times 5$ grid) and $279,653$ non-overlapped bars using **a** Ogden-based material and linear material, each carrying a 5kN load (these two materials under 5kN load lead to the same topology); **b** Ogden-based material carrying a 20kN load; and **c** Ogden-based material carrying a 100kN load (online version in color).

Table 3.6: Numerical information for Example 3 (Figure 3.14) - influence of the load level considering material nonlinearity. We use $\alpha_f = 10^{-4}$ during the optimization process followed by an end filter with $\alpha_f = 10^{-2}$.

| | $J(\boldsymbol{x}^*)$ $(\text{kN}\cdot m)$ | $\Psi(\boldsymbol{u}(\boldsymbol{x}^*))$ $\left(\text{kN}/m^2\right)$ | Max$\lvert\boldsymbol{u}\rvert$ $(cm)$ | Max $\lambda$ | Min $\lambda$ | # Opt. Steps | CPU (sec) | $\alpha_{\text{Top}}$ | #Top Elem. |
|---|---|---|---|---|---|---|---|---|---|
| Linear 5kN | 0.00724 | 0.59 | 0.29 | 1.0000** | 0.9999 | 3,005 | 85 | 1.00 | 24 |
| NonL 5kN | 0.00759 | 0.40 | 0.31 | 1.0000** | 0.9999 | 3,005 | 800 | 1.00 | 24 |
| NonL 20kN | 0.0968 | 4.87 | 0.97 | 1.0004 | 0.9996 | 707 | 634 | 0.143 | 48 |
| NonL 100kN | 1.856 | 64.42 | 3.15 | 1.0010 | 0.9984 | 522 | 582 | 0.0108 | 132 |

** The exact maximum stretch value for both linear ($P = 5kN$) and nonlinear ($P = 5kN$) cases is 1.000023.

displacement and a larger objective value.

The proposed filter approach, while offering a nearly identical topology and objective value as the standard GSM, drastically reduces the computational cost. The CPU time used in the optimization process is almost 45 times as fast (54 minutes vs. 40.3 hours), as shown in Table 3.7, all the data are obtained after removing unstable nodes. As explained previously, the use of the proposed filtering scheme with the ROM reduces the sizes of design variables, the stiffness matrices, and the sensitivity vectors, which significantly decrease the CPU time and memory usage; the standard GSM maintains a constant size during the entire optimization process. To quantify the influence of using the proposed filtering scheme with the reduced-order model on the nonlinear optimization problem, we measure the sizes of the DOFs and design variables at optimization step 1 (initial step), 10, 100, and 962 (final step) during the optimization process for the case with 1000kN load level with the proposed scheme (Figure 3.16a). The size reduction history, recorded in Table 3.8, shows that after performing only 10 steps in the optimization process (962 steps in total), the size of the design variables reduces to nearly 1% of its original size.

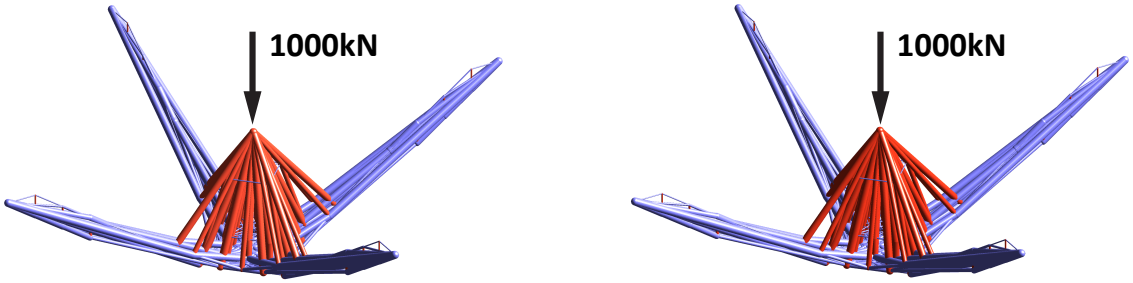


**a** **b**

Figure 3.16: Results of the optimization for the comparison of the filtering scheme with the standard GSM using a level 7 ground structure ($18 \times 18 \times 6$ grid) and 1,062,090 non-overlapped members at a 1,000kN load level: **a** The final topology obtained from the proposed filtering scheme ($\alpha_f = 10^{-4}$), CPU time 54 minutes; and **b** the final topology (almost identical with **a**) obtained from the standard GSM performed in 40.3 hours.

Table 3.7: Numerical information for Example 3 (Figure 3.14) - comparison of filter with standard GSM. For both the filter approach and the standard GSM, we use an end filter with $\alpha_f = 10^{-2}$ at the end of the optimization.

| | $J(\boldsymbol{x}^*)$ $(\mathrm{kN}\cdot m)$ | $\Psi(\boldsymbol{u}(\boldsymbol{x}^*))$ $\left(\mathrm{kN}/m^2\right)$ | Max$\lvert\boldsymbol{u}\rvert$ $(cm)$ | Max $\lambda$ | Min $\lambda$ | # Opt. Steps | CPU | $\alpha_f$ | $\alpha_{\mathrm{Top}}$ | #Top Elem. |
|---|---|---|---|---|---|---|---|---|---|---|
| NonL 1000kN (Filter) | 63.53 | 998 | 8.41 | 1.0024 | 0.9947 | 962 | 54 mins | $10^{-4}$ | 0.0109 | 425 |
| NonL 1000kN (Standard) | 63.74† | 1,001 | 8.43 | 1.0024 | 0.9948 | 1,050 | 40.3 hours | N/A | 0.0101 | 417†† |

† The objective value in the standard GSM before applying the final cutoff (end filter) is 63.72.

†† The number of truss elements in the standard GSM during the entire optimization process is 1,062,090.

Table 3.8: Size reduction history for the proposed filter with reduced-order modeling (NonL, 1000kN & Filter).

| Opt. step | DOFs | | Design Variables | |
|---|---|---|---|---|
| | Size | % of initial size | Size | % of initial size |
| # 1 (initial) | 7,581 | 100% | 1,062,090 | 100% |
| # 10 | 2,457 | 32.4 % | 13,850 | 1.3 % |
| # 100 | 645 | 8.5% | 1,094 | 0.1% |
| # 962 (final) | 303 | 4% | 437 | 0.04% |

### 3.5.4 Arch bridge

To illustrate the influence that nonlinear materials may have on actual structures, we use a 3D bridge design with three Ogden-based materials. The bridge domain in Figures 3.17a and 3.17b has simple supports, a cantilever, a non-designable layer that represents the bridge deck, and a void zone for practical design purposes [113]. In an effort to obtain constructible structures, we use a $10 \times 6 \times 10$ grid to discretize the domain followed by the generation of a full-level initial ground structure that contains 231,567 non-overlapping members. To represent the effect of the bridge deck, we use a layer of beam elements excluded from the optimization process but included in the nonlinear FEM analysis. To study how any alteration in the material behavior changes the optimized structure, we use three Ogden-based materials, shown in Figure 3.17c. Material 1 ($\beta_1 = 1,850$, $\beta_2 = -695$) has higher tensile strength than compressive strength, Material 2 ($\beta_1 = 723$, $\beta_2 = -720$) has the same tension and compression, and Material 3 ($\beta_1 = 698$, $\beta_2 = -1,845$) is relatively stronger in compression than tension. It should be noted that, in addition to a small filter ($\alpha_f = 10^{-4}$) used in the entire optimization, we use a larger filter ($\alpha_f = 10^{-2}$) in the final step of the optimization to control the resolution of the final topology. We ensure the equilibrium of the final structure with the global equilibrium check. Figure 3.18 shows the optimized structures obtained using the three materials. A detailed summary of the numerical results is provided in Table 3.9, and all the data are obtained after removing unstable nodes.

The various topologies obtained from using the three materials shows the importance of accounting for material nonlinearity. As shown from both Figure 3.18 and Table 3.9, while having only a minor effect on the computational cost of the optimization problem, the choice of material models markedly influences the optimized structures. Optimization using Material 2 with identical compressive and tensional behaviors yields a final topology that resembles an arched bridge, with a significantly larger volume of compression members than of tension members, indicating that the structure requires more compression

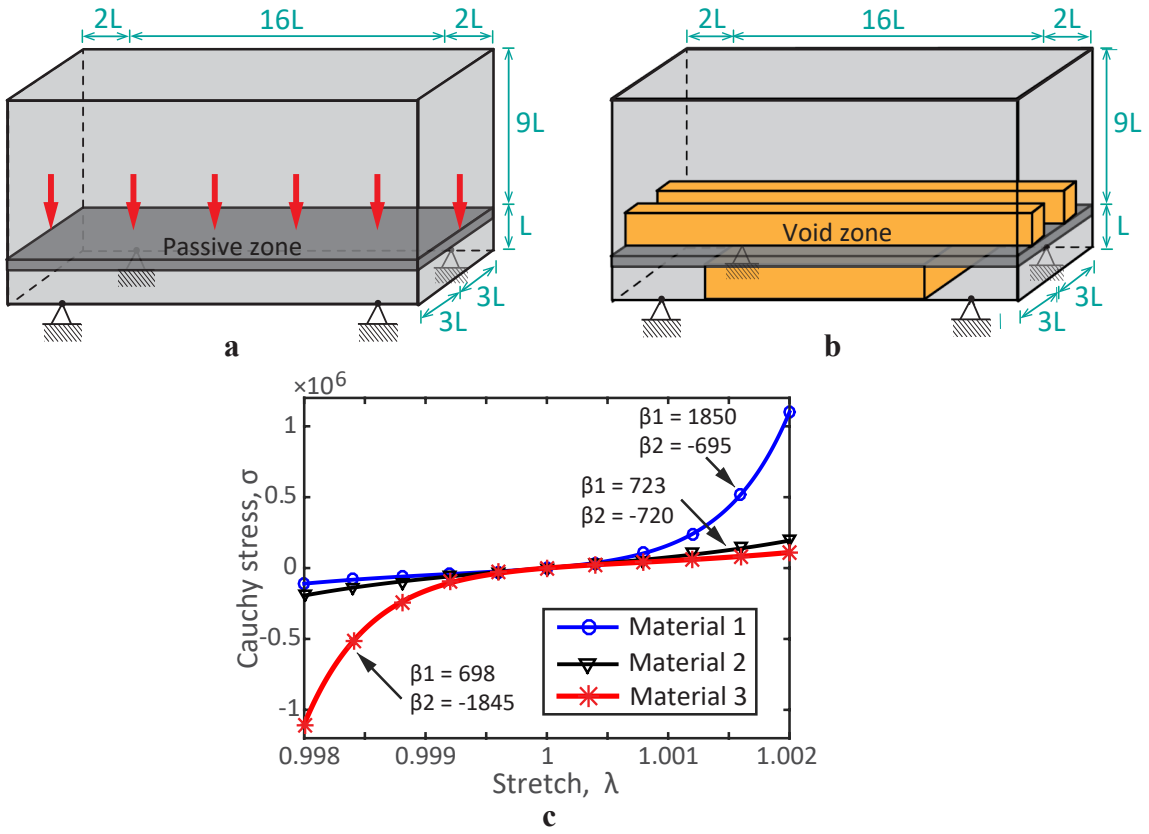


Figure 3.17: 3D bridge design with a level full ground structure ($10 \times 6 \times 10$ grid) and 231,567 non-overlapped members. **a** Design domain ($L = 10m$) with load and boundary conditions; **b** design domain with void zone; **c** Ogden-based material models: Material 1 has high tensile strength, Material 2 has a close-to-linear constitutive relationship, and Material 3 has high compressive strength.

members because of the nature of the design problem. When Material 1 (with a stronger tension behavior) is used for the design, the overall topology features are similar to those obtained with Material 2, but the final topology contains fewer long compression bars, especially those with small areas in the arch region (because long and thin compression bars result in a large internal energy and, therefore, a large objective), which leads to a clearer topology. We also notice that the total volume of the compression members for Material 1, compared to the one obtained for Material 2, increases and the objective value decreases.

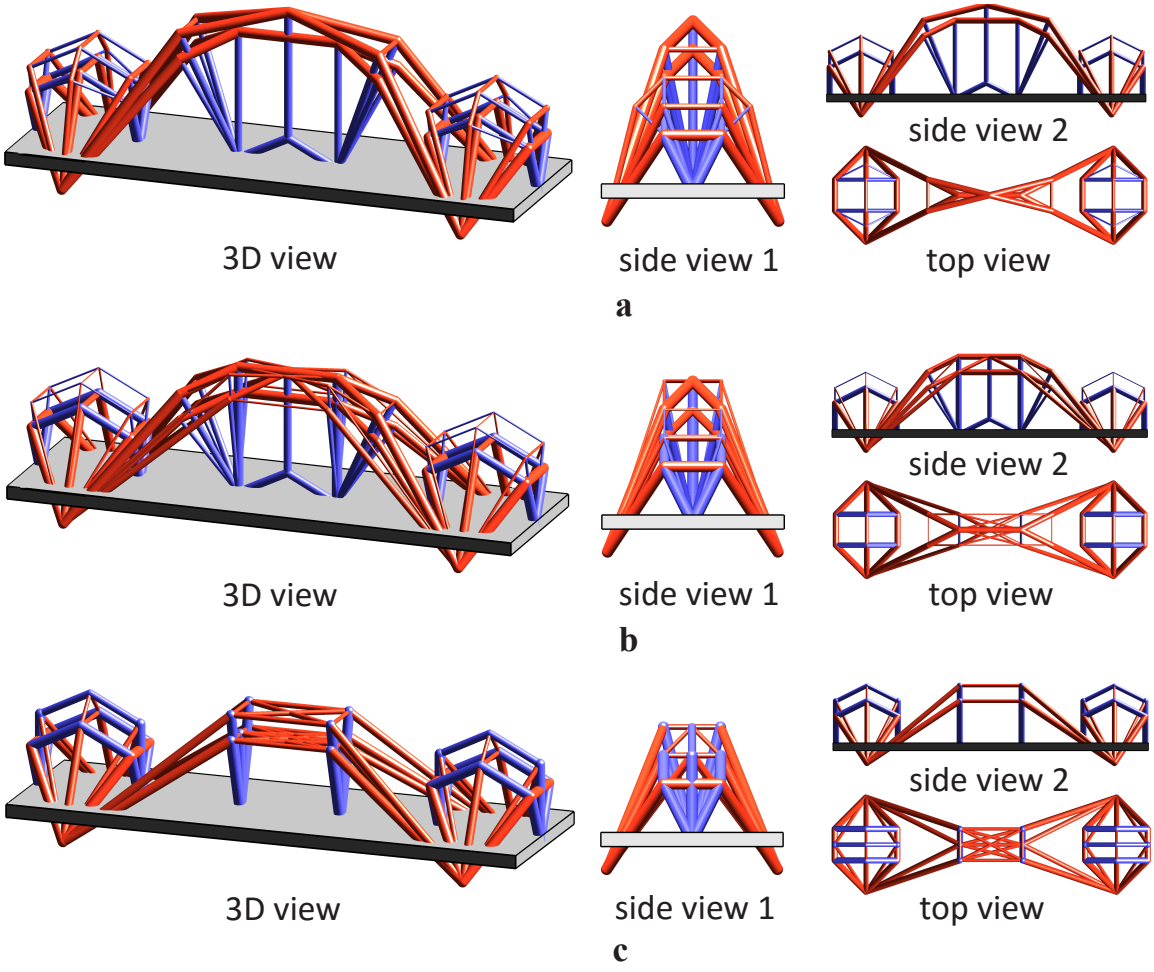


Figure 3.18: Final topologies from the proposed filtering scheme using: **a** Material 1; **b** Material 2; and **c** Material 3. Blue represents bars in tension and red represents bars in compression.

When we use Material 3, with stronger compressive behavior, the final topology shows patterns that differ from those obtained for both Materials 1 and 2, especially in the arch re-

gion. The fan area of the arch contains fewer tension members with larger cross-sectional areas that are all connected by long compression members. Indeed, Material 3 exhibits the clearest final topology, as shown by $\alpha_{\text{Top}}$ values. Moreover, as a result of the relatively weaker tension behavior, the total volume of the tension bars increases. The objective value is the smallest of the three cases because, as mentioned previously, the structure requires compression members in this problem. A comparison of the heights of the three optimized structures in Figure 3.20 shows that higher tensile strength in a material leads to a higher arch in the optimized design. As the tensile strength of the material decreases and compressive strength increases, the height of the arch gradually decreases. The design with Material 3 has the lowest height $5.2L$. The observed differences in the final topologies associated with the three materials with various constitutive relationships demonstrate the importance of accounting for nonlinearity in material models in the practical design optimizations of 3D structures. This example shows that the proposed filtering scheme, which combines the practical demands of material behavior and manufacturing, is a functional design tool. The optimized bridge design with Material 3 (Figure 3.18c) is further manufactured by the 3D printing technique using a fused deposition modeling (FDM) process, as shown in Figure 3.19. This bridge model is directly manufactured without post-processing of the numerical result.

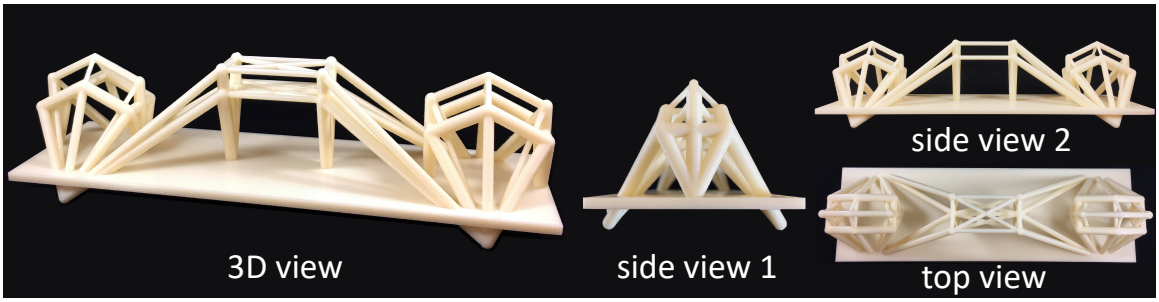


Figure 3.19: 3D printed model of the optimized bridge design with Material 3 using a FDM process. The dimension of the manufactured model is 11.5 in $\times$ 3.5 in $\times$ 3 in.

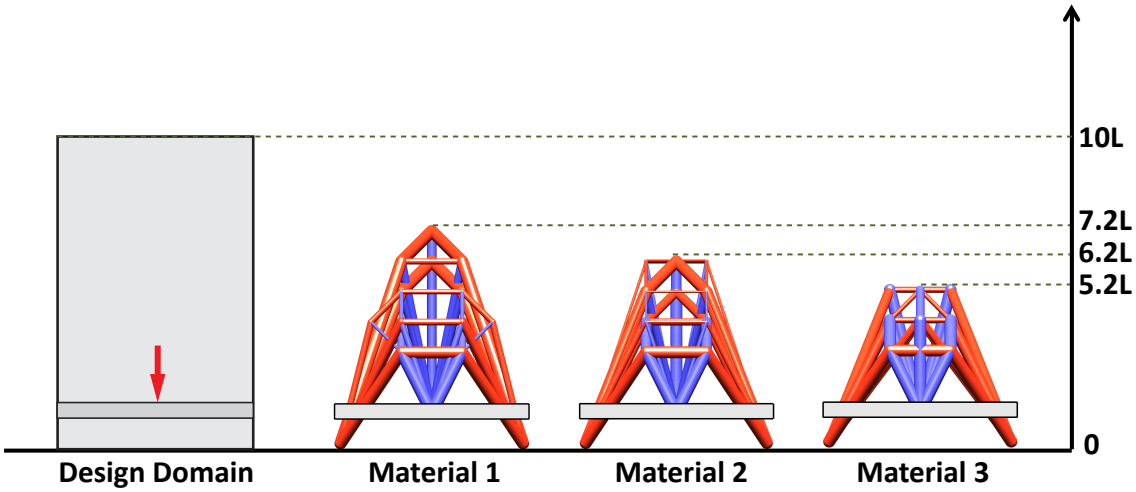


Figure 3.20: Comparison of bridge heights for optimized structures using three materials.

Table 3.9: Numerical information for Example 4 with the proposed reduced-order filter. We use $\alpha_f = 10^{-4}$ during optimization process followed by an end filter with $\alpha_f = 10^{-2}$.

| Material | $J(\boldsymbol{x}^*)$ | $\Psi(\boldsymbol{u}(\boldsymbol{x}^*))$ | Max$\lvert\boldsymbol{u}\rvert$ | Max $\lambda$ | Min $\lambda$ | Tension Vol. | Compr. Vol. | CPU (sec) | $\alpha_{Top}$ |
|---|---|---|---|---|---|---|---|---|---|
| 1 | 370.6 | 3,934 | 1.15 | 1.0030 | 0.9926 | 19.8% | 80.2% | 771 | 0.0474 |
| 2 | 394.2 | 4,742 | 1.20 | 1.0066 | 0.9935 | 30.4% | 69.6% | 643 | 0.0115 |
| 3 | 259.9 | 2,773 | 0.72 | 1.0074 | 0.9972 | 41.0% | 59.0% | 637 | 0.121 |

## 3.6 Summary and Discussion

This chapter proposes an efficient reduced-order discrete filter that can be applied to truss optimization considering single and multiple load cases, and nonlinear constitutive behavior. The proposed scheme utilizes reduced-order modeling on both the state and optimization problems. It examines two types of materials: hyperelastic Ogden-based and bilinear materials, both of which offer alternative options for material behavior. Using a Tikhonov regularization, we solve the singular state equations in the modified standard formulation with design variable $\boldsymbol{x} \geq \boldsymbol{0}$ (see Eq. (3.4)). This modification on the lower bound of design variables transforms the sizing problem (standard formulation) into a topology optimization problem (modified standard formulation). We prove the convexity of the modified standard formulation (Eq. (3.4)) under the assumptions of convex energy density function and equilibrium satisfaction. This proof is valid even when the tangent stiffness matrix is positive

semidefinite. Furthermore, as shown by the KKT conditions (see Section 2.6), our formulation leads to constant weighted sum of specific strain energy under $m_\ell$ load cases for those members whose optimal design variables are in the optimum range $0 < x^{(e)^*} < x^{(e)}_{\max}$ (Eq. (4.12)). An inexact (Armijo-type) line search is adopted in the Newton-Raphson method, which is shown to improve convergence in the first few FEM iterations of the nonlinear structural problem. The line search is essential for convergence.

Based on the present investigation and outcome of the examples, we conclude that the discrete filter with material nonlinearity is a practical tool that accounts for real-life demands of materials, layout, and manufacturing. While traditional topology optimization typically assumes linear material behavior, which may be limiting; we examine material nonlinearity in the optimization that takes into account the effect of proper load levels. Through several examples, we observe the difference in topologies resulting from changes in the material models and load levels, which shows the importance of accounting for nonlinear material behavior in practical design optimization of 2D and 3D structures. In addition, while the optimized structures under single load case obtained from the proposed algorithm (elastic nonlinear formulation with filter) and those from the plastic linear formulation lead to similar structures, the designs accounting for multiple load cases provide alternative structures, illustrating the capabilities of the elastic formulation in accounting for multiple load cases and nonlinear behavior.

With the proposed filtering scheme, we solve structural problems solely from information about truss members remaining in the structure. In addition, through comparison with the standard GSM, we conclude that while including the small area members that are below the cut-off (i.e., standard GSM) to solve nonlinear structural problems may result in artificial stiffness and convergence difficulties, excluding them with the Tikhonov regularization technique (with or without the filtering scheme) provides better control in the condition number of the tangent stiffness matrix. Moreover, since we can use the proposed filter to control the final resolution of the optimized structure, the results may be achieved

without post-processing.

The use of the (fully) reduced-order modeling in the proposed filtering scheme significantly reduces the size of both the structural and optimization problems within a few optimization steps, leading to drastically improved computational performance. Through one study conducted in this chapter (see Section 5.3), the proposed filter algorithm, while offering almost the same optimized structure, was 45 times faster than the standard GSM for nonlinear optimization problems.

# CHAPTER 4

# MULTI-MATERIAL TOPOLOGY OPTIMIZATION WITH MULTIPLE CONSTRAINTS: A GENERAL FORMULATION BASED ON THE ZPR UPDATE ALGORITHM

Multi-material topology optimization is a practical tool that allows for improved structural designs. However, most studies are presented in the context of continuum topology optimization – few studies focus on truss topology optimization. Moreover, most work in this field has been restricted to linear material behavior with limited volume constraint settings for multiple materials. To address these issues, we propose an efficient multi-material topology optimization formulation considering material nonlinearity. The proposed formulation handles an arbitrary number of candidate materials with flexible material properties, features freely specified material layers, and includes a generalized volume constraint setting. To efficiently handle such arbitrary volume constraints, we derive a design update scheme that performs robust updates of the design variables associated with each volume constraint independently. The derivation is based on the separable feature of the dual problem of the convex approximated primal subproblem with respect to the Lagrange multipliers, and thus the update of design variables in each volume constraint only depends on the corresponding Lagrange multiplier. Through examples in 2D and 3D using combinations of Ogden-based, bilinear, and linear materials, we demonstrate that the proposed multi-material topology optimization framework with the presented update scheme leads to a design tool that not only finds the optimal topology but also selects the proper type and amount of material. The design update scheme is named ZPR (phonetically, zipper), after the initials of the authors' last names (Zhang-Paulino-Ramos Jr.).

## 4.1 Introduction

Topology optimization is a powerful computational design tool used to find optimal layouts of structures and material microstructures. Within the field of topology optimization, multi-material topology optimization is an emerging trend because practical engineering designs, such as buildings, aircraft, and composite materials typically consist of multiple material types. The literature on multi-material topology optimization is vast and growing but mostly focuses on the continuum setting. With the density-based approach, various generalizations and extensions of the Solid Isotropic Material with Penalization (SIMP) [114] or other material interpolation schemes for single-material topology optimization are made to accommodate multiple materials. For example, Sigmund and Torquato ([60]) and Gibiansky and Sigmund ([61]) present extensions of the SIMP model to three-phase materials (two material phases plus one void phase) and apply them to the design of material microstructures with extreme thermal expansion and extreme bulk moduli. Hvejsel and Lund ([62]) generalize the SIMP scheme and the Rational Approximation of Material Properties (RAMP) scheme [45] to include an arbitrary number of material phases. However, in order to enforce the selection of, at most or exactly, one material at each design subdomain, their study uses a large number of sparse linear constraints. A similar generalization of the SIMP scheme that includes an arbitrary number of material phases is made by Stegmann and Lund ([72]), who use the Discrete Material Optimization (DMO) in the design of laminated composite structures. Another variation of the scheme by Yin and Ananthasuresh ([63]) proposes a peak function approach that uses only one density variable to interpolate the effective material properties as opposed to multiple density variables. Their scheme uses a Gaussian distribution peak function as the weight of each material phase, and the selection of a given material phase is made if the density variable corresponds to a material peak. In addition to the density-based approach, phase-field [64], [115], [116] and level set [66]–[69] approaches have also been used for multi-material topology optimization formu-

lations.

While the majority of existing studies of multi-material topology optimization deal with the continuum setting, only a small number of studies in multi-material topology optimization include discrete elements, e.g., truss and lattice networks. Among these studies, [117] propose a multi-material formulation to optimize lattice structures, incorporating manufacturing constraints. Their study uses the Young's modulus of each truss as the design variables and optimizes them on a layout with fixed cross-sectional areas. Other studies have attempted to integrate truss elements into continuum topology optimization by considering concrete as a continuum solid and steel rebars as truss members (see, e.g., [10]–[14]) for the purpose of designing reinforced concrete structures and studying strut and tie models. However, in the literature, few multi-material topology optimization studies focus on truss layout optimization, which is the emphasis of our work.

A promising technique to optimize truss layouts is the ground structure method (GSM), see, e.g., [27], [28], [30], [31], [118], [119]. In this technique, the design domain is discretized by a set of nodes, which are interconnected by truss members to form an initial ground structure (GS). By means of an update scheme and sensitivity information, the final design is then obtained by gradually removing unnecessary members from the initial GS (subtractive method).

For the initial assignment of material layers in the GSM in the present chapter, each candidate material is associated with a design layer (ground structure); thus, users are free to specify the location of each material. The multiple material layers can either share or split the design domain, or combine both, as demonstrated in Figure 4.1. Scenario 1 (Figure 4.1c) shows the case where the initial ground structures associated with the four materials are overlapping and is designed to enable automatic assignment of the materials. Scenario 2 (Figure 4.1d) can be used to fulfill various design requirements such as assigning certain materials in specific locations of a structure. As shown in Figure 4.1e, sharing & splitting can be combined to enable a more flexible design space.

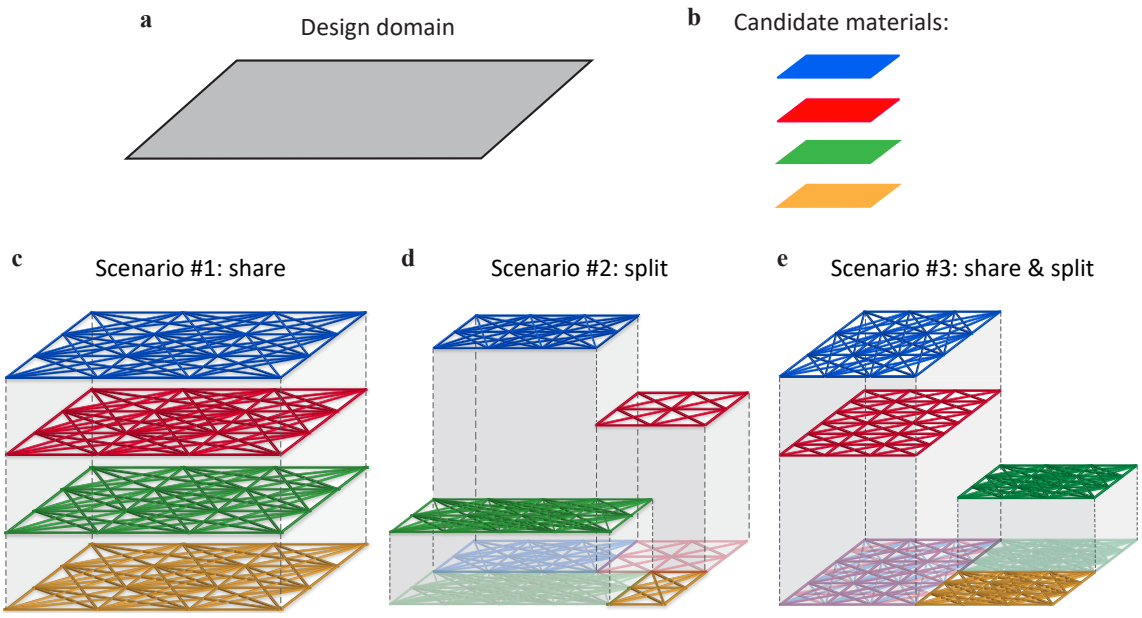


Figure 4.1: Illustration of the combinations of material layers: **a** Design domain; **b** candidate materials; **c** Scenario #1, four materials share the domain (initial ground structures of all materials overlap) enabling automatic material assignment; **d** Scenario #2, four materials split the domain, which can be used to fulfill certain design needs; **e** Scenario #3, four materials share & split the domain, which enables a more flexible design space. (Online version in color.)

One limitation of most existing work in multi-material topology optimization is that only linear material behavior is considered (for the study that considers nonlinear material behavior, see [115] for multi-material phase-field topology optimization under finite deformation). However, real materials generally display nonlinear constitutive relations. Studies of material nonlinearity in single material topology optimization (e.g., [39], [41], [83], [84], [120]) have demonstrated the impact of accounting for nonlinear material behavior in structural optimization. For instance, it has been shown that various optimal topologies can be obtained in material nonlinear cases by changing the material behavior and load level. In the case of multiple materials with linear material behavior, an individual volume constraint has to be assigned to each candidate material to ensure its presence in the optimized topology. If one total/global volume constraint is assigned to all the linear candidate materials, the optimizer always favors the best linear candidate material, e.g. the stiffest material in the minimum compliance optimization, and final topologies consisting of only a single material type can occur, as shown in Figure 4.2b. However, if the nonlinear material behavior is incorporated in multi-material topology optimization, the optimizer naturally avoids consistently favoring the stiffest linear material and, therefore, enables a more general setting of volume constraints. As demonstrated in Figure 4.2c, when a global volume constraint is assigned to two nonlinear candidate materials (one tension-dominated and the other compression-dominated), the resulting topology contains both nonlinear candidate materials. To address the aforementioned issues, we incorporate material nonlinearity into multi-material optimization because it produces various optimized structures and enables enhanced freedom of volume constraints.

From the optimization formulation perspective, another limitation of multi-material topology optimization is related to the limited settings of volume constraints and the subsequent need for a tailored update scheme. Most studies on multi-material topology optimization either use a total/global volume constraint for all materials (e.g., [10]–[13], [62], [63]), which may lead to issues with linear materials (see Figure 4.2b); or assign an individual

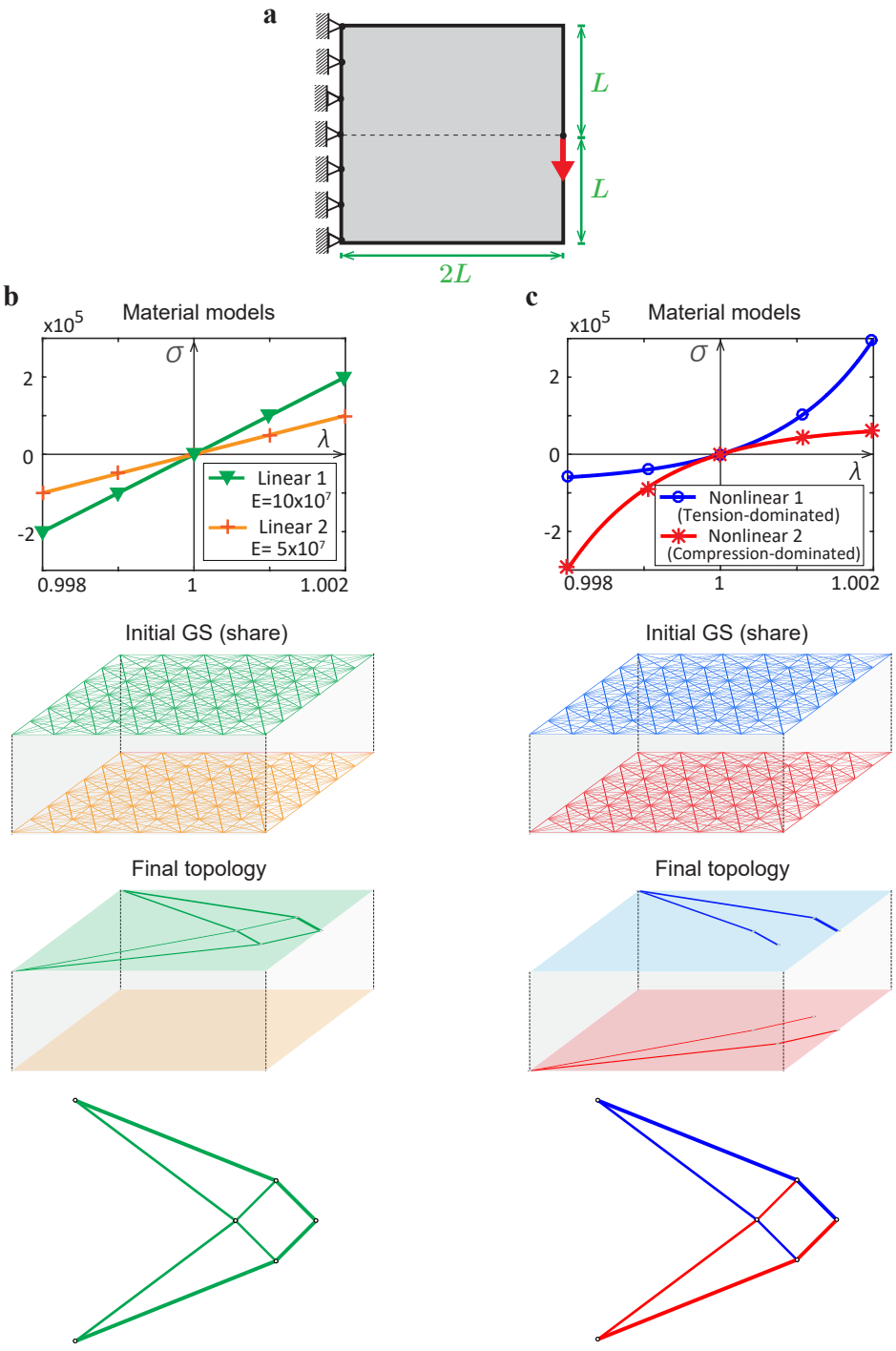


Figure 4.2: Multi-material topology optimization (with one total/global volume constraint): Linear versus nonlinear materials. **a** Design domain; **b** two linear material models, initial material distribution (schematic GSs), and the corresponding optimized structure that favors the stiffer linear material; **c** two nonlinear Ogden-based material models, initial material distribution (schematic GSs), and the corresponding optimized structure that contains both nonlinear materials. (Online version in color.)

volume constraint to each material (e.g., [60], [61], [64], [66], [68], [115], [116]), which may impose higher demands on computational implementations and update schemes. A more general setting, e.g., the combination of both types of constraints for various design scenarios, is rarely considered. In an effort to enable a more general setting of the volume constraints for multi-material topology optimization, an update scheme that handles multiple constraints is naturally needed. Although the Optimality Criteria (OC) method is a robust update scheme for single material topology optimization (see, for example, [31], [70]) , it generally deals with one constraint, and thus, cannot be directly applied into multi-material topology optimization. An OC method that handles multiple constraints is discussed in [121], and an extension of the OC method to handle multiple displacement constraints is presented in [122]; both methods require the calculation of coupled Lagrange multipliers. On the other hand, the multi-material topology optimization literature typically adopts general-purpose update schemes, such as sequential linear programming [60] or the Method of Moving Asymptotes (MMA) [71]. An active-phase algorithm that extends the OC method for multi-material topology optimization is proposed by Tavakoli and Mohseni ([116]). Similar to the Gauss-Seidel and Jacobi iterative optimization methods, the active-phase algorithm arranges the material phases by stiffness and performs sequential binary updates using the OC method. This active-phase algorithm is further studied in the work of [123] and [124] with improved performance. However, the active-phase algorithm only applies to linear material behavior and loses efficiency as the number of candidate materials increases. When nonlinear material behavior is considered in multi-material topology optimization, the sequential binary updates of the active-phase algorithm become challenging with respect to arranging a pre-defined ordering scheme for nonlinear candidate materials. *Therefore, an effective and efficient update method, tailored for multi-material topology optimization with an arbitrary number of volume constraints and capable of handling general nonlinear material behavior, is needed.*

Taking into account the aforementioned limitations, we propose an efficient multi-

material optimization formulation. This formulation incorporates nonlinear material behavior and is designed to account for an arbitrary number of candidate materials with general scenarios of volume constraints. In this study, we present a design update scheme, called ZPR (Zhang-Paulino-Ramos Jr.), that is capable of handling an arbitrary number of volume constraints. This tailored update scheme performs efficient and robust updates of the design variables associated with each volume constraint (in an independent fashion). A comparison between topology optimization considering single and multiple materials is shown in Figure 4.3, which shows various conceptual designs of a long-span bridge by exploring various candidate materials within the proposed topology optimization framework.

If only one linear candidate material (e.g. steel-like) is considered, we always obtain an arch bridge design as shown on the left of Figure 4.3, regardless of the stiffness of the material. However, if we choose to consider two bilinear candidate materials: concrete-like (compression-dominated material) and cable-like (tension-dominated material), the optimal design becomes a suspension bridge, as shown in the middle of Figure 4.3. In another case, if we use three types of candidate materials, a bridge design, which combines the features of both the arch bridge and the suspension bridge, is obtained. This example highlights that the proposed topology optimization framework allows the structural engineers and architects to explore various materials types, as well as material combinations, to come up with innovative designs tailored for the properties and behaviors of the selected materials.

The remainder of the chapter is organized as follows. Section 2 proposes the multi-material topology optimization formulation using the GSM, followed by sensitivity analysis, Karush-Kuhn-Tucker (KKT) conditions, incorporation of a discrete filter, and remarks of the proposed formulation. Section 3 presents the ZPR design update scheme and is followed by its detailed derivation. Section 4 describes selected material nonlinear models and their corresponding strain energy density functions. Section 5 presents numerical examples in two- and three-dimensions, highlighting the properties of the proposed formulation, and

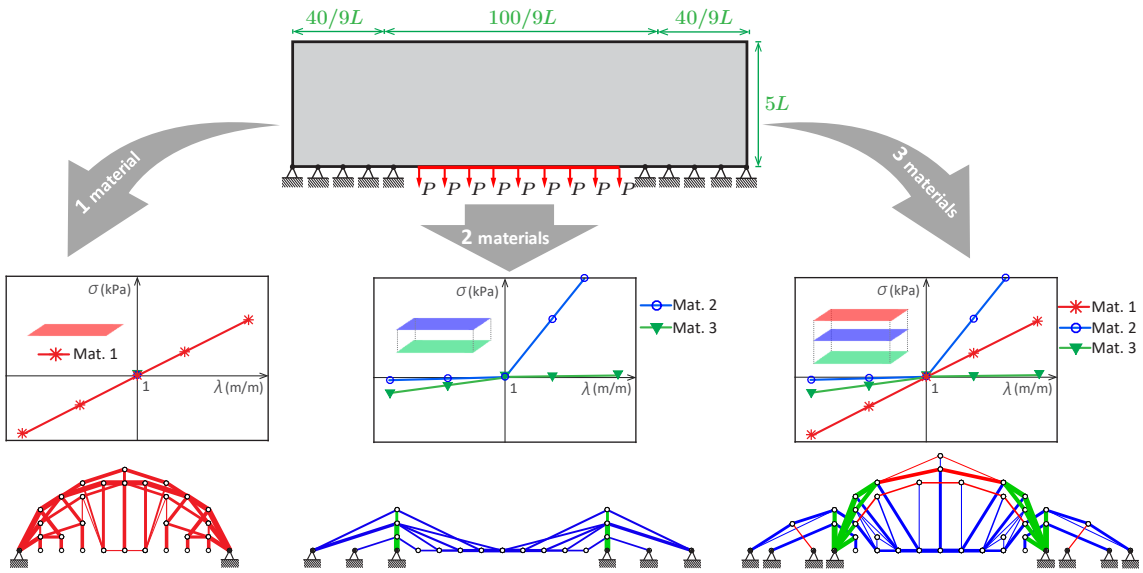


Figure 4.3: Topology optimization of long-span bridge: Single versus multiple materials. Left: single material bridge design; middle: optimized design using two materials; right: optimized design using three materials. (Online version in color.)

Section 6 provides concluding remarks with suggestions for expanding our work.

## 4.2 Multi-Material Topology Optimization

This section introduces the proposed formulation of multi-material topology optimization using the GSM, its sensitivity analysis, the KKT conditions, and the incorporation of the discrete filter. We further provide some remarks on the proposed formulation.

### 4.2.1 Formulation

First, we present the proposed multi-material topology optimization formulation for trusses with the assumption of small deformation. The topology design consists of determining the cross-sectional areas of the truss members using the GSM. Assuming a total of $m$ types of materials, we denote $\boldsymbol{x}_i$ as the design variables (cross-sectional areas of the truss elements) associated with material $i$, where $i = 1, ..., m$ are the material indices. We also assume a total of $nc$ independent volume constraints, where $1 \leq nc \leq m$, and denote $\mathscr{G}^j$ as the set of

material indices associated with the $j$th volume constraint. The proposed formulation of multi-material topology optimization using the GSM is given as

$$\begin{aligned}
\min_{\boldsymbol{x}_1,...,\boldsymbol{x}_m} \; & J(\boldsymbol{x}_1,...,\boldsymbol{x}_m) = \min_{\boldsymbol{x}_1,...,\boldsymbol{x}_m} -\Pi(\boldsymbol{x}_1,...,\boldsymbol{x}_m,\boldsymbol{u}(\boldsymbol{x}_1,...,\boldsymbol{x}_m)) \\
\text{s.t. } & g^j(\boldsymbol{x}_1,...,\boldsymbol{x}_m) = \sum_{i\in\mathscr{G}^j} \boldsymbol{L}_i^{\mathrm{T}}\boldsymbol{x}_i - V_{\max}^j \le 0,\ j=1,...,nc, \\
& x_{\min} \le x_i^{(e)} \le x_{\max},\ i=1,...,m, \text{ and } e=1,...,M_i, \\
\text{with } & \boldsymbol{u}(\boldsymbol{x}_1,...,\boldsymbol{x}_m) = \arg\min_{\boldsymbol{u}} \Pi(\boldsymbol{x}_1,...,\boldsymbol{x}_m,\boldsymbol{u}).
\end{aligned} \tag{4.1}$$

The objective function $J$ is the negative total potential energy of the system in the equilibrium state, where $\Pi$ is the total potential energy of the equilibrated system, and $\boldsymbol{u}(\boldsymbol{x}_1,...,\boldsymbol{x}_m)$ is the equilibrating displacement field (state variable). The term $V_{\max}^j$ is the prescribed upper bound on the total volume associated with the $j$th volume constraint, $g^j$; $x_{\min}$ and $x_{\max}$ are the lower and upper bounds of the design variables; $x_i^{(e)}$ is the cross-sectional area of truss member $e$ with the $i$th material; $\boldsymbol{L}_i$ is the length vector corresponding to the $i$th material; $M_i$ is the number of truss members in the ground structure of the $i$th material. As a demonstration of the notation in the proposed multi-material optimization formulation (4.1), Figure 4.4 and Table 4.1 summarize the parameters for a case with four materials ($m=4,\ M_1=5, M_2=6, M_3=9, M_4=9$) and three volume constraints ($nc=3$, $\mathscr{G}^1=\{1,2\}, \mathscr{G}^2=\{3\}, \mathscr{G}^3=\{4\}$).

The total potential energy of the entire system $\Pi$ is defined as

$$\Pi(\boldsymbol{x}_1,...,\boldsymbol{x}_m,\boldsymbol{u}) = \sum_{i=1}^{m}\sum_{e=1}^{M_i} x_i^{(e)} L_i^{(e)} \Psi_i^{(e)}(\boldsymbol{u}) - \boldsymbol{f}^T\boldsymbol{u}, \tag{4.2}$$

where $L_i^{(e)}$ and $\Psi_i^{(e)}(\boldsymbol{u})$ are the length and strain energy density function of the $e$th member of material $i$, and $\boldsymbol{f}$ is the external force vector. The strain energy density function, $\Psi_i^{(e)}(\boldsymbol{u})$, is assumed to be convex and differentiable for any given $\boldsymbol{u}$. The expressions of $\Psi_i^{(e)}(\boldsymbol{u})$ for Ogden and bilinear materials are described in Section 3.3.1. According to Eq.

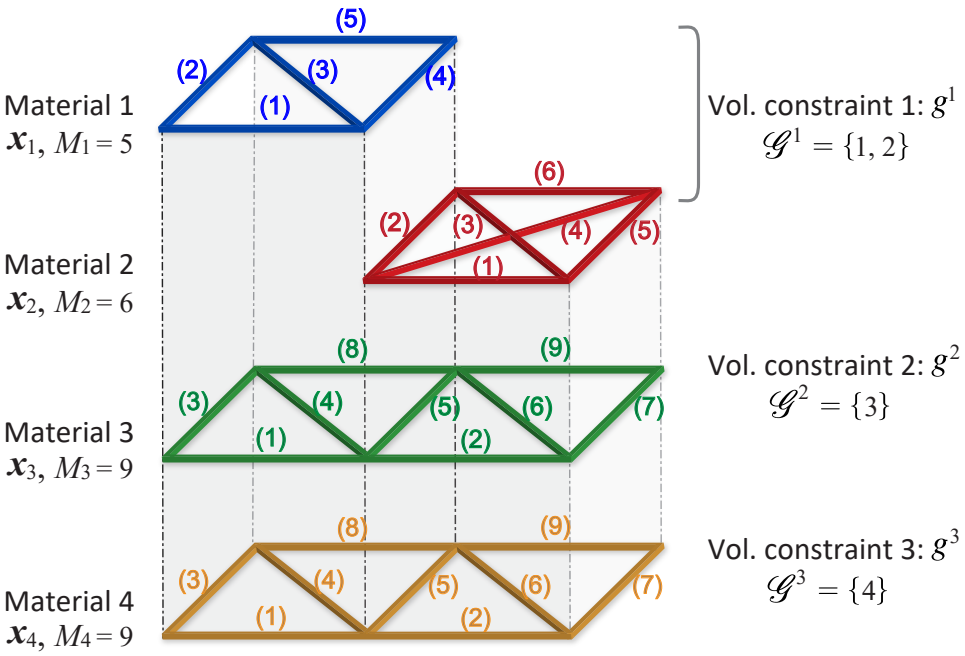


Figure 4.4: Illustration of parameters in multi-material optimization formulation: four materials share & split the design domain ($m = 4$, $M_1 = 5, M_2 = 6, M_3 = 9, M_4 = 9$) with three volume constraints ("Material 1" and "Material 2" share one volume constraint while "Material 3" and "Material 4" have individual constraints, $nc = 3$, $\mathscr{G}^1 = \{1,2\}, \mathscr{G}^2 = \{3\}, \mathscr{G}^3 = \{4\}$). (Online version in color.)

Table 4.1: Illustration of parameters in multi-material optimization formulation (Figure 4.4).

| Materials, $m=4$ | $M_i$ | $\boldsymbol{x}_i=\{x_i^{(e)}\}^T, \quad i=1,...,m, \quad e=1,...,M_i$ |
|---|---|---|
| 1 | $M_1=5$ | $\boldsymbol{x}_1=\{x_1^{(1)},x_1^{(2)},x_1^{(3)},x_1^{(4)},x_1^{(5)}\}^T$ |
| 2 | $M_2=6$ | $\boldsymbol{x}_2=\{x_2^{(1)},x_2^{(2)},x_2^{(3)},x_2^{(4)},x_2^{(5)},x_2^{(6)}\}^T$ |
| 3 | $M_3=9$ | $\boldsymbol{x}_3=\{x_3^{(1)},x_3^{(2)},x_3^{(3)},x_3^{(4)},x_3^{(5)},x_3^{(6)},x_3^{(7)},x_3^{(8)},x_3^{(9)}\}^T$ |
| 4 | $M_4=9$ | $\boldsymbol{x}_4=\{x_4^{(1)},x_4^{(2)},x_4^{(3)},x_4^{(4)},x_4^{(5)},x_4^{(6)},x_4^{(7)},x_4^{(8)},x_4^{(9)}\}^T$ |
| Vol. constraints, $nc=3$ | $\mathscr{G}^j$ | $g^j=\sum_{i\in\mathscr{G}^j}\boldsymbol{L}_i^{\mathrm{T}}\boldsymbol{x}_i-V_{\max}^j\leq 0, \quad j=1,...,nc$ |
| 1 | $\mathscr{G}^1=\{1,2\}$ | $g^1=\boldsymbol{L}_1^{\mathrm{T}}\boldsymbol{x}_1+\boldsymbol{L}_2^{\mathrm{T}}\boldsymbol{x}_2-V_{\max}^1\leq 0$ |
| 2 | $\mathscr{G}^2=\{3\}$ | $g^2=\boldsymbol{L}_3^{\mathrm{T}}\boldsymbol{x}_3-V_{\max}^2\leq 0$ |
| 3 | $\mathscr{G}^3=\{4\}$ | $g^3=\boldsymbol{L}_4^{\mathrm{T}}\boldsymbol{x}_4-V_{\max}^3\leq 0$ |

(4.2), the total potential energy $\Pi$ is interpolated as a linear function of the design variable (after the strain energy density function of each member, $\Psi_i^{(e)}(\boldsymbol{u})$, is obtained through the nonlinear structural analysis). The nonlinear structural equations are solved through Newton-Raphson method, the Tikhonov regularization, and inexact line search. The details of the derivation are referred to Section 3.3.3, 3.3.4, and 3.3.5.

Here, we compute the sensitivity for the above optimization formulation. The sensitivity of the objective function is as follows,

$$\begin{aligned}\frac{\partial J}{\partial x_i^{(e)}}(\boldsymbol{x}_1,...,\boldsymbol{x}_m)=&-\frac{\partial \Pi}{\partial x_i^{(e)}}(\boldsymbol{x}_1,...,\boldsymbol{x}_m,\boldsymbol{u}(\boldsymbol{x}_1,...,\boldsymbol{x}_m))\\&-\left[\frac{\partial \Pi}{\partial \boldsymbol{u}}(\boldsymbol{x}_1,...,\boldsymbol{x}_m,\boldsymbol{u}(\boldsymbol{x}_1,...,\boldsymbol{x}_m))\right]\left[\frac{\partial \boldsymbol{u}}{\partial x_i^{(e)}}(\boldsymbol{x}_1,...,\boldsymbol{x}_m,\boldsymbol{u}(\boldsymbol{x}_1,...,\boldsymbol{x}_m))\right].\end{aligned} \tag{4.3}$$

Under the assumption of global equilibrium, $\boldsymbol{u}$ is the equilibrating displacement field under external load $\boldsymbol{f}$ in the objective function, therefore, the second term on the right-hand-side of Eq. (4.3) vanishes. By using Eq. (4.2) and the fact that the term $\boldsymbol{f}^T\boldsymbol{u}$ is (explicitly)

independent of the design variables, we obtain the sensitivity as

$$\frac{\partial J}{\partial x_i^{(e)}}\left(\boldsymbol{x}_1,...,\boldsymbol{x}_m\right) = -\frac{\partial \Pi}{\partial x_i^{(e)}}\left(\boldsymbol{x}_1,...,\boldsymbol{x}_m,\boldsymbol{u}\left(\boldsymbol{x}_1,...,\boldsymbol{x}_m\right)\right) = -L_i^{(e)}\Psi_i^{(e)}\left(\boldsymbol{u}\left(\boldsymbol{x}_1,...,\boldsymbol{x}_m\right)\right). \quad (4.4)$$

Note that the sensitivity given by Eq. (4.4) is always non-positive because $L_i^{(e)}\Psi_i^{(e)}\left(\boldsymbol{u}\left(\boldsymbol{x}_1,...,\boldsymbol{x}_m\right)\right) \geq 0$, and the computation of sensitivity does not involve an adjoint vector. The sensitivity of the $j$th volume constraint for member $e$ is calculated as

$$\frac{\partial g^j\left(\boldsymbol{x}_1,...,\boldsymbol{x}_m\right)}{\partial x_i^{(e)}} = \begin{cases} L_i^{(e)} & \text{if} \quad i \in \mathscr{G}^j, \\ \\ 0 & \text{otherwise.} \end{cases} \quad (4.5)$$

### 4.2.2 KKT conditions

In this subsection, we show the KKT conditions of the multi-material optimization formulation (4.1). To derive the KKT conditions, the Lagrangian takes the following form by introducing a set of Lagrange multipliers $\overline{\phi}_V^j, j = 1,...,nc$, corresponding to the volume constraints:

$$\overline{\mathscr{L}}\left(\boldsymbol{x}_1,...,\boldsymbol{x}_m,\overline{\phi}_V^1,...,\overline{\phi}_V^{nc}\right) = J\left(\boldsymbol{x}_1,...,\boldsymbol{x}_m\right) + \sum_{j=1}^{nc}\overline{\phi}_V^j\left(\sum_{i\in\mathscr{G}^j}\boldsymbol{L}_i^{\mathrm{T}}\boldsymbol{x}_i - V_{\max}^j\right). \quad (4.6)$$

If we denote $\boldsymbol{x}_1^*,...,\boldsymbol{x}_m^*$ as the optimal solutions of design variables and $\overline{\phi}_V^{1,*},...,\overline{\phi}_V^{nc,*}$ as the corresponding Lagrange multipliers; for any $i \in \mathscr{G}^j, j = 1,...,nc$, we have:

$$\begin{aligned}
\frac{\partial\overline{\mathscr{L}}}{\partial x_i^{(e)}}\left(\boldsymbol{x}_1^*,...,\boldsymbol{x}_m^*,\overline{\phi}_V^{1,*},...,\overline{\phi}_V^{nc,*}\right) &\leq 0, \quad \text{if} \quad x_i^{(e),*} = x_{\max}, & (4.7)\\
\frac{\partial\overline{\mathscr{L}}}{\partial x_i^{(e)}}\left(\boldsymbol{x}_1^*,...,\boldsymbol{x}_m^*,\overline{\phi}_V^{1,*},...,\overline{\phi}_V^{nc,*}\right) &= 0, \quad \text{if} \quad x_{\min} < x_i^{(e),*} < x_{\max}, & (4.8)\\
\frac{\partial\overline{\mathscr{L}}}{\partial x_i^{(e)}}\left(\boldsymbol{x}_1^*,...,\boldsymbol{x}_m^*,\overline{\phi}_V^{1,*},...,\overline{\phi}_V^{nc,*}\right) &\geq 0, \quad \text{if} \quad x_i^{(e),*} = x_{\min}, & (4.9)
\end{aligned}$$

where the derivative of the Lagrangian is given by

$$\frac{\partial \overline{\mathscr{L}}}{\partial x_i^{(e)}}\left(\boldsymbol{x}_1,...,\boldsymbol{x}_m,\overline{\phi}_V^1,...,\overline{\phi}_V^{nc}\right) = -L_i^{(e)}\Psi_i^{(e)}\left(\boldsymbol{u}\left(\boldsymbol{x}_1,...,\boldsymbol{x}_m\right)\right) + \overline{\phi}_V^j L_i^{(e)}, \quad \forall i \in \mathscr{G}^j. \tag{4.10}$$

Combining Eq. (4.10) with Eqs. (4.7) – (4.9), we obtain the KKT conditions for the optimal solution $\left(\boldsymbol{x}_1^*,...,\boldsymbol{x}_m^*,\overline{\phi}_V^{1,*},...,\overline{\phi}_V^{nc,*}\right)$ of the optimization formulation (4.1) as follows (for any $i \in \mathscr{G}^j, j = 1,...,nc$):

$$\Psi_i^{(e)}\left(\boldsymbol{u}\left(\boldsymbol{x}_1^*,...,\boldsymbol{x}_m^*\right)\right) \geq \overline{\phi}_V^{j,*}, \quad \text{if} \quad x_i^{(e),*} = x_{\max}, \tag{4.11}$$

$$\Psi_i^{(e)}\left(\boldsymbol{u}\left(\boldsymbol{x}_1^*,...,\boldsymbol{x}_m^*\right)\right) = \overline{\phi}_V^{j,*}, \quad \text{if} \quad x_{\min} < x_i^{(e),*} < x_{\max}, \tag{4.12}$$

$$\Psi_i^{(e)}\left(\boldsymbol{u}\left(\boldsymbol{x}_1^*,...,\boldsymbol{x}_m^*\right)\right) \leq \overline{\phi}_V^{j,*}, \quad \text{if} \quad x_i^{(e),*} = x_{\min}. \tag{4.13}$$

From Eq. (4.12), we observe that at the optimal design, the strain energy density values for the members (with inactive box constraints) within the same volume constraint are identical (equal to the optimal solution of the associated Lagrange multiplier, $\overline{\phi}_V^{j,*}$), regardless of the material type. This idea is further verified by a numerical example in Section 5.3. For instance, let's assume that "Material 1" and "Material 2" have different material models. If these two materials are assigned to one constraint, the members associated with "Material 1" and "Material 2" in the optimal design should have the same values of strain energy density (even though the material behaviors differ). This observation concerning multi-material topology optimization is analogous to the full-stress design in the linear case with single material [31].

### 4.2.3 Incorporation of the discrete filter into the proposed multi-material formulation

To improve the computational efficiency and define structures that satisfy global equilibrium, we implement the discrete filter [85], [120] into the nonlinear multi-material topology optimization framework in Eq. (4.1). To control the resolution of the topology, the filter parameter $\alpha_f$ is introduced in Eq. (3.5).

We perform the filter operation during the optimization process to remove the information associated with the set of truss members with normalized areas below the filter parameter $\alpha_f$. Therefore, the complete multi-material topology optimization formulation with the discrete filter is as follows:

$$
\begin{aligned}
\min_{\boldsymbol{x}_1,\ldots,\boldsymbol{x}_m} \; & J(\boldsymbol{x}_1,\ldots,\boldsymbol{x}_m) = \min_{\boldsymbol{x}_1,\ldots,\boldsymbol{x}_m} \; -\Pi\left(\overline{\boldsymbol{x}}_1(\boldsymbol{x}_1),\ldots,\overline{\boldsymbol{x}}_m(\boldsymbol{x}_m),\boldsymbol{u}\left(\boldsymbol{x}_1,\ldots,\boldsymbol{x}_m\right)\right) \\
\text{s.t. } & g^j\left(\boldsymbol{x}_1,\ldots,\boldsymbol{x}_m\right) = \sum_{i\in\mathscr{G}^j} \boldsymbol{L}_i^{\mathrm{T}}\overline{\boldsymbol{x}}_i(\boldsymbol{x}_i) - V_{\max}^j \leq 0,\ j=1,\ldots,nc, \\
& 0 \leq x_i^{(e)} \leq x_{\max},\ i=1,\ldots,m, \text{ and } e=1,\ldots,M_i, \\
\text{with } & \boldsymbol{u}\left(\boldsymbol{x}_1,\ldots,\boldsymbol{x}_m\right) = \arg\min_{\boldsymbol{u}} \left\{ \Pi\left(\overline{\boldsymbol{x}}_1(\boldsymbol{x}_1),\ldots,\overline{\boldsymbol{x}}_m(\boldsymbol{x}_m),\boldsymbol{u}\right) + \frac{\Gamma}{2}\boldsymbol{u}^{\mathrm{T}}\boldsymbol{u} \right\}, \\
& \overline{x}_i^{(e)} = Filter\left(\boldsymbol{x}_i,\alpha_f,e\right),\ i=1,\ldots,m, \text{ and } e=1,\ldots,M_i,
\end{aligned}
\tag{4.14}
$$

where $\overline{\boldsymbol{x}}_i$ denotes the filtered design variables associated with the $i$th material. In formulation (4.14), the lower bound is taken as $x_{\min} = 0$ to account for the removal of members, which transforms the sizing problem in (4.1) into a topology optimization problem. A Tikhonov regularization term $\frac{\Gamma}{2}\boldsymbol{u}^{\mathrm{T}}\boldsymbol{u}$ is added to the total potential energy in the state equation to prevent singular stiffness matrices [85], [101]–[103].

### 4.2.4 Remarks

The properties of the proposed multi-material topology optimization framework relate to several aspects. *First,* the optimization formulations in Eqs. (4.1) and (4.14) are capable of handling a general number of materials. The constitutive relationship of each material is flexible (e.g., linear, bilinear, or nonlinear). For example, we can obtain a variety of materials by changing the parameters of the Ogden-based model (see Section 4). *Second,* the specific choice of the material model is independent for each material. For instance, we can use an Ogden-based model for certain material layers and a bilinear model for others. *Third,* in the optimization formulation, the assignment of volume constraints for multiple materi-

als contains general scenarios, meaning that the number of volume constraints satisfies the relation $1 \leq nc \leq m$. As a demonstration, Table 4.2 summarizes three possible combinations of volume constraints if three materials ($m = 3$) are used in the optimization problem. Figure 4.5 shows the three representative scenarios of the volume constraint assignment, i.e., sharing (Figure 4.5c), splitting (Figure 4.5d), and a combination of sharing & splitting (Figure 4.5e). The case of assigning a total/global volume constraint to all materials corresponds to $nc = 1$ and $\mathscr{G}^1 = \{1,2,3\}$ (Figure 4.5c), and the case of assigning individual volume constraint to each material corresponds to $nc = m = 3, \mathscr{G}^1 = \{1\}, \mathscr{G}^2 = \{2\}, \mathscr{G}^3 = \{3\}$ (Figure 4.5d). To handle an arbitrary number of volume constraints, we propose a design update scheme in Section 3. This update scheme performs efficient and robust updates of the design variables associated with each volume constraint in an independent fashion.

Table 4.2: Three possible combinations of volume constraints for three materials

| Materials | Scenarios of volume constraints | | |
|---|---|---|---|
| | (Figure 4.5c) | (Figure 4.5d) | (Figure 4.5e) |
| 1 | $V^1_{\max}$ | $V^1_{\max}$ | $V^1_{\max}$ |
| 2 | | $V^2_{\max}$ | $V^2_{\max}$ |
| 3 | | $V^3_{\max}$ | |

### 4.3 The ZPR Design Update Scheme

In this section, we present the ZPR (zipper, phonetically) design update scheme. In the proposed multi-material formulations in Eqs. (4.1) and (4.14), we have multiple ($nc$) volume constraints. Accordingly, we need an update scheme that can handle multiple constraints. The standard OC method is a robust and efficient update scheme for single material topology optimization, however, it only handles a single volume constraint. Consequently, the OC method cannot be directly applied to the proposed multi-material formulations in Eqs. (4.1) and (4.14), unless only one volume constraint is used, i.e., $nc = 1$. To address such limitation, we present the ZPR design update scheme, which is capable of handling an arbitrary number of volume constraints while preserving the efficiency and effectiveness of

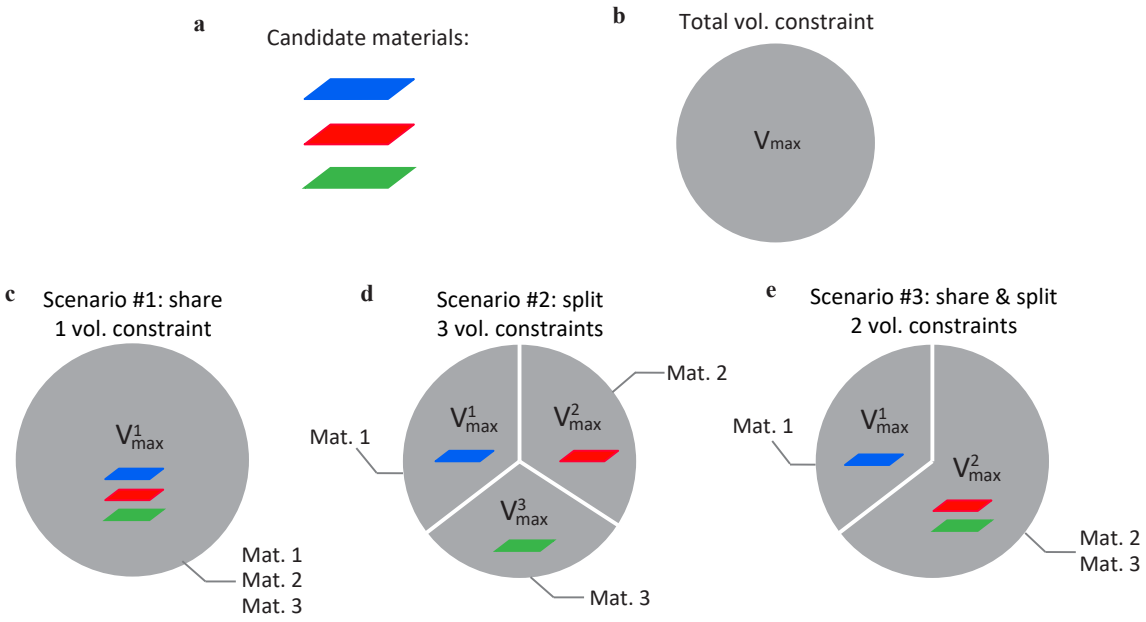


Figure 4.5: Potential combination of volume constraints: **a** Candidate materials; **b** total volume constraint, $V_{\max}$; **c** Scenario #1: three materials share the (single) total volume constraint, $nc = 1$, $\mathscr{G}^1 = \{1,2,3\}$; **d** Scenario #2: three materials split the total volume constraint, (i.e., each material is associated with an individual constraint, $nc = 3$, $\mathscr{G}^1 = \{1\}, \mathscr{G}^2 = \{2\}, \mathscr{G}^3 = \{3\}$); **e** Scenario #3: three materials share & split the volume constraint (i.e., "Material 1" has an individual constraint while both "Material 2" and "Material 3" share another volume constraint, $nc = 2$, $\mathscr{G}^1 = \{1\}, \mathscr{G}^2 = \{2,3\}$). (Online version in color.)

the standard OC method. The proposed ZPR design update scheme allows for the separation and independent updating of design variables associated with each volume constraint. In computational implementations, the ZPR update scheme loops over the set of volume constraints. For the $j$th volume constraint, only the associated design variables are updated by using the Lagrange multiplier associated with the $j$th volume constraint.

In the remainder of this section, we present the derivation of the ZPR design update scheme for the proposed optimization formulation in Eq. (4.1) containing an arbitrary number of volume constraints ($nc$). The first step of the derivation is to perform an explicit convex approximation of the objective at each optimization step [31]. In this convex approximation, we first introduce a set of intervening variables $\boldsymbol{y}_i(\boldsymbol{x}_i)$ such that $y_i^{(e)}(x_i^{(e)}) = (x_i^{(e)})^{-\alpha}$, $i = 1,...,m$, and $e = 1,...,M_i$, where $\alpha$ is an arbitrary and strictly positive number. At the $k$th optimization step, we then approximate the objective function as a linear function of $\boldsymbol{y}_i$ as follows:

$$\begin{aligned} J(\boldsymbol{x}_1,...,\boldsymbol{x}_m) &\approx J^k(\boldsymbol{x}_1,...,\boldsymbol{x}_m) = J\left(\boldsymbol{x}_1^k,...,\boldsymbol{x}_m^k\right) + \sum_{i=1}^{m}\left[\frac{\partial J}{\partial \boldsymbol{y}_i}(\boldsymbol{x}_1^k,...,\boldsymbol{x}_m^k)\right]^T\left[\boldsymbol{y}_i(\boldsymbol{x}_i) - \boldsymbol{y}_i(\boldsymbol{x}_i^k)\right] \\ &= J\left(\boldsymbol{x}_1^k,...,\boldsymbol{x}_m^k\right) + \sum_{i=1}^{m}\left[\boldsymbol{b}_i(\boldsymbol{x}_1^k,...,\boldsymbol{x}_m^k)\right]^T\left[\boldsymbol{y}_i(\boldsymbol{x}_i) - \boldsymbol{y}_i(\boldsymbol{x}_i^k)\right], \end{aligned} \tag{4.15}$$

where $\boldsymbol{x}_i^k$ and $\boldsymbol{y}_i(\boldsymbol{x}_i^k)$ are the design and intervening variables, respectively, at the $k$th optimization step of material $i$. Notice that for a given optimization step $k$, the vector $\boldsymbol{b}_i(\boldsymbol{x}_1^k,...,\boldsymbol{x}_m^k)$ is a constant vector whose component $(e)$ is given by

$$b_i^{(e)}(\boldsymbol{x}_1^k,...,\boldsymbol{x}_m^k) = \frac{\partial J}{\partial y_i^{(e)}}(\boldsymbol{x}_1^k,...,\boldsymbol{x}_m^k) = -\frac{(x_i^{(e),k})^{1+\alpha}}{\alpha}\frac{\partial J}{\partial x_i^{(e)}}(\boldsymbol{x}_1^k,...,\boldsymbol{x}_m^k), \tag{4.16}$$

where $\partial J/\partial x_i^{(e)}(\boldsymbol{x}_1^k,...,\boldsymbol{x}_m^k)$ is the $e$th component of the sensitivity vector of the $i$th material at step $k$. Therefore, the approximated subproblem of the original problem at the $k$th step

is given by

$$\begin{aligned}
\min_{\boldsymbol{x}_1,...,\boldsymbol{x}_m} \; & J^k(\boldsymbol{x}_1,...,\boldsymbol{x}_m) = \min_{\boldsymbol{x}_1,...,\boldsymbol{x}_m} \sum_{i=1}^{m} \left[\boldsymbol{b}_i(\boldsymbol{x}_1^k,...,\boldsymbol{x}_m^k)\right]^T \boldsymbol{y}_i(\boldsymbol{x}_i) \\
\text{s.t.} \; & \sum_{i\in\mathscr{G}^j} \boldsymbol{L}_i^{\mathrm{T}}\boldsymbol{x}_i - V_{\max}^j \le 0, \; j=1,...,nc, \\
& x_{i,\mathrm{L}}^{(e),k} \le x_i^{(e)} \le x_{i,\mathrm{U}}^{(e),k}, \; i=1,...,m, \text{ and } e=1,...,M_i, \\
& \text{with } y_i^{(e)}(x_i^{(e)}) = (x_i^{(e)})^{-\alpha}, \; i=1,...,m, \text{ and } e=1,...,M_i,
\end{aligned} \tag{4.17}$$

where $x_{i,\mathrm{L}}^{(e),k} = \max(x_{\min}, x_i^{(e),k} - move)$ and $x_{i,\mathrm{U}}^{(e),k} = \min(x_{\max}, x_i^{(e),k} + move)$ are the lower and upper bounds of the design variables in the subproblem, and *move* is the prescribed move limit. In vector notation, the lower and upper bounds are denoted as $\boldsymbol{x}_{i,\mathrm{L}}^k$ and $\boldsymbol{x}_{i,\mathrm{U}}^k$. When we introduce a set of Lagrange multipliers $\phi_V^j$ for each volume constraint, the above Lagrangian function of the subproblem in Eq. (4.17) takes the form

$$\begin{aligned}
\mathscr{L}^k\left(\boldsymbol{x}_1,...,\boldsymbol{x}_m,\phi_V^1,...,\phi_V^{nc}\right) &= \sum_{i=1}^{m}\left[\boldsymbol{b}_i(\boldsymbol{x}_1^k,...,\boldsymbol{x}_m^k)\right]^T \boldsymbol{y}_i(\boldsymbol{x}_i) + \sum_{j=1}^{nc}\phi_V^j\left(\sum_{i\in\mathscr{G}^j}\boldsymbol{L}_i^{\mathrm{T}}\boldsymbol{x}_i - V_{\max}^j\right) \\
&= \sum_{j=1}^{nc}\left\{\sum_{i\in\mathscr{G}^j}\left[\left[\boldsymbol{b}_i(\boldsymbol{x}_1^k,...,\boldsymbol{x}_m^k)\right]^T \boldsymbol{y}_i(\boldsymbol{x}_i) + \phi_V^j\boldsymbol{L}_i^{\mathrm{T}}\boldsymbol{x}_i\right]\right. \\
&\quad \left. -\phi_V^j V_{\max}^j\right\}.
\end{aligned} \tag{4.18}$$

The dual objective function is given by

$$\begin{aligned}
\mathscr{D}^k\left(\phi_V^1,...,\phi_V^{nc}\right) &= \min_{\boldsymbol{x}_{1,\mathrm{L}}^k\le\boldsymbol{x}_1\le\boldsymbol{x}_{1,\mathrm{U}}^k,...,\boldsymbol{x}_{m,\mathrm{L}}^k\le\boldsymbol{x}_m\le\boldsymbol{x}_{m,\mathrm{U}}^k} \mathscr{L}^k\left(\boldsymbol{x}_1,...,\boldsymbol{x}_m,\phi_V^1,...,\phi_V^{nc}\right) \\
&= \sum_{j=1}^{nc}\left\{\min_{\boldsymbol{x}_{i,\mathrm{L}}^k\le\boldsymbol{x}_{i\in\mathscr{G}^j}\le\boldsymbol{x}_{i,\mathrm{U}}^k}\sum_{i\in\mathscr{G}^j}\left[\left[\boldsymbol{b}_i(\boldsymbol{x}_1^k,...,\boldsymbol{x}_m^k)\right]^T \boldsymbol{y}_i(\boldsymbol{x}_i) + \phi_V^j\boldsymbol{L}_i^{\mathrm{T}}\boldsymbol{x}_i\right]\right. \\
&\quad \left. -\phi_V^j V_{\max}^j\right\}.
\end{aligned} \tag{4.19}$$

Notice that the dual objective function has a clear separable structure and thus can be recast

as $\mathscr{D}^k(\phi_V^1,...,\phi_V^{nc}) = \sum_{j=1}^{nc} \mathscr{D}^{j,k}(\phi_V^j)$, where $\mathscr{D}^{j,k}(\phi_V^j)$ has the form

$$\mathscr{D}^{j,k}\left(\phi_V^j\right) = \min_{\boldsymbol{x}_{i,\mathrm{L}}^k \le \boldsymbol{x}_{i\in\mathscr{G}^j} \le \boldsymbol{x}_{i,\mathrm{U}}^k} \sum_{i\in\mathscr{G}^j} \left\{ \left[\boldsymbol{b}_i(\boldsymbol{x}_1^k,...,\boldsymbol{x}_m^k)\right]^T \boldsymbol{y}_i(\boldsymbol{x}_i) + \phi_V^j \boldsymbol{L}_i^{\mathrm{T}} \boldsymbol{x}_i \right\} - \phi_V^j V_{\max}^j. \quad (4.20)$$

The optimality condition of the first term on the right-hand-side of Eq. (4.20) takes the form

$$\begin{aligned} &\frac{\partial \left\{ \left[\boldsymbol{b}_i(\boldsymbol{x}_1^k,...,\boldsymbol{x}_m^k)\right]^T \boldsymbol{y}_i(\boldsymbol{x}_i) + \phi_V^j \boldsymbol{L}_i^{\mathrm{T}} \boldsymbol{x}_i \right\}}{\partial x_i^{(e)}} \\ =& -\alpha b_i^{(e)}(\boldsymbol{x}_1^k,...,\boldsymbol{x}_m^k) \left(x_i^{(e)}\right)^{(-\alpha-1)} + \phi_V^j L_i^{(e)} = 0, \quad \forall i \in \mathscr{G}^j, \end{aligned} \quad (4.21)$$

which gives

$$x_i^{(e)*} = Q_i^{(e),k}\left(\phi_V^j\right) = \left[\frac{\alpha b_i^{(e)}(\boldsymbol{x}_1^k,...,\boldsymbol{x}_m^k)}{\phi_V^j L_i^{(e)}}\right]^{\frac{1}{1+\alpha}}, \quad \forall i \in \mathscr{G}^j. \quad (4.22)$$

Having obtained $x_i^{(e)*}$, we then check if the assumption that it is within the interval $[x_{i,L}^{(e),k}, x_{i,U}^{(e),k}]$ holds. The final form of the primal-dual relationship is given by

$$\begin{aligned} x_i^{(e)*} =& Q_i^{(e),k}\left(\phi_V^j\right) \\ =& \begin{cases} x_{i,\mathrm{L}}^{(e),k} & \text{if } \left[\frac{\alpha b_i^{(e)}(\boldsymbol{x}_1^k,...,\boldsymbol{x}_m^k)}{\phi_V^j L_i^{(e)}}\right]^{\frac{1}{1+\alpha}} < x_{i,\mathrm{L}}^{(e),k} \\ \left[\frac{\alpha b_i^{(e)}(\boldsymbol{x}_1^k,...,\boldsymbol{x}_m^k)}{\phi_V^j L_i^{(e)}}\right]^{\frac{1}{1+\alpha}} & \text{if } x_{i,\mathrm{L}}^{(e),k} \le \left[\frac{\alpha b_i^{(e)}(\boldsymbol{x}_1^k,...,\boldsymbol{x}_m^k)}{\phi_V^j L_i^{(e)}}\right]^{\frac{1}{1+\alpha}} \le x_{i,\mathrm{U}}^{(e),k} \\ x_{i,\mathrm{U}}^{(e),k} & \text{if } \left[\frac{\alpha b_i^{(e)}(\boldsymbol{x}_1^k,...,\boldsymbol{x}_m^k)}{\phi_V^j L_i^{(e)}}\right]^{\frac{1}{1+\alpha}} > x_{i,\mathrm{U}}^{(e),k} \end{cases} \quad ,\forall i \in \mathscr{G}^j. \end{aligned} \quad (4.23)$$

Inserting the above primal-dual relation into the dual function, we obtain the dual problem:

$$\max_{\phi_V^1,...,\phi_V^{nc}} \mathscr{D}^k\left(\phi_V^1,...,\phi_V^{nc}\right) = \sum_{j=1}^{nc} \max_{\phi_V^j} \mathscr{D}^{j,k}\left(\phi_V^j\right). \quad (4.24)$$

Notice that the dual objective function is also separable, and the stationary condition with

respect to $\phi_V^j$ yields:

$$\frac{\partial \mathscr{D}^k}{\partial \phi_V^j} = \sum_{i \in \mathscr{G}^j} \sum_{e=1}^{M_i} L_i^{(e)} x_i^{(e)*} \left( \phi_V^j \right) - V_{\max}^j = 0. \tag{4.25}$$

Observe that the above equation is a monotonic algebraic equation of $\phi_V^j$ [31], and thus can be solved by various algorithms, such as the bisection method. In addition, the calculation of the Lagrange multipliers can be done independently. We hereby denote $\phi_V^{j*}$ as the solution to the $j$th of Eq. (4.25). The update of the $e$th component of the design variables then takes the form:

$$x_i^{(e),k+1} = Q_i^{(e),k} \left( \phi_V^{j*} \right), \quad \forall i \in \mathscr{G}^j. \tag{4.26}$$

By plugging in the sensitivity information (Eq. (4.4)), a simplified expression for the design variable update of the ZPR update scheme can be obtained as

$$x_i^{(e),k+1} = \begin{cases} x_{i,\mathrm{L}}^{(e),k} & \text{if } \left[ \frac{\Psi_i^{(e)}(\boldsymbol{u}(\boldsymbol{x}_1^k,\ldots,\boldsymbol{x}_m^k))}{\phi_V^{j*}} \right]^\eta x_i^{(e),k} < x_{i,\mathrm{L}}^{(e),k} \\ \left[ \frac{\Psi_i^{(e)}(\boldsymbol{u}(\boldsymbol{x}_1^k,\ldots,\boldsymbol{x}_m^k))}{\phi_V^{j*}} \right]^\eta x_i^{(e),k} & \text{if } x_{i,\mathrm{L}}^{(e),k} \leq \left[ \frac{\Psi_i^{(e)}(\boldsymbol{u}(\boldsymbol{x}_1^k,\ldots,\boldsymbol{x}_m^k))}{\phi_V^{j*}} \right]^\eta x_i^{(e),k} \leq x_{i,\mathrm{U}}^{(e),k} \\ x_{i,\mathrm{U}}^{(e),k} & \text{if } \left[ \frac{\Psi_i^{(e)}(\boldsymbol{u}(\boldsymbol{x}_1^k,\ldots,\boldsymbol{x}_m^k))}{\phi_V^{j*}} \right]^\eta x_i^{(e),k} > x_{i,\mathrm{U}}^{(e),k} \end{cases}, \forall i \in \mathscr{G}^j. \tag{4.27}$$

In the above expression, the parameter $\eta$ is introduced as $\eta = 1/(1+\alpha)$, which is commonly referred as the damping factor. It can be either constant (e.g. [31]) or adaptive ([70]).

*We remark that from Eqs.* (4.26) *and* (4.27)*, the update of the design variable depends only on the Lagrange multiplier of the corresponding volume constraint.* Therefore, in the case of multiple volume constraints, the design variables associated with each volume constraint can be updated independently. Note that because the update of design variables in each volume constraint is independent, the update can be done either in sequence or in parallel. The procedure of multi-material topology optimization with the ZPR design update scheme using sequential updates is illustrated in Algorithm 2.

**Algorithm 2** Multi-material topology optimization with the ZPR design update scheme

**Initialize:** $\boldsymbol{x}_1^0,...,\boldsymbol{x}_m^0$, $\text{iter}_{\max}$, $\tau_{\text{opt}}$
**for** $k = 0,1,...,\text{iter}_{\max}$ **do**
  Solve: $\boldsymbol{u}\left(\boldsymbol{x}_1^k,...,\boldsymbol{x}_m^k\right) = \arg\min_{\boldsymbol{u}}\left[\Pi\left(\boldsymbol{x}_1^k,...,\boldsymbol{x}_m^k,\boldsymbol{u}\right)\right]$
  Compute: $J\left(\boldsymbol{x}_1^k,...,\boldsymbol{x}_m^k\right)$, $g^j\left(\boldsymbol{x}_1^k,...,\boldsymbol{x}_m^k\right)$, $\partial J\left(\boldsymbol{x}_1^k,...,\boldsymbol{x}_m^k\right)/\partial x_i^{(e)}$,
    and $\partial g^j\left(\boldsymbol{x}_1^k,...,\boldsymbol{x}_m^k\right)/\partial x_i^{(e)}$
  **for** $j = 1,2,...,nc$ **do**
    Compute $\phi_{V*}^j$ by solving Eq. (4.25)
    Update $x_i^{(e),k+1} = Q_i^{(e),k}\left(\phi_V^{j*}\right), \quad \forall i \in \mathscr{G}^j$ according to Eq. (4.27)
  **end for**
  **if** $\max\left(||\boldsymbol{x}_1^{k+1}-\boldsymbol{x}_1^k||_\infty,...,||\boldsymbol{x}_m^{k+1}-\boldsymbol{x}_m^k||_\infty\right) < \tau_{\text{opt}}$ **then**
    quit
  **end if**
**end for**
Remove aligned nodes
Plot final topology

### 4.4 Material Nonlinear Models

In this section, we briefly review the theory of hyperelastic constitutive models on which the structural analysis part of the chapter is based. For details of the derivation, readers are referred to the studies by [84], [120]. For the kinematics and constitutive models, we assume small deformation kinematics and nonlinear constitutive relationships. We compute the linearized stretch $\lambda$ for the truss element in Eq. (3.21).

We account for nonlinear constitutive relationships by using the energy density function based on [106], which allows for various materials to be represented and has the capability to reproduce a variety of hyperelastic models. The strain energy density function and tangent modulus for this hyperelastic Ogden material is expressed in Eqs. (3.25) and (3.26). The tangent modulus (in an undeformed state) reduces to Young's modulus in linear elasticity, as shown in Eq. (3.27).

Note that the material model is convex, i.e., $\hat{\Psi}_{OG}(\lambda)$ is convex for $\lambda > 0$, if the parameters satisfy the following conditions: $\beta_1 \geq 1$, $\beta_2 \leq 1$, $\beta_1 \neq \beta_2$, $\gamma_1 > 0$, and subsequently

$E_T > 0$ ($\mathrm{d}\sigma_{OG}(\lambda)/\mathrm{d}\lambda > 0$). The stress-stretch relationship of the Ogden model is expressed Eq. (3.30). By varying the set of parameters $(\beta_1, \beta_2)$, as shown in Figure 3.5a, this Ogden-based model generates a variety of material behaviors.

Another constitutive model used in this chapter is the bilinear material. The bilinear constitutive model has a kink at the origin (see Figure 3.5b). To treat this class of nonsmooth problems, we refer the reader to [107]. Using the same format of the Ogden-based model to describe the bilinear model, the energy density function and stress are in Eqs. (3.31) and (3.32). Note that this bilinear material model is always convex as $\mathrm{d}\sigma_{\mathrm{Bi}}(\lambda)/\mathrm{d}\lambda \geq 0$.

## 4.5 Numerical Examples

In this section, we provide several numerical examples to demonstrate the proposed multi-material topology optimization using the GSM. Example 1 verifies the proposed multi-material methodology by comparing the results obtained from the proposed scheme with the results obtained from the single material topology optimization. Example 2 compares different combinations of initial material distributions and their optimized results. Example 3 demonstrates combinations of volume constraints and their optimized results. The last example considers multiple load cases and illustrates the application of the proposed multi-material formulation to a 3D crane design using a combination of various material models and general volume constraint setting.

We generate the initial ground structures without overlapped members in each material layer using the collision zone technique by [112], [113] and plot final topologies in 3D using the program GRAND3 [113]. It is worth noting that we do not verify the stability of members. For studies that address stability issues, readers are referred to [35], [36], [125]–[127]. The ground structure method without stability constraints may lead to structures with aligned nodes, i.e., hinges connecting two collinear members. The procedure for removing aligned nodes consists of identifying the nodes that connect only two

collinear members (except those nodes connecting to load or displacement boundary conditions). Then we remove the aligned node by replacing two collinear members with one long member that takes the larger (or equal) area from the two. Therefore, the resulting objective value decreases (or remains unchanged). For all GSM results, we remove aligned nodes and floating members and check the final topologies to ensure that they are at global equilibrium. A detailed explanation can be found in the references [120], [128]. The nonlinear solution scheme is based on a Newton-Raphson approach with line search (see [120] for a detailed explanation). For all the examples, the discrete filter is used to obtain valid structures and improve computational efficiency (see Section 4.2.3). We use the filter value $\alpha_f = 10^{-4}$ during the optimization process, and the filter operation is performed at every optimization step. Consistent units are implied throughout, and all the examples have initial tangent modulus, $E_0 = 7 \times 10^7 kPa$; stopping criterion: $\tau_{\text{opt}} = 10^{-9}$; move value: $move = 10^4 x^0$, where $x^0$ is the initial guess of the design variables; and initial damping factor for the ZPR design update scheme: $\eta = 0.5$. Subsequent damping factors are updated according to the scheme provided by [70]. The upper bound for the design variable is defined by $x_{\max} = 10^4 x^0$. *All of our examples are solved by the ZPR design update scheme proposed in Section 3.* The examples are summarized in Table 4.3.

### 4.5.1 Verification of the multi-material topology optimization framework

The first example verifies the proposed multi-material methodology and the ZPR design update scheme by comparing the results obtained from the proposed formulation (using two bilinear materials) with the results obtained from the standard GSM using a single (bilinear) material. We use a 2D box domain, discretized by a $30 \times 10$ grid. The geometry ($L = 10m$), load ($P = 100kN$), and support conditions (two fixed supports) are shown in Figure 4.6. The total prescribed maximum volume takes the following value, $V_{\max} = 0.15m^3$.

For the single material case, using a level-10 initial ground structure with 19,632 non-overlapped members and 341 nodes, we perform optimization with a bilinear material ($E_t =$

Table 4.3: Brief description of the numerical examples.

| Example | Dimension | Material model | Description | Feature |
|---|---|---|---|---|
| 1 | 2D | 2 bilinear | Opposite loads in a simply supported rectangular domain | Verification |
| 2 | 2D | 4 Ogden based | Opposite loads in a simply supported rectangular domain | Influence of initial material distributions |
| 3 | 2D | 2 bilinear and 1 linear | Long-span bridge design | Generality of formulation including combinations of volume constraints |
| 4 | 3D | 2 Ogden based and 1 linear | Crane design subjected to multiple load cases | Potentially translational design: from academia to structural engineering practice |

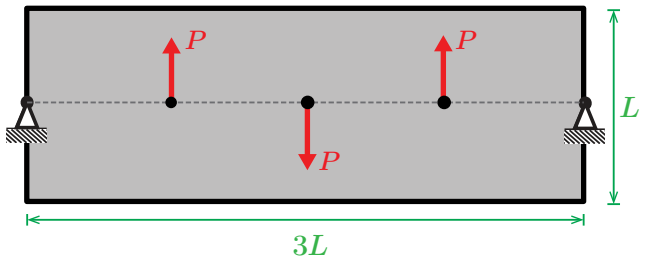


Figure 4.6: Example 1: geometry ($L = 10m$), load ($P = 100kN$), and boundary conditions. The domain is discretized using a $30 \times 10$ grid.

$7E$ and $E_c = 2E$, $E = 10^7 kPa$). For the two multi-material cases, two materials share the entire domain. Hence, we use two layers of level-10 initial ground structures (one for each material) with 39,264 members (truss members within each material layer are not overlapped), 341 nodes, and two bilinear materials ($E_{t1} = 7E$, $E_{c1} = 0$ and $E_{t2} = 0$, $E_{c2} = 2E$). The combination of these two materials is designed to reproduce the results from the single material case. For multi-material cases, two scenarios of assignments for volume constraints are used. In one scenario, two materials are assigned to one total volume

constraint ($nc = 1$), i.e., $V_{\max}^1 = V_{\max}$; in another scenario, each material is assigned to an individual volume constraint ($nc = 2$), i.e., $V_{\max}^j = 0.5V_{\max},\ j = 1,2$. Note that in all single and multiple materials cases, the prescribed maximum volume, $V_{\max}$, is the same. The initial ground structures, material models, and optimized structures obtained using one bilinear material and two bilinear materials are shown in Figures 4.7 and 4.8, respectively. The associated numerical information is summarized in Table 4.4.

The multi-material formulation with one volume constraint (Figure 4.8c) yields a structure and an optimal objective value identical to those obtained using the single material formulation (Figure 4.7c). This comparison verifies the proposed formulation and the ZPR design update scheme. In addition, for the case that two materials share the entire domain and are assigned to one volume constraint, the optimizer assigns materials to appropriate locations with proper amounts according to each material's property. For the case with two constraints (Figure 4.8d), the optimized structure differs from the one volume constraint case (Figure 4.8c) and has a slightly (3.7%) higher objective value.

Table 4.4: Numerical information for Example 1 (Figures 4.6, 4.7, and 4.8), $E = 10^7 kPa$.

| 2D cases | $J(\boldsymbol{x}_i^*)$ | Material | | Volume | Final | # |
|---|---|---|---|---|---|---|
| | $(kN \cdot m)$ | $E_t$ | $E_c$ | constraint, $V_{\max}^j$ | $V_{\text{frac}}$ | Elements |
| 1 material | 1.136 | $7E$ | $2E$ | $V_{\max}$ | 1.00 | 48 |
| 2 materials | 1.136 | $7E$ | 0 | $V_{\max}$ | 0.63 | 25 |
| (1 vol. constraint) | | 0 | $2E$ | | 0.37 | 19 |
| 2 materials | 1.179 | $7E$ | 0 | $0.5V_{\max}$ | 0.5 | 42 |
| (2 vol. constraints) | | 0 | $2E$ | $0.5V_{\max}$ | 0.5 | 33 |

### 4.5.2 Opposite loads in a simply supported rectangular domain

In the second example, we demonstrate the different scenarios of initial material distributions using four Ogden-based materials in the proposed methodology and compare their optimized results. The design domain with load and boundary conditions ($L = 10m, P =$

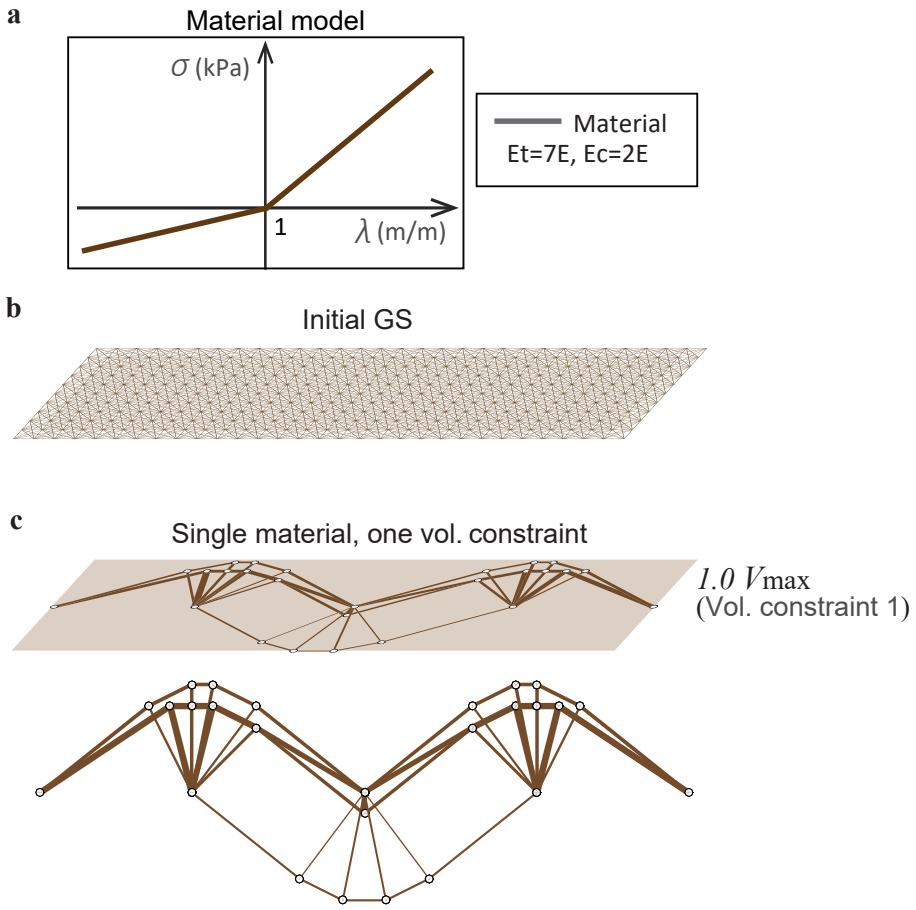


Figure 4.7: Example 1: single material topology optimization. **a** The material model of one bilinear material; **b** the initial level-10 (schematic) GS; **c** the corresponding optimized structure (cf. Figure 4.8c). (Online version in color.)

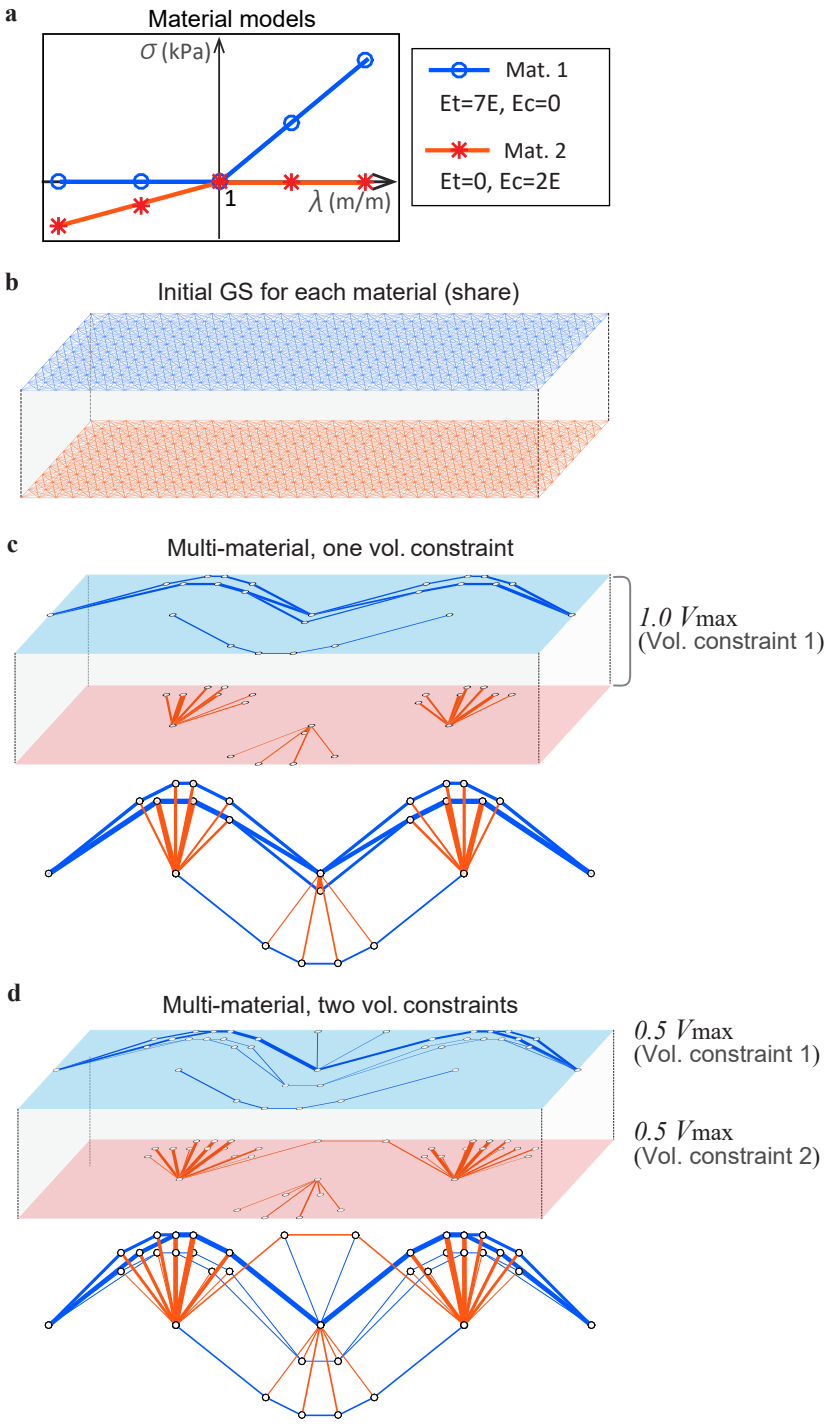


Figure 4.8: Example 1: multi-material topology optimization. **a** Material models of two bilinear materials; **b** two layers of identical initial level-10 (schematic) GSs; **c** the optimized structure of two bilinear materials with one total volume constraint (cf. Figure 4.7c); **d** the optimized structure of two bilinear materials with two individual volume constraints. (Online version in color.)

$1000kN$) and material models are shown in Figures 4.9a and 4.9b. We compare two scenarios of initial material distributions. In the first scenario, four materials share & split the domain (Figure 4.9c), resulting 55,818 members and 341 nodes. The total prescribed maximum volume takes the following value, $V_{\max} = 0.15m^3$. Each material is associated with an individual volume constraint ($nc = 4$), as shown in Table 4.5. The initial GS for each material and the corresponding optimized structures are shown in Figure 4.9c. The multi-material framework with materials sharing & splitting the domain leads to a structure without overlapping members (selecting at most one material for each subdomain). In the final design without any overlapping members, the values of strain energy density of all the truss members for the same material are identical [84], [120].

In the second scenario, four materials share the entire domain (Figure 4.9d). Four layers (one for each material) of identical level-10 initial ground structures (based on a $30 \times 10$ grid) with a total of 78,528 members and 341 nodes are used. Similar to the first scenario, the total prescribed maximum volume takes the value, $V_{\max} = 0.15m^3$, and each material is associated with an individual volume constraint ($nc = 4$), see Table 4.5. The initial GSs for the second scenario and the corresponding optimized structures are shown in Figure 4.9d. The associated numerical information is summarized in Table 4.5. In the optimized structure, we observe that the selection of more than one material for some truss members (i.e., overlapping of truss members from different materials) occurs when materials share the entire domain. In this case of selecting more than one material, truss members with several materials may have unequal strain energy density values. While the selection of multiple materials at certain subdomains is beyond the scope of the present work, the results with overlapping members may be realized through composite materials.

### 4.5.3 Long-span bridge design using linear and bilinear materials

This bridge example investigates different combinations of volume constraints using one linear and two bilinear materials in the proposed multi-material formulation. The de-

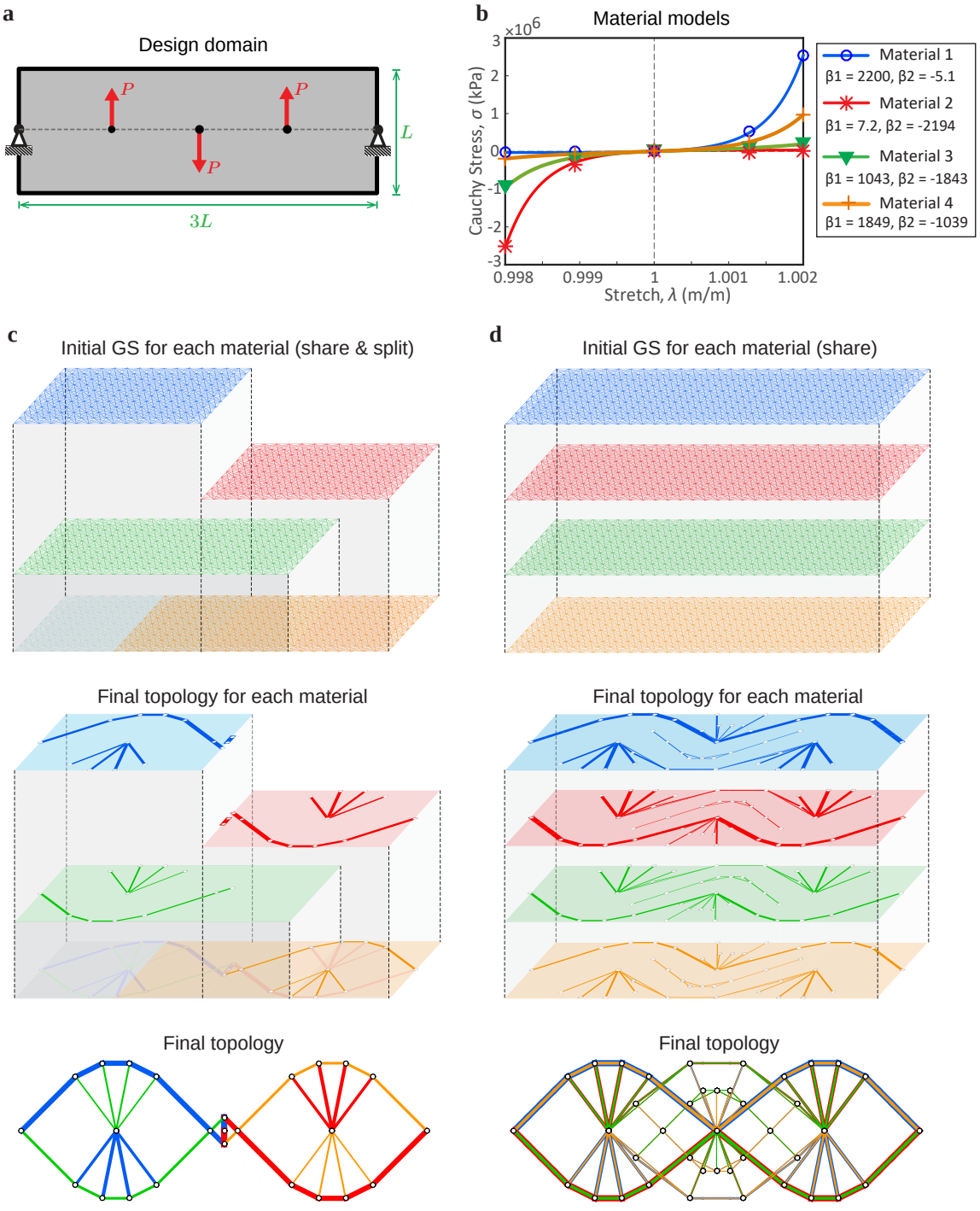


Figure 4.9: Example 2: influence of initial material distributions. **a** Design domain ($L = 10m, P = 1000kN$); **b** material models: four Ogden-based materials; **c** initial material distribution (schematic GSs) and the corresponding optimized structure for the case of materials sharing & splitting the domain; **d** initial material distribution (schematic GSs) and the corresponding optimized structure for the case of materials sharing the entire domain. (Online version in color.)

Table 4.5: Numerical information for Example 2 (Figure 4.9).

| 2D cases | $J(\boldsymbol{x}_i^*)$ | Material | | Volume | # |
|---|---|---|---|---|---|
| | $(kN \cdot m)$ | $\beta_1$ | $\beta_2$ | constraint, $V_{\max}^j$ | Elements |
| 4 materials (share & split) | 35.44 | 2200.3 | -5.1 | $0.4V_{\max}$ | 11 |
| | | 7.2 | -2194.0 | $0.4V_{\max}$ | 11 |
| | | 1043.3 | -1843.1 | $0.1V_{\max}$ | 10 |
| | | 1848.8 | -1039.2 | $0.1V_{\max}$ | 10 |
| 4 materials (share) | 27.53 | 2200.3 | -5.1 | $0.4V_{\max}$ | 42 |
| | | 7.2 | -2194.0 | $0.4V_{\max}$ | 42 |
| | | 1043.3 | -1843.1 | $0.1V_{\max}$ | 42 |
| | | 1848.8 | -1039.2 | $0.1V_{\max}$ | 42 |

sign domain with load and boundary conditions ($L = 1m, P = 100kN$) is shown in Figure 4.10a. Two bilinear and one linear materials are used to represent cable-like ("Material 1"), steel-like ("Material 2"), and concrete-like ("Material 3") materials ($[E_t, E_c]^{\text{cable}} = [17E, 0.007E]$; $[E_t, E_c]^{\text{steel}} = [7E, 7E]$; $[E_t, E_c]^{\text{concrete}} = [0.002E, 2E]$; where $E = 10^7 kPa$), as shown in Figure 4.10b. Three materials share the entire domain, as shown in Figure 4.10c, leading to three identical layers of full-level initial ground structures (based on an $18 \times 7$ grid) with 21,249 non-overlapping members and 152 nodes. We use two combinations of assignments for volume constraints. In one combination (three volume constraints, $nc = 3$), each material is assigned to an individual volume constraint (Figure 4.11a). In the other combination (two volume constraints, $nc = 2$), cable-like and steel-like materials are assigned to one volume constraint, and the concrete-like material is assigned to another volume constraint (Figure 4.11b), see Table 4.6. Note that in both combinations, the prescribed maximum volume, $V_{\max} = 0.05m^3$, is the same. The optimized structures for the two combinations of volume constraints are shown in Figure 4.11. The associated numerical information is summarized in Table 4.6. Different combinations of volume constraints lead to varied optimized structures. The case with two constraints has smaller objective value than the case with individual volume constraint for each material (i.e., three constraints). The amount of usage for the cable-like material decreases when its volume con-

straint is combined with a steel-like material. The strain energy density for each member in these two combinations of volume constraints are shown in Figure 4.12. In the optimized design, we observe that the members within the same volume constraint have the same strain energy density value regardless of the material type, verifying the KKT conditions discussed in Section 2.2. In the case that "Material 1" and "Material 2" are assigned to one volume constraint, the strain energy density values in the optimized structure are the same even though the properties of the two candidate materials are different.

Table 4.6: Numerical information for Example 3 (Figures 4.10, 4.11, and 4.12), $E = 10^7 kPa$.

| 2D cases | $J(\boldsymbol{x}_i^*)$ | Material | | Volume | Final | # |
|---|---|---|---|---|---|---|
| | $(kN \cdot m)$ | $E_t$ | $E_c$ | constraint, $V_{\max}^j$ | $V_{\text{frac}}$ | Elements |
| 3 materials | 20.957 | $17E$ | $0.001E$ | $0.4V_{\max}$ | 0.40 | 35 |
| | | $7E$ | $7E$ | $0.1V_{\max}$ | 0.10 | 27 |
| (3 vol. constraints) | | $0.002E$ | $2E$ | $0.5V_{\max}$ | 0.50 | 27 |
| 3 materials | 14.755 | $17E$ | $0.001E$ | $0.5V_{\max}$ | 0.16 | 31 |
| | | $7E$ | $7E$ | | 0.34 | 31 |
| (2 vol. constraints) | | $0.002E$ | $2E$ | $0.5V_{\max}$ | 0.50 | 31 |

### 4.5.4 Three-dimensional crane design subjected to multiple load cases

Using a combination of different materials with a more general volume constraint setting, we apply the proposed multi-material formulation to a 3D crane design subjected to multiple load cases. These load cases are implemented using the weighted-sum formulation, which averages the objective functions from all load cases. For a randomized approach that efficiently and effectively optimizes structures with many load cases, readers are referred to the work in [129]. The geometry of the crane ($L = 1m, P = 60kN$), in Figures 4.13a and 4.13b, has a fixed end and a void zone for practical design purposes [113]. To obtain constructible structures, we use a $14 \times 2 \times 2$ grid (with a level 6 GS) for the top domain and a $2 \times 2 \times 10$ grid (with a level 3 GS) for the bottom domain, containing a total of 10,276 members and 216 nodes. As shown in Figure 4.13c, five equal-weighted load

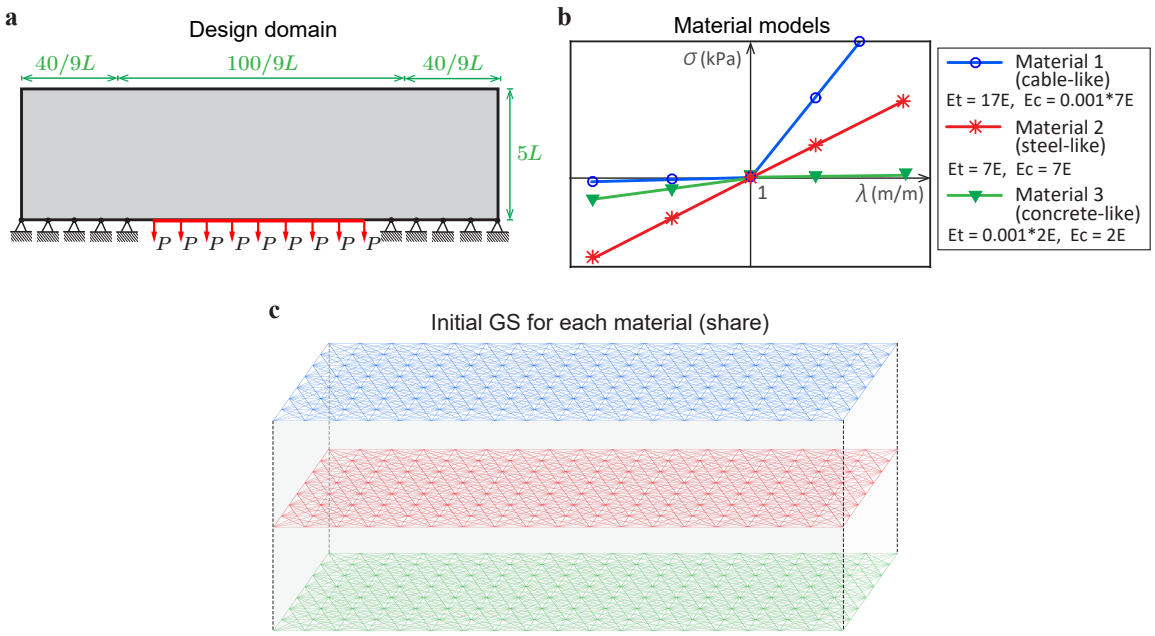


Figure 4.10: Example 3: influence of volume constraint combinations. **a** Design domain ($L = 1m, P = 100kN$); **b** material models: two bilinear and one linear materials; **c** initial full-level (schematic) GS for each material. (Online version in color.)

cases are applied to the crane. We perform optimization with three materials (one linear and two Ogden-based materials), as shown in Figure 4.14a. As indicated by the initial GSs (Figure 4.14b), these three materials share & split the domain, we assign two Ogden-based materials to the top domain and the linear material to the bottom domain.

Two volume constraints are used ($nc = 2$) where two Ogden-based materials are associated with one constraint, and the linear material is associated with the second constraint. The total prescribed maximum volume takes the following value, $V_{\max} = 0.014m^3$. In addition to a small filter ($\alpha_f = 10^{-4}$) used in the entire optimization, we apply a larger filter ($\alpha_f = 10^{-2}$) in the final step of the optimization to control the resolution of the final topology. The optimized structure is shown in Figure 4.15. The associated numerical information is summarized in Table 4.7. The multi-material framework with multiple load cases leads to a crane design with a clear layout and no overlapping members. In fact, the lower part of the crane design exhibits the $2/3$ bracing rule [130], which is shown to be the optimal bracing point for lateral loads. The values of initial and final volume fractions

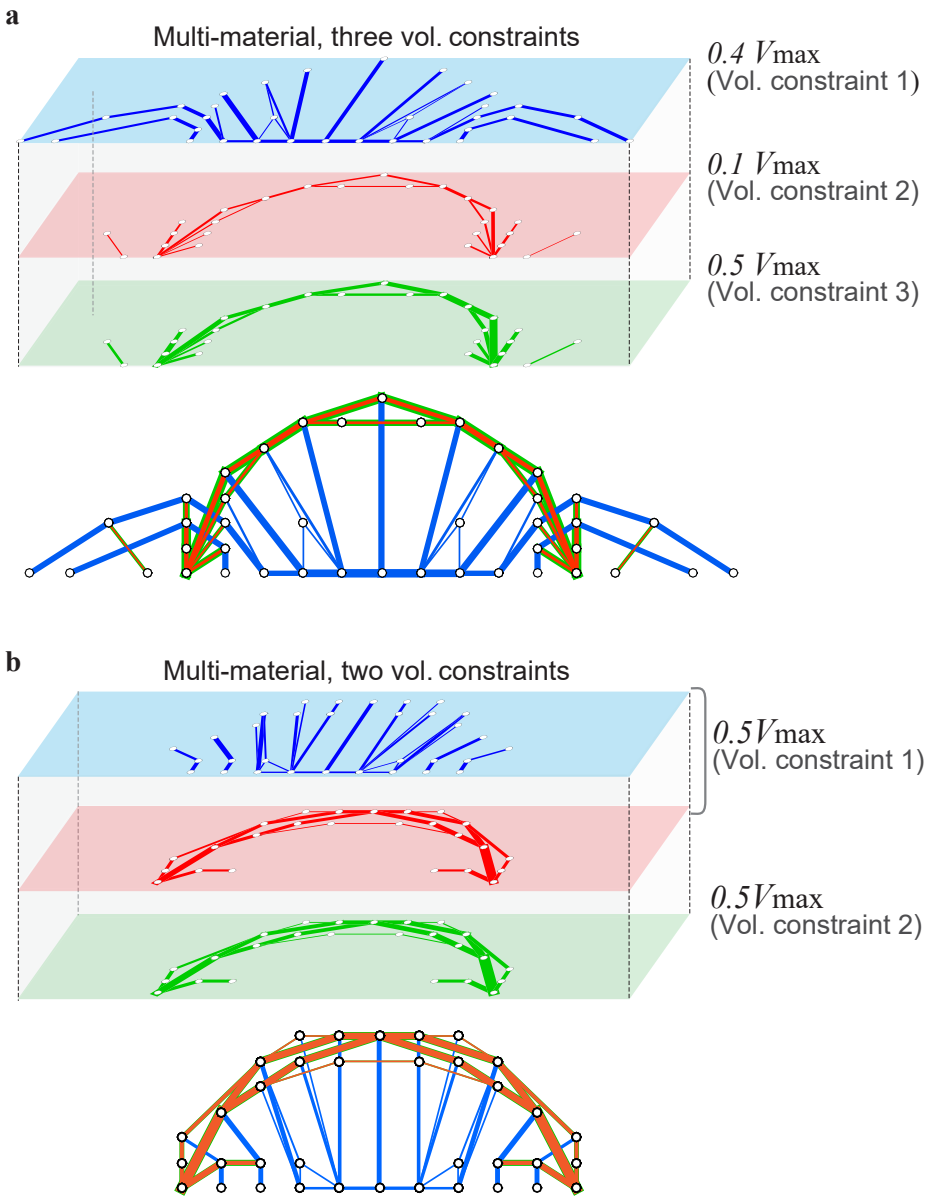


Figure 4.11: Example 3: influence of volume constraint combinations. **a** Optimized structure for the first volume constraint combination (3 constraints) where each material is assigned to an individual constraint; **b** optimized structure for the second volume constraint combination (2 constraints) where cable-like and steel-like materials are assigned to one constraint and the concrete-like material is assigned to another constraint. (Online version in color.)

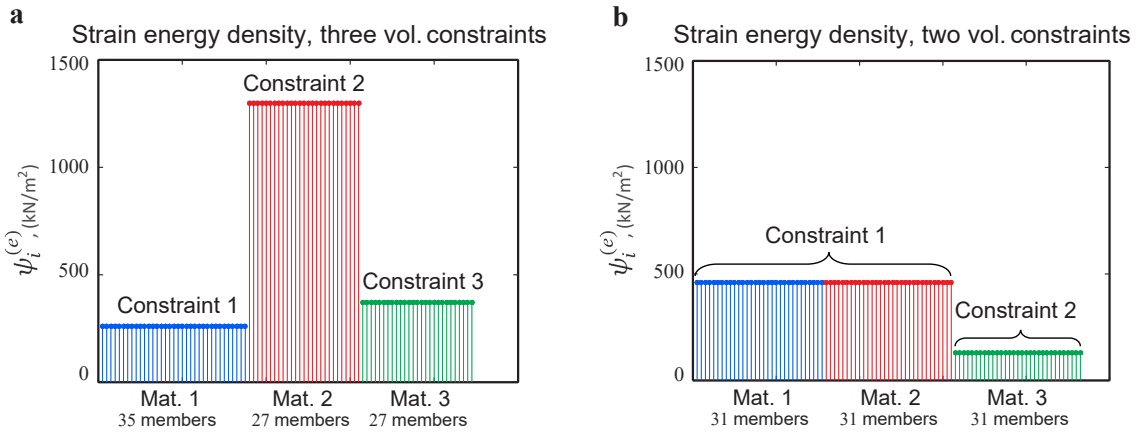


Figure 4.12: Example 3: influence of volume constraint combinations. **a** Strain energy density for the first volume constraint combination (3 constraints); the members within the same volume constraint have identical values of strain energy density. **b** Strain energy density for the second volume constraint combination (2 constraints); the members within the same volume constraint have identical values of strain energy density, regardless of the material type, which verifies the KKT conditions discussed in Section 2.2. (Online version in color.)

of the two Ogden-based materials in Table 4.7 indicate that the optimizer chooses and distributes the materials according to their properties. The geometry data of this crane design (Figure 4.15) is exported to STL (or stereolithography) format using the method proposed by [6]. The design is then manufactured with 3D printing using a fused deposition modeling (FDM) process and painted using multiple colors, each corresponding to one material, as shown in Figure 4.16.

Table 4.7: Numerical information for Example 4 (Figures 4.13, 4.14, 4.15, and 4.16), $E = 10^7 kPa$.

| 3D case | $J(\boldsymbol{x}_i^*)$ | Material | | Constraint | $V_{\text{frac}}$ | | # |
|---|---|---|---|---|---|---|---|
| | $kN \cdot m$ | type | property | $V_{\max}^j$ | initial | final | Elements |
| 3 mats. | 457 | Ogden | $\beta_1 = 1197, \beta_2 = -43$ | $0.4V_{\max}$ | 0.2 | 0.20 | 18 |
| (share | | Ogden | $\beta_1 = 45, \beta_2 = -1193$ | | 0.2 | 0.20 | 26 |
| & split) | | Linear | $E_T = E_c = 7E$ | $0.6V_{\max}$ | 0.60 | 0.60 | 84 |

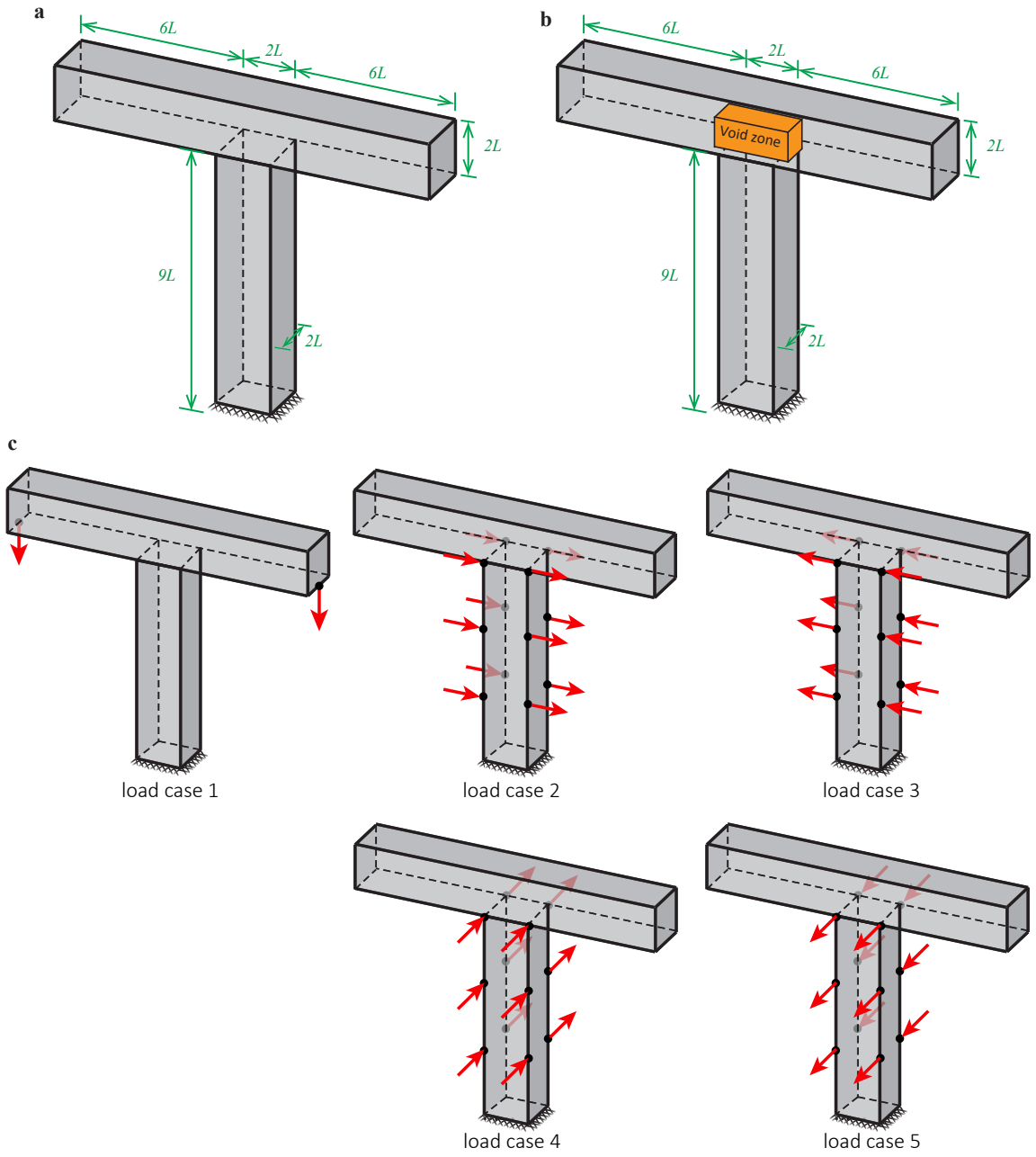


Figure 4.13: Example 4: multi-material crane design with multiple load cases. **a** Design domain discretized using a $14 \times 2 \times 2$ grid for the top domain and a $2 \times 2 \times 10$ grid for the bottom domain; **b** design domain with void zone; **c** five equal-weighted load cases.

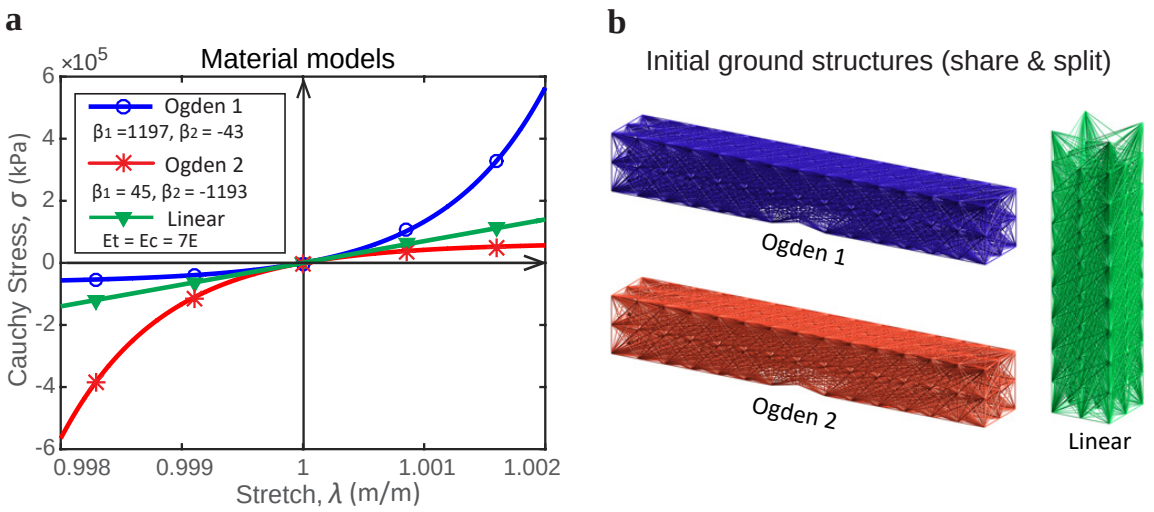


Figure 4.14: Example 4: multi-material crane design with multiple load cases. **a** Material models: two Ogden-based and one linear materials; **b** illustration of the initial material distribution. (Online version in color.)

## 4.6 Summary and Discussion

In this chapter, we propose a general multi-material formulation for truss topology optimization using the GSM considering material nonlinearity. This formulation is designed to handle an arbitrary number of candidate materials. Each candidate material is associated with an individual layer of the ground structure. Therefore, the location of each material layer can be freely specified – multiple material layers can either share or split the design domain, or combine both. For each material, the choice of the constitutive model is flexible and independent. As shown by the KKT conditions (see Section 2.2), our formulation leads to identical values of strain energy density for members within the same volume constraint (and whose optimal design variables are in the optimum range $x_{\min} < x_i^{(e),*} < x_{\max}$), regardless of the material type (see Eq. (4.12) and Figure 4.12). Furthermore, the assignment of volume constraints is generalized in the proposed formulation (e.g., one volume constraint can be assigned to either one or multiple materials). To efficiently handle the generalization of volume constraints, the ZPR design update scheme is utilized, which performs efficient and robust updates of the design variables associated with each volume constraint

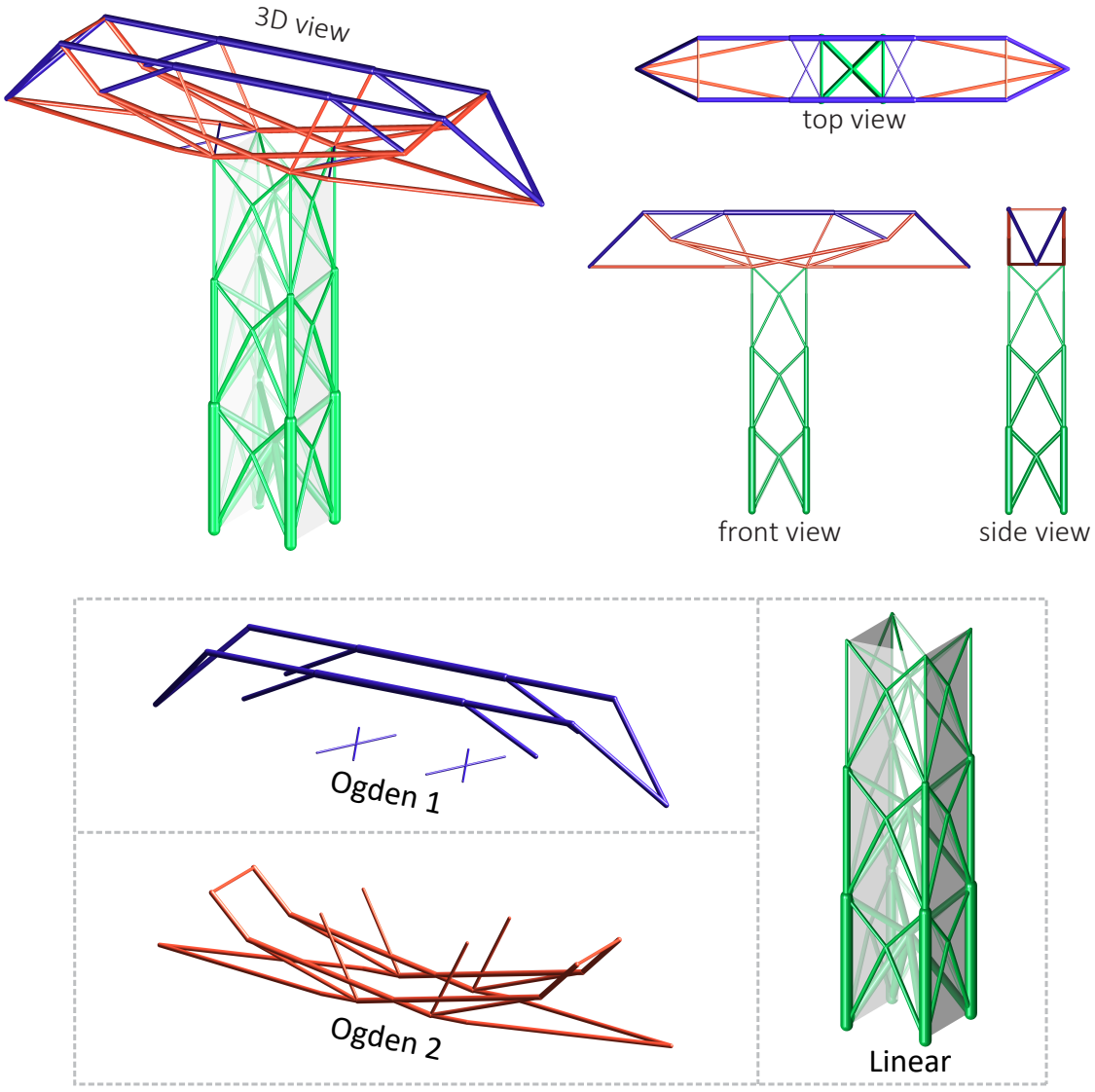


Figure 4.15: Example 4: the optimized structure for the 3D crane design – no overlapping members are observed in the final design. (Online version in color.)

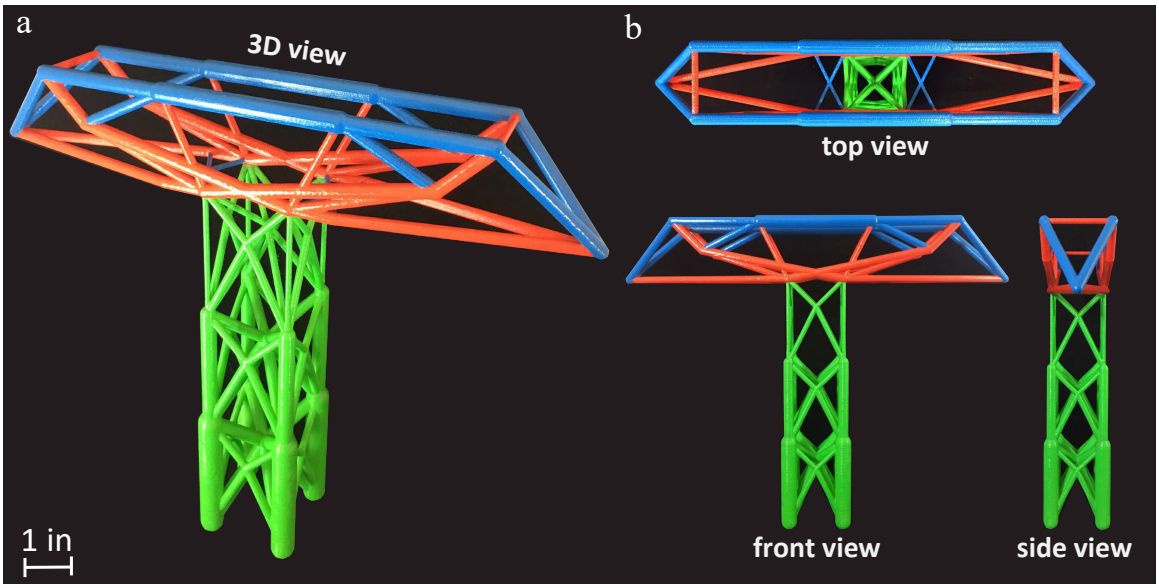


Figure 4.16: Example 4: printed model of the optimized crane design with three materials using FDM process. **a** 3D view; **b** top, front, and side views. The dimension of the manufactured model is 12.8 in $\times$ 2.3 in $\times$ 10.2 in. (Online version in color.)

independently.

By means of several 2D and 3D examples, using combinations of Ogden-based, bilinear, and linear materials, we verify and demonstrate the effectiveness of the proposed multi-material formulation and the ZPR design update scheme. The incorporation of material nonlinearity is shown to naturally eliminate the tendency of multi-material optimization, using linear materials, to favor the stiffest material. In addition, different initial material distributions are found to provide a variety of optimized structures. In certain scenarios (e.g., the scenario of multiple materials sharing the domain), the selection of more than one material for truss members (the overlapping of truss members from different materials) in the final design may occur, which may denote a composite material configuration. Furthermore, the comparison of different combinations of volume constraints shows that fewer constraints on the material volume lead to stiffer optimized structures. In the case of one total/global volume constraint with all materials sharing the entire domain, we achieve automatic assignment of the materials, that is, the optimizer chooses and distributes the materials according to their properties. In this case, the stiffest optimized structures are

achieved. Multiple load cases using a combination of various materials and a more general volume constraint assignment are considered in the 3D crane design. The multi-material framework with multiple load cases leads to a crane design exhibiting the $2/3$ bracing rule [130], which has been shown to be the optimal bracing point for lateral loads. The optimized crane was manufactured with 3D printing (using FDM) and painted using multiple colors that are consistent with the material assignment scheme.

Given the present investigation and outcome of the examples, we conclude that the proposed multi-material topology optimization framework, which accounts for material nonlinearity using the ZPR update scheme, leads to a design tool that not only finds the optimal topology but also selects the proper type and the amount of material. The ZPR design update scheme is flexible and customized to handle a general number of volume constraints – it is also applicable to continuum topology optimization with multiple volume constraints.

# CHAPTER 5
# MULTI-MATERIAL TOPOLOGY OPTIMIZATION WITH MULTIPLE CONSTRAINTS: COMBINING THE ZPR UPDATE WITH A GROUND-STRUCTURE ALGORITHM TO SELECT A SINGLE MATERIAL PER OVERLAPPING SET

Multi-material topology optimization often leads to members containing composite materials. However, in some instances, designers might be interested in using only one material for each member. Therefore, we propose an algorithm that selects a single preferred material from multiple materials per overlapping set. We develop the algorithm, based on the evaluation of both the strain energy and the cross-sectional area of each member, to control the material profile (i.e., number of materials) in each subdomain of the final design. This algorithm actively and iteratively selects materials to ensure a single material is used for each member. In this work, we adopt a multi-material formulation that handles an arbitrary number of volume constraints and candidate materials. To efficiently handle such volume constraints, we employ the Zhang-Paulino-Ramos (ZPR) design variable update scheme for multi-material optimization, which is based upon the separability of the dual objective function of the convex subproblem with respect to Lagrange multipliers. We provide an alternative derivation of this update scheme based on the Karush-Kuhn-Tucker (KKT) conditions. Through numerical examples, we demonstrate that the proposed material selection algorithm, which can be readily implemented in multi-material optimization, along with the ZPR update scheme, is robust and effective for selecting a single preferred material among multiple materials.

## 5.1 Introduction

Multi-material topology optimization may lead to members containing more than one material. Thus, in this chapter, we propose a material selection algorithm that ensures the selection of a single material for each member. This algorithm, based on the evaluation of both the strain energy and the cross-sectional area of each member, performs iteratively and actively throughout the optimization process. In the context of truss layout optimization using the ground structure method (GSM), we consider three scenarios of initial assignment of material layers. As shown in Figure 4.5, the multiple material layers can either share (Scenario #1) or split (Scenario #2) the design domain, or combine both (Scenario #3).

Through an illustrative example in Figure 5.1, we demonstrate the difference between optimization processes without controlling the number of materials in each subdomain (typical approach) and with controlling the selection of at most one material from each subdomain by using the proposed algorithm. The design domain and boundary conditions are provided in Figure 5.1a, while Figure 5.1b displays the material models in which "Material 1" has a larger Young's Modulus than "Material 2" in both tension and compression regions. The initial ground structures (GS) of the two bilinear materials share the entire domain, and each material is assigned to an individual volume constraint. As demonstrated by Figure 5.1c, overlapping of two materials occurs in the optimized design when we allow the selection of more than one material. On the other hand, the final result of employing the material selection algorithm (Figure 5.1d), which ensures the selection of a single material, shows that each truss member in the optimized design contains at most one material.

Based on the aforementioned description, the remainder of the chapter is organized as follows. Section 2 provides motivation and a review of related work on multi-material topology optimization. Section 3 describes the proposed multi-material topology optimization formulation, followed by the sensitivity analysis and the incorporation of a discrete filter. Section 4 introduces an alternative derivation of the ZPR design variable update

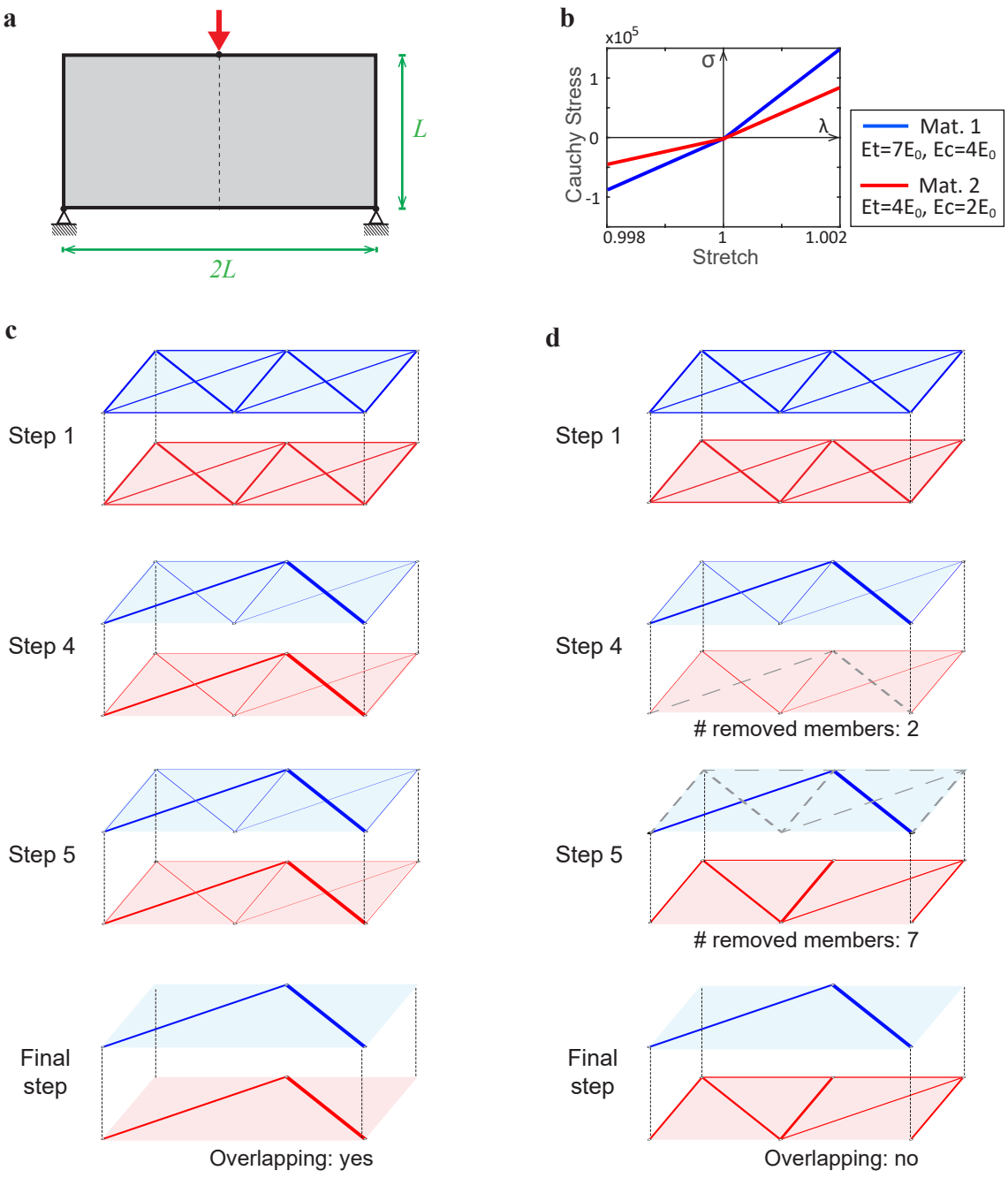


Figure 5.1: Demonstration of the algorithm that selects one single material among multiple materials at each subdomain. **a** Design domain; **b** two bilinear material models: "Material 1" has a larger Young's Modulus than "Material 2" in both tension and compression regions; **c** multi-material topology optimization that allows the selection of more than one material from each subdomain; **d** multi-material topology optimization with the algorithm that selects at most one material from each subdomain. Dotted lines represent removed members. (Online version in color.)

scheme, which is based on the Karush-Kuhn-Tucker (KKT) conditions. Section 5 proposes an algorithm that selects a single preferred material among multiple materials. Section 6 presents numerical examples in two and three dimensions, highlighting the properties of the proposed material selection algorithm, and Section 7 provides concluding remarks.

## 5.2 Motivation and Related Work

Topology optimization with multiple materials is a powerful design tool because it not only finds the optimal topology but also selects the proper type and amount of materials. One common feature of practical engineering designs is that they typically consist of multiple material types, such as high-rise buildings and composite materials in the macro- and micro-scale, respectively. The literature on multi-material topology optimization mainly deal with the continuum setting, such as the density-based approach. Various generalizations and extensions of the Solid Isotropic Material with Penalization (SIMP) [114] and other material interpolation schemes in the single-material topology optimization are made to accommodate multiple materials – see, e.g., [60]–[63], [72]. In addition to density-based formulations, phase-field [64], [115], [116] and level set [66]–[69] approaches have also been used for multi-material topology optimization formulations.

In addition to the continuum setting, some studies perform multi-material topology optimization using discrete elements, e.g., truss and lattice networks. Among these studies, most focus on integrating truss elements into continuum topology optimization for the purpose of designing reinforced concrete structures and strut-and-tie models, see, e.g., [10]–[14]. However, few multi-material topology optimization studies focus on truss networks using the GSM.

Another limitation in multi-material topology optimization literature is that it mostly assumes material linearity, yet real materials generally display nonlinear constitutive relations. In addition, most studies on multi-material topology optimization use a limited setting for volume constraints. These studies either assign a total volume constraint for all

candidate materials (e.g., [10]–[13], [62], [63]), which may cause issues if linear materials are used; or assign an individual volume constraint to each material (e.g., [60], [61], [64], [66], [68], [115], [116]), which may impose higher computational demand on formulation and update scheme implementations. A general setting, i.e., the combination of both types of constraints for various design purposes, and a tailored update scheme that handles arbitrary volume constraints, are needed in multi-material optimization.

To address the aforementioned limitations, we adopt our multi-material topology optimization framework [131] utilizing the ZPR update scheme, which can handle an arbitrary number of candidate materials with flexible material properties and a general setting of volume constraints. The ZPR design variable update scheme separates the updates of the design variables associated with each volume constraint and performs updates independently in series or in parallel. The update scheme is derived based on the separable feature of the dual objective function of the convex subproblem with respect to the Lagrange multipliers. The update of design variables thus depends only on the Lagrange multiplier of its associated volume constraint. *Thus, the ZPR update scheme is capable of handling an arbitrary number of volume constraints while preserving efficiency. In addition to volume constraints, the ZPR update scheme can be used to handle other types of linear constraints.*

The adopted multi-material formulation may lead to members containing more than one material (i.e., members with composite materials). In general, this phenomenon occurs under three conditions, which need to be satisfied simultaneously. *First*, two or more materials are assigned to share a domain in the initial material assignment (e.g., the initial ground structures in Figures 4.1a and 4.1c). *Second,* among the materials that share a domain, one material is stronger at least within a certain range of stretch values (e.g., in Figure 5.1b, "Material 1" is stronger than "Material 2" in the entire range of stretch values). *Third,* these materials are associated with individual volume constraints.

In the literature, several attempts have been made in continuum multi-material topology optimization to overcome the issues of selecting more than one material. One common

strategy is to consider the "product interpolation" in the Discrete Material Optimization (DMO) technique [72], which is based on a penalization scheme. However, this approach does not completely eliminate selecting of multiple materials at subdomains, especially at material interfaces. In order to enforce the selection of at most or exactly one material at each design subdomain, material selection constraints are introduced by employing discrete variables, which converts the optimization to a mixed integer problem, see, e.g., reference [62]. In the context of truss topology optimization with multiple materials, the above-reviewed approaches cannot be directly nor efficiently adopted, and currently no work allows for control of the material profile (i.e., number of materials) in each truss member of the final design.

The goal of this chapter is to propose an effective algorithm that enforces a single material selection in each subdomain in the multi-material topology optimization of trusses. We highlight that the proposed algorithm is active and iterative in nature and performed throughout the optimization process. This is conceptually different from the following two post-processing approaches. Post-processing of the final designs with composite materials, i.e., removing truss members with less contribution at the end of optimization step, causes a decrease in volume and an increase in displacement, and most importantly, may remove all the truss members with less favorable materials leading to designs only containing the most favorable material. Additionally, treating all composite members at the same time may, again, lead to designs only containing the most favorable material.

## 5.3 Multi-Material Topology Optimization

This section introduces the adopted multi-material topology optimization formulation and its sensitivity analysis, followed by the incorporation of a discrete filter. Within the context of the GSM and assuming a total of $m$ candidate materials, the framework consists of $m$ layers of initial ground structures. We assume that the $i$th GS layer with material $i$ (where $i = 1, ..., m$ is the material index) contains $M_i$ truss members and denote $\boldsymbol{x}_i$ as the

associated vector of design variables. The $e$th design variable component, $x_i^{(e)}$, is the cross-sectional area of the $e$th truss member of material $i$. Additionally, the formulation contains $nc$ independent volume constraints, where $1 \leq nc \leq m$. For the $j$th volume constraint, we denote $\mathscr{G}^j$ as the set of material indices associated with that volume constraint.

The formulation for such multi-material truss topology optimization is given as follows:

$$\begin{aligned} \min_{\boldsymbol{x}_1,\ldots,\boldsymbol{x}_m} \; & J(\boldsymbol{x}_1,\ldots,\boldsymbol{x}_m) = \min_{\boldsymbol{x}_1,\ldots,\boldsymbol{x}_m} \; -\Pi(\boldsymbol{x}_1,\ldots,\boldsymbol{x}_m,\boldsymbol{u}(\boldsymbol{x}_1,\ldots,\boldsymbol{x}_m)) \\ \text{s.t. } & g^j(\boldsymbol{x}_1,\ldots,\boldsymbol{x}_m) = \sum_{i\in\mathscr{G}^j} \boldsymbol{L}_i^{\mathrm{T}}\boldsymbol{x}_i - V_{\max}^j \leq 0,\ j=1,\ldots,nc, \\ & x_{\min} \leq x_i^{(e)} \leq x_{\max},\ i=1,\ldots,m, \text{ and } e=1,\ldots,M_i, \\ & \text{with } \boldsymbol{u}(\boldsymbol{x}_1,\ldots,\boldsymbol{x}_m) = \arg\min_{\boldsymbol{u}} \Pi(\boldsymbol{x}_1,\ldots,\boldsymbol{x}_m,\boldsymbol{u}). \end{aligned} \tag{5.1}$$

where $J$ is the objective function, $\boldsymbol{u}(\boldsymbol{x}_1,\ldots,\boldsymbol{x}_m)$ is the equilibrating displacement field (state variable), $\Pi$ is the total potential energy, $V_{\max}^j$ is the prescribed upper bound on the total volume associated with the $j$th volume constraint, $g^j$; $x_{\min}$ and $x_{\max}$ are the prescribed lower and upper bounds of the design variables, and $\boldsymbol{L}_i$ is the length vector of the $i$th material. As a demonstration of the notation in multi-material optimization formulation (5.1), Figure 4.4 and Table 4.1 summarize the parameters for a case with three materials ($m=3$, $M_1 = 5, M_2 = 5, M_3 = 9$) and two volume constraints ($nc = 2$, $\mathscr{G}^1 = \{1\}, \mathscr{G}^2 = \{2,3\}$).

In the topology optimization formulation (5.1), we aim to maximize the total potential energy of the multi-material truss system in its equilibrium state. The total potential energy $\Pi$ of the truss system is defined in (4.2), i.e., the difference of the total internal strain energy $\Psi_i^{(e)}(\boldsymbol{u})$ and the external work done by the applied force $\boldsymbol{f}$. The sensitivity information of the objective function and volume constraints with respect to the design variable are in (4.4) and (4.5), respectively.

In this work, we assume small deformation and nonlinear constitutive relations provided that the strain energy density function, $\Psi_i^{(e)}(\boldsymbol{u})$, is convex and differentiable for any given $\boldsymbol{u}$. We account for the nonlinear constitutive relationship through the Ogden-based

model [106] and the bilinear model. The strain energy density function for the Ogden-based model is given (3.25). The strain energy density function for the bilinear model is defined in (3.31). For more details of these material models, readers are referred to Chapter 3.3.1.

The above multi-material topology optimization formulation has several features. It is capable of handling an arbitrary number of materials with flexible initial material assignment (i.e., the materials can either share or split the design domain, or combine both) and independent constitutive relations (e.g., each candidate material can be either linear, bilinear, or nonlinear). The assignment of volume constraints is general – we can assign a total/global volume constraint to all the materials, an individual volume constraint to each material, or a combination of both.

The discrete filtering technique in the GSM is proposed in [85] and is extended in [120] to problems considering nonlinear materials. The discrete filtering allows users to control the resolution of the design and ensure global equilibrium of the final topology. For optimization with nonlinear structural analysis, the discrete filtering is further shown to significantly improve computational efficiency [120]. Therefore, in this chapter, the discrete filtering technique is incorporated in the multi-material optimization formulation, as shown in (4.14). The modified formulation (4.14) relaxes the lower bound of design variables to $x_{\min} = 0$ to account for the removal of members. Thus, a Tikhonov regularization term $(\Gamma/2)\boldsymbol{u}^{\mathrm{T}}\boldsymbol{u}$ is used in the total potential energy to prevent singular tangent stiffness matrices in the structural equations.

## 5.4 Alt-ZPR: Alternative Derivation of the ZPR Update Scheme

The Zhang-Paulino-Ramos or ZPR (zipper, phonetically) design variable update scheme [131] is adopted here for multi-material topology optimization. This design variable update scheme is capable of updating an arbitrary number of volume constraints while preserving efficiency and robustness. In particular, the ZPR update scheme separately and

independently updates the design variables associated with each volume constraint.

The derivation of the ZPR update scheme that utilizes primal-dual relationship is presented in reference [131]. Here we show an alternative derivation of this update scheme using the Karush-Kuhn-Tucker (KKT) conditions. At each optimization step $k$, we introduce a convex approximation of the objective function over the intervening variable $\boldsymbol{y}_i(\boldsymbol{x}_i)$ such that $y_i^{(e)}(x_i^{(e)}) = (x_i^{(e)})^{-\alpha}$, $i = 1,...,m$, and $e = 1,...,M_i$, as follows:

$$\begin{aligned} J(\boldsymbol{x}_1,...,\boldsymbol{x}_m) &\approx J^k(\boldsymbol{x}_1,...,\boldsymbol{x}_m) = J\left(\boldsymbol{x}_1^k,...,\boldsymbol{x}_m^k\right) + \sum_{i=1}^{m}\left[\frac{\partial J}{\partial \boldsymbol{y}_i}(\boldsymbol{x}_1^k,...,\boldsymbol{x}_m^k)\right]^T\left[\boldsymbol{y}_i(\boldsymbol{x}_i) - \boldsymbol{y}_i(\boldsymbol{x}_i^k)\right] \\ &= J\left(\boldsymbol{x}_1^k,...,\boldsymbol{x}_m^k\right) + \sum_{i=1}^{m}\left[\boldsymbol{b}_i(\boldsymbol{x}_1^k,...,\boldsymbol{x}_m^k)\right]^T\left[\boldsymbol{y}_i(\boldsymbol{x}_i) - \boldsymbol{y}_i(\boldsymbol{x}_i^k)\right], \end{aligned} \tag{5.2}$$

where $\alpha$ is a strictly positive arbitrary number, $\boldsymbol{x}_i^k$ and $\boldsymbol{y}_i(\boldsymbol{x}_i^k)$ are the design and intervening variables at the $k$th optimization step for material $i$, and $\boldsymbol{b}_i(\boldsymbol{x}_1^k,...,\boldsymbol{x}_m^k)$ is a constant vector, whose component is given as the following function of the corresponding $e$th component of the sensitivity vector:

$$b_i^{(e)}(\boldsymbol{x}_1^k,...,\boldsymbol{x}_m^k) = \frac{\partial J}{\partial y_i^{(e)}}(\boldsymbol{x}_1^k,...,\boldsymbol{x}_m^k) = -\frac{(x_i^{(e),k})^{1+\alpha}}{\alpha}\frac{\partial J}{\partial x_i^{(e)}}(\boldsymbol{x}_1^k,...,\boldsymbol{x}_m^k). \tag{5.3}$$

Using the approximated objective function $J^k$, we obtain a subproblem at step $k$, formulated as follows:

$$\begin{aligned} \min_{\boldsymbol{x}_1,...,\boldsymbol{x}_m} \; & J^k(\boldsymbol{x}_1,...,\boldsymbol{x}_m) = \min_{\boldsymbol{x}_1,...,\boldsymbol{x}_m} J\left(\boldsymbol{x}_1^k,...,\boldsymbol{x}_m^k\right) + \sum_{i=1}^{m}\left[\frac{\partial J}{\partial \boldsymbol{y}_i}(\boldsymbol{x}_1^k,...,\boldsymbol{x}_m^k)\right]^T\left[\boldsymbol{y}_i(\boldsymbol{x}_i) - \boldsymbol{y}_i(\boldsymbol{x}_i^k)\right] \\ \text{s.t.} \; & \sum_{i\in\mathscr{G}^j} \boldsymbol{L}_i^{\mathrm{T}}\boldsymbol{x}_i - V_{\max}^j \le 0, \; j = 1,...,nc, \\ & x_{i,\mathrm{L}}^{(e),k} \le x_i^{(e)} \le x_{i,\mathrm{U}}^{(e),k}, \; i = 1,...,m, \text{ and } e = 1,...,M_i, \\ & \text{with } y_i^{(e)}(x_i^{(e)}) = (x_i^{(e)})^{-\alpha}, \; i = 1,...,m, \text{ and } e = 1,...,M_i, \end{aligned} \tag{5.4}$$

where $\mathscr{G}^j$ is the set of material indices associated with $j$th volume constraint, $x_{i,\mathrm{L}}^{(e),k} = \max(x_{\min}, x_i^{(e),k} - move)$ and $x_{i,\mathrm{U}}^{(e),k} = \min(x_{\max}, x_i^{(e),k} + move)$ are the upper and lower bounds

of the design variables that are determined through the prescribed allowable move limit, *move*.

By introducing a set of Lagrange multipliers $\phi_V^j, j = 1,...,nc$, the Lagrangian of the subproblem in Eq. (5.4) takes the following form:

$$\mathscr{L}\left(\boldsymbol{x}_1,...,\boldsymbol{x}_m,\phi_V^1,...,\phi_V^{nc}\right) = \sum_{i=1}^{m}\left[\boldsymbol{b}_i(\boldsymbol{x}_1^k,...,\boldsymbol{x}_m^k)\right]^T\boldsymbol{y}_i(\boldsymbol{x}_i) + \sum_{j=1}^{nc}\phi_V^j\left(\sum_{i\in\mathscr{G}^j}\boldsymbol{L}_i^{\mathrm{T}}\boldsymbol{x}_i - V_{\max}^j\right). \tag{5.5}$$

Notice that the above Lagrangian is a separable function for each volume constraint,

$$\begin{aligned}\mathscr{L}\left(\boldsymbol{x}_1,...,\boldsymbol{x}_m,\phi_V^1,...,\phi_V^{nc}\right) &= \sum_{j=1}^{nc}\mathscr{L}^j\left(\boldsymbol{x}_i,...,\boldsymbol{x}_m,\phi_V^j\right)\\ &= \sum_{j=1}^{nc}\left\{\sum_{i\in\mathscr{G}^j}\left[\left[\boldsymbol{b}_i(\boldsymbol{x}_1^k,...,\boldsymbol{x}_m^k)\right]^T\boldsymbol{y}_i(\boldsymbol{x}_i) + \phi_V^j\boldsymbol{L}_i^{\mathrm{T}}\boldsymbol{x}_i\right] - \phi_V^j V_{\max}^j\right\}.\end{aligned} \tag{5.6}$$

The KKT conditions of the subproblem (5.4) require that

$$\frac{\partial\mathscr{L}}{\partial x_i^{(e)}} = \frac{\partial\mathscr{L}^j}{\partial x_i^{(e)}} = -\alpha b_i^{(e)}(\boldsymbol{x}_1^k,...,\boldsymbol{x}_m^k)\left(x_i^{(e)}\right)^{(-\alpha-1)} + \phi_V^j L_i^{(e)} = 0, \quad \forall i\in\mathscr{G}^j, \tag{5.7}$$

and

$$\frac{\partial\mathscr{L}}{\partial\phi_V^j} = \sum_{i\in\mathscr{G}^j}\boldsymbol{L}_i^{\mathrm{T}}\boldsymbol{x}_i - V_{\max}^j = 0, \quad j = 1,...,nc. \tag{5.8}$$

We denote $x_i^{(e)*}$ as the solution of the above KKT conditions. From (5.7), we can write the solution $x_i^{(e)*}$ as

$$x_i^{(e)*} = Q_i^{(e),k}\left(\phi_V^j\right) = \left[\frac{\alpha b_i^{(e)}(\boldsymbol{x}_1^k,...,\boldsymbol{x}_m^k)}{\phi_V^j L_i^{(e)}}\right]^{\frac{1}{1+\alpha}}, \quad \forall i\in\mathscr{G}^j. \tag{5.9}$$

By further incorporating the lower and upper bounds, $\boldsymbol{x}_{i,\mathrm{L}}^k$, and $\boldsymbol{x}_{i,\mathrm{U}}^k$, of the design variables,

the expression for $x_i^{(e)*}$ is modified as

$$
\begin{aligned}
x_i^{(e)*} &= Q_i^{(e),k}\left(\phi_V^j\right) \\
&= \begin{cases} x_{i,\mathrm{L}}^{(e),k} & \text{if } \left[\frac{\alpha b_i^{(e)}(\boldsymbol{x}_1^k,\ldots,\boldsymbol{x}_m^k)}{\phi_V^j L_i^{(e)}}\right]^{\frac{1}{1+\alpha}} < x_{i,\mathrm{L}}^{(e),k} \\ \left[\frac{\alpha b_i^{(e)}(\boldsymbol{x}_1^k,\ldots,\boldsymbol{x}_m^k)}{\phi_V^j L_i^{(e)}}\right]^{\frac{1}{1+\alpha}} & \text{if } x_{i,\mathrm{L}}^{(e),k} \le \left[\frac{\alpha b_i^{(e)}(\boldsymbol{x}_1^k,\ldots,\boldsymbol{x}_m^k)}{\phi_V^j L_i^{(e)}}\right]^{\frac{1}{1+\alpha}} \le x_{i,\mathrm{U}}^{(e),k} \\ x_{i,\mathrm{U}}^{(e),k} & \text{if } \left[\frac{\alpha b_i^{(e)}(\boldsymbol{x}_1^k,\ldots,\boldsymbol{x}_m^k)}{\phi_V^j L_i^{(e)}}\right]^{\frac{1}{1+\alpha}} > x_{i,\mathrm{U}}^{(e),k} \end{cases} \quad , \quad \forall i \in \mathscr{G}^j.
\end{aligned}
\tag{5.10}
$$

By plugging (5.10) back into Eq. (5.8), we obtain

$$
\frac{\partial \mathscr{L}}{\partial \phi_V^j} = \sum_{i\in\mathscr{G}^j}\sum_{e=1}^{M_i} L_i^{(e)} x_i^{(e)*}\left(\phi_V^j\right) - V_{\max}^j = 0, \quad j = 1,\ldots,nc. \tag{5.11}
$$

Notice that the $j$th equation of the above system is an algebraic equation as a function $\phi_V^j$, therefore, each optimal Lagrange multiplier $\phi_V^{j*}$ can be solved independently by its corresponding equation. We then have a decoupled system with respect to the volume constraints.

Finally, the update of the $e$th component of design variables $\boldsymbol{x}_i^{k+1}$ is taken as the optimal solution in subproblem (5.4):

$$
x_i^{(e),k+1} = Q_i^{(e),k}\left(\phi_V^{j*}\right), \quad \forall i \in \mathscr{G}^j. \tag{5.12}
$$

When applied to the multi-material optimization problem in Section 5.3, the ZPR design variable update scheme in Eq. (5.12) takes the following specific form:

$$
x_i^{(e),k+1} = \begin{cases} x_{i,\mathrm{L}}^{(e),k} & \text{if } \left[\frac{\Psi_i^{(e)}(\boldsymbol{u}(\boldsymbol{x}_1^k,\ldots,\boldsymbol{x}_m^k))}{\phi_V^{j*}}\right]^{\eta} x_i^{(e),k} < x_{i,\mathrm{L}}^{(e),k} \\ \left[\frac{\Psi_i^{(e)}(\boldsymbol{u}(\boldsymbol{x}_1^k,\ldots,\boldsymbol{x}_m^k))}{\phi_V^{j*}}\right]^{\eta} x_i^{(e),k} & \text{if } x_{i,\mathrm{L}}^{(e),k} \le \left[\frac{\Psi_i^{(e)}(\boldsymbol{u}(\boldsymbol{x}_1^k,\ldots,\boldsymbol{x}_m^k))}{\phi_V^{j*}}\right]^{\eta} x_i^{(e),k} \le x_{i,\mathrm{U}}^{(e),k} \\ x_{i,\mathrm{U}}^{(e),k} & \text{if } \left[\frac{\Psi_i^{(e)}(\boldsymbol{u}(\boldsymbol{x}_1^k,\ldots,\boldsymbol{x}_m^k))}{\phi_V^{j*}}\right]^{\eta} x_i^{(e),k} > x_{i,\mathrm{U}}^{(e),k} \end{cases} , \forall i \in \mathscr{G}^j,
\tag{5.13}
$$

where $\eta = 1/(1+\alpha)$, which is commonly known as the damping factor. This factor can be either constant [31] or adaptive [70].

We note that from Eqs. (5.12) and (5.13), the updates of design variables are also decoupled in the sense that the update corresponding to $j$th volume constraint only depends on its associated optimal Lagrange multiplier, $\phi_V^{j*}$. This feature, along with the decoupled solution of $\phi_V^{j*}$ in (5.11), allows the associated design variables of each volume constraint to be updated independently, highlighting one of the main advantages of the ZPR design variable update scheme.

## 5.5 Algorithm to Select a Single Preferred Material Per Overlapping Set

As discussed in Section 5.2, under the conditions of 1) multiple materials share the design domain, 2) one of the materials (at least partially) dominates the others, and 3) each of those materials is assigned with an individual volume constraint, optimization formulations (4.1) and (4.14) may lead to final topologies with overlapping sets/connectivities. This is shown in the optimized structure in Figure 5.1c. An overlapping set/connectivity is defined as the truss members with different material properties and with non-zero cross-sectional areas that share the same end nodes. The presence of overlapping connectivities may lead to difficulties in defining a unique material property of each truss member in the final topology. In this section, we propose a simple and effective material selection algorithm to ensure that each connectivity (truss member) of the final topology contains at most one material. The basic concept and procedure of the proposed algorithm are illustrated by the example in Figure 5.1.

Assume that at a given optimization step, we have identified all sets of overlapping members. Each of these sets contains all the non-zero area members that share the same end nodes. The basic idea of the material selection algorithm is to select the best member within each set according to a pre-defined criterion and remove other members. The removal is performed by assigning member cross-sectional areas to zero, and applying

Tikhonov regularization in the structural analysis to regularize the tangent stiffness matrices (regardless of whether the discrete filter is used). Notice that when a member is removed, the total volume of the associated material decreases, and thus, the optimizer assigns the removed materials to other locations in the following optimization steps. By doing this, the optimization effectively redistributes the overlapped materials to other locations. If all the overlapped members at one material layer are removed at the same time, there might be no available members from that material layer to redistribute to the design (because each candidate material can only be redistributed within its associated material layer). To prevent this, a threshold (parameter), $\alpha_{\text{select}} \in [0, 1]$, is defined such that this removing-and-redistributing procedure is performed gradually. In the material selection algorithm, the threshold is applied as follows: the normalized area of each member (ratio of the cross-sectional area to the maximum cross-sectional area in its associated material layer) is first computed, and the removal is then performed to the overlapping sets whose ratios are larger than (or equal to) the prescribed threshold, $\alpha_{\text{select}}$.

We adopt uniform area distribution as the initial guess for design variables, i.e. the initial ratio of member area to the maximum area of the corresponding material layer is one. As a result, if the selection algorithm is applied at the initial optimization step, all overlapping connectivities will be immediately removed according to the previously defined threshold. Additionally, no redistribution of removed material can be done in the subsequent optimization steps. To avoid this, we allow the optimizer to freely develop topologies with non-uniform members areas and initiate the material selection algorithm after $N_{\text{select}}$ optimization steps.

In addition to the parameters $\alpha_{\text{select}}$ and $N_{\text{select}}$, a criterion needs to be defined to determine the best member among the multiple materials in each overlapping set. In this work, we define the criterion to be the strain energy of the member per unit length, i.e. $x\Psi$ (because the overlapping connectivities have the same lengths, the member length $L$ is excluded in the criterion). For a set of overlapping members, we select the member with

the largest strain energy (per unit length). The choice of this criterion is consistent with the objective function in (4.2), because members with larger strain energy (per unit length) contribute to larger total potential energy of the entire structure. Thus, members with larger strain energy are preferred because they are more efficient. More specifically, the proposed material selection algorithm follows the steps listed below:

**1** Detect all sets of overlapping members (connectivities with more than one material selection).

**2** Within each overlapping set, detect the member with the largest strain energy per unit length.

**3** For this detected member in the current set, if its normalized cross-sectional area (with respect to the maximum cross-sectional area in its associated material layer) exceeds or equals to the prescribed threshold $\alpha_{\text{select}}$ go to Step 4, otherwise go to Step 5.

**4** Select the member that has the largest strain energy per unit length and keep its cross-sectional area. Remove other members in the current set by assigning their cross-sectional areas to be zero.

**5** Proceed to the next overlapping set.

To formalize the proposed algorithm, we introduce the following notation. Assuming that there are in total of $p$ overlapping sets, we denote $\widetilde{\boldsymbol{x}}_j$ as the vector containing all the design variables in the $j$th set, where $\widetilde{x}_j^{(i)}$ is the $i$th component of $\widetilde{\boldsymbol{x}}_j$. Accordingly, the vector of corresponding material indices of the $j$th set is defined as $\widetilde{\boldsymbol{m}}_j$ with its $i$th component denoted as $\widetilde{m}_j^{(i)}$. The associated energy density function is denoted as $\Psi_{\widetilde{m}_j^{(i)}}$. As an illustration, Figure 5.2 shows the overlapping of three materials at a connectivity (subdomain) and the corresponding notation. A design consisting of overlapping materials is shown in Figure 5.2a. The 1$^{\text{st}}$ overlapping set/connectivity consists of the 4$^{\text{th}}$ member of "Material 1", the 2$^{\text{nd}}$ member of "Material 2", and the 5$^{\text{th}}$ member of "Material 3", as

shown in Figure 5.2b; therefore, we write $\widetilde{\boldsymbol{x}}_1 = \{\widetilde{x}_1^{(1)}, \widetilde{x}_1^{(2)}, \widetilde{x}_1^{(3)}\}^T = \{x_1^{(4)}, x_2^{(2)}, x_3^{(5)}\}^T$ and $\widetilde{\boldsymbol{m}}_1 = \{\widetilde{m}_1^{(1)}, \widetilde{m}_1^{(2)}, \widetilde{m}_1^{(3)}\}^T = \{1,2,3\}^T$ (Figure 5.2c). Based on the introduced notation, the procedure described in Step 1 to Step 5 are formally given in Algorithm 3.

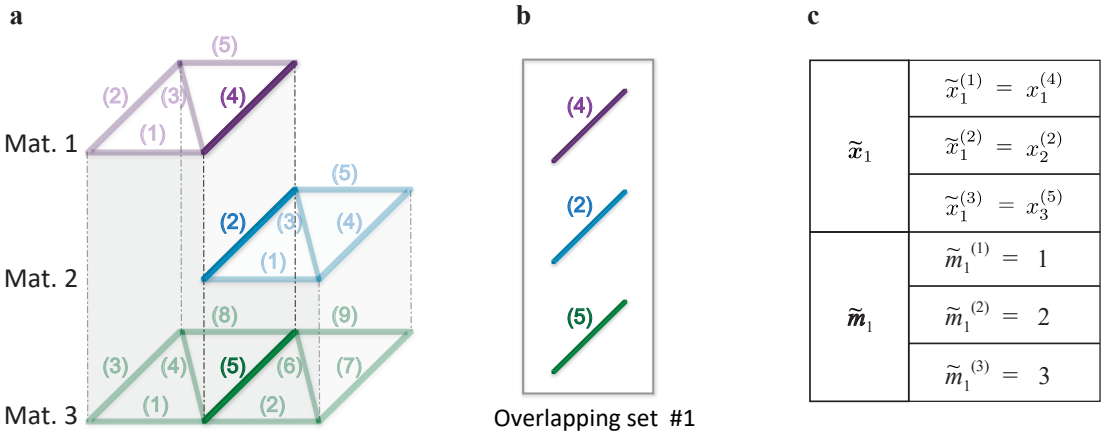


Figure 5.2: Demonstration of overlapping of three materials and corresponding notation. **a** A design consisting of overlapping connectivities; **b** overlapping connectivity set #1 containing: 4th member of "Material 1", 2nd member of "Material 2", and 5th member of "Material 3"; **c** corresponding notation. (Online version in color.)

Algorithm 3 describes the procedure of selecting a single material from each overlapping connectivity at each optimization step. Incorporating Algorithm 3 in the optimization process, the entire implementation is described in Algorithm 4. In Section 5.6.1, we include studies that demonstrate influences of the main algorithmic parameters ($N_{\text{select}}$ and $\alpha_{\text{select}}$) on the final topologies and objective values.

We remark that the above-presented material selection algorithm can also be applied with the discrete filter scheme [85], [120] to control the resolution of the final topology and to improve the computational efficiency. Typically, the discrete filter starts at the initial step of the optimization process. However, in this case the discrete filter may remove the potential members to redistribute the removed overlapping materials. The study in [120] indicates that the discrete filter can remove up to 99% of the members in the first few optimization steps after the filter is applied, which may significantly reduce the space of potential members to redistribute the removed overlapping materials (when we start to

**Algorithm 3** Algorithm to select a single preferred material

**Input:** $\boldsymbol{x}_1,...,\boldsymbol{x}_m$, $\alpha_{\text{select}}$
Detect $p$ sets of members with more than one material selection, $\widetilde{\boldsymbol{x}}_1,...,\widetilde{\boldsymbol{x}}_p$.
**for** $j = 0,1,...,p$ **do**
    Detect member $i^*$ with the largest strain energy per unit length among $\widetilde{\boldsymbol{x}}_j$ such that

$$\widetilde{x}_j^{(i^*)}\Psi_{\widetilde{m}_j^{(i^*)}} = \max(\widetilde{x}_j^{(1)}\Psi_{\widetilde{m}_j^{(1)}},...,\widetilde{x}_j^{(n)}\Psi_{\widetilde{m}_j^{(n)}}), \tag{5.14}$$

    where $n$ indicates the length of vector $\widetilde{\boldsymbol{x}}_j$.
    **if** $\widetilde{x}_j^{(i^*)} / \max(\boldsymbol{x}_{\widetilde{m}_j^{(i^*)}}) \geq \alpha_{\text{select}}$ **then**

$$\widetilde{x}_j^{(i)} = \begin{cases} \widetilde{x}_j^{(i)}, & \text{if} \quad i = i^* \\ 0, & \text{otherwise.} \end{cases} \qquad i = 1,...,n \tag{5.15}$$

    **end if**
**end for**
Update $\boldsymbol{x}_1,...,\boldsymbol{x}_m$ based on corresponding components of $\widetilde{\boldsymbol{x}}_1,...,\widetilde{\boldsymbol{x}}_p$
**Output:** New $\boldsymbol{x}_1,...,\boldsymbol{x}_m$

apply Algorithm 3 after $N_{\text{select}}$ steps). Thus, in the optimization algorithm, we propose to apply the discrete filter after $N_{\text{filter}}$ optimization steps, where $N_{\text{filter}} > N_{\text{select}}$ is a prescribed parameter.

### 5.6 Numerical Examples

In this section, we provide several numerical examples to demonstrate the proposed material selection algorithm in the multi-material topology optimization using the GSM. Example 1 investigates the main parameters of the selecting algorithm, $N_{\text{select}}$ and $\alpha_{\text{select}}$. Example 2 demonstrates the selecting algorithm using four Ogden-based materials and compares the optimized results to the multi-material case without the selecting algorithm. Using one linear and two bilinear material models, Example 3 illustrates the selecting algorithm in a simplified bridge design. The last example shows the application of the proposed multi-material formulation to a three-dimensional cantilever beam design.

We generate non-overlapped (within the same material layer) initial ground structures

**Algorithm 4** Multi-material topology optimization with the proposed algorithm that selects a single preferred material

**Initialize:** $\boldsymbol{x}_1^0, ..., \boldsymbol{x}_m^0$, $\text{iter}_{\max}$, $\tau_{\text{opt}}$, $N_{\text{select}}$, $N_{\text{filter}}$
**for** $k = 0, 1, ..., \text{iter}_{\max}$ **do**
    Solve: $\boldsymbol{u}\left(\boldsymbol{x}_1^k, ..., \boldsymbol{x}_m^k\right) = \arg\min_{\boldsymbol{u}}\left[\Pi\left(\boldsymbol{x}_1^k, ..., \boldsymbol{x}_m^k, \boldsymbol{u}\right)\right]$
    Compute: $J\left(\boldsymbol{x}_1^k, ..., \boldsymbol{x}_m^k\right), g^j\left(\boldsymbol{x}_1^k, ..., \boldsymbol{x}_m^k\right), \partial J\left(\boldsymbol{x}_1^k, ..., \boldsymbol{x}_m^k\right)/\partial x_i^{(e)}$, and $\partial g^j\left(\boldsymbol{x}_1^k, ..., \boldsymbol{x}_m^k\right)/\partial x_i^{(e)}$
    **for** $j = 1, 2, ..., nc$ **do**
        Compute $\phi_{V*}^j$ by solving Eq. (5.11)
        Update $x_i^{(e),k+1} = Q_i^{(e),k}\left(\phi_V^{j*}\right), \quad \forall i \in \mathscr{G}^j$ according to Eq. (5.13)
    **end for**
    **if** $k \geq N_{\text{select}}$ **then**
        Apply Algorithm 3 to the sets of overlapping members
    **if** $k \geq N_{\text{filter}}$ **then**
        Apply discrete filter according to Eq. (3.5)
    **end if**
    **if** $\max\left(||\boldsymbol{x}_1^{k+1} - \boldsymbol{x}_1^k||_\infty, ..., ||\boldsymbol{x}_m^{k+1} - \boldsymbol{x}_m^k||_\infty\right) < \tau_{\text{opt}}$ and $k > N_{\text{select}}$ **then**
        quit
    **end if**
**end for**
Remove aligned nodes
Plot final topology

using the collision zone technique in [112], [113] and plot final topologies in 3D using the program GRAND3 [113]. For all results in the GSM, we remove aligned nodes and floating members and check the final topologies to ensure that they are at global equilibrium. A detailed explanation can be found in reference [128]. It is worth noting that we do not verify the instability of the members, because the issue of stability is beyond the scope of this work. The nonlinear solution scheme is based on a Newton-Raphson approach with line search (see the reference [120] for a detailed explanation). For all the examples, the discrete filter is used during the optimization process to obtain valid structures and improve computational efficiency.

For the constitutive models of the numerical example, we employ linear model, bilinear model, and (hyperelastic) Ogden-based [106] model, which allows varied control of constitutive relationships and has the capability to reproduce a variety of hyperelastic models. For details of the constitutive models and strain energy density functions that form the basis of the structural analysis, readers are referred to the studies in [84], [120].

Consistent units are implied throughout and examples have the initial tangent modulus, $E_0 = 7 \times 10^7$, unless otherwise stated; stopping criterion: $\tau_{\text{opt}} = 10^{-9}$; move value: $move = 10^4 x^0$, where $x^0$ is the initial guess of the design variables; and initial damping factor for the ZPR update scheme: $\eta = 0.5$. Subsequent damping factors are updated according to the scheme provided by the study in [70]. The upper bound for the design variable is defined by $x_{\max} = 10^4 x^0$. *All examples are solved using the ZPR design variable update scheme described in Section 5.4, and all cases that enforce the selection of a single material employ the material selection algorithm described in Algorithm 3.*

### 5.6.1 Parametric study using a cantilever beam

In this example, we demonstrate the effectiveness of the proposed material selection algorithm and investigate the main parameters, $N_{\text{select}}$ and $\alpha_{\text{select}}$. The design domain ($L = 2, P = 1000$) and material models are shown in Figures 5.3a and 5.3b. Three materials

share the entire domain, as shown in Figure 5.3c. Three layers (one for each material) of identical full-level initial ground structures (based on a $8 \times 6$ discretization) with a total of 3,702 members and 63 nodes are used. The total prescribed maximum volume takes the following value, $V_{\max} = 0.024$. Each material is associated with an individual volume constraint ($nc = 3$), as shown in Table 5.1.

To investigate the impact of the step number to initiate the selection algorithm (Algorithm 3), $N_{\text{select}}$, we choose $N_{\text{select}} = 1, 2, 20, 40, 60, 100, 200, 300, 360$. In all the cases, $\alpha_{\text{select}} = 0.05$, $\alpha_{\text{f}} = 0.005$, and we initiate the discrete filter at optimization step 365, $N_{\text{filter}} = 365$. Figure 5.4 shows the optimized objective function value for each $N_{\text{select}}$ and the final topologies from representative $N_{\text{select}}$. For comparison purposes, the optimized objective value and the final topology obtained from the multi-material formulation without the selection algorithm is also plotted in Figure 5.4. The data are summarized in Table 5.1.

Several observations can be made based on Figure 5.4 and Table 5.1. When the selection algorithm is not used, the final topology has the smallest objective function value and every member contains more than one material (18 overlapping connectivities). The cases applying the selection algorithm with $\alpha_{\text{select}} = 0.05$ lead to final topologies with single-material members and no overlapping connectivity for all $N_{\text{select}}$ values. The later we initiate the selection algorithm, the lower final objective function value obtained; in addition, initiating later tends to result in more complex structures and a higher computational time. Moreover, for the cases with $N_{\text{select}} \geq 100$, i.e., $N_{\text{select}} = 100, 200, 300, 360$, we obtain identical $J(\boldsymbol{x}_i^*)$ values and optimized structures. These observations suggest that initiating the selection algorithm early in the optimization process provides access to various solutions, while initiating it later in the optimization results in a similar solution. By varying $N_{\text{select}}$ to initiate the selection algorithm, various optimized structures with similar $J(\boldsymbol{x}_i^*)$ can be obtained, all without overlapping connectivity (i.e., each member contains a single material).

The next study demonstrates the effect of $\alpha_{\text{select}}$ on the optimization results. The

threshold, $\alpha_{\text{select}}$, determines if the material selection algorithm is performed on each connectivity. The value of $\alpha_{\text{select}}$ varies between $0 \leq \alpha_{\text{select}} \leq 1$, where $\alpha_{\text{select}} = 0$ corresponds to applying the selection algorithm to all the overlapping connectivities, and $\alpha_{\text{select}} = 1$ corresponds to never applying the selection algorithm. We choose $\alpha_{\text{select}} = 0, 0.01, 0.05, 0.1, 0.3, 0.5, 0.75, 1$. In this study, $N_{\text{select}} = 60$, $\alpha_f = 0.005$, and $N_{\text{filter}} = 365$. Figure 5.5 shows the optimized objective function value for each $\alpha_{\text{select}}$ and final topologies from representative $\alpha_{\text{select}}$. The data are summarized in Table 5.1.

We observe that larger $\alpha_{\text{select}}$ (more conservative, closer to 1) leads to a lower optimized objective function value. However, if $\alpha_{\text{select}} \geq 0.3$, the resulting structures contain members with more than one material. On the other hand, smaller threshold values (more drastic), e.g., $\alpha_{\text{select}} \leq 0.1$, lead to structures with single preferred material at every subdomain. The threshold, $\alpha_{\text{select}}$, allows the designer to choose the complexity of the design and whether the material profile contains either single materials or composite materials. For the examples in the remainder of this chapter, we choose $\alpha_{\text{select}} = 0.05$ for the selection algorithm unless otherwise stated to effectively and efficiently select a single material among multiple materials.

Table 5.1: Numerical information for Example 1 (see Figures 5.3, 5.4, and 5.5).

| Study of $N_{\text{select}}$ | | | | Study of $\alpha_{\text{select}}$ | | | |
|---|---|---|---|---|---|---|---|
| $N_{\text{select}}$ | $\alpha_{\text{select}}$ | $J(\boldsymbol{x}_i^*)$ | #Overlapping connectivities | $N_{\text{select}}$ | $\alpha_{\text{select}}$ | $J(\boldsymbol{x}_i^*)$ | #Overlapping connectivities |
| 1 | | 27.954 | | | 0.00 | 27.604 | 0 |
| 2 | | 27.501 | | | 0.01 | 27.487 | 0 |
| 20 | | 27.498 | | | 0.05 | 27.475 | 0 |
| 40 | | 27.487 | | | 0.10 | 27.452 | 0 |
| 60 | 0.05 | 27.475 | 0 | 60 | 0.30 | 27.432 | 4 |
| 100 | | 27.452 | | | 0.50 | 27.432 | 12 |
| 200 | | 27.452 | | | 0.75 | 27.432 | 12 |
| 300 | | 27.452 | | | 1.00 | 27.432 | 18 |
| 360 | | 27.452 | | | | | |

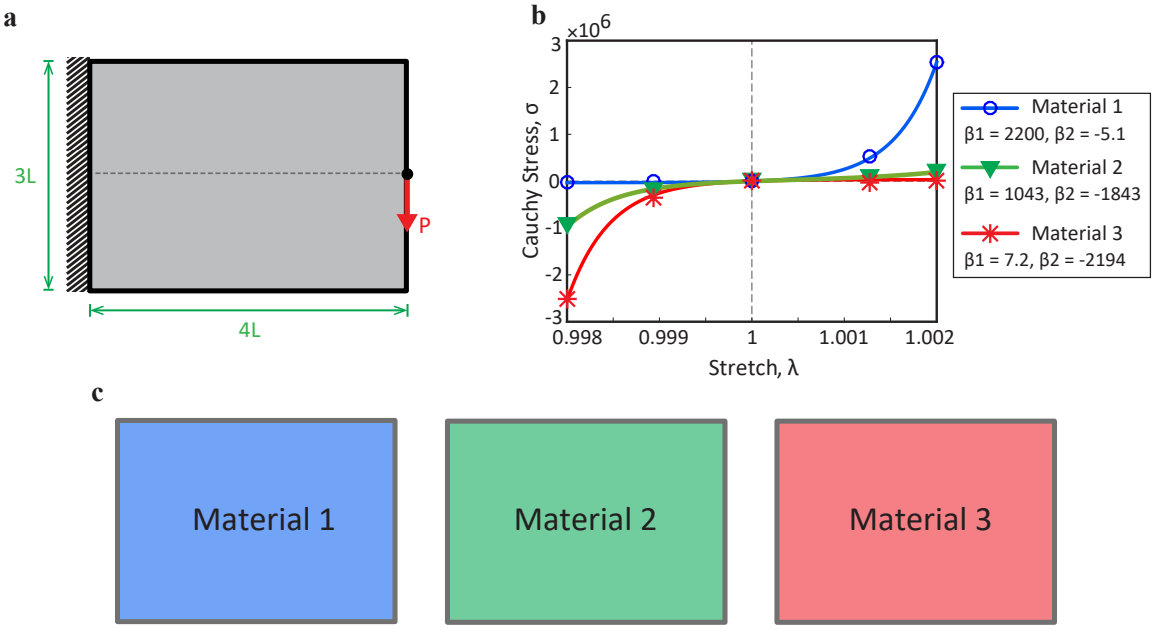


Figure 5.3: Example 1: Cantilever beam with three Odgen-based materials. **a** Design domain ($L = 2, P = 1000$); **b** material models: three Ogden-based materials; **c** initial material distribution: the three materials share the entire domain. (Online version in color.)

### 5.6.2 Opposite loads in a simply supported rectangular domain

This example demonstrates the selection algorithm using four Ogden-based materials in 2D and compares the optimized results with the multi-material case without the material selection algorithm (i.e., no control on the number of the materials selected for each connectivity). The design domain with load and boundary conditions ($L = 10, P = 1000$) and material models are shown in Figures 5.6a and 5.6b. Four materials share the entire domain (Figure 5.6c). Four layers (one for each material) of identical level-10 initial ground structures (based on a $30 \times 10$ grid) with a total of 78,528 members and 341 nodes are used. The total prescribed maximum volume takes the following value, $V_{\max} = 0.15$. Each material is associated with an individual volume constraint ($nc = 4$), as shown in Table 5.2. For the case employing the selection algorithm, we start to select preferred material at $N_{\text{select}} = 30$ with the ratio $\alpha_{\text{select}} = 0.05$. For both cases (with and without the selecting algorithm), the filter parameters are $\alpha_f = 0.001$ and $N_{\text{filter}} = 100$.

Both the optimized structures and convergence plots for the cases with and without

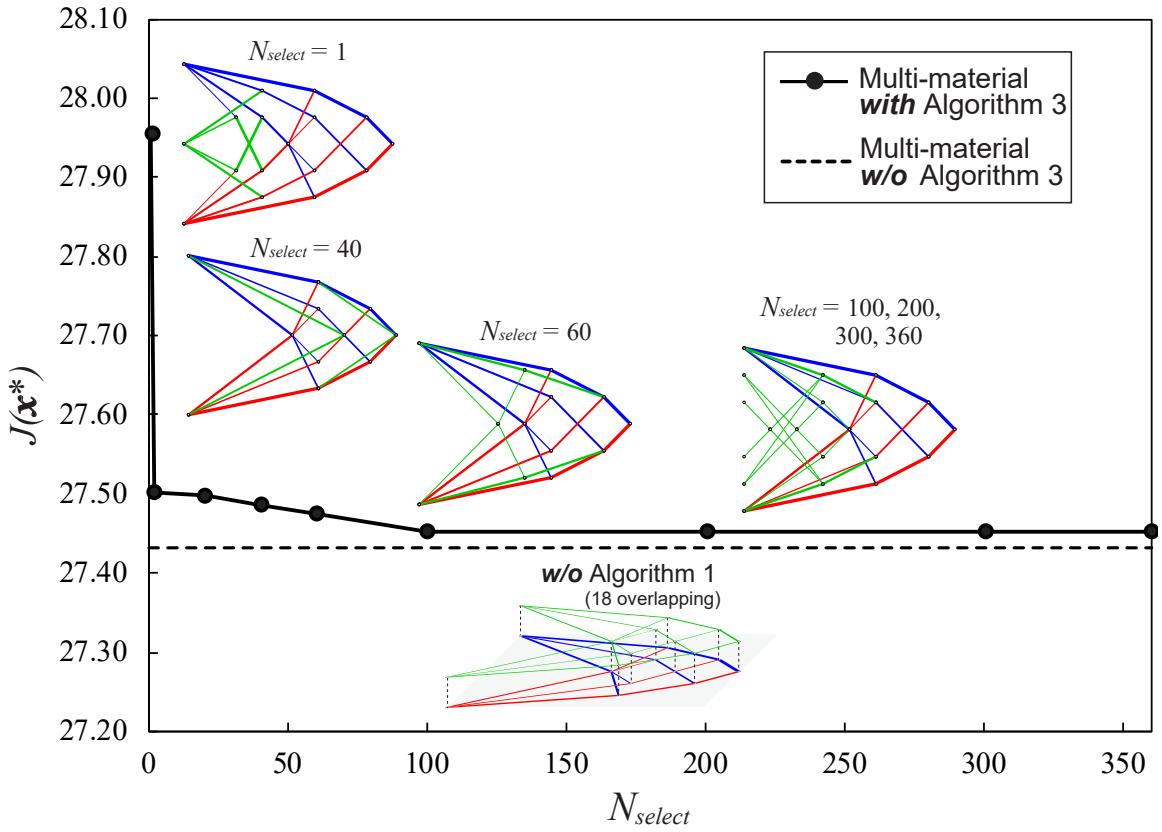


Figure 5.4: Example 1: Study of the step number to initiate the selecting algorithm, $N_{\text{select}}$, ($N_{\text{select}} = 1, 2, 20, 40, 60, 100, 200, 300, 360$) versus the resulting optimized objective value. The final topologies (from representative cases) are included. Other parameters: $\alpha_{\text{select}} = 0.05$, $\alpha_{\text{f}} = 0.005$, and $N_{\text{filter}} = 365$. (Online version in color.)

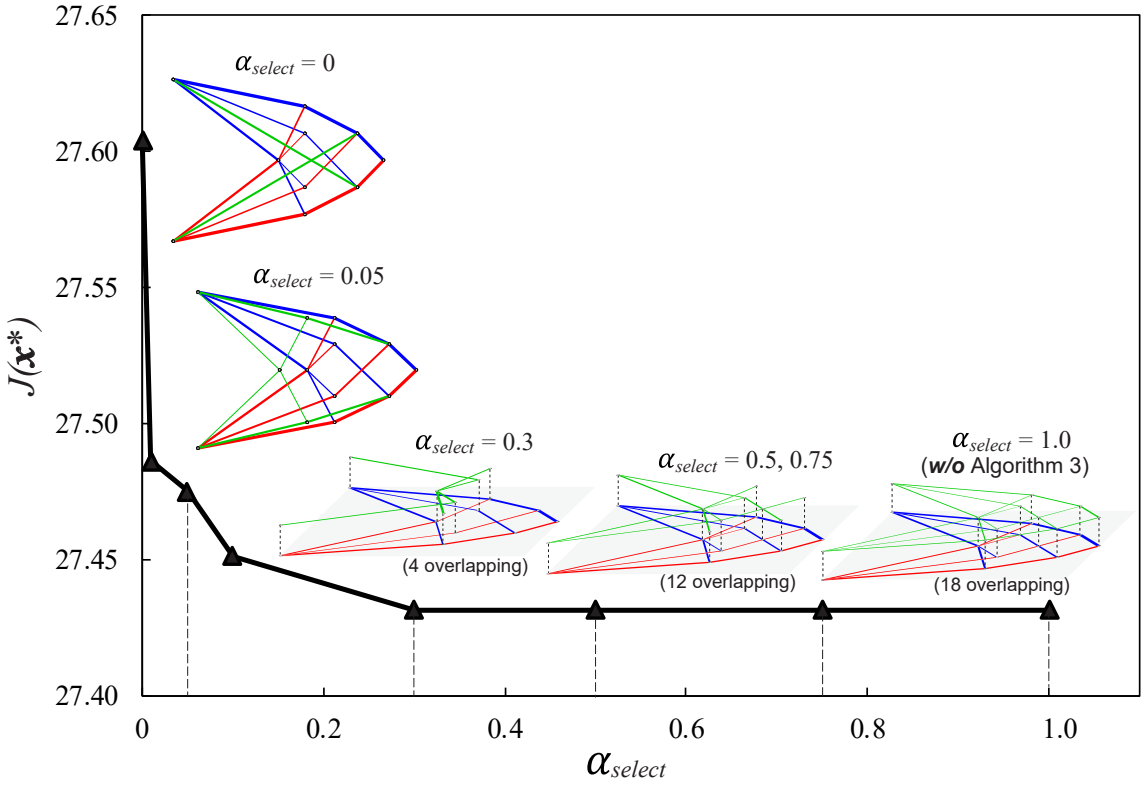


Figure 5.5: Example 1: Influence of $\alpha_{\text{select}}$ on the optimization results, $\alpha_{\text{select}}$ ($\alpha_{\text{select}} = 0, 0.01, 0.05, 0.1, 0.3, 0.5, 0.75, 1$) versus the resulting optimized objective value. The final topologies (from representative cases) are included. Other parameters: $N_{\text{select}} = 60$, $\alpha_f = 0.005$, and $N_{\text{filter}} = 365$. (Online version in color.)

enforcement of the selection of one material are shown in Figures 5.7a and b. The associated numerical information is summarized in Table 5.2. An optimized structure with every member containing more than one material (66 overlapping connectivities in total before removing aligned nodes) is obtained in the case without the selection algorithm. "Material 1" and "Material 4" are selected for the members in tension; "Material 2" and "Material 3" are selected for the members in compression. As shown in Figure 5.8, the multi-material framework with the selection algorithm leads to a structure in which members contain at most one material (no overlapping connectivity) and a slightly larger objective value. In addition, we observe an increase in the objective function at the step the selection algorithm is initiated, i.e. $N_{\text{select}} = 30$. This corresponds to the removal of certain overlapping members, as shown in Figure 5.7b. The convergence of the objective function at other steps is smooth.

Table 5.2: Numerical information for Example 1 (see Figures 5.6, 5.7, and 5.8).

| 2D cases | $J(\boldsymbol{x}_i^*)$ | Material | | Volume | # | #Overlapping |
|---|---|---|---|---|---|---|
| | | $\beta_1$ | $\beta_2$ | constraint, $V_{\max}^j$ | Elements | connectivities |
| 4 materials (standard) | 27.510 | 2200.3 | -5.1 | $0.4V_{\max}$ | 33 | 66 |
| | | 7.2 | -2194.0 | $0.4V_{\max}$ | 33 | |
| | | 1043.3 | -1843.1 | $0.1V_{\max}$ | 33 | |
| | | 1848.8 | -1039.2 | $0.1V_{\max}$ | 33 | |
| 4 materials (**Algorithm 3**) | 27.562 | 2200.3 | -5.1 | $0.4V_{\max}$ | 24 | 0 |
| | | 7.2 | -2194.0 | $0.4V_{\max}$ | 24 | |
| | | 1043.3 | -1843.1 | $0.1V_{\max}$ | 16 | |
| | | 1848.8 | -1039.2 | $0.1V_{\max}$ | 16 | |

### 5.6.3 Long-span bridge design using linear and bilinear materials

This multi-material bridge example illustrates the material selection algorithm using one linear and two bilinear material models. The design domain (with load and boundary conditions) is shown in Figure 5.9a. Two bilinear and one linear materials are used and share the entire domain, as shown in Figures 5.9b and 5.9c, leading to three identical layers of full-level initial ground structures (based on a $18 \times 7$ grid) with 21,249 non-overlapping

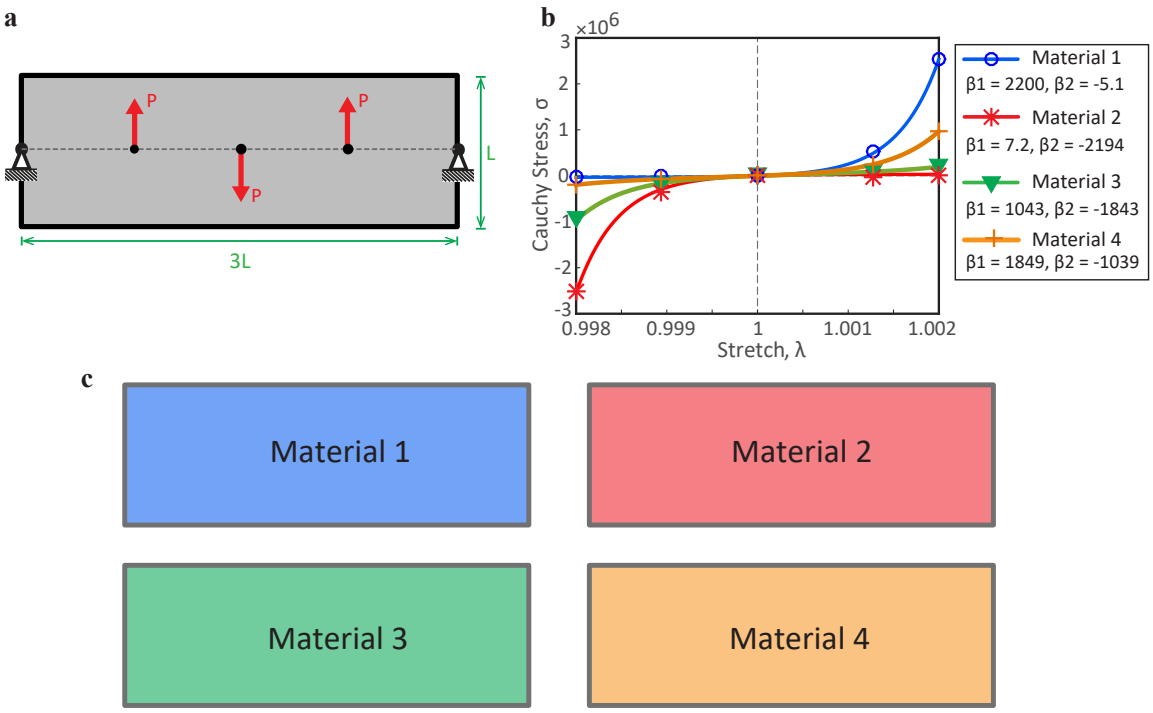


Figure 5.6: Example 2: Opposite loads in a simply supported rectangular domain. **a** Design domain ($L = 10, P = 1000$); **b** material models: four Ogden-based materials; **c** initial material distribution: four materials share the entire domain. (Online version in color.)

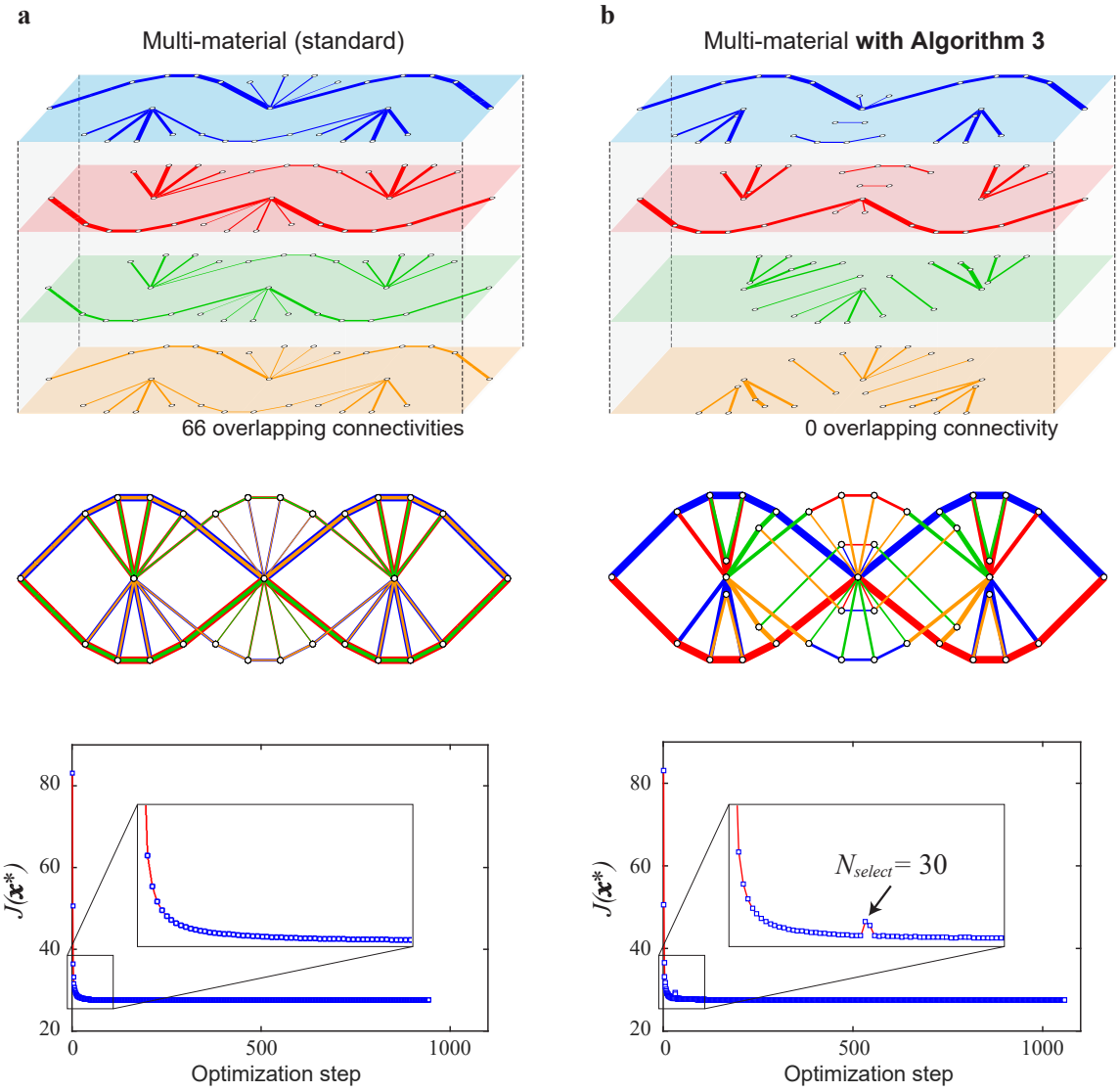


Figure 5.7: Example 2: Opposite loads in a simply supported rectangular domain. **a** Optimized structure and convergence plot without the proposed selection algorithm ($\alpha_f = 0.001$, $N_{\text{filter}} = 100$) that contains 66 overlapped connectivities (before removing aligned nodes); **b** optimized structure and convergence plot with the proposed selection algorithm ($\alpha_{\text{select}} = 0.05$, $N_{\text{select}} = 30$, $\alpha_f = 0.001$, $N_{\text{filter}} = 100$) that selects a single material among multiple materials – no overlapping connectivity is observed in the final design. (Online version in color.)

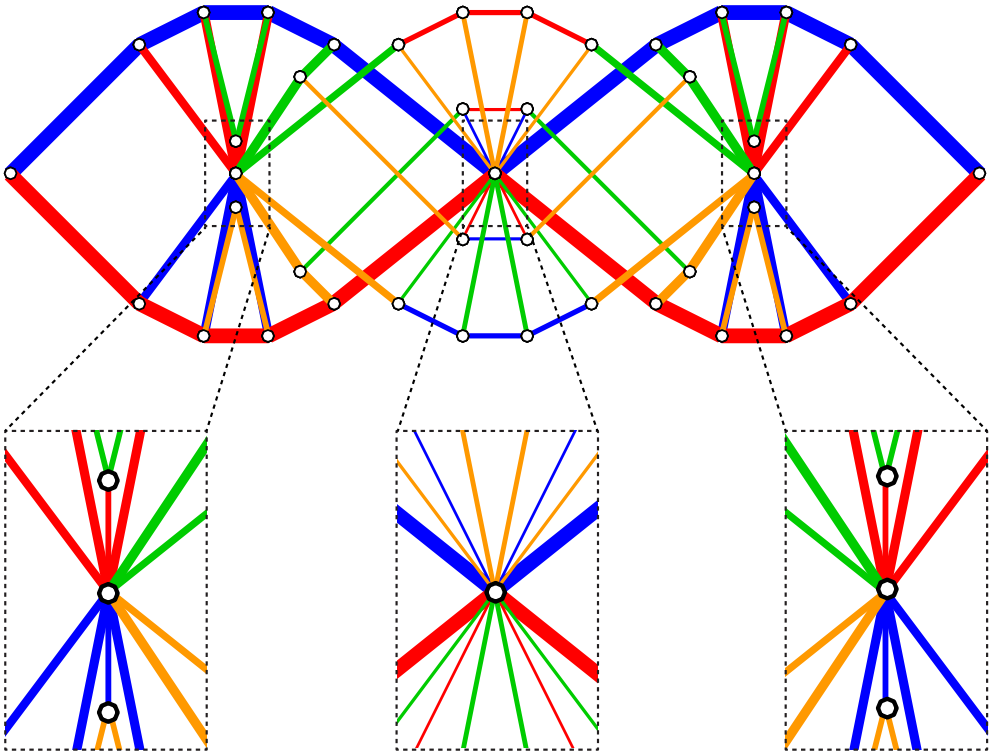

Figure 5.8: Example 2: Zoom-in regions of the optimized structure obtained from the proposed selection algorithm, no overlapping connectivity is observed in the final design. (Online version in color.)

members and 152 nodes. Each material is assigned to an individual volume constraint, see Table 5.3. Here we optimize the bridge problem with and without the proposed algorithm that removes overlapped members from multiple materials. In the case employing the selection algorithm, we choose $N_{\text{select}} = 30$, $\alpha_{\text{select}} = 0.05$. For both cases (with and without the selection algorithm), the filter parameters are $\alpha_f = 0.001$ and $N_{\text{filter}} = 100$.

The optimized structures for the case with and without the enforcement of the selection of one material are shown in Figures 5.10a and b. The associated numerical information is summarized in Table 5.3. The results verify the proposed algorithm that selects a single preferred material. In the optimized structure, we observe that the selection of more than one material for some truss members (i.e., overlapping of truss members from different materials) occurs in the case without the proposed selection algorithm. This leads to an optimized bridge design that contains 25 overlapped composite members and a smaller objective value. This optimized structure contains members with "composite" materials – "Material 2" and "Material 3" are selected for the members in compression. On the other hand, the case with the proposed algorithm leads to the result containing no overlapped members and larger objective value.

Table 5.3: Numerical information for Example 3 (see Figures 5.9 and 5.10), $E_o = 10^7$.

| 2D cases | $J(\boldsymbol{x}_i^*)$ | Material | | Volume | # | # Overlap. |
|---|---|---|---|---|---|---|
| | | $E_t$ | $E_c$ | constraint, $V_{\max}^j$ | Elements | connect. |
| 3 materials | | $17E_o$ | $0.001E_o$ | $0.4V_{\max}$ | 35 | |
| (standard) | 20.920 | $7E_o$ | $7E_o$ | $0.1V_{\max}$ | 25 | 25 |
| | | $0.002E_o$ | $2E_o$ | $0.5V_{\max}$ | 25 | |
| 3 materials | | $17E_o$ | $0.001E_o$ | $0.4V_{\max}$ | 42 | |
| (**Algorithm 3**) | 21.417 | $7E_o$ | $7E_o$ | $0.1V_{\max}$ | 11 | 0 |
| | | $0.002E_o$ | $2E_o$ | $0.5V_{\max}$ | 16 | |

### 5.6.4 Three-dimensional cantilever beam

Using a combination of different materials, we apply the proposed material selection algorithm to a 3D cantilever beam. The geometry, load, and boundary conditions ($L = 1, P =$

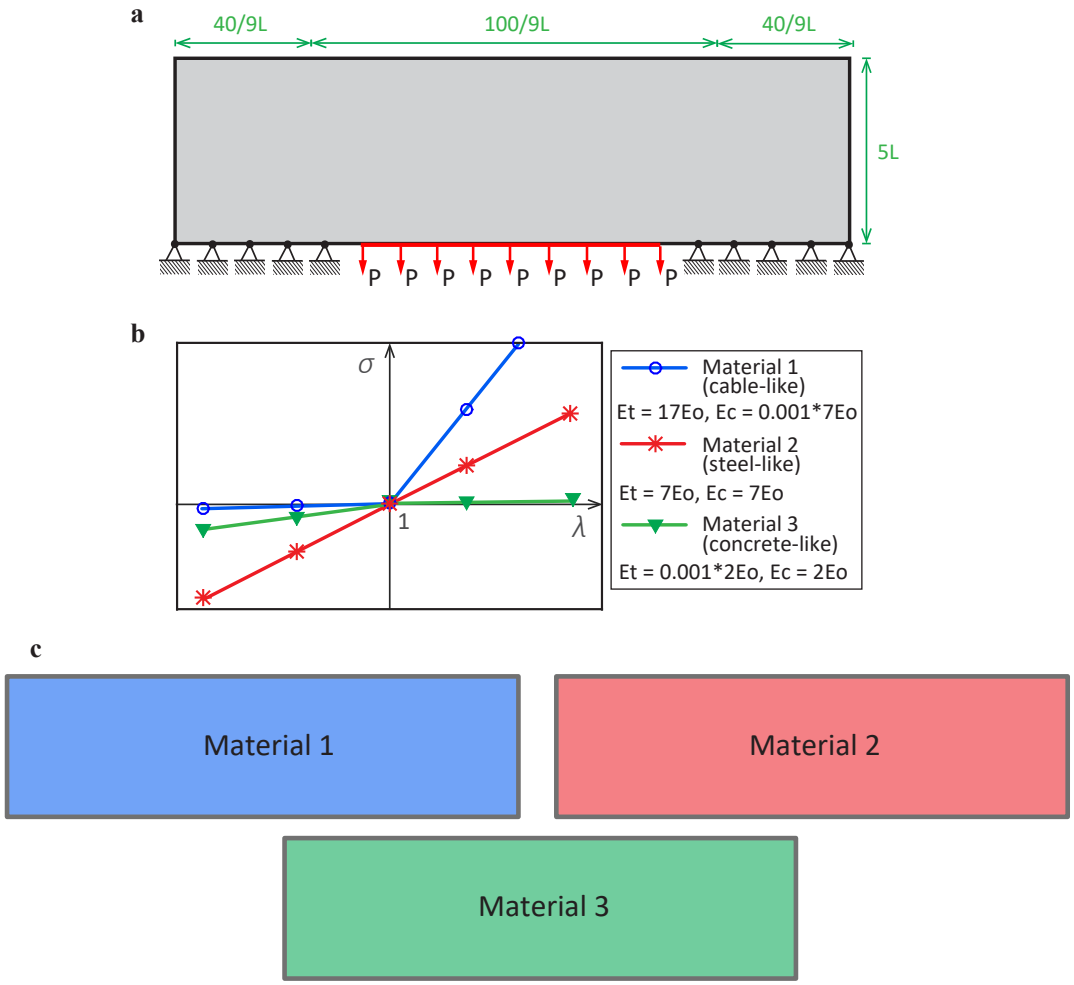


Figure 5.9: Example 3: Multi-material bridge design. **a** Design domain; **b** material models: two bilinear and one linear materials; **c** initial material distribution for each material. (Online version in color.)

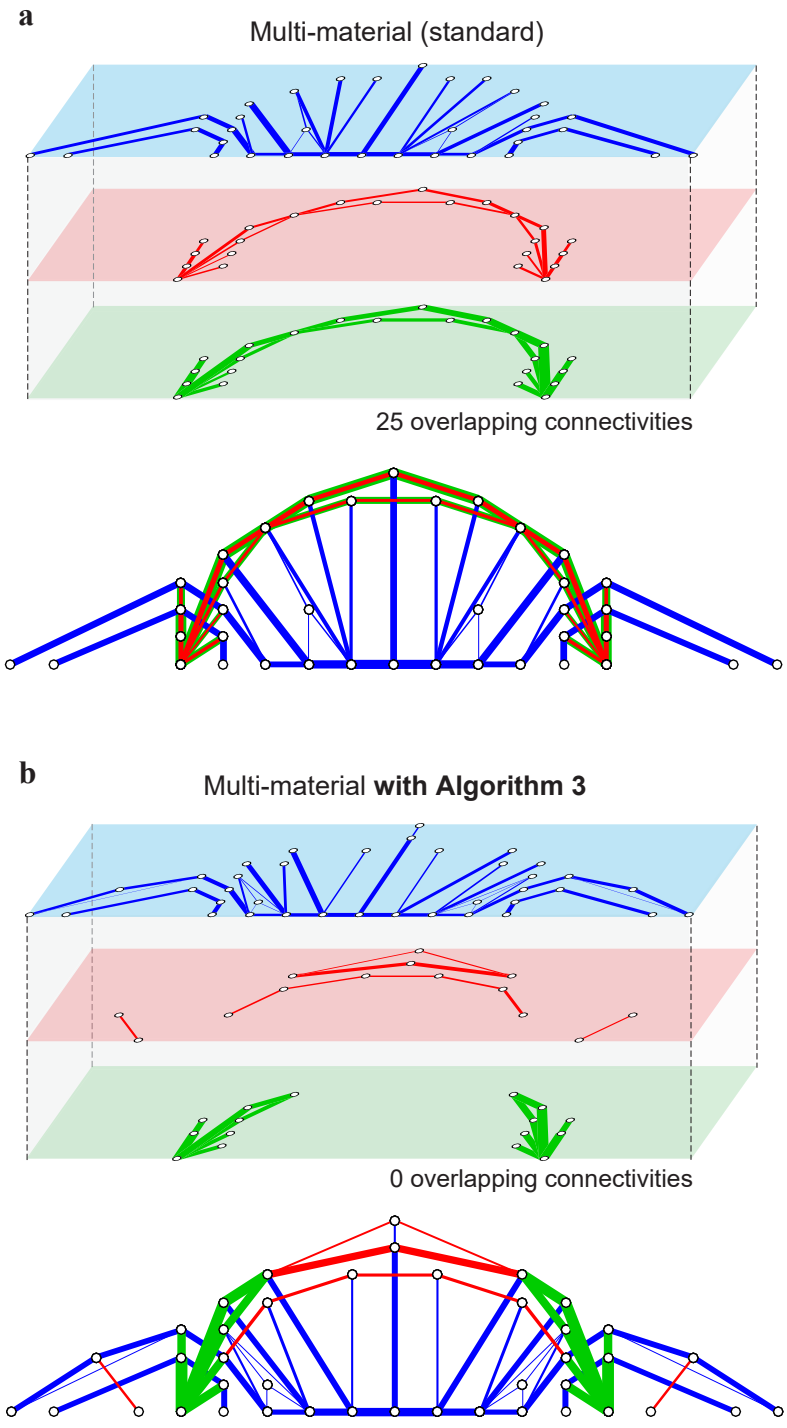


Figure 5.10: Example 3: Multi-material bridge design. **a** Optimized bridge design without the selection algorithm contains 25 overlapped connectivities ($\alpha_f = 0.001$, $N_{\text{filter}} = 100$); **b** optimized bridge design with the proposed selection algorithm that selects a single material among multiple materials at each subdomain ($\alpha_{\text{select}} = 0.05$, $N_{\text{select}} = 30$, $\alpha_f = 0.001$, $N_{\text{filter}} = 100$). (Online version in color.)

60) are shown in Figure 5.11a. To obtain constructible structures, we use a $6 \times 2 \times 2$ discretization (with a level 3 GS) for the domain containing 5,000 members and 63 nodes. We perform optimization with four Ogden-based materials, as shown in Figure 5.11b, and these four materials share the entire domain. Four volume constraints are used ($nc = 4$). The total prescribed maximum volume takes the following value, $V_{\max} = 0.024$. For the selection algorithm, we choose $N_{\text{select}} = 30$, $\alpha_{\text{select}} = 0.05$ and initiate the filter at $N_{\text{filter}} = 60$. In addition to a small filter ($\alpha_f = 10^{-4}$) used throughout the optimization, we use a larger filter ($\alpha_f = 10^{-2}$) in the final step of the optimization to control the resolution of the final topology.

The optimized structure for the case with enforcing the selection of one material is shown in Figure 5.12. The associated numerical information is summarized in Table 5.4. The result indicates that the multi-material framework with the material selection algorithm can also effectively produce a structure with single-material members (i.e., no overlapping connectivity) in three dimensions.

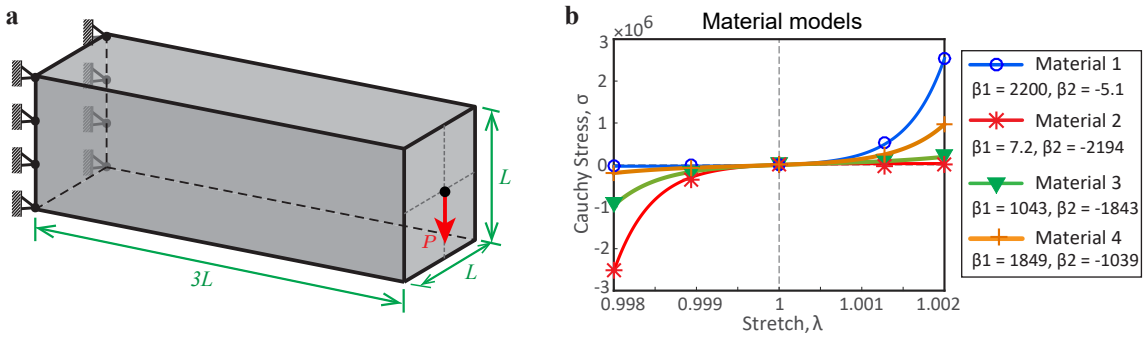


Figure 5.11: Three-dimensional multi-material cantilever beam design. **a** Design domain discretized using a $6 \times 2 \times 2$ grid; **b** material models: four Ogden-based materials. (Online version in color.)

## 5.7 Summary and Discussion

In this chapter, we investigate the issue of selecting more than one material that occurs in multi-material topology optimization in the context of truss layout optimization. We

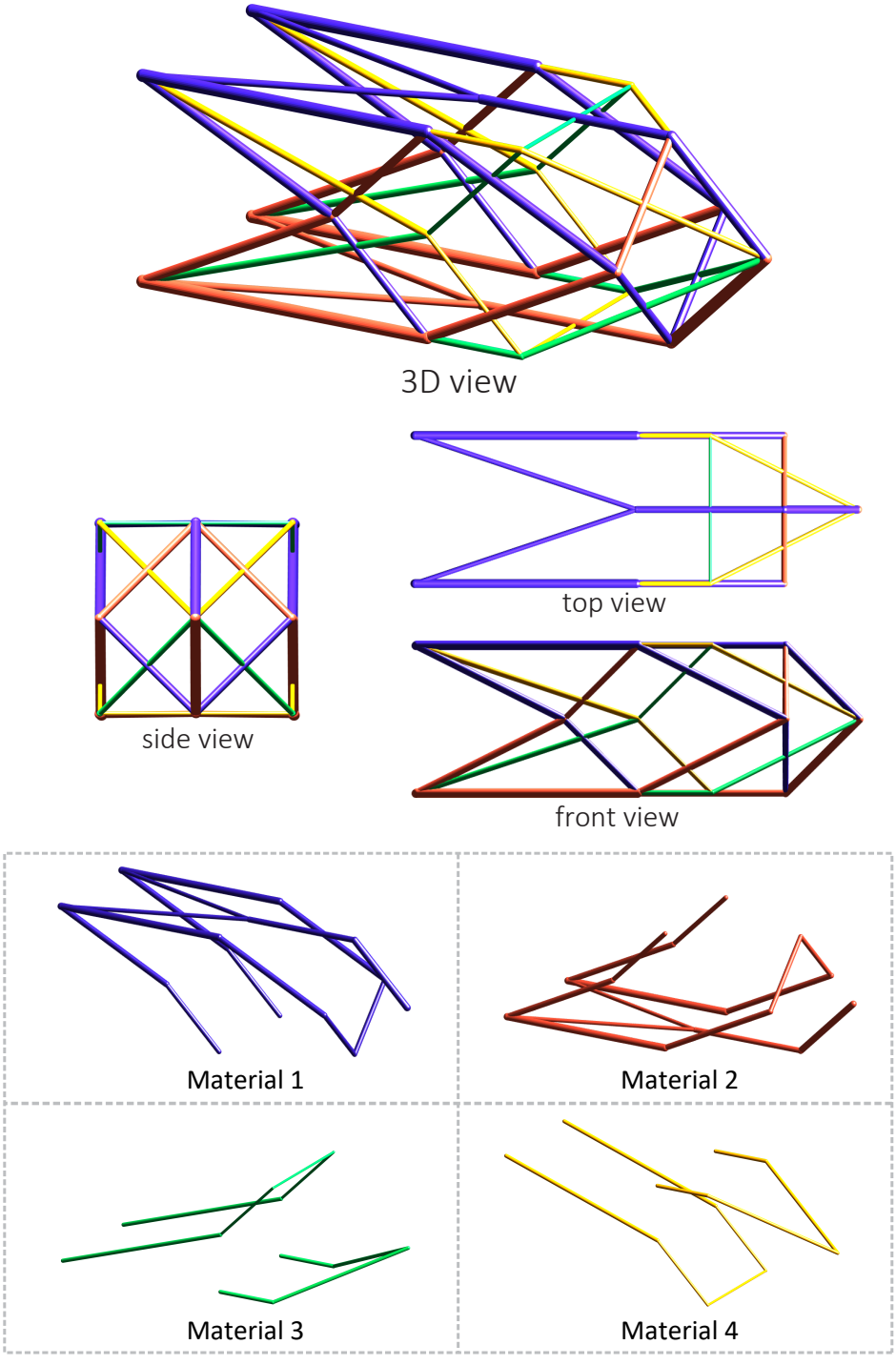


Figure 5.12: The optimized structure for the 3D cantilever design with the selection algorithm (enforcing the selection of one material) with $\alpha_{\text{select}} = 0.05$, $N_{\text{select}} = 30$, $\alpha_f = 0.0001$ (optimization), $\alpha_f = 0.01$ (end), $N_{\text{filter}} = 30$; no overlapping connectivity is observed in the final design. (Online version in color.)

Table 5.4: Numerical information for Example 4 (see Figures 5.11 and 5.12)

| 3D case | $J(\boldsymbol{x}_i^*)$ | Material | | Volume | # | #Overlapping |
|---|---|---|---|---|---|---|
| | | $\beta_1$ | $\beta_2$ | constraint, $V_{\max}^j$ | Elements | connectivities |
| 4 materials (**Algorithm 3**) | 51.01 | 2200.3 | -5.1 | $0.4V_{\max}$ | 14 | 0 |
| | | 7.2 | -2194.0 | $0.4V_{\max}$ | 14 | |
| | | 1043.3 | -1843.1 | $0.1V_{\max}$ | 9 | |
| | | 1848.8 | -1039.2 | $0.1V_{\max}$ | 9 | |

examine the conditions (need to be satisfied simultaneously) in which the selection of multiple materials on a certain connectivity occurs, i.e., more than one material sharing the domain, each of them associated with an individual volume constraint, and one material being stronger at least within a certain range of stretch values. To ensure the selection of a single material at each subdomain, we propose an algorithm (Algorithm 3) that selects a preferred material among multiple materials based on the evaluation of both the strain energy and cross-sectional area of each member. This algorithm actively and iteratively selects materials to ensure the selection of single material for each member. The Zhang-Paulino-Ramos (ZPR) design variable update scheme for multi-material optimization is employed, and we provide an alternative derivation of this update scheme using the KKT conditions.

Using combinations of Ogden-based, bilinear, and linear materials, we verify the proposed selection algorithm and compare the results to the ones obtained without using the selection algorithm. We also demonstrate that the algorithmic parameters, i.e., the step number to initiate and the threshold of the selection algorithm, allow the designers to control both the complexity of the final design as well as the final material profile to use either single materials or composite materials. We conclude that the material selection algorithm for multi-material topology optimization is efficient and effective for selecting a single preferred material per overlapping set.

# CHAPTER 6

# STOCHASTIC SAMPLING FOR DETERMINISTIC STRUCTURAL TOPOLOGY OPTIMIZATION WITH MANY LOAD CASES: DENSITY-BASED AND GROUND STRUCTURE FORMULATIONS

We propose an efficient probabilistic method to solve a fully deterministic problem – we present a randomized optimization approach that drastically reduces the enormous computational cost of optimizing designs under many load cases for both continuum and truss topology optimization. Practical structural designs by deterministic topology optimization typically involve many load cases, possibly hundreds or more. The optimal design minimizes a, possibly weighted, average of the compliance under each load case (or some other objective). This means that, in each optimization step, a large finite element problem must be solved for each load case, leading to an enormous computational effort. On the contrary, the proposed randomized optimization method with stochastic sampling requires the solution of only a few (e.g., 5 or 6) finite element problems (large linear systems) per optimization step. Based on simulated annealing, we introduce a damping scheme for the randomized approach. Through numerical examples in two and three dimensions, we demonstrate that the randomization algorithm drastically reduces computational cost to obtain similar final topologies and results (e.g., compliance) to those of standard algorithms. The results indicate that the damping scheme is effective and leads to rapid convergence of the proposed algorithm.

## 6.1 Introduction

Structural topology optimization is an important tool that, if properly used, can lead to significantly improved designs. In the field of structural topology optimization, designs accounting for many load cases are common practice [73]. Indeed, real-world structural

designs, for example, high-rise buildings and long-span bridges, generally involve numerous load cases [73]. For the end-compliance minimization formulation, several methods that include many load cases have been published [30], [132], [133]. The main idea is to minimize a proper norm of the vector of compliances from all load cases. This chapter concentrates on one popular method, the weighted sum formulation that minimizes a weighted sum of the vector of compliances from all load cases, which requires the solution of the structural equation for each load case. Another formulation that accounts for many load cases is the min-max formulation, which minimizes the worst-case compliance of all load cases, i.e., the infinity norm of the vector of compliances [30], [134]. This formulation also requires the solution of a large system of linear equations for each load case. Therefore, in terms of computational cost, it is similar to the aforementioned weighted sum formulation. In this chapter, we propose a randomized algorithm that drastically reduces the computational cost. Similar techniques have been applied to solve inverse problems – see [135]–[137] and references therein, and least squares problems – see [138] and references therein. More general randomization techniques, especially randomized linear algebra, such as trace estimation and matrix decomposition, are discussed and surveyed in [139]–[142]. In [143], Avron and Toledo discuss and derive bounds on several trace estimators and prove a bound on the number of samples required to guarantee a chosen accuracy. Their results are improved and extended by Roosta-Khorasani and Ascher [144]. More recently, Saibaba et al. [145] present randomized algorithms for estimates of the trace and determinant of positive semidefinite Hermitian matrices. Their algorithms yield more accurate estimates; but the estimates are not unbiased. *We emphasize that the use of random samples in our algorithm does not reflect any uncertainty in the load cases but instead arises from a stochastic optimization approach that avoids solving for a large number of load cases in each optimization step. In our proposed algorithm, randomization is used to solve a deterministic optimization problem with deterministic loads that remain fixed throughout the optimization process.* Thus, our randomized algorithm is conceptually different from

robust topology optimization approaches (see, e.g., [146]–[148]), in which the uncertainty of the loads is characterized by probability distributions.

The remainder of the chapter is organized as follows. We finish this section with a brief review of the weighted sum formulation of the standard nested minimum end-compliance topology optimization with many load cases, using both the density-based method and the ground structure method (GSM). Section 2 reviews the stochastic sampling techniques we use to estimate the trace of a general matrix and proposes the randomized algorithm for minimum end-compliance topology optimization under many load cases. Section 3 discusses the algorithmic parameters and introduces a damping scheme for the randomized algorithm. Section 4 presents numerical examples in two and three dimensions highlighting the efficiency and effectiveness of the proposed algorithm, and Section 5 provides concluding remarks with suggestions for extending the work.

### 6.1.1 Density-based topology optimization formulation with many load cases

For a set of $m_\ell$ given load cases $\boldsymbol{f}_i, i = 1, ..., m_\ell$, the standard weighted sum formulation for the minimum end-compliance design with many load cases using the density-based method can be written as [30],

$$\begin{aligned} \min_{\boldsymbol{\rho}} C(\boldsymbol{\rho}) &= \min_{\boldsymbol{\rho}} \sum_{i=1}^{m_\ell} w_i \, \boldsymbol{f}_i^T \boldsymbol{u}_i(\boldsymbol{\rho}), \\ \text{s.t.} \quad & g(\bar{\boldsymbol{\rho}}) = \sum_{e=1}^{M} V^{(e)} \bar{\rho}^{(e)} - V_{\max} \leq 0, \\ & 0 < \rho_{\min} \leq \rho^{(e)} \leq 1, \, e = 1, ..., M, \\ & \text{with } \boldsymbol{u}_i(\bar{\boldsymbol{\rho}}) = \boldsymbol{K}(\boldsymbol{E}(\bar{\boldsymbol{\rho}}))^{-1} \boldsymbol{f}_i, \, i = 1, ..., m_\ell . \end{aligned} \tag{6.1}$$

In this minimization problem, the objective function $C$ is the weighted-average compliance of the corresponding structure, $\boldsymbol{\rho} \in \mathbb{R}^M$ is the vector of design variables (the density field), and $M$ is the number of elements in the finite element mesh. We define $\bar{\boldsymbol{\rho}}$ and $\boldsymbol{H}$ as the filtered physical density and the filter matrix such that $\bar{\boldsymbol{\rho}} = \boldsymbol{H}\boldsymbol{\rho}$ [42]. In order to ensure

a positive definite stiffness matrix $\boldsymbol{K} \in \mathbb{R}^{dN \times dN}$, a lower bound $\rho_{\min}$ is prescribed on $\rho^{(e)}$, where $N$ is the number of nodes and $d$ is the dimension of the problem, so $dN$ is the number of degrees of freedom. The volume (area) of element $e$ is given by $V^{(e)}$, and $V_{\max}$ is the prescribed upper bound on the total volume. The weight and the displacement vector associated with load case $\boldsymbol{f}_i \in \mathbb{R}^{dN}$ are given by $w_i$ ($w_i > 0, \sum_{i=1}^{m_\ell} w_i = 1$) and $\boldsymbol{u}_i \in \mathbb{R}^{dN}$, respectively. The Young's modulus $\boldsymbol{E}$ is defined by, for example, the Solid Isotropic Material with Penalization (SIMP) [43], [44] approach. Other models, e.g., RAMP (Rational Approximation of Material Properties) [30], [45], can be used and would not alter the conceptual presentation of the topic. For the SIMP approach with the density filter, we have $E^{(e)} = [\bar{\rho}^{(e)}]^p (E_0)$, where $E_0$ is the elastic modulus for solid material, and $p$ is a penalization factor. The gradient (sensitivity) of the objective function corresponds to a weighted sum of the sensitivities of each individual loading case, which can be expressed as

$$\nabla C_\rho^{(e)} = \frac{\partial C}{\partial \rho^{(e)}} = -\sum_{i=1}^{m_\ell} w_i \, \boldsymbol{u}_i^T \frac{\partial \boldsymbol{K}}{\partial \rho^{(e)}} \boldsymbol{u}_i. \tag{6.2}$$

The formulation (6.1) is known to be convex when $p = 1$ [46]. Using $p > 1$ to obtain a solid-void solution, one makes the problem non-convex and, as expected, the solution obtained from the optimization algorithm may not be the global minimum.

### 6.1.2 Ground-structure based formulation with many load cases

The standard weighted sum formulation for the minimum end-compliance design with the ground structure method (GSM) under many load cases takes the following form,

$$\begin{aligned} \min_{\boldsymbol{x}} C(\boldsymbol{x}) &= \min_{\boldsymbol{x}} \sum_{i=1}^{m_\ell} w_i \, \boldsymbol{f}_i^T \boldsymbol{u}_i(\boldsymbol{x}), \\ \text{s.t.} \quad & g(\boldsymbol{x}) = \sum_{e=1}^{M} L^{(e)} x^{(e)} - V_{\max} \leq 0, \\ & 0 < x_{\min} \leq x^{(e)} \leq x_{\max}, \, e = 1, ..., M, \\ & \text{with } \boldsymbol{u}_i(\boldsymbol{x}) = \boldsymbol{K}(\boldsymbol{x})^{-1} \boldsymbol{f}_i, \, i = 1, ..., m_\ell. \end{aligned} \tag{6.3}$$

The vector $\boldsymbol{x} \in \mathbb{R}^M$ is a vector of design variables, with component $x^{(e)}$ being the cross-sectional area of truss member $e$. It is subjected to lower bound $x_{\min}$ and upper bound $x_{\max}$. Furthermore, $M$ is the number of truss members in the ground structure (GS), $L^{(e)}$ is the length of truss member $e$, and $V_{\max}$ is the prescribed upper bound on the total volume. For the $i$th load case $\boldsymbol{f}_i \in \mathbb{R}^{dN}$, $w_i$ and $\boldsymbol{u}_i \in \mathbb{R}^{dN}$ are the corresponding weight factor and displacement vector. As in the density-based method, the sensitivity of the objective function in the GSM is the weighted sum of the sensitivities from each load case:

$$\nabla C_x^{(e)} = \frac{\partial C}{\partial x^{(e)}} = -\sum_{i=1}^{m_\ell} w_i \boldsymbol{u}_i^T \frac{\partial \boldsymbol{K}}{\partial x^{(e)}} \boldsymbol{u}_i. \tag{6.4}$$

The standard nested formulation of the end-compliance objective function with a single load case has been proven to be convex in [37] for a positive definite stiffness matrix and in [38] for a positive semi-definite stiffness matrix. The formulation (6.3) with multiple load cases is easily proven to be convex.

### 6.1.3 Synopsis

The optimization algorithm contains three main components: solving the structural equilibrium problem for a set of given design variables, computing the gradient of the objective function, and updating the design variables. In this chapter, we use the density-based and GS methods – both methods utilize the Optimality Criterion (OC) algorithm [70] as the update scheme, which only requires gradient information of the objective function and the volume constraint. The convergence criterion for optimization used in formulations (6.1) and (6.3) is that the maximum change in design variables drops below a given tolerance, $\tau_{\text{opt}}$.

The overall computational cost of the standard optimization formulations (6.1) and (6.3) can be estimated by the total number of structural equations (large linear system) solves, i.e., $m_\ell \times N_{\text{step}}$, where $N_{\text{step}}$ is the number of optimization steps. For realistic three-

dimensional (3D) problems, where the mesh size, the number of design variables, and the number of load cases are large, the associated computational cost is enormous. Thus, in this chapter, we propose a randomized approach that reduces the problem with many load cases ($m_\ell$) to a sequence of optimization steps with only a few load cases ($n \ll m_\ell$) to solve per step and that yields results similar to those from the standard weighted sum approach.

## 6.2 Stochastic Sampling and Topology Optimization

This section proposes a stochastic sampling approach for the minimum end-compliance topology optimization formulations with many load cases. First, we briefly review a stochastic sampling technique to estimate the trace of a general matrix. Then, the stochastic sampling technique is applied to the minimum end-compliance topology optimization with many load cases using both density-based and GS methods.

### 6.2.1 Stochastic sampling of matrices

For a general matrix $\boldsymbol{A} \in \mathbb{R}^{q\times q}$, stochastic sampling techniques can be used to estimate the trace of $\boldsymbol{A}$. We discuss one popular approach here, the Hutchinson trace estimator [139], but several alternatives exist, e.g., the Gaussian estimators and unit vector estimators – see [143], [144] and references therein. Let $\boldsymbol{\xi} \in \mathbb{R}^q$ be a random vector containing entries that are independent and identically distributed (i.i.d.) with value $\pm 1$ each with probability $1/2$. This distribution is known as the Rademacher distribution. It follows immediately that, for each entry, the expectation $\mathbb{E}(\xi_i) = 0$. Because the entries are independent, the expectation of $\xi_i \xi_j$ is given by,

$$\mathbb{E}\left(\xi_i \xi_j\right) = \begin{cases} 0\,, & \mathrm{i} \neq \mathrm{j}\,, \\ \\ 1\,, & \mathrm{i} = \mathrm{j}\,. \end{cases} \tag{6.5}$$

Now consider the expectation of the random variable $\boldsymbol{\xi}^T \boldsymbol{A} \boldsymbol{\xi}$,

$$\mathbb{E}\left(\boldsymbol{\xi}^T \boldsymbol{A} \boldsymbol{\xi}\right) = \mathbb{E}\left(\sum_{i=1}^{q}\sum_{j=1}^{q} \xi_i A_{ij} \xi_j\right) = \sum_{i=1}^{q}\sum_{j=1}^{q} A_{ij}\,\mathbb{E}\left(\xi_i \xi_j\right). \tag{6.6}$$

Because $\mathbb{E}\left(\xi_i \xi_j\right) = 1$ only when $i = j$, and 0 otherwise, we get

$$\mathbb{E}\left(\boldsymbol{\xi}^T \boldsymbol{A} \boldsymbol{\xi}\right) = \sum_{i=1}^{q} A_{ii} = \operatorname{trace}\left(\boldsymbol{A}\right). \tag{6.7}$$

As a result, the trace of a given matrix $\boldsymbol{A}$ can be estimated using random samples. Here, we utilize the sample average approximation (SAA) technique, see, e.g., [149], which approximates the expected value by the average. The sample average or empirical mean for $n$ samples (or realizations) $\boldsymbol{\xi}_1, \boldsymbol{\xi}_2, ..., \boldsymbol{\xi}_n$, of the random variable $\boldsymbol{\xi}$ is defined as

$$\mathbb{E}_S\left(\boldsymbol{\xi}^T \boldsymbol{A} \boldsymbol{\xi}\right) = \frac{1}{n}\sum_{k=1}^{n} \boldsymbol{\xi}_k^T \boldsymbol{A} \boldsymbol{\xi}_k. \tag{6.8}$$

According to the Law of Large Numbers (LLN) [150], as the number of (independent) samples $n$ approaches $\infty$, the sample average $\mathbb{E}_S\left(\boldsymbol{\xi}^T \boldsymbol{A} \boldsymbol{\xi}\right)$ converges to the expectation $\mathbb{E}\left(\boldsymbol{\xi}^T \boldsymbol{A} \boldsymbol{\xi}\right)$, which is the trace of $\boldsymbol{A}$,

$$\mathbb{E}_S\left(\boldsymbol{\xi}^T \boldsymbol{A} \boldsymbol{\xi}\right) = \frac{1}{n}\sum_{k=1}^{n} \boldsymbol{\xi}_k^T \boldsymbol{A} \boldsymbol{\xi}_k \to \mathbb{E}\left(\boldsymbol{\xi}^T \boldsymbol{A} \boldsymbol{\xi}\right) = \operatorname{trace}\left(\boldsymbol{A}\right). \tag{6.9}$$

The use of trace estimators can be highly efficient if the matrix $\boldsymbol{A}$ is not explicitly available and its computation is expensive. We also have that $\mathbb{E}_S\left(\boldsymbol{\xi}^T \boldsymbol{A} \boldsymbol{\xi}\right)$ is an unbiased estimator of $\mathbb{E}\left(\boldsymbol{\xi}^T \boldsymbol{A} \boldsymbol{\xi}\right)$ [149]. Because the expected accuracy of such estimates is given by the variance, the goal is to obtain the estimates with the smallest variance. The Rademacher distribution, from which we choose the random vectors $\boldsymbol{\xi}$, was shown in [139] to be the distribution that yields the smallest variance. Other studies rank various trace estimators differently according to criteria other than the variance. For further information, readers are

referred to, e.g., [143], [144]. For a symmetric matrix $\boldsymbol{A}$, the variance of $\boldsymbol{\xi}^T\boldsymbol{A}\boldsymbol{\xi}$ is derived as

$$\begin{aligned}
\mathrm{Var}\left(\boldsymbol{\xi}^T\boldsymbol{A}\boldsymbol{\xi}\right) &= \mathbb{E}\left\{\left[\boldsymbol{\xi}^T\boldsymbol{A}\boldsymbol{\xi} - \mathbb{E}\left(\boldsymbol{\xi}^T\boldsymbol{A}\boldsymbol{\xi}\right)\right]^2\right\} = \mathbb{E}\left\{\left[\sum_{i=1}^{q}\sum_{j=1}^{q}\xi_i A_{ij}\xi_j - \sum_{i=1}^{q}A_{ii}\right]^2\right\} \\
&= \mathbb{E}\left\{\left[\sum_{\substack{i,j=1\\ i\neq j}}^{q}\xi_i A_{ij}\xi_j\right]^2\right\} = \mathbb{E}\left\{\sum_{\substack{i,j=1\\ i\neq j}}^{q}\sum_{\substack{k,l=1\\ k\neq l}}^{q}A_{ij}A_{kl}\xi_i\xi_j\xi_k\xi_l\right\} \\
&= \sum_{\substack{i,j=1\\ i\neq j}}^{q}\sum_{\substack{k,l=1\\ k\neq l}}^{q}A_{ij}A_{kl}\,\mathbb{E}\left\{\xi_i\xi_j\xi_k\xi_l\right\} = \sum_{\substack{i,j=1\\ i\neq j}}^{q}\sum_{\substack{k,l=1\\ k\neq l}}^{q}A_{ij}A_{kl}(\delta_{ik}\delta_{jl}+\delta_{il}\delta_{jk}) \\
&= \sum_{\substack{i,j=1\\ i\neq j}}^{q}(A_{ij}A_{ij}+A_{ij}A_{ji}) = 2\sum_{\substack{i,j=1\\ i\neq j}}^{q}A_{ij}^2,
\end{aligned} \tag{6.10}$$

where $\delta_{ij}$ is the Kronecker delta function. In addition, the standard deviation of $\boldsymbol{\xi}^T\boldsymbol{A}\boldsymbol{\xi}$ is given by

$$\mathrm{Dev}\left(\boldsymbol{\xi}^T\boldsymbol{A}\boldsymbol{\xi}\right) = \sqrt{\mathrm{Var}\left(\boldsymbol{\xi}^T\boldsymbol{A}\boldsymbol{\xi}\right)} = \sqrt{2\sum_{\substack{i,j=1\\ i\neq j}}^{q}A_{ij}^2}. \tag{6.11}$$

The variance and standard deviation can be estimated using a finite number of samples. Given the samples above, we define the sample variance and sample standard deviation as

$$\mathrm{Var}_S\left(\boldsymbol{\xi}^T\boldsymbol{A}\boldsymbol{\xi}\right) = \frac{1}{n}\sum_{k=1}^{n}\left[\boldsymbol{\xi}_k^T\boldsymbol{A}\boldsymbol{\xi}_k - \frac{1}{n}\sum_{\ell=1}^{n}\boldsymbol{\xi}_\ell^T\boldsymbol{A}\boldsymbol{\xi}_\ell\right]^2, \tag{6.12}$$

and

$$\mathrm{Dev}_S\left(\boldsymbol{\xi}^T\boldsymbol{A}\boldsymbol{\xi}\right) = \sqrt{\frac{1}{n}\sum_{k=1}^{n}\left[\boldsymbol{\xi}_k^T\boldsymbol{A}\boldsymbol{\xi}_k - \frac{1}{n}\sum_{\ell=1}^{n}\boldsymbol{\xi}_\ell^T\boldsymbol{A}\boldsymbol{\xi}_\ell\right]^2}. \tag{6.13}$$

Below, we use these derivations for estimating the objective function (the compliance), as well as its gradient or sensitivity. A key issue for efficiency is that both can be estimated with the same set of random vectors.

### 6.2.2 Randomized topology optimization with stochastic sampling

We apply the stochastic sampling technique to both the density-based method and the GSM. The basic idea is to replace the compliance and its gradient by stochastic estimates and to use these estimates in the optimization algorithm.

*Density-based method*

Consider the standard topology optimization formulation in (6.1) with $m_\ell$ load cases $\boldsymbol{f}_i$, $i = 1, ..., m_\ell$, and corresponding weights $w_i$. We define a weighted load matrix $\boldsymbol{F} \in \mathbb{R}^{dN \times m}$ as $\boldsymbol{F} = \left[\sqrt{w_1}\boldsymbol{f}_1, ..., \sqrt{w_m}\,\boldsymbol{f}_m\right]$. In a similar fashion, we define the weighted displacement matrix $\boldsymbol{U} \in \mathbb{R}^{dN \times m} = \left[\sqrt{w_1}\,\boldsymbol{u}_1, ..., \sqrt{w_m}\,\boldsymbol{u}_m\right]$, whose columns are the corresponding displacement fields. The matrix $\boldsymbol{U}$ is defined by the equilibrium equation, $\boldsymbol{U} = \boldsymbol{K}^{-1}\boldsymbol{F}$. So, we can write the end-compliance and its sensitivities as traces of symmetric matrices

$$C(\boldsymbol{\rho}) = \sum_{i=1}^{m_\ell} w_i \boldsymbol{f}_i^T \boldsymbol{u}_i = \text{trace}\left(\boldsymbol{F}^T \boldsymbol{U}\right) = \text{trace}\left(\boldsymbol{F}^T \boldsymbol{K}^{-1} \boldsymbol{F}\right) \tag{6.14}$$

and

$$\nabla C_{\boldsymbol{\rho}}^{(e)} = -\sum_{i=1}^{m_\ell} w_i \boldsymbol{u}_i{}^T \frac{\partial \boldsymbol{K}}{\partial \rho^{(e)}} \boldsymbol{u}_i = -\,\text{trace}\left(\boldsymbol{U}^T \frac{\partial \boldsymbol{K}}{\partial \rho^{(e)}} \boldsymbol{U}\right) = -\,\text{trace}\left(\boldsymbol{F}^T \boldsymbol{K}^{-1} \frac{\partial \boldsymbol{K}}{\partial \rho^{(e)}} \boldsymbol{K}^{-1} \boldsymbol{F}\right). \tag{6.15}$$

With the random variable $\boldsymbol{\xi}$ as defined above, the end-compliance and the topology optimization problem can be expressed as

$$C(\boldsymbol{\rho}) = \text{trace}\left(\boldsymbol{F}^T \boldsymbol{K}^{-1} \boldsymbol{F}\right) = \mathbb{E}\left(\boldsymbol{\xi}^T \boldsymbol{F}^T \boldsymbol{K}^{-1} \boldsymbol{F} \boldsymbol{\xi}\right) = \mathbb{E}\left[\left(\boldsymbol{F}\boldsymbol{\xi}\right)^T \boldsymbol{K}^{-1} \left(\boldsymbol{F}\boldsymbol{\xi}\right)\right], \tag{6.16}$$

and

$$\begin{aligned} \min_{\boldsymbol{\rho}} C(\boldsymbol{\rho}) &= \min_{\boldsymbol{\rho}} \mathbb{E}\left[(\boldsymbol{F}\boldsymbol{\xi})^T \boldsymbol{K}(\boldsymbol{\rho})^{-1}(\boldsymbol{F}\boldsymbol{\xi})\right], \\ \text{s.t.} \quad & g(\bar{\boldsymbol{\rho}}) = \sum_{e=1}^{M} V^{(e)}\rho^{(e)} - V_{\max} \leq 0, \\ & 0 < \rho_{\min} \leq \rho^{(e)} \leq 1, e = 1, ..., M. \end{aligned} \tag{6.17}$$

The sensitivity of the objective function can be expressed as

$$\nabla C_{\boldsymbol{\rho}}^{(e)} = -\operatorname{trace}\left(\boldsymbol{F}^T \boldsymbol{K}^{-1} \frac{\partial \boldsymbol{K}}{\partial \rho^{(e)}} \boldsymbol{K}^{-1} \boldsymbol{F}\right) = -\mathbb{E}\left[(\boldsymbol{F}\boldsymbol{\xi})^T \boldsymbol{K}^{-1} \frac{\partial \boldsymbol{K}}{\partial \rho^{(e)}} \boldsymbol{K}^{-1} (\boldsymbol{F}\boldsymbol{\xi})\right]. \tag{6.18}$$

Equations (6.17) and (6.18), stated as a stochastic programming problem, are equivalent to the standard formulation (6.1) and (6.2). We approximate the compliance and its gradient by replacing their expectation in the equations above by their sample average estimates. Given the i.i.d. random sample $\boldsymbol{\xi}_1, \boldsymbol{\xi}_2, ..., \boldsymbol{\xi}_n$ as $n$ realizations of the random vector $\boldsymbol{\xi}$, we define

$$\widehat{C}^S(\boldsymbol{\rho}) = \frac{1}{n} \sum_{k=1}^{n} (\boldsymbol{F}\boldsymbol{\xi}_k)^T \boldsymbol{K}(\boldsymbol{\rho})^{-1} (\boldsymbol{F}\boldsymbol{\xi}_k), \tag{6.19}$$

and

$$(\nabla \widehat{C}_{\boldsymbol{\rho}}^S)^{(e)} = \frac{\partial \widehat{C}^S}{\partial \rho^{(e)}} = -\frac{1}{n} \sum_{k=1}^{n} (\boldsymbol{F}\boldsymbol{\xi}_k)^T \boldsymbol{K}^{-1} \frac{\partial \boldsymbol{K}}{\partial \rho^{(e)}} \boldsymbol{K}^{-1} (\boldsymbol{F}\boldsymbol{\xi}_k). \tag{6.20}$$

We remark that $\widehat{C}^S(\boldsymbol{\rho})$ and $\nabla \widehat{C}_{\boldsymbol{\rho}}^S$ are unbiased estimators for the compliance and its gradient. By the LLN, $\widehat{C}^S(\boldsymbol{\rho}) \to C(\boldsymbol{\rho})$ and $\nabla \widehat{C}_{\boldsymbol{\rho}}^S \to \nabla C_{\boldsymbol{\rho}}$ (with probability 1) for any feasible $\boldsymbol{\rho}$ as $n \to \infty$ [151].

Within each step of the optimization algorithm, we use the same random vectors to estimate the compliance and its gradient using (6.19) and (6.20). However, to avoid convergence for a specific random load case, a new set of $n$ random vectors is selected at each optimization step. If $n \ll m_\ell$, our proposed algorithm reduces the computational cost from $m_\ell \times N_{\text{step}}$ to roughly $n \times N_{\text{step}}$ if the convergence of the optimization is not affected.

The idea to approximate the gradient and the objective function in a structural optimization problem is similar to the use of stochastic gradient-based methods in other areas,

e.g., stochastic gradient descent (SGD) [152], and stochastic meta-descent (SMD) [153], which are optimization methods mainly for unconstrained optimization problems. Stochastic gradient methods use small sub-samples (also referred as mini-batches) to estimate the gradient and have been applied in other fields, such as large-scale machine learning [154], [155]. For our application, the SAA gradient estimate always has a positive angle with the gradient, and hence the negative SAA gradient estimate is a descent direction for the unconstrained case. We demonstrate numerically how effective the approximation is in Section 4. Because the optimization problem for the density-based method with penalization is non-convex, deterministic gradient-based methods may not converge to the global minimum (as expected). The randomized approach leads to solutions that are (roughly) as accurate in terms of the end-compliance as those from the standard weighted sum approach. This is demonstrated by the results in Section 4.2.

In general, for stochastic gradient methods, a damping or averaging scheme (also referred to as a decay schedule of the scalar gain or gain vector adaptation) is needed to achieve convergence [155]. Various damping or averaging methods for step sizes have been proposed for different types of problems [156]. For the structural optimization problems in this chapter, we propose a damping scheme that adjusts the move limits (reminiscent of a trust region), which especially befits the structural optimization framework. The idea of the proposed damping scheme is similar to adjusting the size of the update in simulated annealing [157], [158] and is discussed in detail in Section 6.3.1. Robbins and Monro [152] have given conditions for the convergence of stochastic gradient methods that use such damping schemes; see also [155]. A more recent (and accessible) chapter discussing the convergence of stochastic gradient methods in detail, and considering more general cases than Robbins and Monro [152], is the one by Bottou, Curtis and Nocedal [159].

The numerical results (see Section 4) show that the convergence of the proposed approach is typically rapid if our damping scheme is properly used, roughly as fast as for the standard weighted sum approach and sometimes faster. Because the randomized ap-

proach solves only $n$ linear systems at each optimization step, compared with $m_\ell$ for the standard weighted sum approach, and $n \ll m_\ell$, the proposed randomized approach is computationally much more efficient. Moreover, randomized approaches with a proper damping scheme can be more robust in finding the global minimum for non-convex optimization problems than deterministic algorithms. We demonstrate this with numerical examples in Section 4. In general, such increased robustness comes at the price of slower convergence.

To analyze the effects of randomization on the proposed approaches, we consider the variance and sample variance for the compliance estimate and its gradient.

$$\mathrm{Var}\left[(\boldsymbol{F}\boldsymbol{\xi})^T \boldsymbol{K}^{-1}(\boldsymbol{F}\boldsymbol{\xi})\right] = 2\sum_{\substack{i,j=1 \\ i\neq j}}^{m_\ell} \left(\boldsymbol{F}^T\boldsymbol{K}^{-1}\boldsymbol{F}\right)_{ij}^2, \tag{6.21}$$

and

$$\mathrm{Var}\left[(\boldsymbol{F}\boldsymbol{\xi})^T \boldsymbol{K}^{-1}\frac{\partial \boldsymbol{K}}{\partial \rho^{(e)}}\boldsymbol{K}^{-1}(\boldsymbol{F}\boldsymbol{\xi})\right] = 2\sum_{\substack{i,j=1 \\ i\neq j}}^{m_\ell} \left(\boldsymbol{F}^T\boldsymbol{K}^{-1}\frac{\partial \boldsymbol{K}}{\partial \rho^{(e)}}\boldsymbol{K}^{-1}\boldsymbol{F}\right)_{ij}^2. \tag{6.22}$$

Similarly, the sample variance of the compliance and its gradient can be expressed as

$$\mathrm{Var}_S\left[(\boldsymbol{F}\boldsymbol{\xi})^T \boldsymbol{K}^{-1}(\boldsymbol{F}\boldsymbol{\xi})\right] = \frac{1}{n}\sum_{k=1}^{n}\left(\boldsymbol{\xi}_k^T\boldsymbol{F}^T\boldsymbol{K}^{-1}\boldsymbol{F}\boldsymbol{\xi}_k - \frac{1}{n}\sum_{\ell=1}^{n}\boldsymbol{\xi}_\ell^T\boldsymbol{F}^T\boldsymbol{K}^{-1}\boldsymbol{F}\boldsymbol{\xi}_\ell\right)^2, \tag{6.23}$$

and

$$\begin{aligned}&\mathrm{Var}_S\left[(\boldsymbol{F}\boldsymbol{\xi})^T \boldsymbol{K}^{-1}\frac{\partial \boldsymbol{K}}{\partial \rho^{(e)}}\boldsymbol{K}^{-1}(\boldsymbol{F}\boldsymbol{\xi})\right] \\ &= \frac{1}{n}\sum_{k=1}^{n}\left(\boldsymbol{\xi}_k^T\boldsymbol{F}^T\boldsymbol{K}^{-1}\frac{\partial \boldsymbol{K}}{\partial \rho^{(e)}}\boldsymbol{K}^{-1}\boldsymbol{F}\boldsymbol{\xi}_k - \frac{1}{n}\sum_{\ell=1}^{n}\boldsymbol{\xi}_\ell^T\boldsymbol{F}^T\boldsymbol{K}^{-1}\frac{\partial \boldsymbol{K}}{\partial \rho^{(e)}}\boldsymbol{K}^{-1}\boldsymbol{F}\boldsymbol{\xi}_\ell\right)^2.\end{aligned} \tag{6.24}$$

*Ground structure method*

A randomized version of the optimization problem for the GSM with the weighted force matrix $\boldsymbol{F}$ is analogous to that for the density-based method (6.17). The minimization problem for the GSM is given by

$$\begin{aligned} \min_{\boldsymbol{x}} C(\boldsymbol{x}) &= \min_{\boldsymbol{x}} \mathbb{E}\left[ (\boldsymbol{F}\boldsymbol{\xi})^T \boldsymbol{K}(\boldsymbol{x})^{-1} (\boldsymbol{F}\boldsymbol{\xi}) \right], \\ \text{s.t.} \quad g(\boldsymbol{x}) &= \sum_{e=1}^{M} L^{(e)} x^{(e)} - V_{\max} \leq 0, \\ & 0 < x_{\min} \leq x^{(e)} \leq x_{\max}, \, e = 1, ..., M, \end{aligned} \tag{6.25}$$

and the sensitivity of the objective function can be expressed as,

$$\nabla C_{\boldsymbol{x}}^{(e)} = -\mathbb{E}\left[ (\boldsymbol{F}\boldsymbol{\xi})^T \boldsymbol{K}^{-1} \frac{\partial \boldsymbol{K}}{\partial x^{(e)}} \boldsymbol{K}^{-1} (\boldsymbol{F}\boldsymbol{\xi}) \right]. \tag{6.26}$$

Here too, we replace the objective function and its gradient by their sample average approximation. Using the same assumptions, for an i.i.d. random sample $\boldsymbol{\xi}_1, \boldsymbol{\xi}_2, ..., \boldsymbol{\xi}_n$, the compliance $C(\boldsymbol{x})$ and its gradient can be estimated by

$$\widehat{C}^S(\boldsymbol{x}) = \frac{1}{n} \sum_{k=1}^{n} (\boldsymbol{F}\boldsymbol{\xi}_k)^T \boldsymbol{K}(\boldsymbol{x})^{-1} (\boldsymbol{F}\boldsymbol{\xi}_k), \tag{6.27}$$

and

$$(\nabla \widehat{C}_{\boldsymbol{x}}^S)^{(e)} = \frac{\partial \widehat{C}^S}{\partial x^{(e)}} = -\frac{1}{n} \sum_{k=1}^{n} (\boldsymbol{F}\boldsymbol{\xi}_k)^T \boldsymbol{K}^{-1} \frac{\partial \boldsymbol{K}}{\partial x^{(e)}} \boldsymbol{K}^{-1} (\boldsymbol{F}\boldsymbol{\xi}_k), \tag{6.28}$$

where $\widehat{C}^S(\boldsymbol{x})$ and $(\nabla \widehat{C}_{\boldsymbol{x}}^S)^{(e)}$ are the estimated compliance and estimated sensitivity of the corresponding structure analogous to (6.19) and (6.20). The variance and sample variance of the objective function and its sensitivity take the same form as (6.21)-(6.24), and therefore are not listed. Because the standard optimization formulation for the GSM is convex, it has a unique global minimum. Hence, we expect the approximated minima obtained with the randomized method to be equal to or larger than the one obtained from the standard

formulation. This is confirmed by the results in Section 4.

We conclude this subsection by making a remark on the flexibility of our proposed randomized algorithm for topology optimization. This algorithm can be combined with many types of update schemes that are based on gradient information, such as the Optimality Criterion (OC) method [70] and the Method of Moving Asymptotes (MMA) [71]. In this work, because the estimated sensitivities in (6.20) and (6.28) are guaranteed to be non-positive, we adopt OC as the update scheme for both continuum and truss topology optimization. The OC method is a highly efficient update scheme that is tailored for self-adjoint problems and widely used in topology optimization: see, e.g. [160]–[162].

### 6.2.3 Discrete filter for ground structure method with stochastic sampling

In the GSM, a discrete filter similar to the filter proposed in [85] (see below) is applied to the truss topology optimization with both the standard and the randomized algorithms to extract valid structures out of ground structures. The use of the discrete filter reduces the number of redundant bars and the size of the structural problem within each solve, which reduces the cost of subsequent optimization steps. For the standard multiple load case optimization problem (6.3), the discrete filter is expressed in (3.5). The parameter $\alpha_f$ is the prescribed filter value and $x_k^{(e)}$ is the design variable for truss member $e$ at the $k$th step. The discrete filter is applied to the GS at each step and removes the truss members with normalized areas smaller than the filter parameter $\alpha_f$.

For the randomized algorithm for the GSM, we define a discrete filter that slightly differs from the standard discrete filter. To avoid inadvertent removal of truss members due to an (occasional) poor estimate in the randomized algorithm, the discrete filter removes truss members only when their normalized areas have remained below the prescribed filter

value for $n_f$ steps, namely,

$$Filter^S\left(\boldsymbol{x}_k, \alpha_f\right) = \begin{cases} 0, & \text{if} \quad \max\left(\frac{x^{(e)}_{k-n_f+1}}{\max\left(\boldsymbol{x}_{k-n_f+1}\right)}, ..., \frac{x^{(e)}_k}{\max(\boldsymbol{x}_k)}\right) < \alpha_f < 1\,, \\ x^{(e)}_k, & \text{otherwise}, \end{cases} \tag{6.29}$$

where $Filter^S(\boldsymbol{x}_k, \alpha_f)$ denotes the filter for the randomized algorithm, and $n_f$ is a chosen number of monitored steps (see the discussion of parameters below). The use of the filter for the randomized algorithm ($Filter^S$) leads to a more efficient GSM with stochastic sampling than if the filter were not used (see numerical examples section).

## 6.3 A Damping Scheme and Algorithmic Parameters for Randomized Optimization

This section introduces a damping scheme to facilitate convergence and demonstrates the effectiveness of this scheme through a three-bar truss example. We further discuss the algorithmic parameters that are used in the proposed randomized optimization framework and comment on the range of values chosen for those parameters.

### 6.3.1 The proposed damping scheme: effective step ratio and step size reduction

In the randomized algorithm, the structure must be adjusted based on the random linear combination of load cases that changes at each optimization step. Therefore, the convergence criteria commonly used for the standard structural optimization framework are insufficient for the proposed framework. Based on ideas from simulated annealing [157], [158], we propose a damping scheme that evaluates the average progress per step and reduces the move limit (similar to the scalar gain in SGD) accordingly. We define the effective step ratio $R$ as follows (using the GSM notation):

$$R = \frac{\frac{1}{n_{\text{step}}} || \left(\boldsymbol{x}_k - \boldsymbol{x}_{k-n_{\text{step}}+1}\right) ||}{||\boldsymbol{x}_k - \boldsymbol{x}_{k-1}||}, \tag{6.30}$$

where $n_{\text{step}}$ is the sample window size (see below). The average step size over a sample window is divided by the current step length. This effective step ratio serves as an indicator of the optimizer's status, i.e., the ratio is relatively large when the optimizer is making progress; and relatively small (typically smaller than 0.1) when the step is not effective. Once $R$ is below a prescribed tolerance $\tau_{\text{step}}$, i.e., $R < \tau_{\text{step}}$, we reduce the allowable move limit of the optimizer by a prescribed scale factor $\gamma$. The move limit is not adjusted in the first $n_{\text{step}}$ optimization steps.

The effectiveness of the damping scheme is illustrated through a simple numerical example for the GSM. This example is not representative for the effectiveness of the randomized algorithm; it is selected to emphasize the poor performance of the randomized optimization algorithm without a damping scheme. We consider a three-bar truss structure supported at their left ends and subjected to a set of 9 equal-weighted load cases, $\boldsymbol{f}_1, \ldots, \boldsymbol{f}_9$, at their right joint, as shown in Figure 6.1. The problem formulation is given as follows:

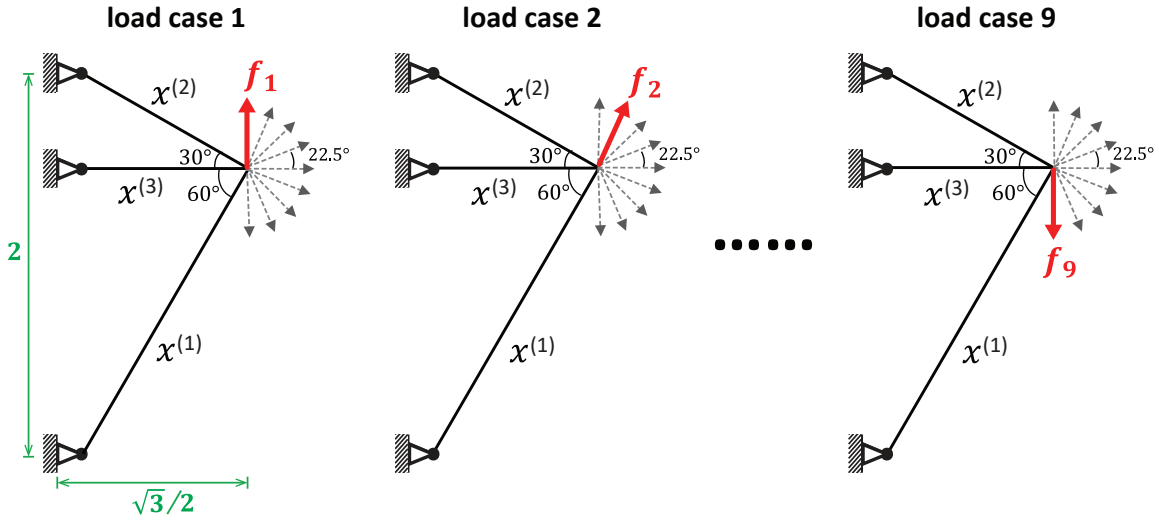


Figure 6.1: Three-bar truss structure under 9 load cases: initial ground structure, load and boundary conditions.

$$
\begin{aligned}
&\min_{\boldsymbol{x}} C(\boldsymbol{x}) = \sum_{i=1}^{9} \boldsymbol{f}_i^T \boldsymbol{u}_i(\boldsymbol{x}), \\
\text{s.t.} \quad &\sum_{e=1}^{3} L^{(e)} x^{(e)} - V_{\max} \leq 0, \\
&0 < x_{\min} \leq x^{(e)} \leq x_{\max},\ e = 1, ..., 3, \\
&\text{with } \boldsymbol{u}_i(\boldsymbol{x}) = \boldsymbol{K}(\boldsymbol{x})^{-1} \boldsymbol{f}_i,\ i = 1, ..., 9.
\end{aligned}
\tag{6.31}
$$

We set the volume constraint as $V_{\max} = 0.1$, and take initial guess as $x_0 = V_{\max} / \sum_e L^{(e)} = 0.0278$. In addition, we choose the lower and upper bounds to be $x_{\min} = 10^{-8} x_0$ and $x_{\max} = 10^4 x_0$, respectively. The initial move limit is taken as $move = 10^{-1} x_0$. The tolerance for convergence of the optimization is $10^{-8}$. For the randomized algorithm, we choose the sample size as $n = 6$ (i.e., 6 sample load cases), and select a new sample at each iteration.

We use the proposed randomized algorithm with and without the damping scheme. The contour plots of the objective function with the optimization history of $x^{(1)}$ and $x^{(2)}$ ($x^{(3)}$ can be computed from the volume constraint because, in practice, the sum of volumes will always be equal to $V_{\max}$) for both cases are shown in Figures 6.2a and 6.2b. The optimization history from the standard weighted sum approach is plotted for reference. The standard approach obtains the global minimum of the given problem within 25 steps where $\boldsymbol{x}^* = \left[x^{(1)}, x^{(2)}, x^{(3)}\right]^T = [0.0344, 0.0290, 0.0132]^T$ and $C(\boldsymbol{x}^*) = 8.1666$. The randomized algorithm without damping does not converge, and the updates become ineffective after roughly 10 steps (Figure 6.2a). The randomized algorithm with our damping scheme converges to $\widehat{\boldsymbol{x}}^S = [0.0343, 0.0290, 0.0134]^T$ with $C(\widehat{\boldsymbol{x}}^S) = 8.1667$. This is close to the optimal solution obtained by the standard algorithm. The results are summarized in Table 6.1. For this small problem, we use $n_{\text{step}} = 10$, $\tau_{\text{step}} = 0.05$, and $\gamma = 2$. Because the solution of this example is relatively trivial, the randomized algorithm with our damping scheme converges slower than the standard algorithm. For more complicated and realistic problems (e.g., examples in Section 4), the convergence rates for the randomized and standard algorithms are comparable.

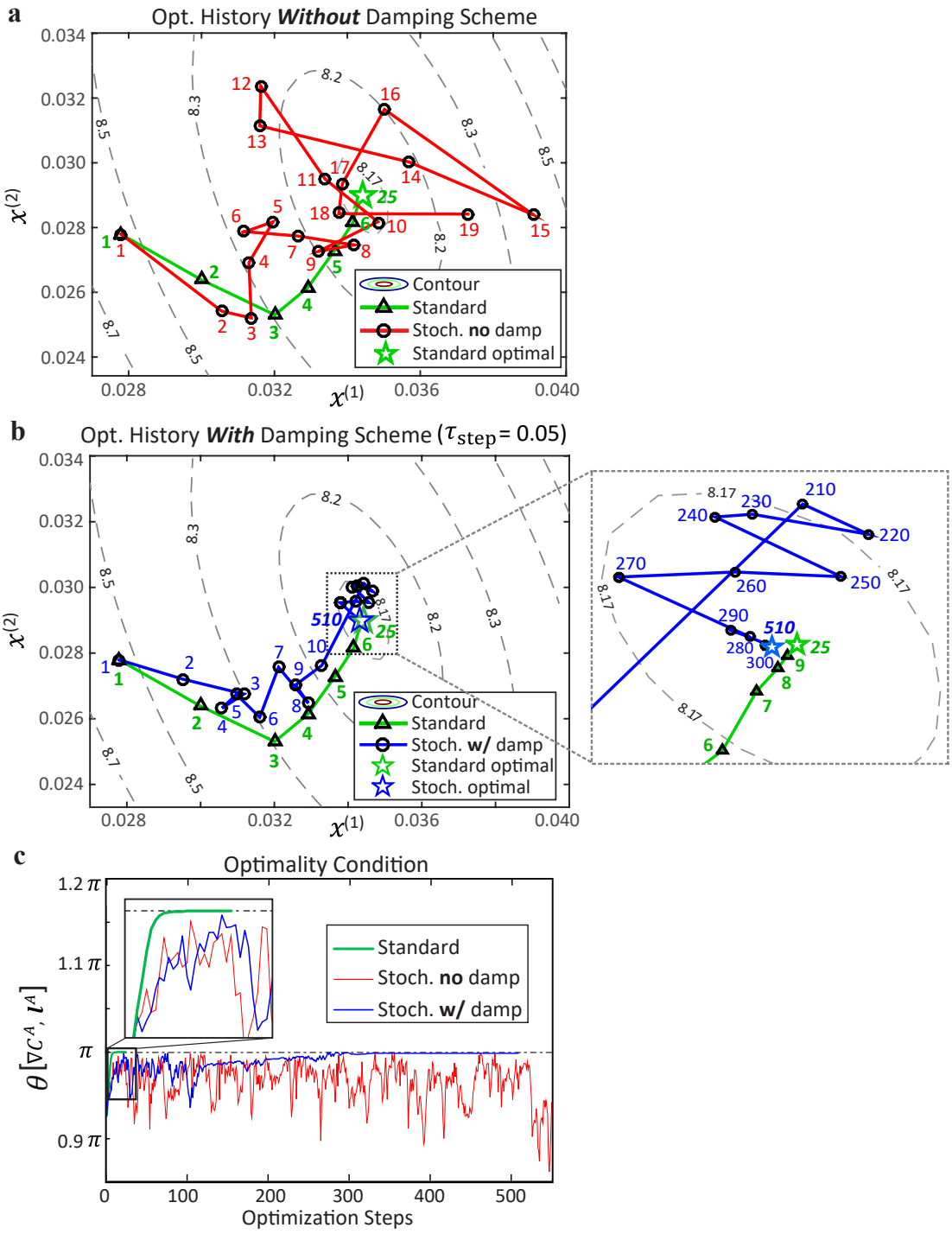


Figure 6.2: Illustration of the damping scheme in the three-bar truss example: contour plots of the objective function with the optimization history of $x^{(1)}$ and $x^{(2)}$ for **a** the standard weighted sum approach and the randomized approach without a damping scheme; **b** the standard weighted sum approach and the randomized approach with the proposed damping scheme. **c** The angle between the reduced gradient vectors of the objective function and the volume constraint.

Table 6.1: Solution of the 3-bar truss of Figure 6.1 using the standard GSM and the GSM with stochastic sampling and damping.

| | Standard GSM | Randomized GSM w/ damping |
|---|---|---|
| $x^{(1)}$ | 0.0344 | 0.0344 |
| $x^{(2)}$ | 0.0290 | 0.0290 |
| $x^{(3)}$ | 0.0132 | 0.0134 |
| $C^*$ | 8.1666 | 8.1667 |

To verify that the solution from the randomized algorithm with damping converges to a KKT (Karush-Kuhn-Tucker) point (optimal solution in case of the GSM), we examine the angle $\theta^{\mathscr{A}}$ between $\nabla C^{\mathscr{A}}$ (reduced gradient vector of the objective function) and $\boldsymbol{L}^{\mathscr{A}}$ (reduced gradient vector of the volume constraint) for the standard algorithm, and randomized algorithm with and without damping, as shown in Figure 6.2c. The solution is a KKT point if $\theta^{\mathscr{A}} = \pi$. For the standard algorithm, $\theta^{\mathscr{A}}$ converges quickly to $\pi$. For the randomized algorithm with damping, $\theta^{\mathscr{A}}$ gradually converges to $\pi$ (the case without damping does not converge). Hence, we numerically show that the solution from the randomized algorithm with damping converges to the optimal solution in the truss optimization framework.

### 6.3.2 Overview of algorithmic parameters for randomized optimization

This subsection summarizes the important parameters that are used in the randomized optimization framework, with some comments on the possible range of values to be used in practice.

**Sample size** In the proposed randomized optimization framework, the larger the number of sample load cases $n$, the more accurate the estimate of the compliance will be. However, the computational cost increases with the number of sample load cases, because in each optimization step we need to solve $n$ systems of equations. Thus, we need to balance the accuracy of the estimates and the computational complexity. Typically, the results from the randomized algorithm are relatively insensitive to the number of sample load

cases. Indeed, with a small number of sample load cases ($n \ll m_\ell$) we obtain solutions comparable to those from the standard algorithm in terms of topology and compliance value, and sometimes even better in terms of compliance value. It seems that for these problems the estimated gradient is fairly accurate even for small sample sizes. This is also demonstrated in the numerical examples in the next section. To provide some insight into the choice of sample size, a study is conducted using different sample sizes in Section 4.1. For the examples in the remainder of this chapter, we choose the number of sample load cases $n = 6$, unless otherwise stated, to demonstrate the accuracy and computational efficiency of the randomized optimization framework.

**Frequency to select a new sample** The frequency to select a new sample, $n_s$, or the number of optimization steps with a fixed random sample, influences the convergence rate of the optimization. If the frequency is too low, optimization steps are influenced too much by specific sets of random loads, and convergence may be slow. In this work, we select a new random sample every step, i.e., $n_s = 1$.

**Filter parameters** Applying the discrete filter in the GSM reduces the number of redundant bars, which drastically reduces the computational cost, for both standard and randomized algorithms. The discrete filter for the randomized algorithm, as discussed in Section 2.3, also helps to limit the effects of the stochastic estimates. For the randomized algorithm, we choose a relatively small filter size $\alpha_f = 10^{-4}$ and remove truss members when their normalized cross-sectional areas have remained below $\alpha_f$ for $n_f = 10$ cumulative steps. Further details about the filter parameters can be found in [85], [120]

**Parameters in the damping scheme** The damping scheme introduced in Section 6.3.1 has four parameters, the effective step ratio ($R$), the sample window size ($n_{\text{step}}$), the tolerance ($\tau_{\text{step}}$), and the scale factor ($\gamma$). The parameter choices in this damping scheme are crucial to the quality of the final solution. We average over a moving window. As the

window size $n_{\text{step}}$ increases, we average over more steps. If $n_{\text{step}}$ is too large, it slows down convergence because the algorithm adapts more slowly. In practice, we have found $n_{\text{step}} = 100$ is sufficient for problems containing more than one thousand design variables. At the start of the optimization, the number of steps after which we start to dampen the allowable move limit is typically chosen to be the same as the window size.

The tolerance for the effective step ratio, $\tau_{\text{step}}$, serves as a threshold to determine when updates become ineffective. Therefore, the choice of $\tau_{\text{step}}$ affects the rate of convergence and sometimes the quality of the solutions. In general, a loose tolerance leads to faster convergence (reduces the move limit more frequently) at the expense of the quality of design (in terms of the compliance value). One must balance the quality of the results and the convergence rate. The GSM is more sensitive to $\tau_{\text{step}}$ than the density-based method. This is demonstrated in Section 6.4.1. Therefore, a stricter tolerance is needed for the GSM. In practice, we choose $\tau_{\text{step}} = 0.05$ for the GSM and $\tau_{\text{step}} = 0.1$ for the density-based method. For the move limit scale factor $\gamma$, we have found that $\gamma = 2$ is typically a good choice.

## 6.4 Numerical Examples

We present several numerical examples in both two and three dimensions to demonstrate the effectiveness as well as the computational efficiency of the proposed randomized algorithm for topology optimization. Both density-based method and GSM are used. The first two examples (Section 6.4.1) investigate the sensitivity of the density-based method and the GSM to the tolerance $\tau_{\text{step}}$ (see Eq. (6.30)). Moreover, Example 1 (Section 6.4.1) shows the relation between sample size and quality of the optimized design. Example 2 (Section 6.4.1) illustrates the effect of the discrete filter in the GSM for the proposed randomized algorithm. The last two examples (Sections 6.4.2 and 6.4.3) in 3D demonstrate the capability of the proposed algorithm to create practical structural designs at greatly reduced computational cost.

To quantify the computational cost of the standard and randomized optimization algorithms, we define $N_{\text{solve}} = n \times N_{\text{step}}$ as the total number of linear systems of equations to solve in the optimization process, where $N_{\text{step}}$ is the number of optimization steps. This is a measure of the computational efficiency of an optimization formulation. The optimization process is considered converged if the current step size (bounded by the move limit) is below a prescribed tolerance $\tau_{\text{opt}}$ for the optimization process, that is, $||\boldsymbol{x}_k - \boldsymbol{x}_{k-1}|| < \tau_{\text{opt}}$.

For the density-based method (continuum), we incorporate the proposed technique into the computer program PolyTop [163] in 2D and the topology optimization code in 3D [164]. For plotting 3D continuum results, we utilize TOPSlicer [6]. All the problems are initialized as follows. The initial guess is taken as $\rho_0 = V_{\max}/\sum_{e=1}^{M} V^{(e)}$, where $V^{(e)}$ is the volume (area) of element $e$. The convergence tolerance is $\tau_{\text{opt}} = 10^{-2}$; the initial move limit is chosen as $move = 0.05$; the damping factor for the OC update scheme is $\eta = 0.5$ (or 1). We use a continuation scheme, in which the penalization factor starts at $p = 1$ and each time increases by 0.5 until $p = 3$ (for 2D problems [163]) or 4 (for 3D problems [6]). For example, $p = [1, 1.5, 2, 2.5, 3]$.

For the GSM (truss-layout), we generate initial ground structures (without overlapped bars) using the collision zone technique from references [112], [113] and plot final topologies in 3D using the program GRAND3 [113]. The initial guess of the design variables is taken as $x_0 = V_{\max}/\sum_{e=1}^{M} L^{(e)}$; the convergence tolerance is $\tau_{\text{opt}} = 10^{-8}$; the initial move limit is chosen as $move = x_0 \times 10^4$; the damping factor for the OC update scheme is $\eta = 0.5$. When the discrete filter is used in the GSM, we use $n_f = 10$ and $\alpha_f = 10^{-4}$ during the optimization process, unless otherwise stated; the lower and upper bounds on the design variables are $x_{\min} = 0$ and $x_{\max} = 10^4 x_0$ (unbounded in practical terms). For the standard GSM (without the discrete filter), we apply a cut-off value $10^{-2}$ that defines the final structure at the end of the optimization [31]. The lower and upper bounds are defined by $x_{\min} = 10^{-2} x_0$ and $x_{\max} = 10^4 x_0$, respectively. For all results in the GSM, we remove unstable nodes and floating bars and then check the final topologies to ensure that they are at global equilibrium

– a detailed explanation can be found in references [128].

In both the continuous and truss-layout optimization, the randomized algorithm uses the following parameters. Unless otherwise stated, the sample size is chosen to be $n = 6$; in the damping scheme, the window size is $n_{\text{step}} = 100$, and we use step size reduction factor $\gamma = 2$. For the density-based method, we use a tolerance for the effective step ratio $\tau_{\text{step}} = 0.1$, and for the GSM we use $\tau_{\text{step}} = 0.05$. Let $\boldsymbol{\rho}^*$ and $\boldsymbol{x}^*$ represent the optimal solutions of the standard formulations in (6.1) and (6.3), $\widehat{\boldsymbol{\rho}}^S$ and $\widehat{\boldsymbol{x}}^S$ represent the optimal solutions obtained from the randomized algorithm for density-based and GS methods. To evaluate the quality of the solutions, in the case of the randomized algorithm, we present the *true values* of the objective function $C(\widehat{\boldsymbol{\rho}}^S)$ and $C(\widehat{\boldsymbol{x}}^S)$ at the approximated solutions $\widehat{\boldsymbol{\rho}}^S$ and $\widehat{\boldsymbol{x}}^S$ (instead of their estimators $\widehat{C}^S(\widehat{\boldsymbol{\rho}}^S)$ and $\widehat{C}^S(\widehat{\boldsymbol{x}}^S)$) and compare them with those obtained from the standard algorithm $C(\boldsymbol{\rho}^*)$ and $C(\boldsymbol{x}^*)$. The relative difference is defined as $\Delta C = \left(C(\widehat{\boldsymbol{x}}^S) - C(\boldsymbol{x}^*)\right)/C(\boldsymbol{x}^*)$.

### 6.4.1 Two-dimensional box domain with 108 load cases

We present a two-dimensional (2D) topology optimization problem whose design domain and boundary conditions are shown in Figure 6.3. A total of 108 equal-weighted load cases are applied at three given points, with each point having 36 load cases applied along different angles (from $0^\circ$ to $350^\circ$). In this section, both the density-based and the GS methods are used.

*Continuum topology optimization with density-based method*

Using the density-based method, we demonstrate the reduction of the computational cost by means of the randomized algorithm. We further investigate the sensitivity of the final optimized topologies to the tolerance $\tau_{\text{step}}$ in the damping scheme and the sample size $n$. Because the final topology from the standard algorithm is symmetric both horizontally and vertically, we enforce symmetry of the topologies in the randomized case by enforcing

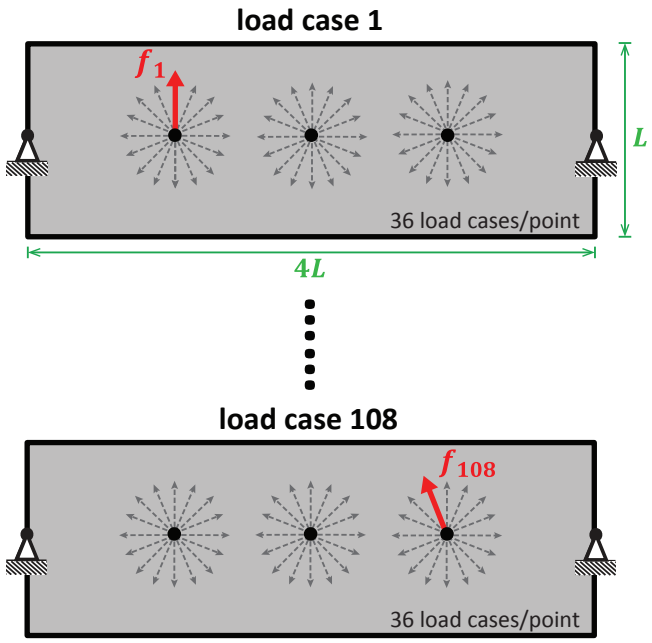


Figure 6.3: Two-dimensional box domain with load and support conditions. A total of 108 equal-weighted load cases are applied at three given points with each point having 36 load cases applied from 0° to 350° (dotted arrows are the schematic illustrations of non-active load cases).

horizontal and vertical symmetry of the distribution of the density field [163]. A total number of 25,600 quadrilateral elements are used to discretize the domain which gives 52,002 degrees of freedom (DOFs). The linear density filter that defines the solid-void boundary takes the radius of 1 (see Section 1.1). For comparison purposes, the final topology obtained from the standard topology optimization is shown in Figure 6.4a. The final topology has $C(\boldsymbol{\rho}^*) = 3.257$ and converges after 1048 steps. In each optimization step, we solve 108 linear systems (corresponding to 108 load cases), which leads to a total 113,184 solves. Because the continuation method is used for the penalization factor, $p$, the jumps in the compliance correspond to $p = 1.5, 2.0, 2.5, 3.0$ (initially $p = 1.0$) [163].

To investigate the sensitivity to $\tau_{\text{step}}$, we consider $\tau_{\text{step}} = 0.1$ and $\tau_{\text{step}} = 0.05$, and the results are compared with that from the standard algorithm [30]. For both cases, the number of sample load cases used is $n = 6$. Figures 6.4b and c show the optimized topologies for the randomized algorithm for a single representative trial (one trial is one run of the

numerical experiment) for each $\tau_{\text{step}}$, and Figure 6.4d shows the convergence histories of the objective function for all cases for the representative trial. Because the sample load cases are generated randomly at each step, the final optimized topology and its compliance vary slightly with each trial. Therefore, the associated results in Table 6.2 are averaged over 5 trials. For the randomized algorithm, we also report the standard deviations of the compliance for 5 trials – the standard deviations for all the cases are small, indicating that the randomized algorithm generates results with similar compliance in every instance. For this example, the standard algorithm leads to a lower compliance and simpler topology. However, the randomized algorithm for both tolerances uses substantially fewer solves for final topologies similar to the one obtained with the standard algorithm. For $\tau_{\text{step}} = 0.1$, the number of linear systems to solve is 27 times fewer than for the standard algorithm (113,184 solves vs. 4170 solves), and the convergence of the optimization is more rapid. The final topologies obtained for the two tolerances and the compliance for each case (see Figure 6.4) suggest that the tolerance in the damping scheme has a minor influence on the final results in the density-based method. The relative differences between the compliance for the standard algorithm and those for the randomized algorithm are 1.79% for $\tau_{\text{step}} = 0.05$ and 2.45% for $\tau_{\text{step}} = 0.1$. It seems that smaller $\tau_{\text{step}}$ leads to slower convergence but a slightly better compliance: the optimization with $\tau_{\text{step}} = 0.05$ takes an average 1052 steps to converge while the one with $\tau_{\text{step}} = 0.1$ takes an average 695 steps. Therefore, the latter is more computationally efficient with only $N_{\text{solve}} = 4170$ compared with $N_{\text{solve}} = 6312$ for the former one.

Next, we check the quality of the estimated gradients by plotting the angle between the true gradient and the estimated gradient. The very small angles show that the estimated gradient is about as effective as the true gradient, and that the negative estimated gradient is a descent direction. As shown in Figures 6.4e and 6.4f, we plot the angle ($\theta$), and the cosine of the angle ($\cos\theta$), between the gradient and the estimated gradient for each of the two tolerances for one representative trial. The moving averages (over 50 steps) of $\cos\theta$,

in both cases, are close to 1.0.

The next study demonstrates the influence of sample sizes on optimization results and the reduction of the computational cost by using the randomized algorithm. In this study, $\tau_{\text{step}} = 0.1$. Figure 6.5 gives the compliances for sample sizes $n = 4, 5, 6, 7, 20, 50$ and final topologies (from one representative trial). Each data point in Figure 6.5 is obtained by averaging 5 trials, and the data are summarized in Table 6.2. Several observations can be made based on Figure 6.5 and Table 6.2. For one, the randomized algorithm leads to similar optimal topologies and compliances compared with the standard algorithm. For $n = 4$, $N_{\text{solve}}$ is significantly smaller than for the standard algorithm, by a factor of 45 on average. Moreover, the compliance improves as we increase $n$, indicating that larger $n$ offers better estimation during the optimization and ultimately yields stiffer optimal structures. However, $N_{\text{solve}}$ also increases as we use more sample load cases. From the optimized structures and compliances, it seems that $n = 6$ is sufficient for this problem with greatly reduced computational cost. The compliance differs from the standard algorithm by only 2.45%. Table 6.2 shows that the cosine of the average angle between the gradient and the estimated gradient, $\cos\bar{\theta}$, ranges from 0.959 and 0.996 for various sample sizes. Using the randomized algorithm, we can almost fully recover the original optimal results by either increasing the sample size (e.g., $n = 50$) or choosing smaller $\tau_{\text{step}}$, as both methods lead to highly accurate designs.

*Truss topology optimization with ground structure method*

As example 2, we study again the problem presented in Figure 3, but this time using the GSM. We demonstrate that our approach greatly reduces the total number of linear solves. In addition, we investigate the sensitivity of the results to $\tau_{\text{step}}$ as well as the influence of the discrete filter on final solutions of the randomized algorithm. We use a full-level GS ($16 \times 4$ grid) with 2,196 non-overlapped bars to discretize the domain [112], [113]. The optimal topology and the convergence of the compliance for the standard algorithm are shown in

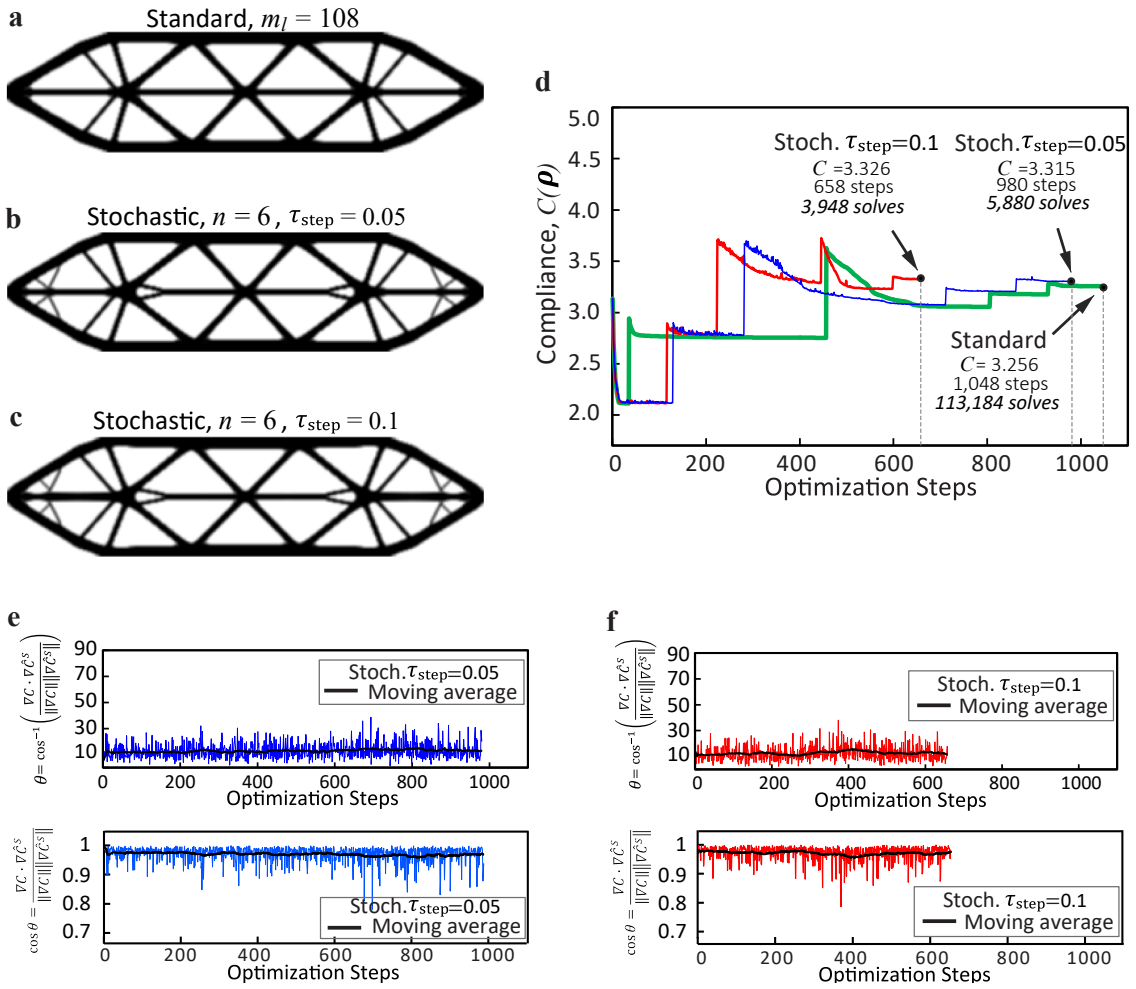


Figure 6.4: Results for Example 1 using the density-based method with 25,600 quadrilateral elements and 52,002 degrees of freedom (DOFs). **a** The optimized topology obtained by the standard algorithm [30]; **b** the optimized topology obtained by the randomized algorithm with $n = 6$ and $\tau_{\text{step}} = 0.05$ (one representative trial); **c** the optimized topology obtained by the randomized algorithm with $n = 6$ and $\tau_{\text{step}} = 0.1$ (one representative trial); **d** the convergence of the compliance for above cases; **e** the angle, and the cosine of the angle, between the gradient $\nabla C_x$ and the estimated gradient $\nabla \widehat{C}_x^S$ for the randomized case with $\tau_{\text{step}} = 0.05$ demonstrate that the directions are aligned. **f** the angle, and the cosine of the angle, between $\nabla C_x$ and $\nabla \widehat{C}_x^S$ for the randomized case with $\tau_{\text{step}} = 0.1$ demonstrate that the directions are aligned.

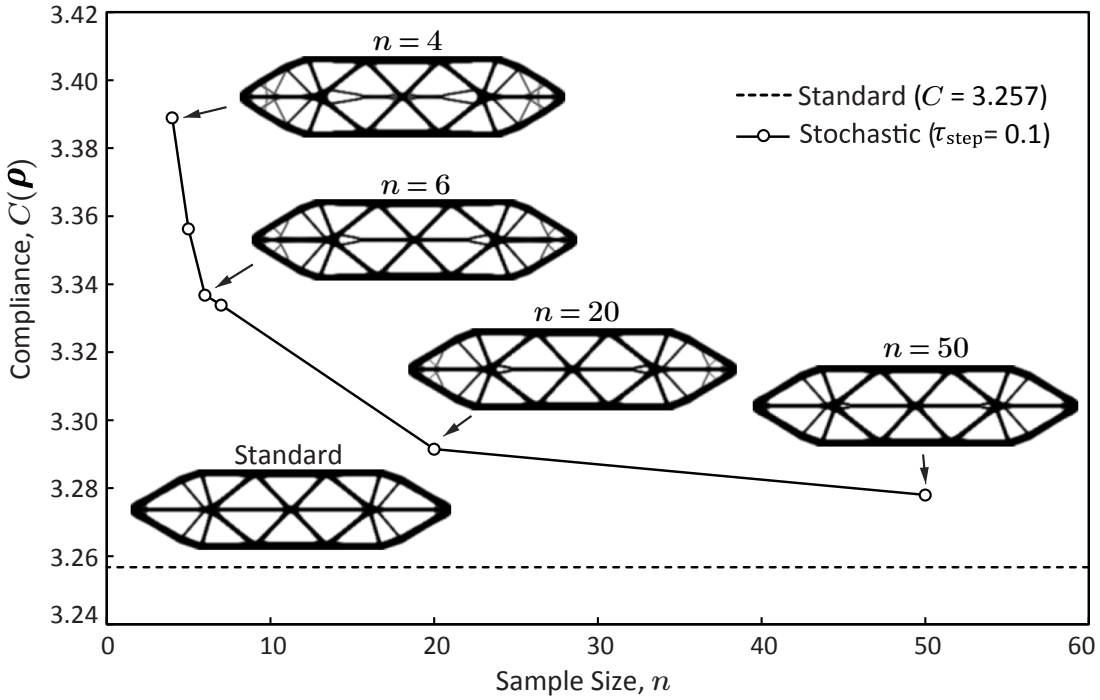


Figure 6.5: Study of sample sizes ($n = 4, 5, 6, 7, 20, 50$) versus the resulting final compliance (or end-compliance) using the randomized algorithm in Example 1. The final topologies (from representative trials) are included.

Figures 6.6a and 6.6d. The optimal compliance for the standard algorithm, $C(\boldsymbol{x}^*) = 4.219$, is obtained in 406 steps and $N_{\text{solve}} = 43,848$. For the randomized algorithm, we compare two cases using different tolerances in the damping scheme, $\tau_{\text{step}} = 0.05$ and $\tau_{\text{step}} = 0.1$. The results are summarized in Table 6.3, averaged over 5 trials. The optimized structures and the convergence of the compliance for a single representative trial are shown in Figures 6.6b-d.

In contrast to the results for the density-based method in Section 4.1.1, the results for the GSM indicate that the choice of $\tau_{\text{step}}$ has a significant impact on the optimized structure. Although $\tau_{\text{step}} = 0.05$ results in a larger number iterations/optimization steps and a larger number of linear system solves, $N_{\text{solve}}$, compared with $\tau_{\text{step}} = 0.1$, its final structure is simpler, has slightly lower compliance, and is similar to the structure obtained by the standard algorithm. This suggests that $\tau_{\text{step}} = 0.05$ is a better choice for this example. The convergence rate for the randomized algorithm is about the same as for the standard algo-

Table 6.2: Results for Example 1 (density-based), averaged over 5 trials.

| Density -based | $C(\boldsymbol{\rho}^*)$ | $C(\widehat{\boldsymbol{\rho}}^S)$ | $\Delta C$ | $Dev_S$ $(C(\widehat{\boldsymbol{\rho}}^S))$ | $\tau_{\text{step}}$ | $\cos\bar{\theta}$ | $n$ | $N_{\text{step}}$ | $N_{\text{solve}}$ |
|---|---|---|---|---|---|---|---|---|---|
| Standard | 3.257 | - | - | - | - | - | - | 1,048 | 113,184 |
| Stoch. $\tau_{\text{step}} = 0.05$ | - | 3.315 | 1.79% | 0.0200 | 0.05 | 0.971 | 6 | 1,052 | 6,312 |
| **Stoch. $\tau_{\text{step}}$=0.1** | - | **3.337** | **2.45%** | **0.0092** | **0.1** | **0.971** | **6** | **695** | **4,170** |
| Stoch. $n = 4$ | - | 3.389 | 4.05% | 0.0215 | 0.1 | 0.959 | 4 | 618 | 2,472 |
| Stoch. $n = 5$ | - | 3.356 | 3.05% | 0.0033 | 0.1 | 0.967 | 5 | 684 | 3,420 |
| Stoch. $n = 7$ | - | 3.334 | 2.36% | 0.0284 | 0.1 | 0.976 | 7 | 684 | 4,788 |
| Stoch. $n = 20$ | - | 3.291 | 1.05% | 0.0033 | 0.1 | 0.991 | 20 | 838 | 16,760 |
| Stoch. $n = 50$ | - | 3.278 | 0.65% | 0.0081 | 0.1 | 0.996 | 50 | 850 | 42,500 |

rithm. Because the standard optimization problem for the GSM is convex, its solution is the global minimum; hence, the compliances obtained with the randomized algorithms will be larger than or equal to those obtained with the standard algorithm. However, the relative differences in compliance are very small, only 0.09% and 0.35% on average, and the randomized algorithm achieves these results with considerably less computational effort ($N_{\text{solve}} = 5627$ and $2,322$ on average for the randomized algorithm versus $N_{\text{solve}} = 43,848$ for the standard algorithm). Symmetry was not enforced for the GSM in the present study. To show the accuracy of estimated gradient of compliance for both tolerances, we plot $\cos\theta$ between the gradient and the estimated gradient for one representative trial in Figure 6.6e. The cosine of the average angle, $\cos\bar{\theta}$, for the two randomized cases are 0.911 and 0.912, indicating that the estimated gradients of both randomized cases are quite accurate and lead to effective optimization steps.

Next, we also include the discrete filter [85] in the randomized algorithm and study its influence on the optimized results. Based on previous observations, we choose $\tau_{\text{step}} = 0.05$ and $n = 6$. We use the following parameters for the discrete filter (see Section 2.3): $n_f = 10$ and $\alpha_f = 0.0001$. Figure 6.7a shows the final topology obtained by the randomized algorithm with the discrete filter in one representative trial (cf. Figure 6.6b, which was obtained without the filter). The convergence of the compliance and $\cos\theta$ in each step are shown in Figures 6.7b-c. The results, averaged over five trials, are summarized in Table 6.3. Similar to Example 1, the standard deviations provided in the table for the randomized algorithm show that the compliance of the optimal structure for each trial is almost identical. The discrete filter combined with the randomized algorithm leads to a simpler final topology. From Figure 6.7c, the direction of the estimated gradient seems to be more accurate than the ones without the discrete filter (Figure 6.6e), which is confirmed by $\cos\bar{\theta} = 0.978$. This indicates that the removal of some non-useful members helps to limit the collateral effects of the stochastic estimates. As compared to the standard algorithm, the discrete filter combined with the randomized algorithm not only leads to a reduction in the number of linear system solves ($N_{\text{solve}} = 5,442$ versus $N_{\text{solve}} = 43,848$), but the size of the linear systems also keeps decreasing due to the discrete filter, which further improves the computational efficiency.

### 6.4.2 Three-dimensional bridge design with density-based method

In this section, we demonstrate the quality of the design and the great reduction in computational work of the proposed randomized algorithm using a 3D bridge design in the non-convex, continuum topology optimization framework. The design domain, load, and boundary conditions are shown in Figure 6.8a. A total of 144 equal-weighted load cases are applied to the bridge deck (non-designable layer). Based on the structural symmetry, we optimize a quarter of the domain, as shown in Figure 6.8b, which reduces the number of load cases to $m_\ell = 36$. We use 10,000 brick elements to discretize the quarter domain, re-

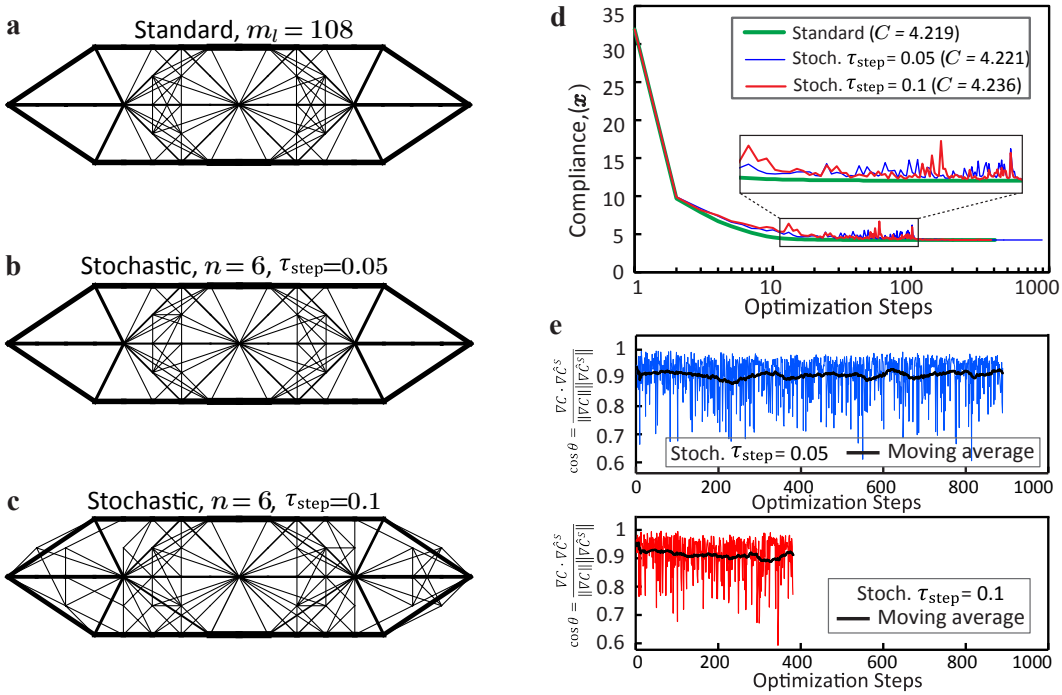


Figure 6.6: Results for the GSM (without the discrete filter) for Example 2 with a full-level GS ($16 \times 4$ grid) and 2,196 non-overlapped bars. **a** The optimized structure obtained by the standard algorithm; **b** the optimized structure obtained by the randomized algorithm with $n = 6$ and $\tau_{\text{step}} = 0.05$; **c** the optimized structure obtained by the randomized algorithm with $n = 6$ and $\tau_{\text{step}} = 0.1$; **d** the convergence of the compliance for all above cases; **e** the cosine of $\theta$ between the gradient $\nabla C_x$ and the estimated gradient $\nabla \widehat{C}_x^S$ for the randomized algorithm ($\tau_{\text{step}} = 0.05$ and $\tau_{\text{step}} = 0.1$).

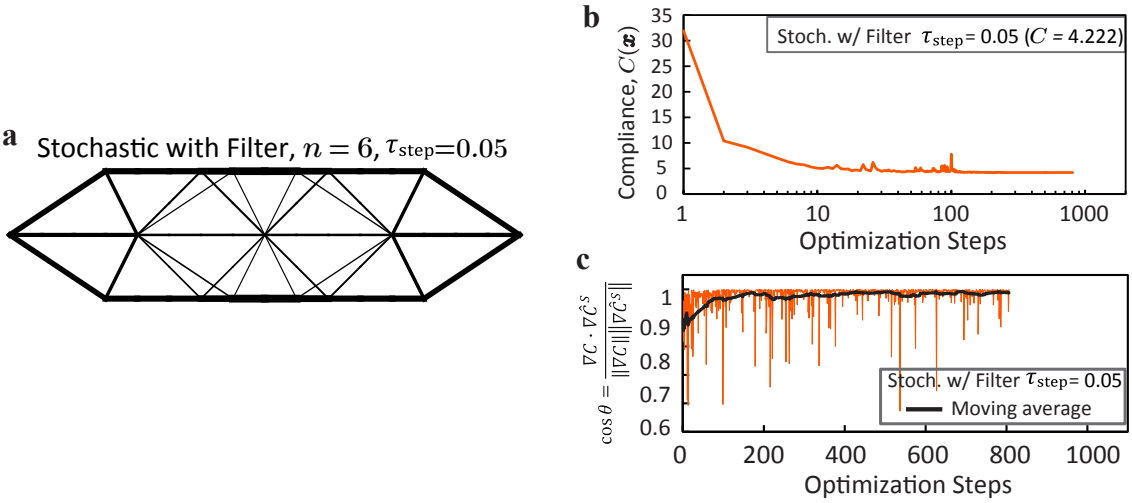


Figure 6.7: Results for the GSM with the discrete filter for Example 2. **a** The optimized structure obtained from randomized algorithm with $n = 6$, $\tau_{\text{step}} = 0.05$, and $\alpha_f = 0.0001$; **b** the convergence of the compliance; **c** the cosine of $\theta$ between the gradient $\nabla C_x$ and the estimated gradient $\nabla \widehat{C}_x^S$ for the randomized case.

Table 6.3: Results for Example 2 (GSM), averaged over 5 trials.

| GSM | $C(\boldsymbol{x}^*)$ | $C(\widehat{\boldsymbol{x}}^S)$ | $\Delta C$ | $Dev_S(C(\widehat{\boldsymbol{x}}^S))$ | $\tau_{\text{step}}$ | $\cos\bar{\theta}$ | $n$ | $N_{\text{step}}$ | $N_{\text{solve}}$ |
|---|---|---|---|---|---|---|---|---|---|
| Standard | 4.219 | - | - | - | - | - | - | 406 | 43,848 |
| Stoch. $\tau_{\text{step}} = 0.05$ | - | 4.222 | 0.09% | 0.00068 | 0.05 | 0.911 | 6 | 938 | 5,627 |
| Stoch. $\tau_{\text{step}} = 0.1$ | - | 4.231 | 0.35% | 0.00336 | 0.1 | 0.912 | 6 | 387 | 2,322 |
| **Stoch. with Filter $\tau_{\text{step}}$=0.05** | - | **4.222** | **0.09%** | **0.00099** | **0.05** | **0.978** | **6** | **907** | **5,442** |

sulting in 35,343 degrees of freedom (DOFs). We take $V_{\max} = 0.1 \times M$ (where $M = 10,000$) and use a quadratic density filter which takes the radius of 2.5 (see Section 1.1). The penalization factor for the continuation scheme takes values $p = 1,2,3,4$ [6]. The randomized case uses the following parameter values: the sample size is chosen to be $n = 6$; the window size $n_{\text{step}} = 100$, $\gamma = 2$ and $\tau_{\text{step}} = 0.1$ (the effective step ratio is calculated in terms of $\boldsymbol{\rho}$). Figure 6.9 shows the optimized structures obtained using the standard algorithm and the randomized algorithm. The results are summarized in Table 6.4.

The standard algorithm leads to final topology with $C(\boldsymbol{\rho}^*) = 542.1$ and converges in 968 steps. In each optimization step, we solve 36 linear systems (load cases), which leads to $N_{\text{solve}} = 34,848$. Our randomized algorithm, while offering a nearly identical topology as the standard algorithm, drastically reduces the computational cost from $34,848$ solves to $4,662$ solves and leads to even better compliance $C(\widehat{\boldsymbol{\rho}}^S) = 523.6$.

Table 6.4: Results for Example 3 (density-based bridge design).

| Study 1 | $C(\boldsymbol{\rho}^*)$ | $C(\widehat{\boldsymbol{\rho}}^S)$ | $\Delta C$ | $\tau_{\text{step}}$ | $n$ | $N_{\text{step}}$ | $N_{\text{solve}}$ |
|---|---|---|---|---|---|---|---|
| Standard | 542.1 | - | - | - | - | 968 | 34,848 |
| Stochastic | - | 523.6 | -3.4% | 0.1 | 6 | 777 | 4,662 |

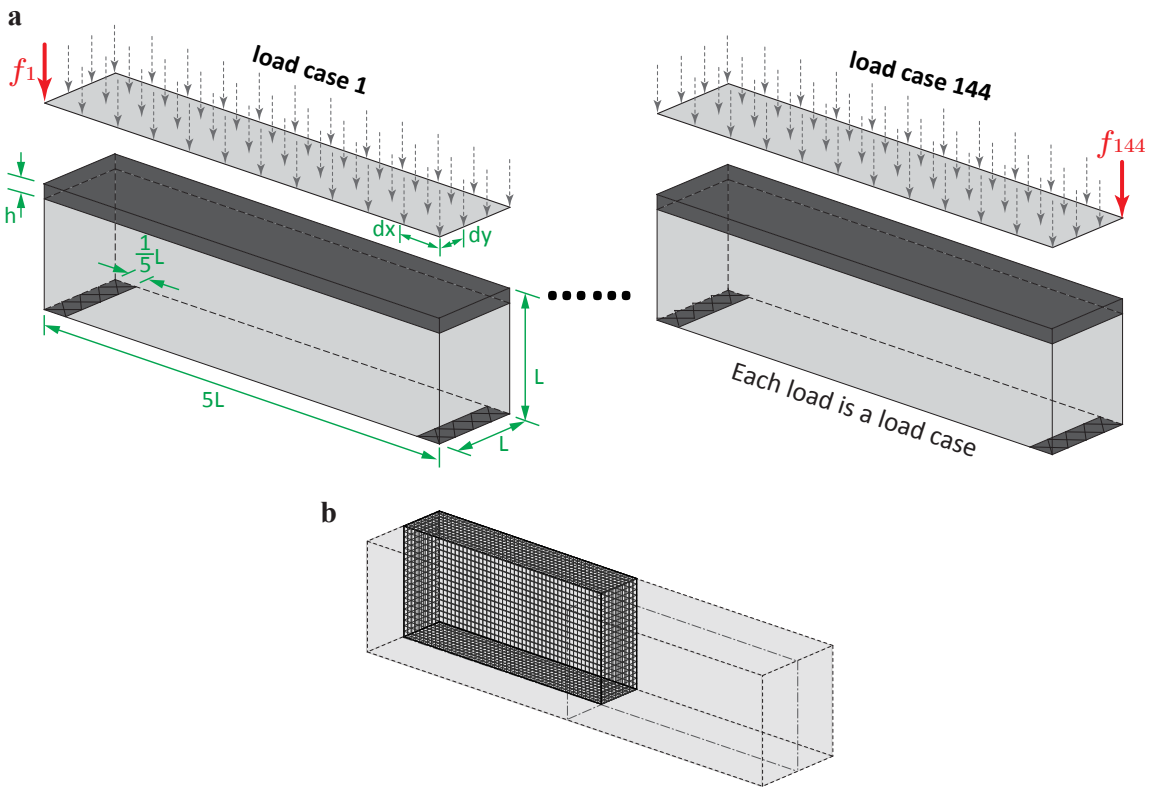


Figure 6.8: Three-dimensional bridge design with **a** the geometry, load and boundary conditions; **b** the quarter domain is modeled by a mesh with 10,000 brick elements and 35,343 DOFs.

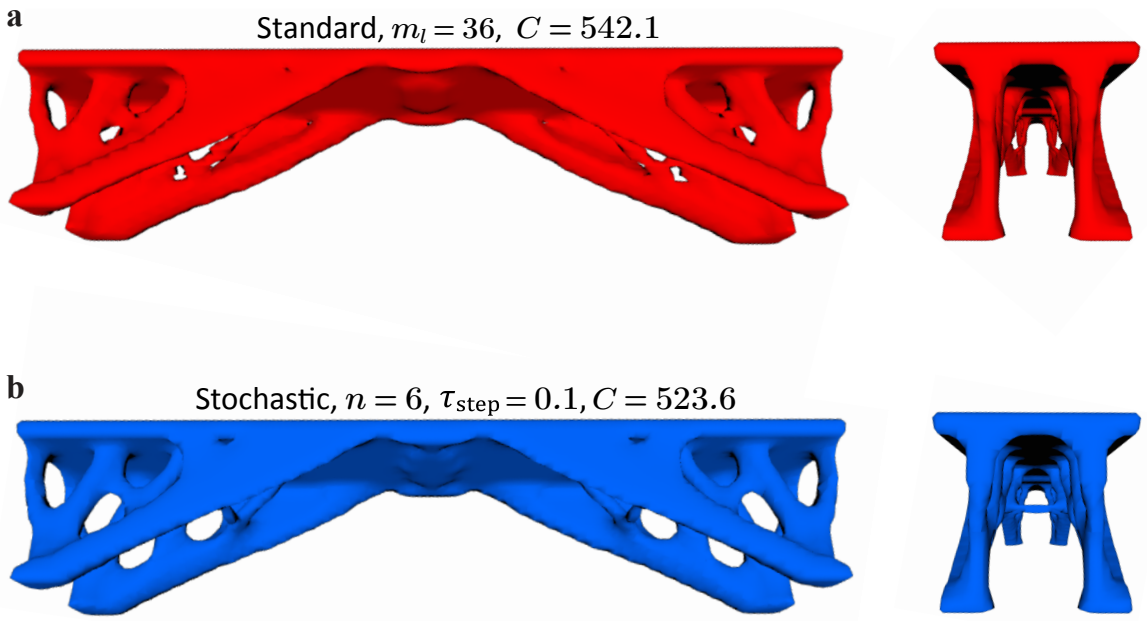


Figure 6.9: Optimized structures of the 3D bridge design obtained from **a** the standard algorithm; **b** the randomized algorithm with $n = 6$ and $\tau_{\text{step}} = 0.1$.

### 6.4.3 Three-dimensional high-rise building design with ground structure method

To illustrate the effectiveness of the randomized algorithm combined with the discrete filter on a practical engineering design, we optimize a simplified 3D high-rise building (twisting tower) in the truss topology optimization framework. The domain of the twisting tower, given in Figure 6.10, has 11 floors with the 1st floor fixed to the ground. The tower twists a full 90 degrees from its base to its crown. To obtain constructible structures, we use a $4 \times 4 \times 11$ grid to discretize the domain followed by the generation of a level 7 initial GS, containing 3,556 non-overlapping members [113]. The base mesh and the void zone are shown in Figure 6.10b. As shown Figure 6.10c, 77 equal-weighted load cases are applied to the building. Based on our previous studies, we choose $\tau_{\text{step}} = 0.05$ and $n = 6$. We apply the discrete filter for both the standard and the randomized algorithms; specifically, we choose $n_f = 10$, a small filter value ($\alpha_f = 0.0001$) used during optimization, and a larger filter value ($\alpha_f = 0.001$) in the final step to control the resolution of the final topology [85], [128]. Figure 6.11 shows the optimized structures obtained using the standard and randomized algorithms. A summary of the results is provided in Table 6.5. The geometry data of this tower design (Figure 6.11) is exported to STL (or stereolithography) format using the method proposed by [6]. The design is then manufactured with 3D printing using a fused deposition modeling (FDM) process, as shown in Figure 6.12.

The optimal compliance for the standard algorithm, $C(\boldsymbol{x}^*) = 4.388$, is obtained in 382 optimization steps and a total of $N_{\text{solve}} = 29,414$ linear solves. With the randomized algorithm, we obtain a similar final structure as well as a compliance that is only 0.46% higher than that obtained with the standard algorithm. These results are obtained at a drastically reduced computational cost, i.e., $N_{\text{solve}} = 4,410$ linear solves. In addition to the reduction in the number of linear system solves obtained by the randomized algorithm, the discrete filter also reduces the size of the linear systems as the optimization proceeds, because the use of the filter scheme reduces the number of design variables, and hence the size of the stiffness matrices. This significantly decreases the CPU time and memory usage [128],

contributing to great computational efficiency.

Table 6.5: Results for Example 4 (tower design).

| 3D GSM | $C(\boldsymbol{x}^*)$ | $C(\widehat{\boldsymbol{x}}^S)$ | $\Delta C$ | $\tau_{\text{step}}$ | $\cos\bar{\theta}$ | $n$ | $N_{\text{step}}$ | $N_{\text{solve}}$ |
|---|---|---|---|---|---|---|---|---|
| Standard | 4.388 | - | - | - | - | - | 382 | 29,414 |
| Stochastic | - | 4.408 | 0.46% | 0.05 | 0.937 | 6 | 735 | 4,410 |

## 6.5 Summary and Discussion

This chapter proposes an efficient randomized optimization approach for topology optimization that drastically reduces the enormous computational cost of optimizing practical structural systems under many load cases while producing high-quality designs. We apply this approach to the nested minimum end-compliance topology optimization using both the density-based method (non-convex) and the ground structure method (convex) by minimizing a weighted sum/average of the compliance over many load cases. Minimizing the weighted average of the compliance over many load cases requires the solution of the state equations for each load case in every optimization step to compute the (weighted) compliance and its gradient. Because the objective function and its gradient can be defined as the traces of symmetric matrices, we use the Hutchinson trace estimator (which provides the lowest variance) combined with the sample average approximation technique, to estimate both quantities. This reduces the computational cost from $m_\ell \times N_{\text{step}}$ to roughly $n \times N_{\text{step}}$, where $m_\ell$ is the number of load cases, and $n \ll m_\ell$ is the sample size. We further propose a damping scheme for the randomized algorithm, derived from simulated annealing, to obtain fast convergence. We discuss the algorithmic parameters for our scheme and provide some information on how to choose them.

The results for several generic examples and practical engineering designs demonstrate that the proposed randomized algorithm provides high-quality designs at a drastically reduced computational cost. Based on the limited number and size of examples investigated, we show that the proposed randomized algorithm substantially reduces the computational

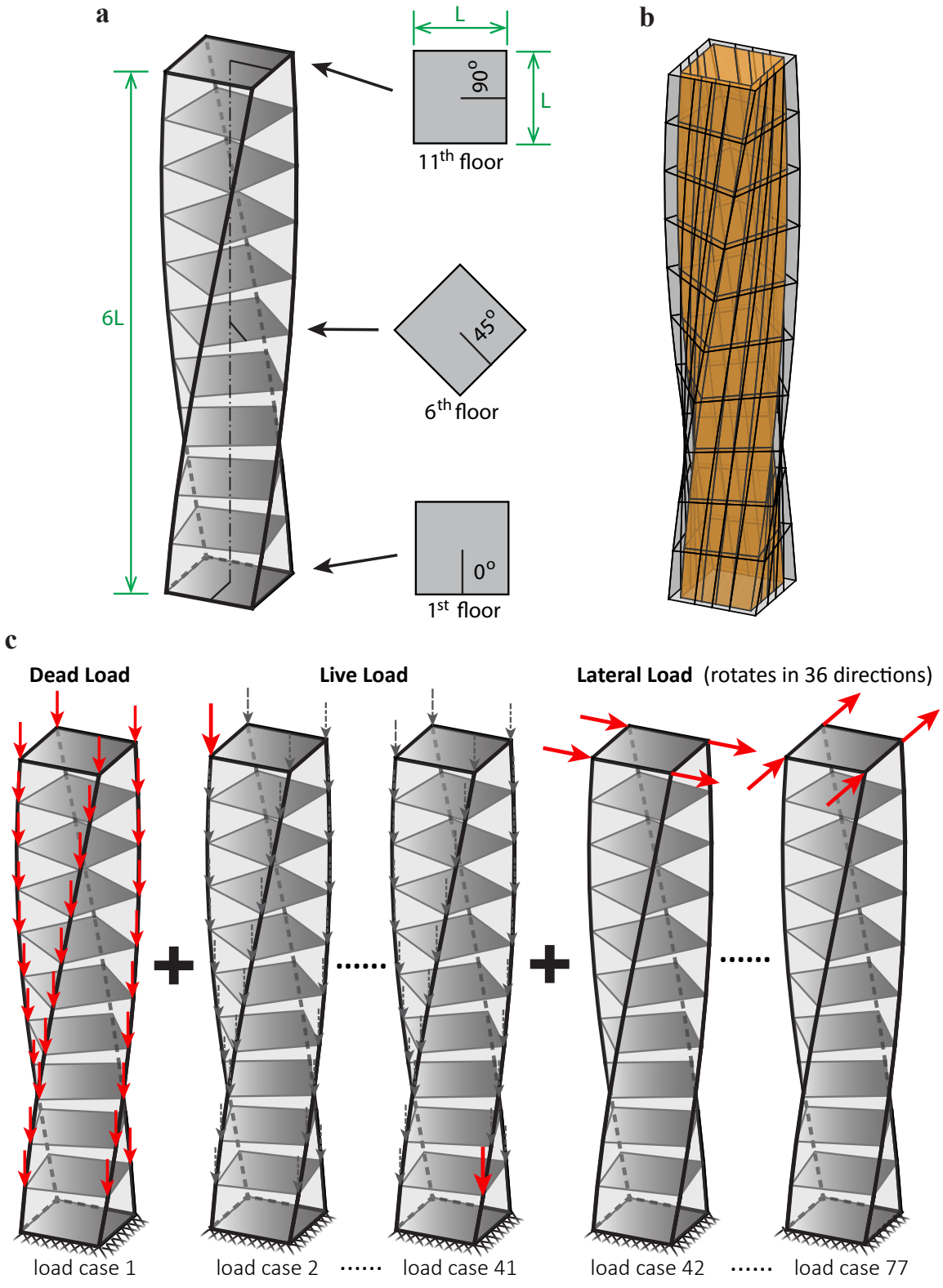


Figure 6.10: Twisting tower (inspired by the Cayan tower [165], which is designed by Skidmore, Owings & Merrill LLP): **a** geometry; **b** base mesh with a void zone in the middle; **c** load and boundary conditions. One dead load case, 40 live load cases, and 36 lateral load cases (the lateral load is applied at 4 corners on the top floor and rotating in 36 directions).

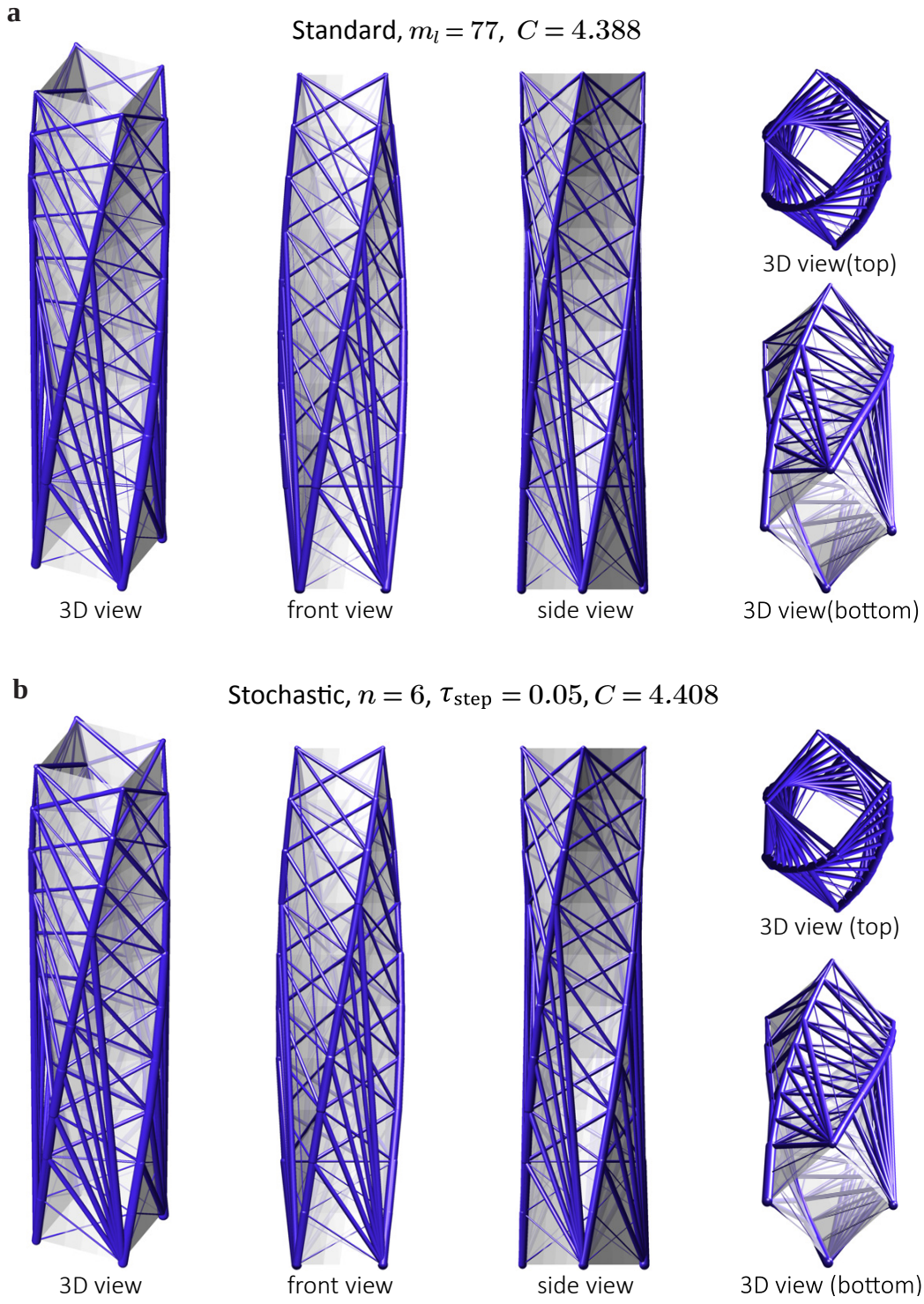


Figure 6.11: Optimized structures of the 3D twisting tower obtained from: **a** the standard algorithm; **b** the proposed randomized algorithm with $n = 6$ and $\tau_{\text{step}} = 0.05$.

Figure 6.12: Comparison of the optimized twisting tower (left) and its printed model (right) using FDM process.

cost by (e.g., a factor of up to 45 in one of the examples), while obtaining a final compliance very close to that obtained by the standard algorithm. Our proposed damping scheme leads to fast convergence of the optimization scheme. In addition, the combination of the discrete filter with the randomized algorithm leads to fewer linear solves with smaller systems, resulting in great computational efficiency.

The proposed randomized algorithm is flexible and can be combined with any gradient-based update scheme. In this chapter, we combine this technique with the optimality criteria, but other optimization methods can be used, such as the method of moving asymptotes (MMA) — see, for example, the book by Christensen and Klarbring [31].

# CHAPTER 7
# CONCLUSIONS AND FUTURE DIRECTIONS

This thesis explores and contributes several areas and topics, including Michell's optimality conditions, multi-material topology optimization, randomized algorithms with stochastic sampling, nonlinear material properties, constructible structures, as well as efficient update algorithms. We focus on both the theoretical foundations as well as the algorithmic developments for topology optimization to enable various innovative applications. More specifically, we develop theories and computational frameworks for the topology optimization to effectively and efficiently handle many materials, many constraints, and many load cases, for both continuum and structural layout optimization methods.

Chapter 2 provides a primer of Michell's optimality conditions, which are the first sufficient conditions that provide analytical closed-form solutions for optimal structures. Michell's optimality conditions and the derived closed-form solutions not only bring insights into functional and creative structural designs but also provide analytical benchmarks for numerical methods to verify with. We explain the main idea of the original and modified conditions followed by a proof of the conditions. In addition, we introduce four forms of Hencky nets, which are orthogonal curvilinear coordinates used to construct Michell structures, and derive closed-form solutions for several 2D and 3D Michell structures.

To account for real-life nonlinearities in structural optimization and address the common issue of the GSM, Chapter 3 proposes a new discrete filter with a reduced-order model that is applied to truss optimization considering single and multiple load cases, and nonlinear constitutive behavior. The proposed filtering scheme extracts valid structures, controls design complexity, and transforms the sizing problem into a topology optimization problem. This framework with the reduced-order modeling significantly reduces the size of both the structural and optimization problems within a few steps, leading to drastically im-

proved computational performance. Through one study (with more than one million design variable), the proposed filter algorithm, while offering almost the same optimized structure, was 45 times faster than the standard GSM.

The proposed regularization technique in Chapter 3 to solve nonlinear problems can be combined with other types of filters, for instance, only applying an end filter at the end of the optimization process, or applying the filter at different intervals, i.e., $N_f \geq 1$, instead of applying at every optimization step. This work provides several directions for future research, including applying the proposed filtering scheme to multi-material optimization and additive manufacturing [6], optimization accounting for geometric nonlinearity, and combining this technique (the filtering scheme with discrete optimization) with the continuum optimization (density-based) method.

In Chapter 4, we propose a general multi-material formulation considering material nonlinearity. This formulation is designed to handle an arbitrary number of candidate materials, feature freely specified material layers (multiple material layers can either share or split the design domain, or combine both), and generalized assignment of volume constraints. To efficiently handle the proposed formulation with many constraints, we derive the design update scheme, ZPR, that performs updates of the design variables associated with each constraint independently. The derivation is based on the separable feature of the dual problem of the convex approximated primal subproblem with respect to the Lagrange multipliers, and thus the update of design variables in each volume constraint only depends on the corresponding Lagrange multiplier. The KKT conditions for the proposed multi-material formulation are examined, which indicates identical values of strain energy density for members within the same volume constraint, regardless of the material type. Based on the outcome of this work, we conclude that the proposed multi-material topology optimization framework, which accounts for material nonlinearity and uses the derived ZPR update scheme, leads to a design tool that not only finds the optimal topology but also selects the proper type and the amount of material. The ZPR design update scheme is

flexible and customized to handle a general number of volume constraints – it is also applicable to continuum topology optimization with multiple volume constraints. This work provides insights for future multi-material topology optimization research. The proposed multi-material formulation can be applied to the design of lattice structures. In addition, the connection of multi-material topology optimization to additive manufacturing should be further explored.

We address the issue of selecting more than one material that occurs in multi-material topology optimization in Chapter 5. To ensure the selection of a single material at each subdomain, we propose an algorithm that selects a preferred material among multiple materials based on the evaluation of both the strain energy and cross-sectional area of each member. This algorithm actively and iteratively selects materials to ensure the selection of single material for each member. In this work, the computational framework is based on the formulation and the ZPR updated algorithm proposed in Chapter 4. In addition, we provide an alternative derivation of the ZPR update scheme using the KKT conditions. Based on the investigations using numerical examples, we conclude that the proposed material selection algorithm for multi-material topology optimization is efficient and effective for selecting a single preferred material per overlapping set.

Chapter 6 proposes an efficient randomized optimization approach for topology optimization that drastically reduces the enormous computational cost of optimizing practical structural systems under many load cases while producing high-quality designs. We apply this approach to both the density-based method and the ground structure method by minimizing a weighted sum/average of the compliance over many load cases. We use the Hutchinson trace estimator (which provides the lowest variance) combined with the sample average approximation technique to estimate both the objective and its gradient. Through numerical examples, we show that the proposed randomized algorithm substantially reduces the computational cost by (e.g., a factor of up to 45 in one of the examples), while obtaining a final compliance value close to that obtained by the standard algorithm. Our

proposed damping scheme leads to fast convergence of the optimization scheme.

There are several important directions for future research. Although we have provided an important proof-of-concept, many questions remain open. One important question concerns optimal choices of parameters for both overall computational cost and quality of design. In this case, we could consider dynamically varying the parameters. For example, if necessary, the quality of designs may be improved by increasing the sample size as the minimum point is approached. Another important question concerns the choice among randomized optimization methods/approaches, both in terms of the overall methods as well as the choices in estimates and approximations. We need to further analyze what topology optimization problems can be solved efficiently using this approach. Finally, it would be useful to prove convergence to either a local or global minimum of the topology optimization problem under appropriate conditions. Thus, we hope that Chapter 6 will motivate further the use of stochastic sampling in various areas connected to (large scale) topology optimization.

# Appendices

# APPENDIX A

# FILTER FUNCTION

```
%--------------------------- Filter Function -----------------------------%
% Ref: X Zhang, AS Ramos Jr., GH Paulino, "A Discrete Filter Scheme for   %
% Material Nonlinear Topology Optimization Using the Ground Structure     %
% Method".                                                                %
%-------------------------------------------------------------------------%
%% An example of the filter for a randomly generated vector
n=20; % Size of the random vector
alpha_f=0.4; % Filter value
xr=rand(n,1)*10; % Generate the random vector
%% ---------------------------------------------------------------------
% Option 1: Perform filter component-wise (see Eq. 6)
xr_f=zeros(n,1);
for i=1:n
    if xr(i)/max(xr)<alpha_f
        xr_f(i)=0;
    else
        xr_f(i)=xr(i);
    end
end
%% ---------------------------------------------------------------------
% Option 2: Perform filter for the entire vector
% xr_f=xr;
% xr_f(xr/max(xr)<alpha_f)=0;
%% ---------------------------------------------------------------------
figure
plot(xr/max(xr),xr_f,'ro')
xlabel('x_r^{(i)}/max(x_r)');ylabel('Filter(x_r,\alpha_f,i)');
% Filtered vector with reduced-order modeling
xr_f=xr_f(xr_f>0);
```

# APPENDIX B

# MAPPING FOR STATE EQUATIONS USING PROPOSED FILTERING SCHEME WITH REDUCED-ORDER MODELING

Based on the equations outlined in Section 4.1, this section illustrates the mapping of the external and internal force vectors and the tangent stiffness matrix from the ground structure to the topology through a simple example. Figure B.1a shows the ground structure with numbered DOFs under the prescribed load and boundary conditions. During the optimization process, once the members are removed by the filter, area of members become zero, (e.g., the dashed members in Figure B.1b), we can define the topology and new numbered DOFs by excluding those zero-area members, as shown in Figure B.1c.

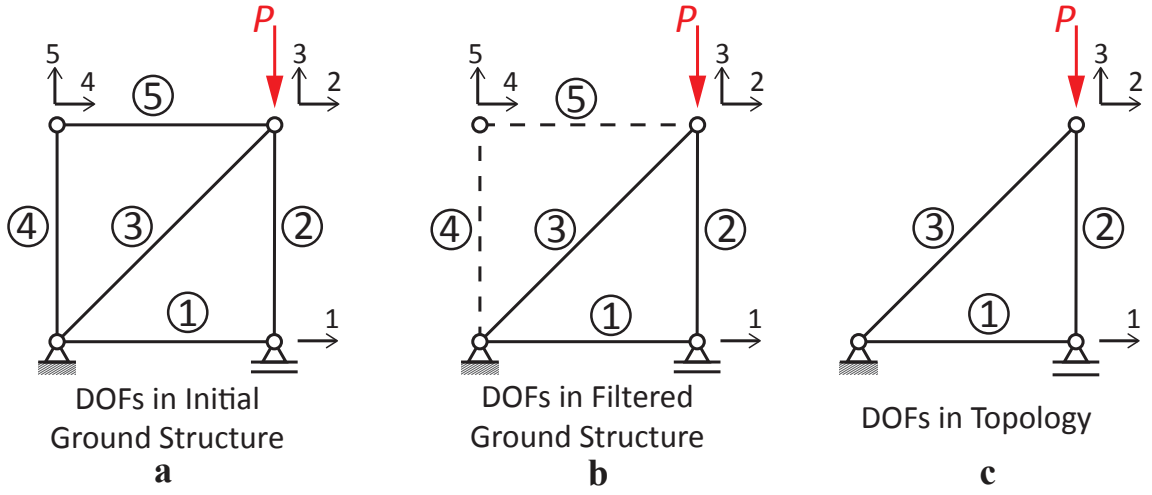


Figure B.1: Mapping of the state equations from the ground structure to the topology with the proposed filtering scheme: **a** Initial ground structure, DOFs, and the load and boundary conditions; **b** ground structure and DOFs after the filtering process at iteration $k$ (dashed lines correspond to bars with zero cross-sectional area); **c** corresponding topology and DOFs after filtering process at iteration $k$.

For the ground structure, the external force vector are given by,

$$\boldsymbol{f} = \left\{ 0 \quad 0 \quad -P \quad 0 \quad 0 \right\}^{\mathrm{T}}. \tag{B.1}$$

The internal force vector and tangent stiffness matrix are obtained by assembling the contributions from each element,

$$\boldsymbol{T} = \begin{Bmatrix} t_1^{(1)} + t_1^{(2)} \\ t_2^{(2)} + t_2^{(3)} + t_2^{(5)} \\ t_3^{(2)} + t_3^{(3)} + t_3^{(5)} \\ t_4^{(4)} + t_4^{(5)} \\ t_5^{(4)} + t_5^{(5)} \end{Bmatrix}, \tag{B.2}$$

$$\boldsymbol{K}_t = \begin{bmatrix} k_{11}^{(1)} + k_{11}^{(2)} & k_{12}^{(2)} & k_{13}^{(2)} & 0 & 0 \\ & k_{22}^{(2)} + k_{22}^{(3)} + k_{22}^{(5)} & k_{23}^{(2)} + k_{23}^{(3)} + k_{23}^{(5)} & k_{24}^{(5)} & k_{25}^{(5)} \\ & & k_{33}^{(2)} + k_{33}^{(3)} + k_{33}^{(5)} & k_{34}^{(5)} & k_{35}^{(5)} \\ & \text{Sym.} & & k_{44}^{(4)} + k_{44}^{(5)} & k_{45}^{(4)} + k_{45}^{(5)} \\ & & & & k_{55}^{(4)} + k_{55}^{(5)} \end{bmatrix}. \tag{B.3}$$

We can define a transformation matrix $\boldsymbol{Q}$ to represent the transformation of the topology displacements to the ground structural displacements (i.e., $\boldsymbol{u} = \boldsymbol{Q}\boldsymbol{u}_{\text{Top}}$),

$$\boldsymbol{Q} = \begin{bmatrix} 1 & 0 & 0 & 0 & 0 \\ 0 & 1 & 0 & 0 & 0 \\ 0 & 0 & 1 & 0 & 0 \end{bmatrix}^{\text{T}}. \tag{B.4}$$

With the transformation matrix, the external force vector for the reduced-order topology is given by

$$\boldsymbol{f}_{\text{Top}} = \boldsymbol{Q}^{\text{T}}\boldsymbol{f} = \begin{Bmatrix} 0 & 0 & -P \end{Bmatrix}^{\text{T}}. \tag{B.5}$$

Similarly, the internal force vector and tangent stiffness matrix for the reduced-order topol-

ogy can be obtained as follows:

$$\boldsymbol{T}_{\text{Top}} = \boldsymbol{Q}^{\text{T}}\boldsymbol{T} = \begin{Bmatrix} t_1^{(1)} + t_1^{(2)} \\ t_2^{(2)} + t_2^{(3)} + t_2^{(5)} \\ t_3^{(2)} + t_3^{(3)} + t_3^{(5)} \end{Bmatrix}, \tag{B.6}$$

$$\boldsymbol{K}_{t,\text{Top}} = \boldsymbol{Q}^{\text{T}}\boldsymbol{K}_t\boldsymbol{Q} = \begin{bmatrix} k_{11}^{(1)} + k_{11}^{(2)} & k_{12}^{(2)} & k_{13}^{(2)} \\ & k_{22}^{(2)} + k_{22}^{(3)} + k_{22}^{(5)} & k_{23}^{(2)} + k_{23}^{(3)} + k_{23}^{(5)} \\ & \text{Sym.} & k_{33}^{(2)} + k_{33}^{(3)} + k_{33}^{(5)} \end{bmatrix}. \tag{B.7}$$

Upon realizing that member 5 is a zero-area member, all the components of its internal force vector and tangent stiffness matrix are zero. As s result, we obtain the final expression for the internal force vector and tangent stiffness matrix for the reduced-order topology as

$$\boldsymbol{T}_{\text{Top}} = \begin{Bmatrix} t_1^{(1)} + t_1^{(2)} \\ t_2^{(2)} + t_2^{(3)} \\ t_3^{(2)} + t_3^{(3)} \end{Bmatrix}, \qquad \boldsymbol{K}_{t,\text{Top}} = \begin{bmatrix} k_{11}^{(1)} + k_{11}^{(2)} & k_{12}^{(2)} & k_{13}^{(2)} \\ & k_{22}^{(2)} + k_{22}^{(3)} & k_{23}^{(2)} + k_{23}^{(3)} \\ & \text{Sym.} & k_{33}^{(2)} + k_{33}^{(3)} \end{bmatrix}. \tag{B.8}$$

## APPENDIX C

## STOCHASTIC SAMPLING OF LOAD CASES

In this appendix, we present an illustration of the stochastic sampling of load cases. As

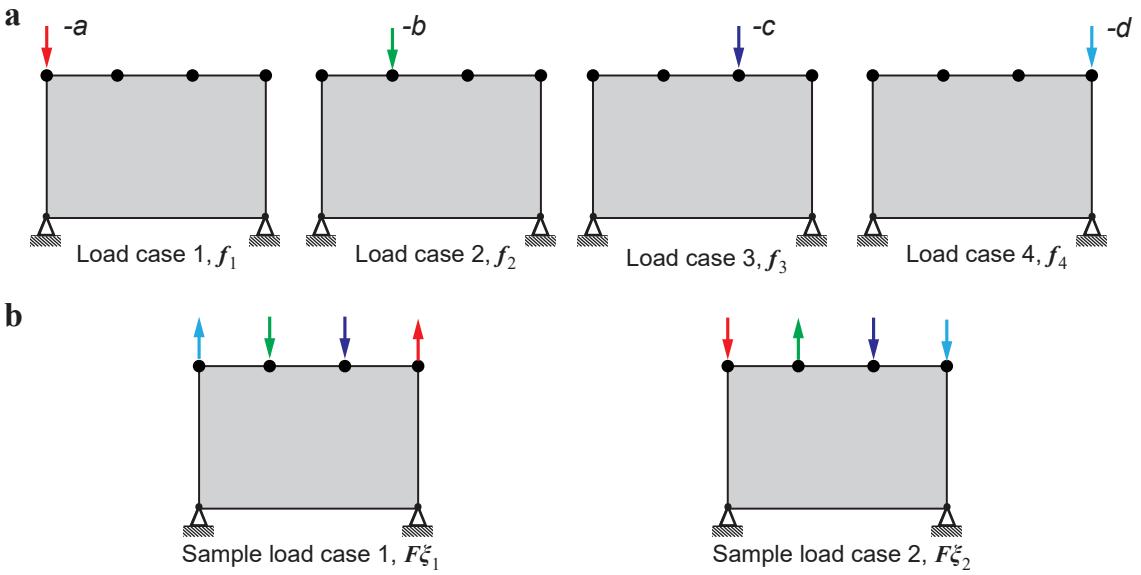


Figure C.1: Demonstration of stochastic sampling of load cases. **a** Design domain with four equally-weighed load cases, $\boldsymbol{f}_1,\ldots,\boldsymbol{f}_4$, acting independently on different nodes; and **b** design domain with two sample load cases based on random vectors $\boldsymbol{\xi}_1$ and $\boldsymbol{\xi}_2$.

shown in Figure C.1 (a), we consider a simply supported rectangle with 4 equally-weighed load cases, $\boldsymbol{f}_1,\ldots,\boldsymbol{f}_4$, acting independently. Numbering the 4 nodes on the top of the rectangle from left to right as 1 to 4, we can express the 4 independent load vectors and load

matrix $\boldsymbol{F}$ as

$$\boldsymbol{f}_1 = \begin{bmatrix} 0 \\ -a \\ 0 \\ 0 \\ 0 \\ 0 \\ 0 \\ 0 \end{bmatrix}, \boldsymbol{f}_2 = \begin{bmatrix} 0 \\ 0 \\ 0 \\ -b \\ 0 \\ 0 \\ 0 \\ 0 \end{bmatrix}, \boldsymbol{f}_3 = \begin{bmatrix} 0 \\ 0 \\ 0 \\ 0 \\ 0 \\ -c \\ 0 \\ 0 \end{bmatrix}, \boldsymbol{f}_2 = \begin{bmatrix} 0 \\ 0 \\ 0 \\ 0 \\ 0 \\ 0 \\ 0 \\ -d \end{bmatrix}, \quad \boldsymbol{F} = \begin{bmatrix} 0 & 0 & 0 & 0 \\ -a & 0 & 0 & 0 \\ 0 & 0 & 0 & 0 \\ 0 & -b & 0 & 0 \\ 0 & 0 & 0 & 0 \\ 0 & 0 & -c & 0 \\ 0 & 0 & 0 & 0 \\ 0 & 0 & 0 & -d \end{bmatrix}. \tag{C.1}$$

From the Rademacher distribution, we randomly select 2 vectors, $\boldsymbol{\xi}_1$ and $\boldsymbol{\xi}_2$, with the following form

$$\boldsymbol{\xi}_1 = \begin{bmatrix} -1 & 1 & 1 & -1 \end{bmatrix}^T \text{ and } \boldsymbol{\xi}_2 = \begin{bmatrix} 1 & -1 & 1 & 1 \end{bmatrix}^T. \tag{C.2}$$

Then, according to Eq. (6.16), we obtain the corresponding sample load cases as

$$\boldsymbol{F}\boldsymbol{\xi}_1 = \begin{bmatrix} 0 & a & 0 & -b & 0 & -c & 0 & d \end{bmatrix}^T \text{ and } \boldsymbol{F}\boldsymbol{\xi}_2 = \begin{bmatrix} 0 & -a & 0 & b & 0 & -c & 0 & -d \end{bmatrix}^T. \tag{C.3}$$

The two sample load cases are shown in the Figure C.1 (b). We can see that in both sample load cases, all the load cases $\boldsymbol{f}_1, ..., \boldsymbol{f}_4$ appear simultaneously but may act in opposing directions.

## REFERENCES


[1] L. L. Beghini, A. Beghini, N. Katz, W. F. Baker, and G. H. Paulino, "Connecting architecture and engineering through structural topology optimization," *Engineering Structures*, vol. 59, pp. 716–726, 2014.

[2] L. Krog, A. Tucker, M. Kemp, and R. Boyd, "Topology optimization of aircraft wing box ribs.," in *10th AIAA/ISSMO Multidisciplinary Analysis and Optimization Conference*, 2004, pp. 2004–4481.

[3] O. Sardan, V. Eichhorn, D. H. Petersen, S. Fatikow, O. Sigmund, and P. Bøggild, "Rapid prototyping of nanotube-based devices using topology-optimized microgrippers," *Nanotechnology*, vol. 19, no. 49, p. 495 503, 2008.

[4] C. Schumacher, B. Bickel, J. Rys, S. Marschner, C. Daraio, and M. Gross, "Microstructures to control elasticity in 3d printing," *ACM Trans. Graph.*, vol. 34, no. 4, 136:1–136:13, Jul. 2015.

[5] A. Sutradhar, G. Paulino, M. Miller, and T. Nguyen, "Topological optimization for designing patient-specific large craniofacial segmental bone replacements," *Proceedings of the National Academy of Sciences*, vol. 107, no. 30, pp. 13 222–13 227, 2010.

[6] T. Zegard and G. H. Paulino, "Bridging topology optimization and additive manufacturing," *Structural and Multidisciplinary Optimization*, vol. 53, no. 1, pp. 175–192, 2016.

[7] B.-C. Chen, E. C. N. Silva, and N. Kikuchi, "Advances in computational design and optimization with application to mems," *International Journal for Numerical Methods in Engineering*, vol. 52, pp. 23–62, 2001.

[8] J. W. Halloran and J. Qi, "Negative thermal expansion artificial material from iron-nickel alloys by oxide co-extrusion with reductive sintering," *Journal of Materials Science*, vol. 39, pp. 4113–4118, 13 2004.

[9] L. L. Beghini, A. Beghini, W. F. Baker, and G. H. Paulino, "Integrated discrete/continuum topology optimization framework for stiffness or global stability of high-rise buildings," *Journal of Structural Engineering*, vol. 141, pp. 04 014 207–1–10, 8 2015.

[10] A. Gaynor, J. Guest, and C. Moen, "Reinforced concrete force visualization and design using bilinear truss-continuum topology optimization," *Journal of Structural Engineering*, vol. 139, no. 4, pp. 607–618, 2012.

[11] M. Victoria, O. M. Querin, and P. Martí, "Generation of strut-and-tie models by topology design using different material properties in tension and compression," *Structural and Multidisciplinary Optimization*, vol. 44, no. 2, pp. 247–258, 2011.

[12] M. Bogomolny and O. Amir, "Conceptual design of reinforced concrete structures using topology optimization with elastoplastic material modeling," *International Journal for Numerical Methods in Engineering*, vol. 90, no. 13, pp. 1578–1597, 2012.

[13] O. Amir and O. Sigmund, "Reinforcement layout design for concrete structures based on continuum damage and truss topology optimization," *Structural and Multidisciplinary Optimization*, vol. 47, no. 2, pp. 157–174, 2013.

[14] T. Zegard and G. H. Paulino, "Truss layout optimization within a continuum," *Structural and Multidisciplinary Optimization*, vol. 48, no. 1, pp. 1–16, 2013.

[15] S. D. Larsen, O. Sigmund, and J. P. Groen, "Optimal truss and frame design from projected homogenization-based topology optimization," *Structural and Multidisciplinary Optimization*, vol. 57, pp. 1461–1474, 4 2018.

[16] A. G. M. Michell, "The limits of economy of material in frame-structures," *Philosophical Magazine Series 6*, vol. 8, no. 47, pp. 589–597, Nov. 1904.

[17] W. S. Hemp, *Optimum structures*. Clarendon Press, 1973.

[18] W. Prager, *Introduction to Structural Optimization*, ser. CISM International Centre for Mechanical Sciences. New York: Springer-Verlag Wien, 1972.

[19] A. S. L. Chan, *The design of Michell optimum structures*. London: Ministry of Aviation, Aeronautical Research Council, 1960, vol. 3303.

[20] G. I. N. Rozvany, "Some shortcomings in michell's truss theory," *Structural and Multidisciplinary Optimization*, vol. 12, pp. 244–250, 4 1996.

[21] G. I. N. Rozvany, "Exact analytical solutions for some popular benchmark problems in topology optimization," *Structural Optimization*, vol. 15, pp. 42–48, 1998.

[22] G. I. N. Rozvany and W. Gollub, "Michell layouts for various combinations of line supports," *International Journal of Mechanical Sciences*, 1990.

[23] T. Lewinski, "Michell structures formed on surfaces of revolution," *Structural and Multidisciplinary Optimization*, vol. 28, pp. 20–30, 1 2004.

[24] C. Graczykowski and T. Lewinski, "The lightest plane structures of a bounded stress level transmitting a point load to a circular support," *Control and Cybernetics*, vol. 34, pp. 227–253, 1 2005.

[25] T. Lewiński and G. I. N. Rozvany, "Exact analytical solutions for some popular benchmark problems in topology optimization II: three-sided polygonal supports," *Structural and Multidisciplinary Optimization*, vol. 33, no. 4-5, pp. 337–349, Feb. 2007.

[26] T. Lewiński and G. I. N. Rozvany, "Exact analytical solutions for some popular benchmark problems in topology optimization III: L-shaped domains," vol. 35, pp. 165–174, 2008.

[27] W. S. Dorn, R. E. Gomory, and H. J. Greenberg, "Automatic design of optimal structures," *Journal de Mecanique*, vol. 3, pp. 25–52, 1964.

[28] U. Kirsch, "Optimal topologies of truss structures," *Computer Methods in Applied Mechanics and Engineering*, vol. 72, no. 1, pp. 15–28, 1989.

[29] G. I. N. Rozvany, *Topology optimization in structural mechanics*, ser. CISM International Centre for Mechanical Sciences. Udine: Ed. SpringerWienNewYork, 1997.

[30] M. P. Bendsøe and O. Sigmund, *Topology optimization: theory, methods, and applications*. Berlin, Germany: Springer, 2003, p. 370, ISBN: 3540429921.

[31] P. W. Christensen and A. Klarbring, *An introduction to structural optimization*. Linköping: Springer Science & Business Media, 2009.

[32] W. K. Rule, "Automatic truss design by optimized growth," *Journal of Structural Engineering*, vol. 120, no. 10, pp. 3063–3070, 1994.

[33] M. Gilbert and A. Tyas, "Layout optimization of large-scale pin-jointed frames," *Engineering Computations*, vol. 20, no. 8, pp. 1044–1064, 2003.

[34] T. Hagishita and M. Ohsaki, "Topology optimization of trusses by growing ground structure method," *Structural and Multidisciplinary Optimization*, vol. 37, no. 4, pp. 377–393, Jan. 2009.

[35] W. Achtziger, "Local stability of trusses in the context of topology optimization part i: Exact modelling," *Structural and Multidisciplinary Optimization*, vol. 17, no. 4, pp. 235–246, 1999.

[36] W. Achtziger, "Local stability of trusses in the context of topology optimization part II: A numerical approach," *Structural Optimization*, vol. 17, no. 4, pp. 247–258, 1999.

[37] K. Svanberg, "On local and global minima in structural optimization," in *New Directions in Optimum Structural Design*, E Gallhager, R. H. Ragsdell, and O. C. Zienkiewicz, Eds., Chichester: John Wiley and Sons, 1984, pp. 327–341.

[38] W. Achtziger, "Topology optimization of discrete structures," in *Topology Optimization in Structural Mechanics*, G. I. N. Rozvany, Ed. Vienna: Springer Vienna, 1997, pp. 57–100, ISBN: 978-3-7091-2566-3.

[39] T. Sokół, "A 99 line code for discretized Michell truss optimization written in Mathematica," *Structural and Multidisciplinary Optimization*, vol. 43, no. 2, pp. 181–190, 2011.

[40] W. Achtziger, "On simultaneous optimization of truss geometry and topology," *Structural and Multidisciplinary Optimization*, vol. 33, no. 4-5, pp. 285–304, Jan. 2007.

[41] W. Achtziger, "Truss topology optimization including bar properties different for tension and compression," *Structural Optimization*, vol. 12, no. 1, pp. 63–74, 1996.

[42] B. Bourdin, "Filters in topology optimization," *International Journal for Numerical Methods in Engineering*, vol. 50, no. 9, pp. 2143–2158, 2001.

[43] M. P. Bendsøe, "Optimal shape design as a material distribution problem," *Structural optimization*, vol. 1, no. 4, pp. 193–202, 1989.

[44] M. Zhou and G. Rozvany, "The coc algorithm, part ii: Topological, geometrical and generalized shape optimization," *Computer Methods in Applied Mechanics and Engineering*, vol. 89, no. 1-3, pp. 309–336, 1991.

[45] M. Stolpe and K. Svanberg, "An alternative interpolation scheme for minimum compliance topology optimization," *Structural and Multidisciplinary Optimization*, vol. 22, no. 2, pp. 116–124, 2001.

[46] J. Petersson, "A finite element analysis of optimal variable thickness sheets," *SIAM Journal on Numerical Analysis*, vol. 36, no. 6, pp. 1759–1778, 1999.

[47] J. Schwerdtfeger, F. Wein, G. Leugering, R. Singer, C. Körner, M. Stingl, and F. Schury, "Design of auxetic structures via mathematical optimization," *Advanced materials*, vol. 23, no. 22-23, pp. 2650–2654, 2011.

[48] E. Andreassen, B. S. Lazarov, and O. Sigmund, "Design of manufacturable 3d extremal elastic microstructure," *Mechanics of Materials*, vol. 69, no. 1, pp. 1–10, 2014.

[49] A. Clausen, F. Wang, J. Jensen, O. Sigmund, and J. Lewis, "Topology optimized architectures with programmable poisson's ratio over large deformations," *Advanced Materials*, 2015.

[50] M. Castilho, M. Dias, U. Gbureck, J. Groll, P. Fernandes, I. Pires, B. Gouveia, J. Rodrigues, and E. Vorndran, "Fabrication of computationally designed scaffolds by low temperature 3d printing," *Biofabrication*, vol. 5, no. 3, p. 035 012, 2013.

[51] H. Kang, C. Lin, and S. Hollister, "Topology optimization of three dimensional tissue engineering scaffold architectures for prescribed bulk modulus and diffusivity," *Structural and Multidisciplinary Optimization*, vol. 42, no. 4, pp. 633–644, 2010.

[52] V. J. Challis, A. P. Roberts, J. Grotowski, L. Zhang, and T. B. Sercombe, "Prototypes for bone implant scaffolds designed via topology optimization and manufactured by solid freeform fabrication," *Advanced Engineering Materials*, vol. 12, no. 11, pp. 1106–1110, 2010.

[53] M. Dias, J. M. Guedes, C. L. Flanagan, S. J. Hollister, and P. R. Fernandes, "Optimization of scaffold design for bone tissue engineering: A computational and experimental study," *Medical engineering & physics*, vol. 36, no. 4, pp. 448–457, 2014.

[54] A. Sutradhar, J. Park, D. Carrau, T. H. Nguyen, M. J. Miller, and G. H. Paulino, "Designing patient-specific 3d printed craniofacial implants using a novel topology optimization method," *Medical & biological engineering & computing*, pp. 1–13, 2015.

[55] D. Brackett, I. Ashcroft, and R. Hague, "Topology optimization for additive manufacturing," in *Proceedings of the Solid Freeform Fabrication Symposium, Austin, TX*, 2011, pp. 348–362.

[56] P. Zhang, J. Toman, Y. Yu, E. Biyikli, M. Kirca, M. Chmielus, and A. To, "Efficient design-optimization of variable-density hexagonal cellular structure by additive manufacturing: Theory and validation," *Journal of Manufacturing Science and Engineering*, vol. 137, no. 2, p. 021 004, 2015.

[57] Z. Doubrovski, J. C. Verlinden, and J. Geraedts, "Optimal design for additive manufacturing: Opportunities and challenges," in *ASME 2011 International Design Engineering Technical Conferences and Computers and Information in Engineering Conference*, American Society of Mechanical Engineers, 2011, pp. 635–646.

[58] M. Leary, L. Merli, F. Torti, M. Mazur, and M. Brandt, "Optimal topology for additive manufacture: A method for enabling additive manufacture of support-free optimal structures," *Materials & Design*, vol. 63, pp. 678–690, 2014.

[59] J. Liu, A. T. Gaynor, S. Chen, Z. Kang, K. Suresh, A. Takezawa, L. Li, J. Kato, J. Tang, C. C. L. Wang, L. Cheng, X. Liang, and A. C. To, "Current and future trends in topology optimization for additive manufacturing," *Structural and Multidisciplinary Optimization*, vol. 57, no. 6, pp. 2457–2483, 2018.

[60] O. Sigmund and S. Torquato, "Design of materials with extreme thermal expansion using a three-phase topology optimization method," *Journal of the Mechanics and Physics of Solids*, vol. 45, no. 6, pp. 1037–1067, 1997.

[61] L. V. Gibiansky and O. Sigmund, "Multiphase composites with extremal bulk modulus," *Journal of the Mechanics and Physics of Solids*, vol. 48, no. 3, pp. 461–498, 2000.

[62] C. F. Hvejsel and E. Lund, "Material interpolation schemes for unified topology and multi-material optimization," *Structural and Multidisciplinary Optimization*, vol. 43, no. 6, pp. 811–825, 2011.

[63] L. Yin and G. Ananthasuresh, "Topology optimization of compliant mechanisms with multiple materials using a peak function material interpolation scheme," *Structural and Multidisciplinary Optimization*, vol. 23, no. 1, pp. 49–62, 2001.

[64] S. Zhou and M. Y. Wang, "Multimaterial structural topology optimization with a generalized Cahn–Hilliard model of multiphase transition," *Structural and Multidisciplinary Optimization*, vol. 33, no. 2, pp. 89–111, 2007.

[65] R. Tavakoli, "Multimaterial topology optimization by volume constrained allen–cahn system and regularized projected steepest descent method," *Computer Methods in Applied Mechanics and Engineering*, vol. 276, pp. 534–565, 2014.

[66] M. Y. Wang and X. Wang, ""Color" level sets: A multi-phase method for structural topology optimization with multiple materials," *Computer Methods in Applied Mechanics and Engineering*, vol. 193, no. 6, pp. 469–496, 2004.

[67] M. Y. Wang and X. Wang, "A level-set based variational method for design and optimization of heterogeneous objects," *Computer-Aided Design*, vol. 37, no. 3, pp. 321–337, 2005.

[68] M. Y. Wang, S. Chen, X. Wang, and Y. Mei, "Design of multimaterial compliant mechanisms using level-set methods," *Journal of Mechanical Design*, vol. 127, no. 5, pp. 941–956, 2005.

[69] Y. Mei and X. Wang, "A level set method for structural topology optimization with multi-constraints and multi-materials," *Acta Mechanica Sinica*, vol. 20, no. 5, pp. 507–518, 2004.

[70] A. A. Groenwold and L. F. P. Etman, "On the equivalence of optimality criterion and sequential approximate optimization methods in the classical topology layout problem," *International journal for numerical methods in engineering*, vol. 73, no. 3, pp. 297–316, 2008.

[71] K. Svanberg, "The method of moving asymptotes – a new method for structural optimization," *International Journal for Numerical Methods in Engineering*, vol. 24, no. 2, pp. 359–373, 1987.

[72] J. Stegmann and E. Lund, "Discrete material optimization of general composite shell structures," *International Journal for Numerical Methods in Engineering*, vol. 62, no. 14, pp. 2009–2027, 2005.

[73] M. Sarkisian, *Designing Tall Buildings: Structure as Architecture*, 2nd ed. New York: Routledge, 2016.

[74] H. Hencky, "Über einige statisch bestimmte F̈alle des gleichgewichts in plastischen körpern," *ZAMM - Journal of Applied Mathematics and Mechanics / Zeitschrift für Angewandte Mathematik und Mechanik*, vol. 747, pp. 241–251, 1923.

[75] L. Prandtl, "Hauptaufsätze: Über die eindringungsfestigkeit (härte) plastischer baustoffe und die festigkeit von schneiden," *ZAMM - Journal of Applied Mathematics and Mechanics / Zeitschrift für Angewandte Mathematik und Mechanik*, vol. 1, no. 1, pp. 15–20, 1921.

[76] G. I. N. Rozvany and T. Sokół, "Validation of numerical methods by analytical benchmarks, and verication of exact solutions by numerical methods," in *Topology Optimization in Structural and Continuum Mechanics*, Springer, Vienna, 2014.

[77] J. C. Maxwell, "On reciprocal figures, frames, and diagrams of forces," *Transactions of the Royal Society of Edinburgh*, vol. 26, pp. 1–40, 1870.

[78] A. Mazurek, "Geometrical aspects of optimum truss like structures for three-force problem," *Structural and Multidisciplinary Optimization*, vol. 45, no. 1, pp. 21–32, Jul. 2011.

[79] A. Mazurek, "Geometrical aspects of optimum truss like structures for three-force problem," *Structural and Multidisciplinary Optimization*, vol. 45, pp. 21–32, 1 2011.

[80] R. Hill, *The mathematical theory of plasticity*. Oxford: Oxford Clarendon Press, 1950.

[81] W. Prager, "A geometrical discussion of the slip line field in plane plastic flow," *Transactions of the Royal Institute of Technology*, no. 65, pp. 1–26, 1953.

[82] L. L. Beghini, J. Carrion, A. Beghini, A. Mazurek, and W. F. Baker, "Structural optimization using graphic statics," *Structural and Multidisciplinary Optimization*, vol. 49, pp. 351–366, 3 2014.

[83] M. Ohsaki, *Optimization of finite dimensional structures*. Boca Raton: CRC Press, 2010.

[84] A. S. Ramos Jr. and G. H. Paulino, "Convex topology optimization for hyperelastic trusses based on the ground-structure approach," *Structural and Multidisciplinary Optimization*, vol. 51, no. 2, pp. 287–304, 2015.

[85] A. S. Ramos Jr. and G. H. Paulino, "Filtering Structures out of Ground Structures – A discrete filtering tool for structural design optimization," *Structural and Multidisciplinary Optimization*, vol. 54, no. 1, pp. 95–116, 2016.

[86] T. Bruns, "Zero density lower bounds in topology optimization," *Computer Methods in Applied Mechanics and Engineering*, vol. 196, no. 1, pp. 566–578, 2006.

[87] T. Washizawa, A. Asai, and N. Yoshikawa, "A new approach for solving singular systems in topology optimization using krylov subspace methods," *Structural and Multidisciplinary Optimization*, vol. 28, no. 5, pp. 330–339, 2004.

[88] S. Wang, E. de Sturler, and G. H. Paulino, "Large-scale topology optimization using preconditioned krylov subspace methods with recycling," *International Journal for Numerical Methods in Engineering*, vol. 69, no. 12, pp. 2441–2468, 2007.

[89] S. Tangaramvong, F. Tin-Loi, and W. Gao, "Optimal retrofit of moment resisting frames using braces accounting for geometric nonlinearity and serviceability conditions," *Engineering Structures*, vol. 80, pp. 189–199, 2014.

[90] M. Stolpe, "Truss optimization with discrete design variables: A critical review," *Structural and Multidisciplinary Optimization*, vol. 53, pp. 349–374, 2016.

[91] J. A. Stricklin and W. E. Haisler, "Formulations and solution procedures for nonlinear structural analysis," *Computers & Structures*, vol. 7, no. 1, pp. 125–136, 1977.

[92] R. Haftka and M. Kamat, "Simultaneous nonlinear structural analysis and design," *Computational Mechanics*, vol. 4, no. 6, pp. 409–416, 1989.

[93] Y. Toklu, "Nonlinear analysis of trusses through energy minimization," *Computers & structures*, vol. 82, no. 20, pp. 1581–1589, 2004.

[94] B. Hassani and E. Hinton, "A review of homogenization and topology optimization iiitopology optimization using optimality criteria," *Computers & structures*, vol. 69, no. 6, pp. 739–756, 1998.

[95] N. Khot and M. Kamat, "Minimum weight design of truss structures with geometric nonlinear behavior," *AIAA journal*, vol. 23, no. 1, pp. 139–144, 1985.

[96] A. Klarbring and N. Strömberg, "A note on the min-max formulation of stiffness optimization including non-zero prescribed displacements," *Structural and Multidisciplinary Optimization*, vol. 45, no. 1, pp. 147–149, Jan. 2012.

[97] A. Klarbring and N. Strömberg, "Topology optimization of hyperelastic bodies including non-zero prescribed displacements," *Structural and Multidisciplinary Optimization*, vol. 47, no. 1, pp. 37–48, 2013.

[98] T. Buhl, C. Pedersen, and O. Sigmund, "Stiffness design of geometrically nonlinear structures using topology optimization," *Structural and Multidisciplinary Optimization*, vol. 19, no. 2, pp. 93–104, 2000.

[99] R. Kemmler, A. Lipka, and E. Ramm, "Large deformations and stability in topology optimization," *Structural and Multidisciplinary Optimization*, vol. 30, no. 6, pp. 459–476, 2005.

[100] T. Sekimoto and H. Noguchi, "Homologous topology optimization in large displacement and buckling problems," *JSME International Journal Series A*, vol. 44, pp. 616–622, 2001.

[101] A. Tikhonov and V. Arsenin, *Methods for solving ill-posed problems*. New York: Wiley, 1977.

[102] C. Felippa. (n.d.). Newton method: General control and variants, University of Colorado.

[103] C. Talischi and G. H. Paulino, "An operator splitting algorithm for Tikhonov-regularized topology optimization," *Computer Methods in Applied Mechanics and Engineering*, vol. 253, pp. 599–608, 2013.

[104] R. Rockafellar, *Convex Analysis*. Princeton, N.J.: Princeton University Press, 1970.

[105] J. Bonet and R. D. Wood, *Nonlinear continuum mechanics for finite element analysis*. Cambridge University Press, 2008.

[106] R. W. Ogden, *Non-linear elastic deformations*. Mineola: Dover Publications Inc, 1984.

[107] A. Klarbring and M. Rönnqvist, "Nested approach to structural optimization in nonsmooth mechanics," *Structural optimization*, vol. 10, no. 2, pp. 79–86, 1995.

[108] P. Wriggers, *Nonlinear finite element methods*. Springer Science & Business Media, 2008.

[109] L. Armijo, "Minimization of functions having Lipschitz continuous first partial derivatives," *Pacific Journal of Mathematics*, vol. 16, no. 1, pp. 1–3, 1966.

[110] D. P. Bertsekas, *Nonlinear programming*. Belmont, MA: Athena Scientific, 1999.

[111] U. M. Ascher and C. Greif, *A First Course on Numerical Methods*. Society for Industrial and Applied Mathematics, 2011, vol. 7.

[112] T. Zegard and G. H. Paulino, "GRAND – Ground structure based topology optimization for arbitrary 2D domains using MATLAB," *Structural and Multidisciplinary Optimization*, vol. 50, no. 5, pp. 861–882, 2014.

[113] T. Zegard and G. H. Paulino, "GRAND3 – Ground structure based topology optimization for arbitrary 3D domains using MATLAB," *Structural and Multidisciplinary Optimization*, vol. 52, no. 6, pp. 1161–1184, 2015.

[114] M. P. Bendsøe and O. Sigmund, "Material interpolation schemes in topology optimization," *Archive of applied mechanics*, vol. 69, no. 9-10, pp. 635–654, 1999.

[115] M. Wallin, N. Ivarsson, and M. Ristinmaa, "Large strain phase-field-based multimaterial topology optimization," *International Journal for Numerical Methods in Engineering*, vol. 104, no. 9, pp. 887–904, 2015.

[116] R. Tavakoli and S. M. Mohseni, "Alternating active-phase algorithm for multimaterial topology optimization problems: A 115-line matlab implementation," *Structural and Multidisciplinary Optimization*, vol. 49, no. 4, pp. 621–642, 2014.

[117] T. Stanković, J. Mueller, P. Egan, and K. Shea, "A generalized optimality criteria method for optimization of additively manufactured multimaterial lattice structures," *Journal of Mechanical Design*, vol. 137, no. 11, p. 111 405, 2015.

[118] U. Kirsch, *Structural optimization: fundamentals and applications*. Springer-Verlag Berlin Heidelberg, 1993.

[119] G. I. N. Rozvany, M. P. Bendsoe, and U. Kirsch, "Layout optimization of structures," *Applied Mechanics Reviews*, vol. 48, no. 2, pp. 41–119, 1995.

[120] X. Zhang, A. S. Ramos Jr., and G. H. Paulino, "Material nonlinear topology design using the ground structure method with a discrete filter scheme," *Structural and Multidisciplinary Optimization*, vol. 55, no. 6, pp. 2045–2072, 2017.

[121] R. T. Haftka and Z. Gürdal, *Elements of Structural Optimization*. Netherlands: Springer Netherlands, 1992.

[122] L. Yin and W. Yang, "Optimality criteria method for topology optimization under multiple constraints," *Computers & Structures*, vol. 79, no. 20, pp. 1839–1850, 2001.

[123] M. Cui and H. Chen, "An improved alternating active-phase algorithm for multi-material topology optimization problems," in *Applied Mechanics and Materials*, Trans Tech Publ, vol. 635, 2014, pp. 105–111.

[124] J. Park and A. Sutradhar, "A multi-resolution method for 3D multi-material topology optimization," *Computer Methods in Applied Mechanics and Engineering*, vol. 285, pp. 571–586, 2015.

[125] G. I. N. Rozvany, "Difficulties in truss topology optimization with stress, local buckling and system stability constraints," *Structural optimization*, vol. 11, no. 3, pp. 213–217, 1996.

[126] A. Ben-Tal, F. Jarre, M. Kočvara, A. Nemirovski, and J. Zowe, "Optimal design of trusses under a nonconvex global buckling constraint," *Optimization and Engineering*, vol. 1, no. 2, pp. 189–213, 2000.

[127] A. Tyas, M. Gilbert, and T. Pritchard, "Practical plastic layout optimization of trusses incorporating stability considerations," *Computers & Structures*, vol. 84, no. 3C4, pp. 115 –126, 2006.

[128] X. Zhang, S. Maheshwari, A. S. Ramos Jr., and G. H. Paulino, "Macroelement and macropatch approaches to structural topology optimization using the ground structure method," *ASCE Journal of Structural Engineering.*, vol. 142, no. 11, pp. 04 016 090–1–14, 2016.

[129] X. S. Zhang, E. de Sturler, and G. H. Paulino, "Stochastic sampling for deterministic structural topology optimization with many load cases: Density-based and ground structure approaches," *Computer Methods in Applied Mechanics and Engineering*, vol. 325, pp. 463–487, 2017.

[130] T. Zegard, F. William F. Baker, A. Mazurek, and G. H. Paulino, "Geometrical aspects of lateral bracing systems: Where should the optimal bracing point be?" *ASCE Journal of Structural Engineering*, vol. 140, no. 9, pp. 04 014 063–1–9, 2014.

[131] X. S. Zhang, G. H. Paulino, and A. S. Ramos Jr., "Multi-material topology optimization with multiple volume constraints: A ground structure approach involving material nonlinearity," *Structural and Multidisciplinary Optimization*, vol. 57, pp. 161–182, 1 2018.

[132] A. R. Diaz and M. P. Bendsøe, "Shape optimization of structures for multiple loading conditions using a homogenization method," *Structural Optimization*, vol. 4, no. 1, pp. 17–22, 1992.

[133] M. P. Bendsøe, A. Ben-Tal, and J. Zowe, "Optimization methods for truss geometry and topology design," *Structural optimization*, vol. 7, no. 3, pp. 141–159, 1994.

[134] W. Achtziger, "Multiple-load truss topology and sizing optimization: Some properties of minimax compliance," *Journal of optimization theory and applications*, vol. 98, no. 2, pp. 255–280, 1998.

[135] E. Haber, M. Chung, and F. Herrmann, "An effective method for parameter estimation with pde constraints with multiple right-hand sides," *SIAM Journal on Optimization*, vol. 22, no. 3, pp. 739–757, 2012.

[136] F. Roosta-Khorasani, K. van den Doel, and U. Ascher, "Stochastic algorithms for inverse problems involving pdes and many measurements," *SIAM Journal on Scientific Computing*, vol. 36, no. 5, S3–S22, 2014.

[137] R. Neelamani, C. E. Krohn, J. R. Krebs, J. K. Romberg, M. Deffenbaugh, and J. E. Anderson, "Efficient seismic forward modeling using simultaneous random sources and sparsity," *Geophysics*, vol. 75, no. 6, WB15–WB27, 2010.

[138] H. Avron, P. Maymounkov, and S. Toledo, "Blendenpik: Supercharging LAPACK's least-squares solver," *SIAM Journal on Scientific Computing*, vol. 32, no. 3, pp. 1217–1236, 2010.

[139] M. Hutchinson, "A stochastic estimator of the trace of the influence matrix for laplacian smoothing splines," *Communication in Statistics-Simulation and Computation*, vol. 18, no. 3, pp. 1059–1076, 1989.

[140] J. A. Tropp, "User-friendly tools for random matrices: An introduction," DTIC Document, Tech. Rep., 2012.

[141] N. Halko, P. Martinsson, and J. A. Tropp, "Finding structure with randomness: Probabilistic algorithms for constructing approximate matrix decompositions," *SIAM review*, vol. 53, no. 2, pp. 217–288, 2011.

[142] P. Drineas and M. W. Mahoney, "Randnla: Randomized numerical linear algebra," *Communications of the ACM*, vol. 59, no. 6, pp. 80–90, 2016.

[143] H. Avron and S. Toledo, "Randomized algorithms for estimating the trace of an implicit symmetric positive semi-definite matrix," *Journal of the ACM*, vol. 58, no. 2, 2011, Article 8.

[144] F. Roosta-Khorasani and U. Ascher, "Improved bounds on sample size for implicit matrix trace estimators," *Foundations of Computational Mathematics*, vol. 15, no. 5, pp. 1187–1212, 2015.

[145] A. K. Saibaba, A. Alexanderian, and I. C. F. Ipsen, "Randomized matrix-free trace and log-determinant estimators," *Numerische Mathematik*, vol. 137, pp. 353–395, 2 2017.

[146] M. Carrasco, B. Ivorra, R. Lecaros, and Á. Ramos del Olmo, "An expected compliance model based on topology optimization for designing structures submitted to random loads," *Differential Equations & Applications*, vol. 4, no. 1, pp. 111–120, 2012.

[147] P. D Dunning and H. A. Kim, "Robust topology optimization: Minimization of expected and variance of compliance," *AIAA Journal*, vol. 51, no. 11, pp. 2656–2664, 2013.

[148] M. Tootkaboni, A. Asadpoure, and J. K. Guest, "Topology optimization of continuum structures under uncertainty–a polynomial chaos approach," *Computer Methods in Applied Mechanics and Engineering*, vol. 201, pp. 263–275, 2012.

[149] A. Shapiro, D. Dentcheva, and A. Ruszczyński, *Lectures on stochastic programming: modeling and theory*, ser. MPS-SIAM Series on Optimization. Philadelphia: SIAM and MPS, 2009.

[150] C. M. Grinstead and J. L. Snell, *Introduction to Probability*, 2nd ed. American Mathematical Society, 2006.

[151] A. J. Kleywegt, A. Shapiro, and T. Homem-de Mello, "The sample average approximation method for stochastic discrete optimization," *SIAM Journal on Optimization*, vol. 12, pp. 479–502, 2002.

[152] H. Robbins and S. Monro, "A stochastic approximation method," *The Annals of Mathematical Statistics*, vol. 22, no. 3, pp. 400–407, 1951.

[153] N. N. Schraudolph, "Local gain adaptation in stochastic gradient descent," in *Intl. Conf. Artificial Neural Networks*, vol. 2, Edinburgh, Scotland: IEE, 1999, pp. 569–574.

[154] S. V. N. Vishwanathan, N. N. Schraudolph, M. W. Schmidt, and K. P. Murphy, "Accelerated training of conditional random fields with stochastic gradient meth-

ods," in *Proceedings of the 23rd international conference on Machine learning*, Pittsburgh, PA: ACM, 2006, pp. 969–976.

[155] N. Schraudolph, J. Yu, and S. Günter, "A stochastic quasi-newton method for online convex optimization," in *11th Intl. Conf. on Artificial Intelligence and Statistics (AIstats)*, Soc. for Artificial Intelligence and Statistics, 2007, pp. 433–440.

[156] A. Nemirovski, A. Juditsky, G. Lan, and A. Shapiro, "Robust stochastic approximation approach to stochastic programming," *SIAM Journal on Optimization*, vol. 19, no. 4, pp. 1574–1609, 2009.

[157] S. Kirkpatrick, C. D. G. Jr., and M. P. Vecchi, "Optimization by simulated annealing," *Sicence*, vol. 220, no. 4598, pp. 671–680, 1983.

[158] P. Salamon, P. Sibani, and R. Frost, *Facts, conjectures, and improvements for simulated annealing*, ser. SIAM Monographs on Mathematical Modeling and Computation. Philadelphia: SIAM, 2002.

[159] L. Bottou, F. E. Curtis, and J. Nocedal, "Optimization methods for large-scale machine learning," *arXiv preprint arXiv:1606.04838*, 2016.

[160] H. Nguyen-Xuan, "A polytree-based adaptive polygonal finite element method for topology optimization," *International Journal for Numerical Methods in Engineering.*, vol. 110, no. 10, pp. 972–1000, 2017.

[161] S. Zargham, T. A. Ward, R. Ramli, and I. A. Badruddin, "Topology optimization: A review for structural designs under vibration problems," *Structural and Multidisciplinary Optimization*, vol. 53, no. 6, pp. 1157–1177, 2016.

[162] J. Lin, Y. Guan, G. Zhao, H. Naceur, and P. Lu, "Topology optimization of plane structures using smoothed particle hydrodynamics method," *International Journal for Numerical Methods in Engineering*, vol. 110, no. 8, pp. 726–744, 2017.

[163] C. Talischi, G. H. Paulino, A. Pereira, and I. F. M. Menezes, "PolyTop: a Matlab implementation of a general topology optimization framework using unstructured polygonal finite element meshes," *Structural and Multidisciplinary Optimization*, vol. 45, no. 3, pp. 329–357, 2012.

[164] K. Liu and A. Tovar, "An efficient 3d topology optimization code written in matlab," *Structural and Multidisciplinary Optimization*, vol. 50, no. 6, pp. 1175–1196, 2014.

[165] Cayan Tower (Infinity Tower), designed by Skidmore, Owings & Merrill. (2013). URL: Http://cayan.net.